Ultracold atomic gases of strontium: production and narrow-line spectroscopy

ACADEMISCH PROEFSCHRIFT

ter verkrijging van de graad van doctor
aan de Universiteit van Amsterdam
op gezag van de Rector Magnificus
prof. dr. ir. K. I. J. Maex
ten overstaan van een door het College voor Promoties ingestelde commissie,
in het openbaar te verdedigen in de Agnietenkapel
op woensdag 5 februari 2020, te 10.00 uur

door

Oleksiy Onishchenko

geboren te Chernihiv

Promotiecommissie

Promotor	prof. dr. F. E. Schreck	Universiteit van Amsterdam
Co-promotor	dr. G. A. Siviloglou	Southern University of Science and Technology of China
Overige leden	prof. dr. H. B. van Linden van den Heuvell	Universiteit van Amsterdam
	prof. dr. C. J. M. Schoutens	Universiteit van Amsterdam
	dr. N. J. van Druten	Universiteit van Amsterdam
	prof. dr. K. S. E. Eikema	Vrije Universiteit Amsterdam
	prof. dr. B. Laburthe-Tolra	Université Paris 13

Faculteit der Natuurwetenschappen, Wiskunde en Informatica (FNWI)

Voor Jacqueline

“Life is not easy for any of us. But what of that? We must have perseverance and above all confidence in ourselves. We must believe that we are gifted for something and that this thing must be attained.” (Marie Skłodowska-Curie)

"Science and everyday life cannot and should not be separated." (Rosalind Franklin)

"For a successful technology, reality must take precedence over public relations, for Nature cannot be fooled." (Richard P. Feynman)

ISBN: 978-946-402-029-8
Printed by Gildeprint B.V., Enschede, The Netherlands

The author can be reached at:
oleksiy1990@gmail.com

The research reported in this Thesis was carried out at the Van der Waals-Zeeman Institute, Institute of Physics, University of Amsterdam. This project has received funding from the European Research Council (ERC) under the European Union's Seventh Framework Programme (FP7/2007-2013) (Grant agreement No. 615117 QuantStro). The collaborators immediately involved in the research described in this Thesis were supported by the Netherlands Organisation for Scientific Research (NWO) through the Gravitation grant No. 024.003.037, Quantum Software Consortium, by the European Commission through Marie Skłodowska-Curie grant SYMULGAS, No. 661171, and by the Ministry of Education of the Republic of China (Taiwan) through an MOE Technologies Incubation Scholarship.

Cover design: Jacqueline Martínez Castillo. A template from ©Marketplace Designers was used in designing the front cover, and a photo from ©Marketplace Designers was used on the front cover, spine, and back cover, all via Canva.com. The silhouette image on the back cover is used under license from Shutterstock.com (Image ID: 70582060, author: Rey Kamensky) Also on the front cover: ballistic expansion of ^{84}Sr Bose-Einstein condensate (credits to Georgios Siviloglou) and a combined spectrum molecular iodine and of the $^1S_0$ - $^3P_2$ line of ^{87}Sr (taken from O. Onishchenko *et. al.* Phys. Rev. A 99, 052503 (2019)).

Contents

Chapter 1

Introduction

The field of what came to be known as "atomic physics" stands at the origin of quantum theory itself. The spectra of different chemical elements, which showed light emission at discrete wavelengths (sharp and well-separated lines of specific colors), were one of the early indications that the energy levels of atoms are quantized. That observation cannot be explained by Maxwell's electromagnetic theory, and it gave a major input into the development of quantum theory. Atomic spectroscopy, which means the measurement of transition energies between different energy levels in atoms, became possibly the single most widespread research direction in atomic physics and one of the major ways to test the predictions and calculations of quantum theory itself; it remains at the forefront up to this day. Atomic spectroscopy underpins the operation of optical atomic clocks, which are among the most precise and stable measurement devices ever constructed [1]; furthermore, one of the ways to test tentative physics theories beyond the Standard Model involves measurements of the possible permanent electric dipole moment (EDM) of the electron using molecular spectroscopy [2], which is a natural extension of atomic spectroscopy in the sense that one measures energy level differences in molecules rather than in single atoms. Spectroscopy and atomic physics have progressed enormously in terms of measurement precision and sensitivity since the observation of the sodium emission lines around 1900, but the fundamental idea still stands. In fact, one of the results of this Thesis is the measurement of a specific ultranarrow transition in atomic strontium.

While atomic physics in general and spectroscopy in particular are by now more than a century old, the technological developments in laser physics in the 1980's opened up a different research direction, namely laser cooling and ultracold atomic gases. It became possible to remove kinetic energy from the atoms up to the point where their quantum statistics becomes a crucial factor in understanding their observed behavior. This gave at once the possibility to create and investigate a new form of matter, known as a Bose-Einstein condensate [3], to perform precision measurements using matter waves, which are in some ways analogous and in other ways different from the commonly known light waves [4, 5], and to create a new experimental approach to investigating difficult problems in condensed matter physics, known as "quantum simulation" [6]. In addition, laser cooling gave a huge boost to precision to spectroscopy itself: optical lattice clock spectroscopy crucially relies on ultracold atoms. A major part of the work described in this Thesis deals with the construction of a new experimental apparatus for producing and investigating ultracold gases of strontium.

1.1 The coolness of strontium

The initial attempts at Bose-Einstein condensation used cryogenic cooling of spin-polarized hydrogen, which is the lightest chemical element and is thus expected to Bose-condense at the highest temperature [7]. However, the first observed condensates were made with alkali metal atoms: rubidium [3], sodium [8], and lithium [9]. Four years after the first Bose-Einstein condensates (BEC), researchers observed the effects of Fermi-Dirac statistics in an ultracold atomic gas of potassium-40 [10]. In general, *quantum degeneracy*[1] is the name for the situation where the effects of quantum statistical distributions (Bose-Einstein or Fermi-Dirac) are experimentally observable. The theoretical concepts behind ultracold Bose and Fermi gases are described in Refs. [11, 12], and the experimental aspects, together with an overview of the early work, are given in Refs. [13, 14].

It later became clear that atoms with the electronic structures that are very different from those of the alkalis can open up new research opportunities. One of the major points is that a new electronic structure can provide laser-accessible transitions with vastly different natural linewidths. This is the arena where strontium comes into play. Strontium is a group-II element of the periodic table, which means that it has two valence electrons, unlike the alkalis, which only have one. According to the addition of angular momentum rules [15], the spin states of the two electrons can be paired in a singlet or triplet configuration [16]. Since the electric dipole transitions that are driven by a laser field are described by the matrix elements of the dipole operator[2], and since that operator acts only on the spatial part of the wavefunction and not on its spinor [17], electric dipole transitions to a first approximation cannot connect two electronic eigenstates one of which is a spin singlet and the other one is a spin triplet. This goes under the name of *dipole-forbidden transitions*. In reality, such transitions are not truly forbidden due to perturbing terms in the atomic Hamiltonian [18] or possibly interactions with an external magnetic field [19], and they can still be excited with a laser, but their linewidths are narrow (kHz) to ultranarrow (mHz).

In the case of strontium, the available electronic transitions are especially convenient, because one has three different classes of them, whose linewidths are orders of magnitude apart. They can be used for different experimental purposes, and Fig. 1.1 shows transitions between the low-lying electronics levels of Sr. There is the $30.5\,\mathrm{MHz}$-wide dipole-allowed transition at $461\,\mathrm{nm}$ that is useful for efficient slowing of a fast atomic beam and for trapping a relatively hot cloud (this will called the "blue transition") [20, 21]. There is the $7.4\,\mathrm{kHz}$-wide singly-forbidden transition at $689\,\mathrm{nm}$, which can be used for making a very cold gas only by laser cooling (this will be

[1] The word *degeneracy* comes from the Latin prefix *de-*, which denotes the absence of something, and the root *gen-*, which has the meaning of "birth" or "origin", or, in a more philosophical sense, "provenance". In this context, the word refers to the fact that the atoms are indistinguishable, the fact which lies at the basis of quantum statistical distributions. So essentially at quantum degeneracy, the atoms have "no origin", they are absolutely identical in all aspects, and this must be explicitly accounted for.

[2] Mathematically speaking, the rate of an electric dipole transition is proportional to the square of the dipole matrix element between the two eigenstates [17]. The singlet and triplet spinor parts are orthogonal, meaning that the dipole operator matrix element between a singlet and a triplet will always evaluate to zero, because the dipole operator cannot affect the spinor.

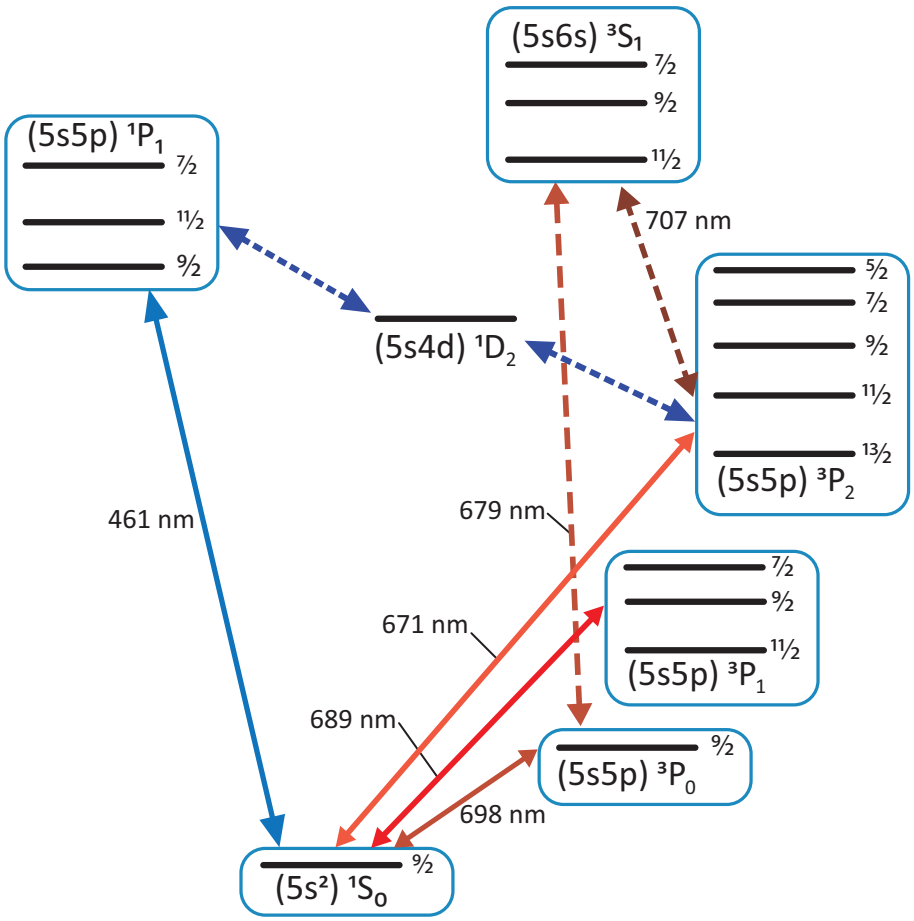

FIGURE 1.1: Electronic transitions, term symbols, and wavelengths of the low-lying levels of ^{87}Sr, which is a fermion. In all bosonic isotopes, the hyperfine structure, represented here by the half-integer values that correspond to the total angular momentum F, collapses to a single level for each term symbol shown in the standard $^{2S+1}L_J$ notation (Figure is courtesy of Sergey Pyatchenkov).

called the "red transition") [22]. The particularly beneficial linewidth of this transition makes it possible to achieve a BEC without an evaporative cooling step [23], or to continuously operate a magneto-optical trap at an exceptionally high phase space density [24]. The linewidth of this transition in Sr has a very fortunate value: the corresponding transition in calcium, which is the closest analog of Sr on the lighter atom side, is too narrow to be of much practical use in cooling without quenching on some broad line [25], while the corresponding one in ytterbium, the closest analog on the heavier atom side, has an approximately 25-fold larger linewidth [26], which leads to a 25-fold larger Doppler temperature [27] and consequently makes it impossible to laser-cool to such a high PSD[3]. Finally, there are the ultranarrow, doubly forbidden, mHz-wide transitions at 698 nm and 671 nm, where the first one can be used for optical atomic clocks [1, 28], and the second one for Raman coupling schemes and the generation of artificial gauge fields

[3]By "closest analog" here we mean the atoms that have a similar electronic structure in the lowest electronic states, differing only by the wavelengths of the transitions and their linewidths, and we also only take into account the species that have already been brought to quantum degeneracy.

[29], or for shelving atoms during the experimental sequence. This last point is important: due to the Fourier relation between the linewidth and the lifetime, an ultranarrow transition is useful in two ways: one can do high-precision spectroscopy, or one can excite the atoms to the upper state, which can be metastable with several seconds of lifetime, and let them temporarily reside there unaffected by laser beams while other parts of the experimental sequence are running. For example, such shelving is at the basis of quantum computation proposals with Sr and other alkaline-earth atoms [30]. Thus, the electronic structure of Sr makes it an interesting choice as an atomic species to work with.

There are also important and interesting properties of Sr, related to its nuclear spin and collisional interactions. Fermionic ^{87}Sr has nuclear spin $I = 9/2$, and the magnetic substates of the nuclear spin do not interact almost at all with the electronic shell in the ground state. As the collisional properties of ultracold atoms are determined by the electrons, this leads to the fact that the collisional interactions do not scramble the nuclear spin substates. This situation is known as SU(N) symmetry and it is especially interesting for engineering systems with exotic forms of magnetism [31, 32]. In fact, a recent major achievement is the experimental observation of SU(N) effects in an atomic system, and it uses the two advantages of Sr, nuclear spin state symmetry during collisions and the presence of ultranarrow spectral lines, in one experiment [33]. One can imagine that this direction provides ample opportunities in the realm of exotic magnetism and frustrated systems. Furthermore, dynamics within the subspace of nuclear m_F states in ^{87}Sr can be viewed as a synthetic dimension; this is the basis for a proposal for quantum simulation of dimensions beyond the three spatial ones (synthetic dimensions) [34]. Finally, in the context of quantum information processing, the collisional independence of nuclear spin substates makes it possible to use them as qubit states; SU(N) symmetry combined with the availability of an ultranarrow clock line and the associated metastable excited state are used in a quantum computation proposal for Sr and other alkaline-earth elements [35].

Regarding the disadvantages of Sr, the single biggest one is the absence of magnetic Feshbach resonances in the electronic ground state due to the fact that the total electronic magnetic moment is zero [36]. However, this turns out to not be a major limitation. First of all, the scattering lengths of bosonic ^{84}Sr and fermionic ^{87}Sr are 124 and 97 Bohr radii respectively [37], which already makes them excellent for evaporative cooling to quantum degeneracy[4]. Secondly, even though the standard magnetic Feshbach resonances in the ground state are not available, the presence of metastable electronic states gives new opportunities for exploring the Feshbach resonances involving the ground and a metastable state [38]. In the case of Sr, this is unexplored territory with potentially many opportunities.

All of the discussion above suggests that a new experimental apparatus for ultracold Sr will provide many interesting research directions. This is the main reason why we set out to build such an apparatus.

[4]Remember that a sample of identical fermions on its own has a scattering length of zero due to Pauli exclusion principle. However, in this case the scattering length refers to non-identical fermions, and so in a Sr sample containing a mixture of 10 nuclear spin substates, the atoms do interact by collisions as long as their nuclear spin substates are different.

1.2 General overview of the experimental apparatus and procedure

A quantum gas machine like ours is fundamentally a long ultrahigh vacuum (UHV) tube with different magnetic field configurations and optical access ports (generally known as *viewports*) for laser beams along the way. The atoms will fly along this tube, and the parts are arranged in the way that allows different slowing processes to happen one after another, removing the atoms' kinetic energy until they can be optically trapped and levitated. Eventually there can be other UHV sections into which the ultracold gas is transported for measurements, as is the case in our setup.

An important design consideration is the necessary UHV quality for quantum gas experiments. A rule of thumb is that the background gas pressure should be at most several $10^{-11}\,\mathrm{mbar}$. The main point is that the lifetime limit caused by background gas collision losses, which are proportional to the background pressure, should be longer, and ideally much longer, than MOT and evaporation time, otherwise atoms would be lost faster than they can be cooled to quantum degeneracy. As two examples, successful achievement of quantum degeneracy with sodium reports the UHV quality of below $10^{-10}\,\mathrm{mbar}$ [39], and a metastable helium BEC is achieved at a background pressure of $1 \times 10^{-10}\,\mathrm{mbar}$ [40]. Therefore, aiming below $1 \times 10^{-10}\,\mathrm{mbar}$ is a good design goal, and the higher the UHV quality, the more future-proof the machine is, because it makes possible a larger range of experiments, which is especially true in Sr, where mHz-wide transitions are available for precision measurements with long interactions times.

Let us take a brief journey through our UHV system and get an overview of the main components. First of all, several small chunks of solid strontium metal are put into a reservoir at the building stage; it will be kept hot at all times and will provide the atoms for our experiments. There is a set of microtubes at one end of the reservoir, which form a directed and collimated beam of atoms; the relevant theoretical results for this are mentioned in Section 4.1, and the construction is described in Section 5.1. Afterwards, it is useful to collimate the atomic beam even better by optical means, which is known as *transverse cooling* (TC), and it is discussed in Sections 2.2 and 5.2 (in addition, the general principles of laser cooling are explained in Section 2.1). The next slowing stage is the *Zeeman slower* (ZS), where the atoms lose the largest portion of their initial kinetic energy. It is also the longest functional unit in the atom flight path, and it is described in detail in Sections 2.2 and 5.3. If we think in terms of temperature, we will realize that the atoms exiting the ZS are already extremely cold compared to any everyday temperature and most lab temperatures; in particular, they can be colder than the approximately $3\,\mathrm{K}$ achievable with a standard liquid helium cryostat, for example. More importantly for us, these atoms are slow enough to be trapped by optical forces in the next step and cooled further.

The end of the ZS opens into the main chamber, where the final stages of laser cooling take place and where some experiments can be performed (in particular, all the experiments within the scope of this Thesis were done in the main chamber). The first trapping and cooling step here is the *magneto-optical trap* (MOT). A MOT is a particular configuration of the laser beams along the three axes, together with a quadrupole magnetic field (see Sections 2.3, 7.1, 7.2). The magnet design and construction are explained in Sections 4.2 and 5.4. In the case of strontium, a

convenient MOT approach involves two stages: at first we will use the broad blue transition (this will be called the "blue MOT"), and afterwards the narrow red one (this will be called the "red MOT"); Sections 7.1, 7.2 describe the details. As we will see, this reduces the atoms' kinetic energy tremendously, to an equivalent of about 1 µK, when converted to temperature; such low energies are only in the realm of laser cooling and they are not achievable by any bulk cryogenic techniques. Note that the MOT in general is used in most ultracold atom experiments; the use of two stages, however, is purely based on the electronic structure of strontium.

The scattered photons from MOT beams, however, cause heating and undesirable momentum transfer to the quantum gas due to the finite linewidth of the laser cooling transition, momentum transfer in the spontaneous emission process, and reabsorption of the previously scattered photons in a dense atomic sample. Therefore, established techniques for reaching quantum degeneracy require cooling by different means, namely without using near-resonant light. A convenient approach involves levitating the atoms against gravity at the focus of a far off-resonant laser beam, known as an *optical dipole trap* (ODT)[5]. Such a laser beam can create a potential energy minimum of a certain depth, compared to the vacuum outside; Section 2.4 explains the theory of ODT and closely related techniques, and Section 7.3 shows our experimental implementation. Thus, the atoms from the MOT are loaded into an ODT, which spatially overlaps with the MOT and confines them to a region measuring several tens of µm across. The ODT can then be slowly lowered in power, which reduces its depth and in this way lets the most energetic atoms escape. Under appropriate conditions, the atomic sample will reach thermal equilibrium at a lower energy. This process is known as *evaporative cooling* and it is explained in Sections 2.5 and 7.4. Finally, when the thermal energy becomes low enough, a sample of bosons undergoes a phase transition to a BEC, while a sample of fermions starts exhibiting measurable effects of the Fermi pressure and becomes a *degenerate Fermi gas* (DFG).

There are also two side chambers in the machine that are not located along the tube through which the atoms travel towards the MOT area. The reason for adding these side chambers is future reconfigurability and optical access. Fundamentally, given a finite area and number of viewports and a particular electromagnet geometry, certain kinds of experiments may become impossible simply because, for example, a laser beam cannot be added or a given magnetic field cannot be achieved in the setup that must be in place in order to achieve quantum degeneracy in the first place. One way to circumvent these limitations is to add a chamber into which a ready-made ultracold gas sample can be transported using a single far off-resonant beam with movable focus. In that chamber then, most of the infrastructure for degenerate quantum gas preparation is not needed, which frees up access. The side chambers of our machine are described in Sections 5.7 and 5.8.

[5]Off-resonant scattering can still happen in such a far off-resonant beam, but it is an undesirable process that we try to minimize by choosing the appropriate laser wavelength and intensity.

Chapter 2

Atom-light interaction, evaporative cooling, and data analysis

We would like to provide concise explanations of the mathematical tools that will allow us to calculate the behavior of atoms in near-resonant and far off-resonant laser beams, as well as the basic data analysis for ultracold gas images. These results are useful for any experiment with laser cooling and trapping. For example, they give the tools for modeling the expected behavior in different parts of an ultracold gas experiment, and thus for minimizing trial-and-error in the design phase. The goal is explain the governing equations and in the end to express them in terms of experimentally accessible or known quantities so that they can be immediately used in numerical simulations or fitting routines. As this is a theoretical discussion, we put emphasis on the clarity of assumptions and interpretation of results, and we try to outline the ranges of their applicability.

2.1 Fundamentals of laser cooling and atom-light interaction

The basic idea behind standard laser cooling techniques, such as optical molasses, Zeeman slowing, or magneto-optical trapping, is momentum conservation during photon absorption and emission, momentum belonging to both the atom and the photon. In fact, in the context of ultracold atom experiments, "cooling" means reducing the kinetic energy of the atoms, so a more descriptive term would be "laser slowing". Consider that for a free massive particle, linear momentum and kinetic energy are in a one-to-one correspondence, related by the equation

$$E = \frac{\hbar^2 k^2}{2m}, \tag{2.1}$$

which is obtained by solving the Schrödinger equation with $V = 0$ [41]. Therefore, reducing kinetic energy is equivalent to reducing momentum. On the other hand, photons carry momentum given by $p = \frac{h}{\lambda} = \hbar k$, where λ denotes photon wavelength and k, defined by $k \equiv \frac{2\pi}{\lambda}$, is the laser wave number (it is the magnitude of the laser *wave vector*, or *k-vector*) [41]. As the total momentum of the atom-photon system is conserved in an interaction, the atom and photon momenta must be added in order to obtain the final momentum of the excited atom. Consequently, when an atom absorbs a perfectly counterpropagating photon, its own momentum must decrease by $\hbar k$. At a later time, given by the lifetime of the excited state, a photon will be

reemitted and the atom will return to the electronic ground state, but the k-vector of that photon has a random direction. The momentum transferred to the atom by spontaneous emission will then also be in a random direction and will average out to zero over many absorption-emission cycles[1]. Here is then the fundamental laser cooling idea: set up a system in such a way that atoms moving in a certain direction preferentially absorb the light propagating in the opposite direction, and let momentum conservation do the job. An important challenge is to find out how to induce this preferential absorption.

An atom that interacts with photons at a frequency close to one of its electronic transition energies and far from all other electronic transition energies can be approximated as a two-level system interacting with an electromagnetic field[2]. We can then use the optical Bloch equations to find the scattering rate (in units of $1/\mathrm{s}$) for this transition:

$$R_{\mathrm{sc}} = \frac{\Gamma}{2}\frac{s}{1+s+4\Delta^2/\Gamma^2}, \tag{2.2}$$

where Γ denotes the transition linewidth and is the inverse of the excited state lifetime τ, $\Gamma = 1/\tau$, s is the saturation parameter, and Δ is the laser detuning from the atomic resonance, given in units of angular frequency. Here, s is defined by $s \equiv I/I_{\mathrm{sat}}$, where I is the excitation laser intensity and $I_{\mathrm{sat}} = \frac{2\pi\hbar^2\Gamma c}{3\lambda^3}$ for a transition at wavelength λ and is known as the *saturation intensity* [27]. Eq. (2.2) describes at once three crucial laser cooling configurations: optical molasses, Zeeman slowing, and magneto-optical trapping (MOT). We will see that appropriate choices of detuning, laser intensity and polarization, together with the use of Zeeman and Doppler effects, make laser cooling possible.

Let us consider the effect of photon scattering events on an atom's motion through space and thus describe the slowing process itself. The calculations will be completely classical, which immediately looks like a strange approach for atoms. However, the Ehrenfest theorem states that the expectation values of quantum observables obey classical physics equations [41]. Consequently, if we do not worry about the exact spread of atomic wave packets, but only about the center of mass motion, and if the atoms are not confined to traps with non-negligible energy level separation due to the quantization rules, we can get an excellent approximation by using only classical equations and viewing atoms as objects with a given mass, position, and velocity[3].

[1] The momentum of the reemitted photons averaging out to zero does not mean that they have no overall effect. This reemission leads to a random walk in momentum space. The combination of cooling and heating due to this random walk will set a cooling limit in this scenario, known as the *Doppler limit* [27]

[2] Let us note here that we only consider transitions starting from an electronic level that is actually occupied. In the context of laser cooling in ultracold atom experiments, we generally only consider the transitions starting either from the electronic ground state or from a metastable state like in the case of He*, because those states are occupied with essentially unity probability in the absence of laser light.

[3] This description is not valid close to and at the point of quantum degeneracy, for systems in deep traps, like ions or optical lattices, and for cooling narrow-line cooling (see Ref. [22] for an example of that). The reason is that the classical approximation is only valid when the spatial extend of the atomic wavepacket is much smaller than the length scale on which laser beam intensity changes appreciably, and the uncertainty in transition frequency, caused by the spread of the atomic wavepacket in momentum space and the associated Doppler effect, is much smaller than the natural linewidth of the cooling transition [42].

By Newton's Second Law:

$$\mathbf{F} = \frac{d\mathbf{p}(t)}{dt} = M\frac{d\mathbf{v}(t)}{dt}, \tag{2.3}$$

and therefore

$$\frac{d\mathbf{v}(t)}{dt} = \frac{1}{M}\frac{d\mathbf{p}(t)}{dt}, \tag{2.4}$$

where M is the mass of the atoms. Photon scattering events can be seen as a time-averaged force on the atoms, because they lead to a change of momentum. Assuming that the atom and the photons counterpropagate, we get

$$\frac{d\mathbf{p}_{\text{atom}}(t)}{dt} = -\frac{d\mathbf{p}_{\text{photons}}(t)}{dt} \tag{2.5}$$

by momentum conservation. Approximating the derivatives as time-averaged quantities, we can write $\frac{d\mathbf{p}_{\text{photons}}}{dt} \approx \frac{\Delta\mathbf{p}_{\text{photons}}}{\Delta t}$, where Δt denotes an arbitrary time period, large compared to the average time between photon scattering events, and $\Delta\mathbf{p}_{\text{photons}} = N\hbar k$ is the total change of the photons' momentum within Δt, N being the total number of photons scattered within Δt, and each photon carrying $\hbar k$ of linear momentum. The average number of scattered photons per unit of time is the photon scattering rate R_{sc}, so $\frac{N}{\Delta t} = R_{sc}$, which means that $\frac{\Delta\mathbf{p}_{\text{photons}}}{\Delta t} = \frac{N}{\Delta t}\hbar k = R_{sc}\hbar k$. Returning to the continuum formulation, we obtain

$$\frac{d\mathbf{p}_{\text{atom}}(t)}{dt} = -R_{sc}\hbar k. \tag{2.6}$$

This result is known as the *radiation pressure force* and it is derived in a more rigorous manner in the text leading up to eq. 5.449 in Ref. [43]. Substituting these results into eq. (2.4), we get:

$$\frac{d^2x(t)}{dt^2} = -\frac{1}{M}R_{\text{sc}}(x,t)\hbar k, \tag{2.7}$$

with $x(t)$ denoting the center position of the atom's wave packet, and we are considering here for simplicity motion in one dimension[4]. Note here that R_{sc} is written as a function of space and time: this is important in experiments because the detuning Δ is a function of space and time due to the Doppler and Zeeman effects; this lies at the basis of Zeeman slowing and MOT.

The limiting value of the radiation pressure force can be found from Eqs. (2.2), (2.3), and (2.7). It is fundamentally determined by the natural linewidth of the chosen atomic transition. Assume that the laser is tuned exactly on resonance to a transition, in which case $\Delta = 0$ so $R_{sc}(\Delta = 0) = \frac{\Gamma}{2}\frac{s}{1+s}$. Since $\lim_{s\to\infty}\frac{s}{1+s} = 1$, we will get $R_{sc}^{(\text{max})} = \frac{\Gamma}{2}$. This makes sense because we are relying on spontaneous reemission of photons, and that process is limited by the natural lifetime of the excited state: higher laser power will simply induce Rabi oscillations by stimulated

[4]For motion in three dimensions, both the position vector of the atom and the k-vector of the laser must be decomposed along the coordinate axes, and then three independent equations must be solved.

emission, which is useless for laser cooling. This observation also explains why one wants to use broad transitions (large Γ) for slowing down atoms from high velocities: one wants to have a large average force to achieve a strong acceleration, which requires a large Γ.

2.2 Shifting transition frequencies: Doppler and Zeeman effects

We have seen that the effective force governing an atom's center of mass motion is described by eq. 2.2, but in order to really describe optical molasses, Zeeman slowing, and MOT using that equation, we should understand what exactly influences Δ. Surely, the simplest way to set that parameter is to detune the laser from the bare atomic transition frequency, onto which a laser can be locked with standard saturated absorption spectroscopy techniques [44, 45]. However, that approach inherently does not have selectivity for particular classes of atoms in the sample and will only globally decrease the scattering rate. On the other hand, Δ is also affected by the velocity of the atoms due to the Doppler effect, and, in case of magnetically sensitive sublevels, by the local magnetic field at the location of the atoms due to the Zeeman effect. It is these two effects that make is possible to efficiently cool and trap atoms with light, and we should understand their governing equations.

The Doppler effect appears because in the frame of reference of moving atoms, the laser light appears upshifted or downshifted in frequency. One can qualitatively understand it by realizing that if an atom moves towards a laser source, it comes from a crest to the next trough of the electromagnetic wave faster than if it were stationary; the result is that the laser frequency appears upshifted to such a moving atom. If an atom is moving away from the laser source, the opposite situation happens and the laser appears downshifted in frequency. Quantitatively then, the resonance condition for an optical transition involving a moving atom is given by [17]

$$\omega_0 = \omega_L - \mathbf{k}_L \cdot \mathbf{v}, \tag{2.8}$$

where ω_0 stands for the angular frequency of the bare atomic transition (stationary atom), ω_L is the laser angular frequency, and $\mathbf{k}_L$ and $\mathbf{v}$ are the laser k-vector and the atom velocity respectively, with all quantities being measured in the lab frame. Assuming that the laser is intentionally detuned from the bare atomic transition, we can find out how the effective value of that detuning changes due to the Doppler effect. Expressing ω_0 as $\omega_0 = \omega_L + \Delta_L$, where Δ_L is the angular frequency detuning actually seen by the atom, we can rewrite eq. (2.8)

$$\omega_L + \Delta_L = \omega_L + \Delta'_L - \mathbf{k}_L \cdot \mathbf{v}, \tag{2.9}$$

where the prime sign denotes the detuning from the bare transition in a stationary atom. Since by definition, ω_L denotes the laser frequency in the lab frame, it is equal on both sides of the equation, and we can subtract it from both sides to obtain

$$\Delta_L = \Delta'_L - \mathbf{k}_L \cdot \mathbf{v}; \tag{2.10}$$

as before, Δ_L is the laser detuning in the atom's reference frame, and Δ'_L is the detuning from the bare transition frequency in a stationary atom. This result makes sense: if we want to achieve a certain target value of Δ_L of the detuning in the atom's frame, which is the value to put into eq. (2.2), and the atom and laser are counterpropagating, which makes $\mathbf{k}_L \cdot \mathbf{v} < 0$, then we must set $\Delta'_L < \Delta_L$. In other words, for the counterpropagating laser beam, the atomic velocity upshifts the laser frequency compared to the lab frame value. Note two important facts about this result: first of all, if the atom is moving exactly perpendicularly to the laser beam, $\mathbf{k} \cdot \mathbf{v} = 0$, so there is no Doppler shift for the atoms moving perpendicularly to the laser beam; secondly, this is a non-relativistic formula, and it can only be applied to atoms moving much slower than the speed of light (this is a very reasonable assumption, because the fastest atoms in an ultracold gas experiment move at most at hundreds of meters per second).

The Zeeman effect shifts the atomic transition frequencies due to the interaction of an atom's magnetic moment with an external magnetic field. If we let $\mathbf{B}$ denote the external magnetic field, then the interaction operator will take the form [46]

$$\hat{H}_Z = \frac{\mu_B}{\hbar}(g_S\hat{\mathbf{S}} + g_L\hat{\mathbf{L}} + g_I\hat{\mathbf{I}}) \cdot \mathbf{B}, \tag{2.11}$$

where the capital subscript Z stands for "Zeeman". By conventional notation, $\hat{\mathbf{S}}$, $\hat{\mathbf{L}}$, $\hat{\mathbf{I}}$ denote the electron spin, electron orbital, and nuclear spin angular momenta respectively, g are the corresponding "g-factors", and μ_B is the Bohr magneton, given in J/T[5]. Labeling the direction of the $\mathbf{B}$-field by z, we can take the dot product in the equation above and obtain

$$\hat{H}_Z^{(z)} = \frac{\mu_B}{\hbar}(g_S\hat{S}_z + g_L\hat{L}_z + g_I\hat{I}_z)B_z. \tag{2.12}$$

Using addition of angular momentum, we can write $J_z = L_z + S_z$, after which $\hat{H}_Z^{(z)}$ can be expressed as

$$\hat{H}_Z^{(z)} = \frac{\mu_B}{\hbar}(g_J\hat{J}_z + g_I\hat{I}_z)B_z, \tag{2.13}$$

where g_J is the *Landé factor* [46]. Let us for now drop the factor $g_I\hat{I}_z$ because $I = 0$ in bosonic Sr (we will get back to the case of fermionic Sr, where $I = 9/2$, and in general atoms with a hyperfine structure). An important assumption in this discussion is that we are interested in the low-field limit case, so we start from the zero-field eigenstates $|J, m_J\rangle$ of the operators $\hat{\mathbf{J}}^2$ and J_z from the atomic Hamiltonian (atomic fine structure is included in this manner); $\hat{H}_Z$ is then treated as a perturbation of these eigenstates[6]. According to first-order perturbation theory, we will have to find the expectation values of the perturbing operators in our chosen initial basis, so we will need the matrix elements of the form $\langle J, m_J| \hat{H}_Z^{(z)} |J, m_J\rangle$ [47]. Angular momentum algebra calculations, combined with the values of 2 and 1 for the electron spin and

[5]For a thorough explanation of the angular momentum operators and the angular momentum algebra, which are the core ideas for the material discussed here, see Chapter 3 of Ref. [47].

[6]The opposite case of the strong magnetic field, called the Paschen-Back limit, is discussed in Chapter 5 of Ref. [47]

orbital g-factors respectively, will lead to the following expression for g_J [46, 27]:

$$g_J \approx 1 + \frac{J(J+1) + S(S+1) - L(L+1)}{2J(J+1)}, \tag{2.14}$$

where J, S, and L denote the angular momentum eigenvalues in conventional notation, and we keep in mind that this expression is only valid when $J \neq 0$, otherwise $\langle J, m_J | \hat{H}_Z^{(z)} | J, m_J \rangle = 0$, which means that the Zeeman effect is absent to first order in perturbation theory. Since we have chosen the basis in which, $\hat{J}_z | J, m_J \rangle = \hbar m_J | J, m_J \rangle$, $\hat{H}_Z^{(z)}$ from eq. (2.13) is diagonal (assuming $I = 0$), and its expectation values give the energy shifts of each m_J state as a function of the applied magnetic field:

$$\Delta E_{m_J} = m_J g_J \mu_B B_z. \tag{2.15}$$

Note here that since we have chosen the direction of the magnetic field to be the quantization axis, so our coordinate axis z, we get $B_z = |\mathbf{B}(\mathbf{r})|$. Basically this means that for a common experimental scenario where we set up a uniform magnetic field and choose the quantization axis to coincide with its direction, the magnitude of the Zeeman shift is determined by the absolute value of the applied magnetic field. The frequency shift of a transition involving a lower electronic level with eigenvalue m_J and an upper electronic level with eigenvalue m'_J will be given, in units of $\mathrm{rad/s}$, by

$$\Delta = \left(\frac{m'_J g'_J \mu_B B_z}{\hbar} - \frac{m_J g_J \mu_B B_z}{\hbar} \right); \tag{2.16}$$

Δ denotes here the detuning from the transition frequency value at $B_z = 0$. This detuning can be used in eq. (2.2) to calculate the scattering rate for atoms in a magnetic field, and logically, any additional laser detuning from the bare transition frequency, including that caused by the Doppler effect, has to be added to this Δ. With a view on Sr, we will mention that for the bosons, which are the subject of this discussion, $m_J = 0$ in $^1S_0$ state. Thus, we now have the general expression for the transition frequency shift between two fine structure levels of an atom in the presence of a weak magnetic field. Note that these expressions are also valid for the atoms in which the hyperfine structure is present ($I > 0$), but the hyperfine splittings are smaller than the magnetic field-induced Zeeman shift [46]; this situation will arise in the particular case of ^{87}Sr $^1P_1$ state.

Let us generalize this discussion to the case of an atom with hyperfine structure splittings that are larger that the expected Zeeman shifts [46], which will apply to ^{87}Sr. In that case, one should define the total angular momentum operator in the magnetic field-free Hamiltonian to be $\hat{\mathbf{F}} = \hat{\mathbf{J}} + \hat{\mathbf{I}}$ [47], which will also lead to $F_z = J_z + I_z$. Since we are still working in the limit of a weak magnetic field, we take the resulting field-free Hamiltonian eigenstates as our basis states, which will be the eigenstates of the operators $\hat{\mathbf{F}}^2$ and F_z, labeled $|F, m_F\rangle$. According to first-order perturbation theory with these eigenstates, one will need to calculate the expectation values of the perturbation operator $\hat{H}_Z^{(z)}$ in this basis; these expectation values have the form

$\langle F, m_F | \hat{H}_Z^{(z)} | F, m_F \rangle$. This calculation will lead to the Landé g-factor being given by [46, 27]:

$$g_F \approx g_J \frac{F(F+1) - I(I+1) + J(J+1)}{2F(F+1)}, \tag{2.17}$$

where g_J is given by eq. (2.14), and the approximation is based on the assumption that the nuclear g-factor is much smaller than g_J. As a consequence, the energy shift of a particular $|F, m_F\rangle$ due to the magnetic field is given by [46, 27]:

$$\Delta E_{m_F} = m_F g_F \mu_B B_z. \tag{2.18}$$

Analogously to eq. (2.16), the modified detuning of a given electronic transition between two hyperfine levels will be [46]

$$\Delta = \left(\frac{m'_F g'_F \mu_B B_z}{\hbar} - \frac{m_F g_F \mu_B B_z}{\hbar} \right), \tag{2.19}$$

with all notation defined in the same way as in eq. (2.16).

This is a good point to discuss the relevant case of the $^1S_0$ ground state Zeeman shifts in Sr; $^1S_0$ is different from the alkali ground states due to the two-electron closed s-shell. First of all, for the bosonic ^{84}Sr, ^{86}Sr, and ^{88}Sr the linear Zeeman shift is absent, as $J = 0$, $I = 0$ (see eq. (2.13)). As for ^{87}Sr, we have $J = 0$, which means that eq. (2.14) cannot be used. However, eq. (2.13) is still well-defined and takes the form

$$\hat{H}_Z^{(z)} = \frac{\mu_B}{\hbar} g_I \hat{I}_z B_z, \tag{2.20}$$

in this case. This perturbing Hamiltonian is diagonal in the $|F, m_F\rangle$ basis, and we will obtain the following expression for the energy shift of an m_F level in the ground state:

$$\Delta E_{m_F}^{(^1\mathrm{S}_0)} = \langle F, m_F | \hat{H}_Z^{(z)} | F, m_F \rangle = \frac{\mu_B}{\hbar} g_I B_z \langle F, m_F | \hat{I}_z | F, m_F \rangle = \mu_B g_I B_z m_F. \tag{2.21}$$

If we compare the definition of our $\hat{H}_Z^{(z)}$ with the eq. (5) in Ref. [48], which expresses the same physical quantity but in slightly different notation, we will see that the nuclear g-factor is given by

$$g_I = \frac{1.0924 \mu_N (1 - \sigma_d)}{2\pi \mu_0 |I|}, \tag{2.22}$$

with the diamagnetic correction $\sigma_d = 0.00345$ for ^{87}Sr [48], and where $\mu_N = 5.051 \times 10^{-27}$ J/T is the nuclear magneton [49], and $\mu_0 = \mu_B/h$, as defined in Ref. [48]. Note that $|I| = \hbar \times 9/2$ for ^{87}Sr. With this, we can rewrite eq. (2.22) to obtain

$$g_I = \frac{1.089 \mu_N h}{2\pi \mu_B \hbar \times 9/2} \approx \frac{2}{9} \frac{\mu_N}{\mu_B}. \tag{2.23}$$

One can show that $\frac{\mu_N}{\mu_B} = \frac{m_e}{m_p}$, so it's equal to the electron-proton mass ratio [41], and thus $\frac{\mu_N}{\mu_B} = 5.45 \times 10^{-4}$. As we saw above, the electronic orbital and spin g-factors are 1 and 2 respectively, but g_I turns out to be approximately 1.21×10^{-4}. Since, according to eq. (2.13), and its diagonalizations (2.15) and (2.18), the energy shift per Gauss of applied magnetic field is proportional to the corresponding g-factor, we can predict that the energy shift of the nuclear m_F substates in the $^1S_0$ state is much less than the shift of the combined nuclear and electronic m_F substates of the $^3P_1$ state to which they couple in the red MOT. This explains the peculiar operation of the ^{87}Sr red MOT (see Section 7.2 and Ref. [37]).

2.3 Optical molasses, Zeeman slower, and magneto-optical trapping

As we have seen in Section 1.2, atoms are initially slowed and trapped inside an ultracold gas machine using TC, ZS, and MOT, and Section 2.1 shows the principle of how the averaged force due to photon scattering lies at the basis of these approaches. We can now use the results from Section 2.2 to get the governing equations for TC, ZS, and MOT. The only difference between these three configurations will be the particular form of the laser detuning Δ seen by the atoms at different points in space and time. In fact, what we will be doing is inserting different expressions for Δ that are appropriate for a given situation, and remembering that the largest possible scattering rate, and thus applied force, occurs for $\Delta = 0$ (all other parameters are either constant by nature, or are kept such); for any $|\Delta| > 0$, the scattering rate is smaller. Note as a reminder that all the analysis of the center of mass motion of atoms is completely classical here (see Section 2.1).

The simplest cooling stage to understand is TC, which is just a two-dimensional implementation of optical molasses. There is no magnetic field involved, so the Zeeman effect can be ignored, and the equations will only involve a Doppler-shifted value for laser detuning. A schematic illustration of the TC setup is shown in Fig. 2.1[7], to which the reader can refer in the discussion below. We remember that Newton's second law is expected to be the appropriate description of the atoms' center-of-mass dynamics and use eqs. (2.2), (2.7), and (2.10), to obtain the expression for the radiation pressure force on the atoms inside the TC beams:

$$F_x = \frac{\Gamma}{2}\hbar\left[-k_L\frac{s}{1+s+4(\Delta'_L+k_L v\sin(\theta))^2/\Gamma^2} + k_L\frac{s}{1+s+4(\Delta'_L-k_L v\sin(\theta))^2/\Gamma^2}\right], \quad (2.24)$$

where x is the coordinate that points along the TC beams, and so across the atomic beam, $k_L = |\mathbf{k}_L|$, M is the atomic mass, Γ is the transition linewidth, s is the saturation parameter, and Δ'_L is the laser detuning from the bare atomic transition, viewed in the lab frame and given in $\mathrm{rad/s}$. Cooling laser power and beam shape will be taken into account by s, which is dependent on the position z along the flight path, as the TC beams are Gaussian and finite in extent. We have evaluated the dot product $\mathbf{k}_L \cdot \mathbf{v}$ in the denominator under the assumption that the laser

[7] That figure and other schematic illustrations in this Thesis were made using the Inkscape [50] open source vector graphics software.

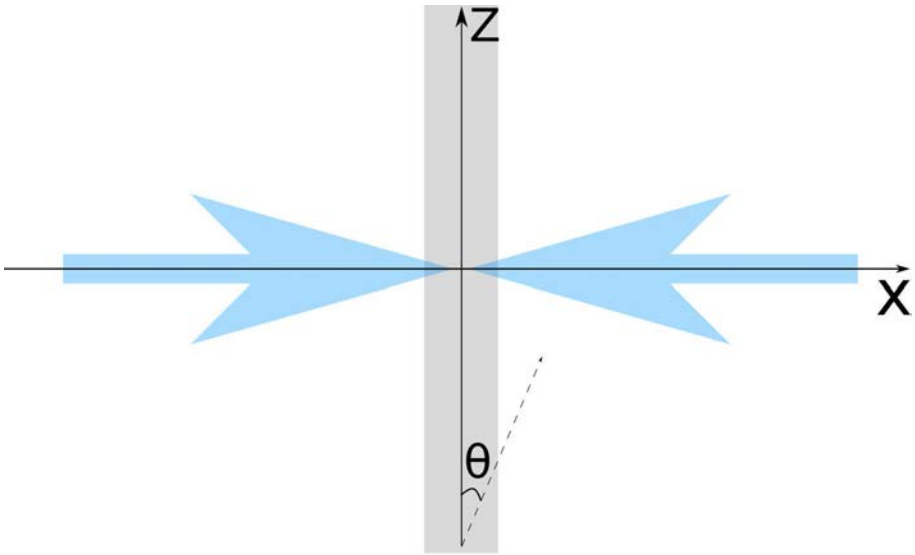

FIGURE 2.1: Schematic illustration of the transverse cooling. The light gray line shows the atomic beam, which is assumed to propagate in the positive z direction. The blue arrows are the TC laser beams. The dashed line signifies the flight path of some atom, and consequently the angle θ is the velocity angle of that atom with respect to the atomic beam path (refer to the main text for further discussion, and note that θ is exaggerated here for illustration purposes). As shown in this case, $\theta > 0$.

beam and the atomic velocity component are in the opposite directions, and θ here denotes the angle between the design direction of the atomic beam and the actual velocity vector of a particular atom. For an idealized perfectly collimated atomic beam, $\theta = 0$ for every atom, and for a real well-collimated atomic beam, θ is small; it can be positive (the atom is moving to the right with respect to the z-axis in Fig. 2.1), or negative (the atom is moving to the left with respect to the z-axis). This θ that will appear later in the angular distribution of the effusing atoms in Section 4.1. Since we are interested in the velocity component perpendicular to the direction of the atoms (that is why it's *transverse* cooling), we use the sine function. In an experiment, Δ'_L is a negative number[8], and $v \geq 0$, because the signs from dot product evaluation are encoded in the $\sin(\theta)$ and $v = |\mathbf{v}|$. Thus, if v is small enough to satisfy $|\Delta'_L| \geq |k_L v \sin(\theta)|$, the product $k_L v \sin(\theta)$ in one of the two terms in square brackets counteracts the effect of Δ'_L and increases the scattering rate, and thus the transverse decelerating force, with increasing v. That is precisely the term that corresponds to the scattering from the laser beam towards which the transverse component of the velocity is pointing, and in fact the first term in square brackets corresponds to the TC beam shining from the right, while the second term is due to the beam shining from the left. This is the logic of optical molasses: the atoms moving against the laser beam get stronger deceleration the faster they move due to a clever use of the Doppler shift, and there is a laser beam shining from each direction in which we want to achieve deceleration. Eq. (2.24) will be used in Section 5.2 for calculating the effects of the TC process. We can also perform the summation in eq. (2.24) and obtain, after some algebra, a single expression for the radiation

[8]This means that the laser has a lower frequency than the bare transition, so we call it a "red-detuned" beam.

pressure force on an atom in the TC configuration:

$$F_x = \frac{\hbar\Gamma k_L}{2} \frac{16\Gamma^2 s \Delta_L k_L v \sin(\theta)}{(\Gamma^2 + \Gamma^2 s + 4(\Delta_L + k_L v \sin(\theta))^2)\,(\Gamma^2 + \Gamma^2 s + 4(\Delta_L - k_L v \sin(\theta))^2)}. \tag{2.25}$$

The first fraction is a prefactor that is completely determined by the properties of the atomic transition in use, and the denominator in the second fraction is simply a positive number that lies within the limits defined by the condition $|\Delta'_L| \geq |k_L v \sin(\theta)|$. Consequently, the numerator of the second fraction tells us that for a given speed v, an atom will experience a stronger restoring force with the increasing angle of deviation θ from the straight path. This is the same conclusion that we reached above by analyzing the two TC beams individually.

The next configuration to understand is the ZS, where we have to take both the Zeeman and the Doppler effects into account. The first demonstration of a ZS is described in Ref. [51]. In this case, four equations must be combined: eqs. (2.2), (2.7), (2.10), and (2.16) or (2.19). The radiation pressure force expression will become then

$$F_z(t) = -\frac{\Gamma}{2}\hbar k_L \frac{s}{1 + s + 4\left(\Delta'_L + \left(\frac{m'_J g'_J \mu_B B_z}{\hbar} - \frac{m_J g_J \mu_B B_z}{\hbar}\right) + kv\right)^2 / \Gamma^2}, \tag{2.26}$$

where all notation has already been defined, and, just like in Fig. 2.1, we take the direction of the atomic motion to be z, and we also assume that the ZS beam is shining in the negative z direction. Notice that in the ZS, the laser and the atomic beam are assumed to exactly counterpropagate, which is why $-\mathbf{k}_L \cdot \mathbf{v} = k_L v$. Furthermore, B_z and v are functions of z, because the magnetic field and the speed change along the ZS path (for simplicity, s is taken to be constant because the laser intensity does not vary much along the ZS for a well-collimated beam). For a real ZS design, a common approach is to require a constant deceleration along the flight path: this is not the optimal but rather a simple solution. For this to happen, we want the scattering rate to not vary along the ZS, which means that the term in parentheses in the denominator of eq. (2.26) must stay constant. Therefore, we require

$$-\Delta'_L = B_z(z)\left(\frac{m'_J g'_J \mu_B}{\hbar} - \frac{m_J g_J \mu_B}{\hbar}\right) + k_L v(z). \tag{2.27}$$

According to simple kinematics of motion with constant acceleration,

$$v(z)^2 = v_0^2 + 2az, \tag{2.28}$$

leading to

$$v(z) = \sqrt{v_0^2 + 2az}, \tag{2.29}$$

where the subscript 0 denotes the initial quantity, z, v, and a are position, velocity, and acceleration, and we assumed $z_0 = 0$. Let us substitute $v(z)$ from eq. (2.29) into eq. (2.27) and solve for

$B_z(z)$. This will result in

$$B_z(z) = -\frac{\Delta'_L}{\xi_Z} - \frac{k_L}{\xi_Z}\sqrt{v_0^2 + 2az}, \tag{2.30}$$

where we have collected all constants into $\xi_Z \equiv \left(\frac{m'_J g'_J \mu_B}{\hbar} - \frac{m_J g_J \mu_B}{\hbar}\right)$ for the ease of notation. Note that $a < 0$ because we are talking about deceleration, and in fact we should choose and set a. One way to do it is to consider that for the optical transition in use, $a_{\text{max}} = -\frac{\hbar k_L \Gamma}{2M}$ according to the discussion in Section 2.1, and we can set $a = \eta_{\text{ZS}} a_{\text{max}}$ for some $0 < \eta_{\text{ZS}} < 1$ [52] (this is the approach that we take in our design and describe further in Section 5.3). Notice also that the magnetic field has a square root dependence on position z. Eq. (2.30) can be directly used for designing a Zeeman slower for a given atomic species. In case the hyperfine states must be taken into account, one has to use eq. (2.19) instead of eq. (2.16) to account for the Zeeman shift of the states involved. The ideal ZS field plots in Section 5.3 use eq. (2.30) with the specific parameters for our setup.

The final laser cooling configuration to understand is the MOT. A common three-dimensional MOT consists of a quadrupole magnetic field and a configuration of three mutually orthogonal, usually retroreflected laser beams; its first experimental demonstration is described in Ref. [53]. There are essentially two ways to analyze a MOT: one is to use one dimension and then simply assume that the orthogonal axes behave completely independently; the other one is to explicitly take the vector nature of the magnetic field into account and to do full 3D analysis. In a simple approach, one is only interested in the slowing efficiency of the MOT; one asks whether atoms with a certain velocity entering the region where the beams cross will be trapped or will escape. In a more advanced analysis, one can look at atom distributions, achievable densities, reabsorption of scattered radiation, or dependence on beam power imbalance, among other things. A theoretical overview of the radiation (optical scattering) force in a MOT is given in Ref. [54], and Ref. [55] presents an analysis of the temperature and density distributions. A 3D analysis of the MOT operation is given in Refs. [56, 57, 58]. We will limit ourselves to the simple analysis along each coordinate axis separately (1D). The reason is that if the atom that one works with has already been brought to quantum degeneracy, then it is clear that the MOT has to work; we are only interested in finding a good beam shape and possibly detuning to use in a particular chamber geometry. The governing equation of motion for atoms in a MOT in the simple analysis will essentially be the same as for the ZS, but the expression for the magnetic field will be different. A quadrupole magnetic field is described by [57]

$$\mathbf{B} = B'[\hat{x}, \hat{y}, -2\hat{z}], \tag{2.31}$$

where B' parametrizes the magnetic field gradient, usually given in $\mathrm{G/cm}$, and determined by the current and the geometry of the coil (see Sections 4.2 and 5.4), and $\hat{x}$, $\hat{y}$, $\hat{z}$ denote the unit vectors along the cartesian coordinate axes. The main message is that it is linear in position along each coordinate axis. Therefore, keeping z as our coordinate, the 1D equation for the

optical force in a MOT takes the form

$$F_z(t) = \frac{\Gamma}{2}\hbar\Bigg[-k_L \frac{s}{1+s+4\left(\Delta'_L + \left(\frac{m'_J g'_J \mu_B}{\hbar} - \frac{m_J g_J \mu_B}{\hbar}\right) B'z + k_L v\cos(\alpha)\right)^2/\Gamma^2} + k_L \frac{s}{1+s+4\left(\Delta'_L - \left(\frac{m'_J g'_J \mu_B}{\hbar} - \frac{m_J g_J \mu_B}{\hbar}\right) B'z - k_L v\cos(\alpha)\right)^2/\Gamma^2}\Bigg], \tag{2.32}$$

where all the notation is the same as above, and α is taken to be the angle between the z-axis and the atomic velocity vector. Notice that this equation describes a cooling configuration (optical molasses) and a trap at the same time. The first term in square brackets corresponds to the laser beam shining in the negative z-direction, and the second term is for the beam in the positive z-direction. If we red-detune the MOT lasers ($\Delta'_L < 0$), then, for small v, the scattering rate increases with increasing v due to the first term when the velocity is positive (then $\alpha = 0$), providing a force in the negative z-direction, or due to the second term when the velocity is negative (then $\alpha = \pi$), providing a force in the positive z-direction. In addition, for a constant v, as the position z increases, the optical restoring force increases as well due to the terms in round brackets and the magnetic field gradient B', which describes a trap. One can also carry out the summation in eq. (2.32) to obtain an analog of eq. (2.25), but we will not do that here and rather clearly see what the two terms of the sum in eq.(2.32) represent[9], and immediately have the expression ready for numerical simulations.

2.4 Off-resonant atom-light interaction and optical traps

Let us now go into a different regime and describe the fundamentals of atom-light interaction for a far off-resonant, instead of a near-resonant, light field in this section. We would like to clarify the meaning of parameters in this case and to make the discussion immediately applicable to current experiments. This topic is often discussed in a two-level approximation [17, 59], but that is not sufficiently detailed to be useful in our work. Just as a simple example, any optical potential is anti-magic (see the next paragraph for the explanation) in a two-level approximation because the energy shift of both levels involved is equal in magnitude by the construction of the problem; in reality we know that this is not true, and in fact we are often interested in the magic wavelength condition [60] (see the next paragraph for the definition of "magic" and "anti-magic" in this context), or in the differences between the polarizabilities of some electronic states in question (this often goes under the name of *light shifts*). We will thus show how to calculate, without resorting to the two-level approximation, some quantities of interest for real atoms interacting with the laser beams that are far off-resonant from any transition involving an initially populated electronic state. This is a crucial topic for current ultracold atom experiments

[9] Of course eq. (2.32) is to be applied along each coordinate axis in order to describe a 3D MOT that is used in the experiment.

because far off-resonant beams are the tools that make an ODT [61] (see Sections 1.2 and 7.3), optical lattices [62, 63], and optical tweezers [64, 65] (see Chapter 9).

Here is a good time to define two important terms: *magic wavelength* and *anti-magic wavelength*, and the ones originating from them, like "magic lattice", "magic ODT", etc. As we have seen above, we are interested in how a far off-resonant beam affects the two electronic states between which we will drive a transition (the transition can be an optical clock line, for example). This is often the electronic ground state and an excited state, although in work with metastable helium, the role of the ground state is taken by a metastable state. Then, if the dynamical polarizabilities [66, 67] of the two electronic states in question are exactly equal at a certain far off-resonant wavelength, is it called the "magic wavelength"; the measured transition frequency will not depend on the trap beam power, shape, etc., so essentially the transition frequency light shift "magically" disappears. In the case that the polarizabilities of the two electronic states are equal in magnitude and opposite in sign at a given wavelength, it is an "anti-magic wavelength". Such a situation can be useful in generating interesting optical potential landscapes, for example [68].

2.4.1 Basic relations for the energy shift in an off-resonant beam

Off-resonant atom-light interaction calculations are, at their basis, the calculations of an atom's electronic eigenenergies in the presence of an oscillating electric field. From standard atomic physics we know that the Hamiltonian for an isolated atom in the absence of external fields generates the electronic eigenstates and their eigenvalues[10] that are labeled as ${}^{2S+1}L_J$, which we call the *term symbols* in spectroscopic notation [16]. If we now apply an electric field to the atom, the new Hamiltonian will reflect that fact according to [43]

$$\hat{H} = \hat{H}_A + \hat{H}_{AF}, \tag{2.33}$$

where $\hat{H}_A$ is the old free atom Hamiltonian whose eigenstates are the given by the term symbols and $\hat{H}_{AF}$ stands for "atom-field interaction". A very commonly used form of $\hat{H}_{AF}$ is $\hat{H}_{AF} = -\hat{\mathbf{d}} \cdot \mathbf{E}$, where $\hat{\mathbf{d}}$ stands for the dipole moment operator for the atom, $\hat{\mathbf{d}} \equiv -e\hat{\mathbf{r}}_e$, $\hat{\mathbf{r}}_e$ is the position operator for the electron, and $\mathbf{E}$ is the applied electric field; this form is known as the electric dipole approximation[11] [43]. We also adopt the semiclassical treatment of the problem: this means that we work in the Hilbert space spanned only by the electronic basis states and we find the matrix elements of the appropriate components of $\hat{\mathbf{d}}$ after having taken its dot product with $\mathbf{E}$, but $\mathbf{E}$ itself is a classical vector field, not a quantum operator [17, 43]. For example, if the electric field is linearly polarized and we take its direction of oscillation to be z, then $-\hat{\mathbf{d}} \cdot \mathbf{E} = -\hat{d}_z E_z$, and

[10] These are only approximate eigenstates for many-electron atoms. Accurate calculation of the eigenstates and eigenvalues is an active research question in computational physics [69, 70].

[11] One can get an intuitive sense of why this interaction Hamiltonian is reasonable by considering that it has the same form as the classical energy of a dipole in an electric field. However, see Refs. [17, 71] for more rigorous mathematical explanations and derivations.

from this point E_z is only a multiplicative factor for the matrix elements of the operator $\hat{d}_z$[12].

A convenient approach to finding the approximate electronic eigenenergies in the presence of atom-field interaction in our parameter regime is time-dependent second-order perturbation theory[13] [15, 72]. Such a calculation will lead to an expression for the energy shift of the perturbed electronic state with respect to the unperturbed one; it directly shows how different the energy of an atom in a given electronic state is inside an applied electric field compared to its energy in a field-free region. Experimentally, the applied electric field here is the off-resonant laser beam. If the energy of an atom inside the beam is lower than outside, such a beam is called an *optical trap*, because it provides an energy well in which an atom can be held. The resulting expression for the light-induced energy shift of an electronic eigenvalue a is [43]

$$U_a = -\alpha_a(\omega)|E_0^+|^2, \tag{2.34}$$

where $\alpha(\omega)$ is the dynamical polarizability of that eigenstate, which is a function of the off-resonant laser angular frequency ω, and $|E_0^+|^2$ expresses the electric field of the laser[14]. Note that in this subsection we only consider the electric field and the energy shift at a single spatial location, because we are interested in the effects related to their magnitude; the discussion will be extended to the spatial variation in the next subsection. The polarizability is given by [43, 73]

$$\alpha_a(\omega) = \sum_j \frac{2\omega_{ja}|\langle a|\,\hat{\epsilon}\cdot\hat{\mathbf{d}}\,|j\rangle|^2}{\hbar(\omega_{ja}^2 - \omega_L^2)}, \tag{2.35}$$

where a is the level of interest, j are all other electronic levels of an atom[15], ω_L is the off-resonant laser frequency, ω_{ja} is the transition frequency from level a to level j, and $\hat{\epsilon}$ is the unit polarization vector of the laser electric field. The calculation of the matrix elements $\langle a|\,\hat{\epsilon}\cdot\hat{\mathbf{d}}\,|j\rangle$ and the polarizabilities themselves from first principles is in itself a research project in computational atomic physics [74, 75, 76], and we will not be doing that directly. We can either directly use the published values of those matrix elements and transition frequencies from theoretical papers, such as Ref. [77][16], or evaluate the matrix elements according to the theory given in Chapter 7

[12] The fully quantum approach would be to quantize the electric field as well and to treat the system in the full Hilbert space of the electronic basis states and mode occupation numbers of the electric field. See Refs. [17, 43] for an explanation of this approach.

[13] It is second order because the first-order terms are zero: the dipole operator has odd parity, so its matrix elements with the bra and ket corresponding to the same state will vanish [43].

[14] We give the symbol U to the quantity that is labeled as ΔE in Ref. [43]. This is simply to underscore that this energy shift is precisely the optical potential that an atom experiences inside the off-resonant beam, and it is conventional to label a potential as U.

[15] Of course in practice one cannot sum over all eigenstates of an atom, because for a real atom, not all matrix elements and transition frequencies are known, and it is not practical to try to calculate them all. One chooses a subset of the ones that have the highest contribution to the sum.

[16] Note an important point that in many theoretical papers, one finds lists of *reduced matrix elements*; in order to find the actual matrix elements to be used in eq. (2.35), one must multiply the reduced matrix elements by the appropriate prefactors that are calculated from the angular momentum algebra of the fine and hyperfine states involved; the reason for which this is possible is the *Wigner-Eckart theorem*, which is described in Chapter 7 of Ref. [43] or in Ref. [15]. Furthermore, the reduced matrix elements are often given in atomic units, in which the electron charge has the value of 1 and the unit of distance is the Bohr radius a_0. In order to convert them to SI units, one must multiply them by $a_0 e$, where e is the electron charge in coulombs.

of Ref. [43] starting from the transition frequencies and the measured decay rates, given in a database [78].

One often already knows very well the polarizabilities of the atomic states of interest at the relevant trap laser wavelengths (the clock states of ^{87}Sr at the magic wavelength or the polarizabilities at $1064\,\mathrm{nm}$ are prominent examples), and one wants to calculate the trap parameters for a given experiment. In that case, the simple eq. (2.34) can be applied immediately. However, in order to correctly write the necessary equations in terms of the quantities measured in the lab, let us take a look at the expression for the electric field of the trap laser, because it can lead to confusion. This electric field is given at some location $\mathbf{r}$ by [43]:

$$\mathbf{E}^{+}(t) = \hat{\epsilon} E_0^{+} e^{-i\omega t}. \tag{2.36}$$

This expression is a mathematical convenience: an electric field is a physical observable, so it is by definition a real, rather than a complex, quantity. The true electric field must be expressed as [43]:

$$\mathbf{E}(t) = \hat{\epsilon} E_0 \cos(\omega t + \phi) = \hat{\epsilon}\left(E_0 \frac{e^{-i\phi}}{2} e^{-i\omega t} + E_0 \frac{e^{i\phi}}{2} e^{i\omega t}\right), \tag{2.37}$$

from which we can identify the relations between the true electric field amplitude E_0 and the amplitudes E_0^{+} and E_0^{-} of the two components of the complex decomposition of the cosine wave as

$$E_0^{+} = E_0 \frac{e^{-i\phi}}{2},\ E_0^{-} = E_0 \frac{e^{i\phi}}{2}. \tag{2.38}$$

What is important here is a factor 2 difference in absolute value between E_0 and E_0^{+} or E_0^{-}, and one must always keep in mind what kind of "amplitude" of the electric field is assumed in any given equation. Finally, substituting eq. (2.38) into eq. (2.34), we can express the energy shift of level a in terms of the real electric field amplitude or the laser:

$$U_a = -\frac{1}{4}\alpha_a(\omega)|E_0|^2, \tag{2.39}$$

and this result agrees with the expression given in Ref. [73].

The commonly measured quantity in a lab is the total beam power[17], from which an expression for intensity can be found under some reasonable assumptions about laser beam properties (see next subsection). It is thus appropriate to give optical trap parameters in terms of off-resonant laser intensity. The time-averaged intensity of an oscillating electric field (meaning, averaged at least through one optical cycle) is given by [79]

$$I = \frac{E_0^2 n}{2Z_0}, \tag{2.40}$$

[17]Sensor S121C from Thorlabs Inc, Newton, NJ, USA is one commonly used device for this.

where we note again that E_0 denotes the amplitude of the real electric field, n is the refractive index of the material where the light wave propagates, and $Z_0 \approx 376.7\,\Omega$ is the impedance of free space. Ultracold atom experiments are done in vacuum, so $n = 1$, and we will set it to be such from now on. We can substitute eq. (2.40) into eq. (2.39) to obtain the energy shift of level a as

$$U_a = -\frac{1}{2}\alpha_a(\omega) Z_0 I, \tag{2.41}$$

which is in agreement with the expression in terms of intensity reported in Ref. [61][18]. A note on units is in order here: polarizabilities are often reported in literature in atomic units. In order to get the energy shift in joules using eq. (2.41) with a value of $\alpha_a(\omega)$ in atomic units (assuming that all other quantities are in SI units), one must multiply that $\alpha_a(\omega)$ by $4\pi\epsilon_0 a_0^3$, where ϵ_0 is the permittivity of free space. In addition, in the case of weak traps, we may have to consider the influence of gravity on the potential in the vertical direction. Gravity effectively makes the trap depth, defined below, smaller, and at some point the trap cannot hold against gravity anymore[19]. This influence is taken into account by adding the gravitational potential to the optical potential, leading to

$$U_a^{(g)} = -\frac{1}{2}\alpha_a(\omega) Z_0 I + Mgy, \tag{2.42}$$

where M is the mass of the atom, $g \approx 9.81\,\mathrm{m/s}$ is the acceleration due to gravity, and the vertical coordinate is taken to be y, because z is used to point along the beam, and the beams are assumed to be horizontal, as in our setup.

2.4.2 Trap depth and trap frequency expressions

The light intensity was expressed in eq. (2.41) as a number rather than as a function of spatial coordinates to underscore the value of the energy shift at a single point in space where a nonzero electric field intensity is present, compared to any point in vacuum where $I = 0$. We can now extend the discussion and consider, $I = I(\mathbf{r})$, so we will account for the spatial variation of the intensity in a real laser beam. Thus, the energy shift will also be given as a function of space, $U_a = U_a(\mathbf{r})$, and this spatial variation will give the trap shape, from which one can evaluate the trap frequencies and the trap depth in the case of dipole traps, or the parameters related to tunneling in the case of an optical lattice formed by retroreflection or a two-beam interference.

The laser beams used for optical trapping are commonly Gaussian in the TEM00 mode [79, 80]. This assumption allows us to write their intensity everywhere in space in terms of the measured total power and beam waist, and thus to express the trap shape in terms of those quantities. These beams often have a cylindrically-symmetric intensity profile, where the

[18] Note that $\alpha(\omega)$, as defined in this text, is the real part of the more general complex polarizability α [43].

[19] In a zero-gravity environment, a harmonic trap would only need to be made deep enough to support one vibrational level in order to hold an atomic gas, provided that the gas can be made sufficiently cold.

following relations hold [80]:

$$I(r,z) = \frac{2P}{\pi w(z)^2} e^{-\frac{2r^2}{w(z)^2}}, \tag{2.43}$$

$$w(z) = w_0 \sqrt{1 + \left(\frac{z}{z_R}\right)^2}, \tag{2.44}$$

$$z_R = \frac{\pi w_0^2}{\lambda}, \tag{2.45}$$

P being the total beam power, w_0 the minimum waist, λ the laser wavelength, r and z the radial and longitudinal coordinates of space respectively, and z_R the Rayleigh range (as written, the beam central axis is assumed to be $r = 0$, and w_0 occurs at $z = 0$). The waist is expressed in the conventional $1/e^2$ sense. In an important case of an elliptical beam, the intensity is given by

$$I(w_x, w_y, z) = \frac{2P}{\pi w_x(z) w_y(z)} e^{-\frac{2x^2}{w_x(z)^2}} e^{-\frac{2y^2}{w_y(z)^2}}, \tag{2.46}$$

where w_x and w_y are the half-lengths of the ellipse axes (semimajor and semiminor axes) given in the $1/e^2$ sense, and each of them evolves according to eq. (2.44), with its own minimum waist and Rayleigh range. Then the trap depth $U_{a,0}$ is defined to be the maximum absolute value of the energy shift compared to vacuum; this maximum occurs at the point of maximum laser intensity, and it is found by setting $r = 0$, $z = 0$ in eq. (2.43):

$$U_{a,0} = -\frac{1}{2}\alpha_a(\omega) Z_0 \frac{2P}{\pi w_0^2}, \tag{2.47}$$

with an analogous expression for an elliptical beam, where w_0^2 is replaced by $w_{x,0}$, $w_{y,0}$[20]. This can be expressed in Kelvins or in Hz by dividing by k_B or h respectively. If there are two beams involved, like in a crossed dipole trap, then we simply take the sum of their intensities (equivalently, powers) for trap depth calculations because they are normally shifted far enough in frequency for their interference to be neglected.

The trap frequency is defined as the frequency splitting between the two lowest energy levels in a harmonic trapping potential, which can be optical or magnetic in nature, but we will focus exclusively on optical trapping. We have thus made the assumption that the potential has harmonic form[21], which is not true in a real trap created by a focused Gaussian beam. However, if the kinetic and potential energy of the atoms are much lower than the total depth of the trap (meaning that the atoms are ultracold), then we can expand the true potential as a Taylor series around the minimum point and approximate it very well with only the quadratic term[22]; that approximation does yield the functional form of a quantum harmonic oscillator potential.

[20] Note that this assumes no astigmatism of the beam; $w_{x,0}$, $w_{y,0}$ are taken to occur at the same point $z = 0$.

[21] This means that the potential energy has the form of a parabola as a function of the spatial coordinates.

[22] According to the properties of derivatives, the linear term is zero when a function is expanded around its extremum.

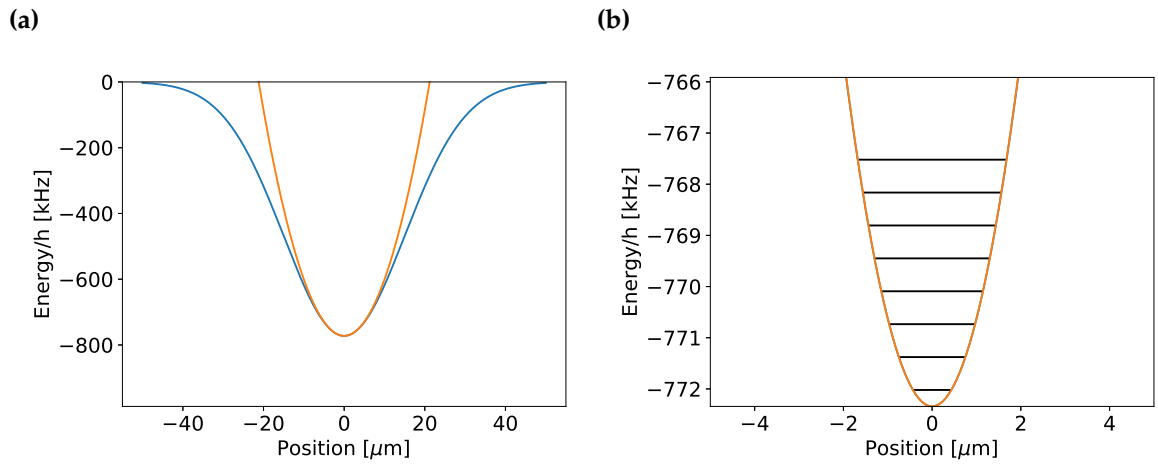

FIGURE 2.2: Harmonic fitting procedure for a Gaussian ODT potential. Subfigure (a) full optical trap (blue) and its quadratic fit (orange); subfigure (b) shows the zoomed in trap bottom with several of its lowest vibrational levels. In this case, the trap laser is assumed to have a waist of $30\,\mu\mathrm{m}$ and $1\,\mathrm{W}$ of power, which are common values for real ODTs. Notice that the normal trap frequencies (see text) are several hundred Hz; one often works with much broader electronic transitions in experiments, which explains why the vibrational sidebands are not resolved in a normal ODT (in optical lattices or optical tweezers, however, trap frequencies can reach hundreds of kHz, and then the sidebands can be easily resolved).

This procedure is graphically illustrated in Fig. 2.2[23]. Immediately performing the calculation for an elliptical beam, given by eq. (2.46), we will first set $z = 0$ and $y = 0$ and find the trap frequencies in the transverse x direction. A Taylor expansion to the second order around $x = 0$ of the x-dependent exponential in eq. (2.46) leads to

$$e^{-2\left(\frac{x}{w_{x,0}}\right)^2} \approx 1 - \frac{2x^2}{w_{x,0}^2}, \tag{2.48}$$

and then by substitution into eq. (2.46) and (2.41) we get

$$U_{\mathrm{H},a}(x) = \frac{1}{2}\alpha_a(\omega) Z_0 \frac{2P}{\pi w_{x,0} w_{y,0}} \frac{2x^2}{w_{x,0}^2}, \tag{2.49}$$

where subscript H stands for "harmonic part" of the potential. We neglected the factor 1 from the Taylor expansion because that gives a total offset (trap depth), and we are interested in the quadratic dependence in order to get the trap frequencies. Setting eq. (2.49) equal to the standard form of the quantum harmonic oscillator potential leads to

$$\frac{1}{2} M \omega_{\mathrm{HO},x}^2 x^2 = \frac{1}{2}\alpha_a(\omega) Z_0 \frac{2P}{\pi w_{x,0} w_{y,0}} \frac{2x^2}{w_{x,0}^2}, \tag{2.50}$$

[23]This figure, and many other calculations and plots in this Thesis were made using the *Python* programming language and the scientific, numerical, and plotting libraries *NumPy* [81], *SciPy* [82], and Matplotlib [83]. Many of the least-squares fits in this Thesis were made using the *LMFIT* [84] library for *Python*.

where ω_{HO} denotes the trap angular frequency and M is the atomic mass ("HO" keeps track of the fact that it's the harmonic oscillator approximation). Algebraic manipulations then yield

$$\omega_{\text{HO},x} = \sqrt{\frac{4}{M}\alpha_a(\omega)Z_0\frac{P}{\pi w_{x,0}w_{y,0}}\frac{1}{w_{x,0}^2}} \tag{2.51}$$

as the expression for trap angular frequency. The corresponding result for the y-axis is obtained by interchanging w_x and w_y, and the value for a round beam is found by having $w_x = w_y = w$. Notice that in the case of a circular trap, we will have the following scaling behavior of the trap frequency as a function of power and beam waist:

$$\omega_{\text{HO},x} \propto \sqrt{P},\ \omega_{\text{HO},x} \propto \frac{1}{w_0^2}. \tag{2.52}$$

The longitudinal trap frequency for a circular Gaussian beam[24] can be found by setting $r = 0$ and Taylor-expanding eq. (2.43) around $z = 0$ to obtain

$$\frac{2P}{\pi w_0^2}\left(1+\left(\frac{z}{z_R}\right)^2\right)^{-1} \approx \frac{2P}{\pi w_0^2}\left(1-\left(\frac{z}{z_R}\right)^2\right). \tag{2.53}$$

As before, we ignore the constant 1 and we only use the z-dependent term to obtain the quadratic expression for intensity:

$$I(z) \approx \frac{2P}{\pi w_0^2}\left(\frac{z}{z_R}\right)^2. \tag{2.54}$$

This can be inserted into the optical potential eq. (2.41) and then again set equal to the standard harmonic oscillator form to get

$$\frac{1}{2}M\omega_{\text{HO},z}^2 z^2 = \frac{1}{2}\alpha_a(\omega)Z_0\frac{2P}{\pi w_0^2}\left(\frac{z}{z_R}\right)^2. \tag{2.55}$$

From this we obtain the expression for the trap frequency in the direction along a single-beam optical trap:

$$\omega_{\text{HO},z} = \sqrt{\frac{2}{M}\alpha_a(\omega)Z_0\frac{P}{\pi^3}\frac{\lambda^2}{w_0^6}}, \tag{2.56}$$

where the Rayleigh range expression has already been substituted. Results (2.51) and (2.56) can be used for calculations in optical tweezer experiments or in single-beam ODT.

It is a common situation that a single-beam ODT does not provide sufficient trapping in its longitudinal direction. One can start to see that by comparing eqs. (2.51) and (2.56), where there is a factor of wavelength squared in the numerator in the second equation. Since the wavelength

[24] Fundamentally, one can do this for an arbitrary beam by numerically fitting a polynomial around the minimum and reading off the coefficient of the quadratic term.

of commonly used Nd:YAG lasers is $1.064 \times 10^{-6}\,\mathrm{m}$, the longitudinal trap frequency tends to be orders of magnitude smaller than the axial one. One can improve the confinement in the longitudinal direction by crossing a second ODT beam at 90° (or at any other angle, in fact[25]); this configuration is called a "crossed ODT". In this case, one normally aligns the beams so that both focuses are as close as possible to the crossing point. The optical potential in a crossed ODT is simply the algebraic sum of the two individual beam potentials[26]. If, as is usually the case, each of the two individual potentials can itself be approximated as a harmonic trap in a given direction x, we can express them in the standard form as

$$U_{\mathrm{H},1} = \frac{1}{2} M \omega_{\mathrm{HO},1}^2 x^2, \tag{2.57}$$

$$U_{\mathrm{H},2} = \frac{1}{2} M \omega_{\mathrm{HO},2}^2 x^2, \tag{2.58}$$

where the subscripts "1" and "2" refer to each potential. Their algebraic sum is then

$$U_{\mathrm{H,total}} = U_{\mathrm{H},1} + U_{\mathrm{H},2} = \frac{1}{2} M (\omega_{\mathrm{HO},1}^2 + \omega_{\mathrm{HO},2}^2) x^2. \tag{2.59}$$

One can see from this result that the harmonic oscillation frequencies add as squares, namely

$$\omega_{\mathrm{HO,total}}^2 = \omega_{\mathrm{HO},1}^2 + \omega_{\mathrm{HO},2}^2. \tag{2.60}$$

In fact, one can imagine more than two beams crossing at a given point; if they can all be approximated as harmonic potentials in a particular direction, then trap frequency addition in squares will hold for all of them and the resulting trap frequency can be calculated according to

$$\omega_{\mathrm{HO,total}}^2 = \sum_{j=1}^{N} \omega_{\mathrm{HO,j}}^2, \tag{2.61}$$

with the index j labeling each of the N crossing beams. Writing out the results above explicitly for the strongly confining direction (vertical) of two Gaussian beams crossing perpendicularly in the horizontal plane, we obtain the optical potential

$$U_{\mathrm{H},a}(x) = \frac{1}{2} \alpha_a(\omega) Z_0 \left(\frac{2P_1}{\pi w_{x,0} w_{y,0}} \frac{2x^2}{w_{x,0}^2} + \frac{2P_2}{\pi w_{\tilde{x},0} w_{\tilde{y},0}} \frac{2x^2}{w_{\tilde{x},0}^2} \right), \tag{2.62}$$

where we have neglected the influence of gravity[27], P_1 and P_2 are the powers of the beams, and the coordinates are defined so that z and $\tilde{z}$ point along each beam, and x, $\tilde{x}$ are in the vertical

[25] See Refs. [85, 86] for a discussion and analysis of a successful implementation of a crossed dipole trap where the beams are specifically set to cross at an angle other than 90°, and the additional effects to consider in such cases.

[26] Remember that it is common in experiments to shift the individual beam frequencies sufficiently far apart so that their interference can be neglected and we can directly add their intensities.

[27] The trap frequencies are an important concept mainly in deep traps, and in that case the influence of gravity is negligible. Gravity is a higher-order effect in trap frequency calculations because it only changes the point around which the original Gaussian beam profile is Taylor-expanded. However, if it is necessary, the effect of gravity can be found by numerically evaluating the second derivative at the new minimum point.

direction across each beam, and y, $\tilde{y}$ are in the horizontal direction across. In this manner, $x = \tilde{x}$, so we use x as the common variable in the equation above, and $w_{x,0}, w_{y,0}, w_{\tilde{x},0}, w_{\tilde{y},0}$ denote the waists. We then get the trap frequency in the vertical direction at the crossing point:

$$\omega_{\mathrm{HO},x} = \sqrt{\frac{4}{M}\alpha_a(\omega)Z_0\left(\frac{P_1}{\pi w_{x,0}w_{y,0}}\frac{1}{w_{x,0}^2} + \frac{P_2}{\pi w_{\tilde{x},0}w_{\tilde{y},0}}\frac{1}{w_{\tilde{x},0}^2}\right)}. \tag{2.63}$$

Finally, if we are interested in the trap frequency that is radial for one beam and longitudinal for the other one, and if we assume that the longitudinal beam has a circular cross-section with the waist w_0 and again neglect the effect of gravity, we can sum up the Taylor expansions in eqs. (2.49) and (2.54) and obtain

$$\omega_{\mathrm{HO},y} = \sqrt{\frac{2}{M}\alpha_a(\omega)Z_0\left(\frac{2P_1}{\pi w_{x,0}w_{y,0}}\frac{1}{w_{x,0}^2} + \frac{P_2}{\pi^3}\frac{\lambda^2}{w_0^6}\right)}, \tag{2.64}$$

where the coordinate systems are defined in the same way as above, and so y means the horizontal direction across for one beam, which by definition will be the longitudinal one for the other beam.

It is also useful to calculate the effect of the off-resonant beam on a transition frequency between two electronic levels of interest, not only the shift of a single level with respect to vacuum. The transition frequency change is determined by the difference in polarizability between the two levels involved, and we will keep working under the assumption of a Gaussian beam ODT and the harmonic approximation for its lowest energy levels. In the roughest calculation, the transition frequency change is the difference between the trap depths for the two levels, divided by h, so it is

$$\Delta\nu_{\mathrm{Stark}} = \left|\frac{1}{2h}(\alpha_a(\omega) - \alpha_b(\omega))Z_0\frac{2P}{\pi w_0^2}\right|, \tag{2.65}$$

based on eq. (2.47) for a single beam trap. Here, "Stark" means that it is the modification of an atom's bare transition frequency by the AC Stark shift, and a and b denote the two electronic levels of interest. This calculation can be improved by considering that we must take the trap vibrational level into account in this problem: an atom will not just go from the electronic ground state to the electronic excited state, but rather it will do so while going from harmonic oscillator level n in the lower state to level n' in the upper state. If $n = n'$, we call such a transition the *carrier*, if $n > n'$, we call this a *red sideband*, and if $n < n'$, it is a *blue sideband*. Notice now an important fact that has already come up in the eq. (2.65): the polarizabilities of the two states involved are in general not equal[28]. Therefore, the shapes of the harmonic potential are not the same, and so the trap frequencies are not the same either. The AC Stark-shift of the transition frequency that involves vibrational level transfer $n = 0 \to n' = 0$ in the transverse direction of

[28] If they are, that's a magic wavelength trap.

the trap beam will be given by

$$\Delta\nu_{\text{Stark}}^{(0-0)} = \left| \left(\frac{1}{2h}\alpha_a(\omega) Z_0 \frac{2P}{\pi w_0^2} + \frac{1}{2}\frac{1}{2\pi}\sqrt{\frac{4}{M}\alpha_a(\omega) Z_0 \frac{P}{\pi w_{x,0} w_{y,0}} \frac{1}{w_{x,0}^2}} \right) - \right.$$
$$\left. - \left(\frac{1}{2h}\alpha_b(\omega) Z_0 \frac{2P}{\pi w_0^2} + \frac{1}{2}\frac{1}{2\pi}\sqrt{\frac{4}{M}\alpha_b(\omega) Z_0 \frac{P}{\pi w_{x,0} w_{y,0}} \frac{1}{w_{x,0}^2}} \right) \right| =$$
$$= \left| \Delta\nu_{\text{Stark}} + \frac{1}{2}\frac{1}{2\pi}(\omega_{a,\text{HO}} - \omega_{b,\text{HO}}) \right|, \tag{2.66}$$

where we used eqs. (2.47), (2.51), and (2.65) and added the zero-point energy to the bottom of each harmonic oscillator. The modified transition frequency between any other two levels, as well as the frequencies of any sidebands, can now be easily calculated by adding the appropriate number of ω_{HO} units in both electronic states.

Finally, for completeness of the discussion, let us derive the relevant equations for a two-beam interference setup that will result in an optical lattice. Consider two counterpropagating laser beams of equal frequency and both being linearly polarized in the same plane. We will ignore the effects of Gaussian beam curvatures and the Gouy phase[87], and model them as plane waves, in which case they will be described by the equations

$$E^{\text{right}}(x,t) = E_0 \cos(kx - \omega t), \tag{2.67}$$
$$E^{\text{left}}(x,t) = E_0 \cos(kx + \omega t + \phi), \tag{2.68}$$

where k is the off-resonant laser's wave vector and ω is its angular frequency. Here we are working in one dimension, we assume that both beams are propagating along the x-axis and are linearly polarized in the same plane (that's why the unit polarization vectors are ignored), and "right" and "left" are seen according to the conventional way of drawing the x-axis pointing to the right. An arbitrary phase difference between the two beams is denoted by ϕ. Notice that the electric field amplitude E_0 is assumed here to be the same for both beams (this is an approximation, but not a perfect description, for a retroreflected beam, where the losses along the optical path are small). The total electric field at every point of space and time will be a linear sum of both beams, so

$$E^{\text{total}}(x,t) = E^{\text{right}}(x,t) + E^{\text{left}}(x,t) = E_0 \cos(kx - \omega t) + E_0 \cos(kx + \omega t + \phi). \tag{2.69}$$

This equation can be simplified using trigonometric identities [88]. Since

$$\cos(\alpha) + \cos(\beta) = 2\cos(\frac{\alpha+\beta}{2})\cos(\frac{\alpha+\beta}{2}), \tag{2.70}$$

we will get

$$E^{\text{total}}(x,t) = 2E_0 \cos(kx + \phi/2)\cos(\omega t - \phi/2). \tag{2.71}$$

This result is the equation of a standing wave. Unlike $E^{\text{right}}(x,t)$ and $E^{\text{left}}(x,t)$ on their own, where at each point along the axis the field magnitude oscillates between $\pm E_0$, and the plane of constant phase is moving in time to the right or left, in the case of $E^{\text{total}}(x,t)$, at any given point x_0 the field has a constant oscillation amplitude given by $2E_0\cos(kx_0+\phi/2)$. In particular, if $x_0 = \frac{\pi/2-\phi/2}{k}$, such a point has no field oscillation, which is the characteristic of a standing wave. From now on, let's set $\phi = 0$ because it only causes a constant offset of the standing wave, which is in the most cases unimportant. According to eq. (2.41), the energy shift is determined by the wave intensity, which is proportional to the absolute square of the field amplitude (see eq. (2.40)). This means that

$$U_a^{\text{lattice}} = -\frac{1}{4}\alpha_a(\omega)|2E_0|^2\cos^2(kx) = -\frac{1}{2}\alpha_a(\omega)Z_0(4I)\cos^2(kx), \tag{2.72}$$

where we skip the time dependence because it only enters the polarizability calculation, and it does not affect the optical potential shape itself[29]. Comparing eq. (2.72) with eq. (2.41), we notice the new factor 4 multiplying the intensity, which means that the depth of a lattice formed by retroreflecting an off-resonant beam is four times greater than the depth of a dipole trap formed by the same beam without retroreflection. In addition, the period of an optical lattice is one-half of the lattice laser wavelength due to $\cos^2$ dependence. Finally, the vibrational frequency gaps within one optical lattice well can be estimated by Taylor-expanding the $\cos^2$ function[30], which results in

$$\cos^2(x) \approx 1 - x^2, \tag{2.73}$$

so, skipping again the constant 1, we get

$$U_{\text{H},a}^{\text{lattice}} = \frac{1}{2}\alpha_a(\omega)Z_0(4I)k^2x^2. \tag{2.74}$$

Unlike in the Gaussian ODT cases above, where the two-beam interference is washed out on purpose by detuning beam frequencies by over $100\,\text{MHz}$, here we do not expand the laser intensity's Gaussian envelope; we expand the $\cos^2$ intensity profile around the bottom of one lattice well. At the sub-micron length scale of a single well, the longitudinal Gaussian beam profile of the laser is essentially uniform. Setting this Taylor expansion equal to the standard harmonic oscillator potential,

$$\frac{1}{2}M\omega_{\text{HO,lattice}}^2x^2 = \frac{1}{2}\alpha_a(\omega)Z_0(4I)k^2x^2, \tag{2.75}$$

[29]This may initially sound strange. To make sense of it, one has to immediately go back to the idea of a standing wave, where the field at each point in space is oscillating in time with a generally different amplitude, and with the frequency given by that time dependence. The time dependence is the same for the entire wave and it determines the resonance and off-resonance for atom-light interaction. The position in space, however, given the local strength of the light field, and thus the strength of the atom-light interaction compared to all other points in space.

[30]Note that in the quantum gas microscope calculations in Chapter 3 we do not do it in this manner, but rather we directly numerically solve the Schrödinger equation for a $\cos^2$-shaped potential and find the eigenenergies.

we obtain the vibrational frequency gaps for the lowest energy states in an optical lattice:

$$\omega_{\text{HO,lattice}} = \sqrt{\frac{4}{M}\alpha_a(\omega)Z_0 I k^2}. \tag{2.76}$$

Assuming now that the lattice is formed around the intensity maximum of the off-resonant beam, so setting $I = \frac{2P}{\pi w_0^2}$, and expressing $k = \frac{2\pi}{\lambda}$, we get

$$\omega_{\text{HO,lattice}} = \sqrt{\frac{4}{M}\alpha_a(\omega)Z_0 \frac{2P}{\pi w_0^2}\frac{4\pi^2}{\lambda^2}}. \tag{2.77}$$

Comparing this result to eq. (2.51), we realize that the last factor here is $\frac{1}{\lambda^2}$ instead of $\frac{1}{w_0^2}$, and so since normally $w_0 >> \lambda$, we expect $\omega_{\text{HO,lattice}} >> \omega_{\text{HO},x}$.

2.5 Basic dynamics of evaporative cooling

Looking back at Section 1.2, we notice that normally, the last step on the road to a quantum degenerate gas is evaporative cooling [89, 90, 91]. This cooling method has been used in all quantum gas experiments so far, with the exception of very few recent demonstrations, one of them being from our group, that managed to produce a BEC without evaporative cooling [23, 92]. Evaporation was used in classic experiments with alkali atoms, such as Rb, Na, and Li at the beginning of the BEC era, in all work with H and He*, and in more modern experiments with alkaline-earth atoms and lanthanides. At the rough conceptual level, the evaporation process is easy to understand: the hottest atoms escape the trapping potential, leaving the remaining sample with a lower total internal energy, which is similar to a cup of hot water that cools as it evaporates. However, first-principles mathematical modeling of an ultracold gas around the BEC phase transition, or when the effects of Fermi degeneracy become important in the case of a Fermi gas, is very difficult. We will not go into this topic here and restrict ourselves to the models for a classical gas, so a sample much hotter than quantum degeneracy. With the experimental knowledge that evaporation to a quantum gas does work, it is possible to use effective models based on classical physics assumptions to obtain reasonable quantitative estimates of the evaporation process[31].

One simple and convenient model is based on scaling laws and is described in Ref. [95]; its development was inspired by the first demonstration of a BEC directly by evaporation in an ODT [96]. The basic idea is to assume that the trap depth is being adiabatically lowered and show how the relevant quantities scale with this lowering of the trap depth in dependence of the initial temperature, trap frequencies, and scattering length. We will note immediately that this model is not directly applicable to radiofrequency knife evaporation methods that are used

[31] In case one is interested in quantum mechanical effects, the cases of bosons and fermions must be viewed differently. For bosons, quantum statistics actually makes the evaporation process more efficient as the gas approaches quantum degeneracy; an elegant explanation for this is given in the lecture notes of Jean Dalibard [93] and it is based on combinatorics with indistinguishable bosons. For fermions, quantum statistics decreases cooling efficiency as the temperature decreases, and these effects are analyzed in Ref. [94].

in magnetic traps [3, 97], but rather only to direct lowering of the ODT, which is the case in our experiment and in multiple other ones. Let us summarize the main results from Ref. [95]. The two-atom collision rate γ is given in units of $1/\mathrm{s}$ by

$$\gamma_i = \frac{4\pi N_i M \nu_i^3 \sigma}{k_B T_i}, \tag{2.78}$$

$$\sigma = 8\pi a^2, \tag{2.79}$$

where N is the atom number, M is the atomic mass, ν is the geometric mean of trap frequencies ($\nu = (\nu_x \nu_y \nu_z)^{\frac{1}{3}}$), σ is the scattering cross-section, and a is the scattering length; the subscripts i denote "initial", so we evaluate these quantities at the beginning of evaporation. We then define parameter

$$\eta = \frac{U_0}{k_B T}, \tag{2.80}$$

which is the ratio between trap depth and sample temperature at any point during the evaporation sequence. The crucial idea is to keep this parameter constant in time. Ref. [95] suggests having $\eta = 10$ as the target value, but that can be too high and can mean that the trap is too deep and evaporation is too slow, so one can aim for $\eta = 7$, for example. We also define an auxiliary expression to be used in further equations:

$$\eta' \equiv \eta + \frac{\eta - 5}{\eta - 4}. \tag{2.81}$$

The time evolution of the trap depth that will keep the condition of constant η, while preserving adiabaticity, is given by

$$\frac{U_0(t)}{U_0} = \left(1 + \frac{t}{\tau}\right)^{\frac{-2(\eta'-3)}{\eta'}}, \tag{2.82}$$

$$\frac{1}{\tau} = \frac{2}{3}\eta'(\eta - 4)e^{-\eta}\gamma_i. \tag{2.83}$$

Notice that the time constant for trap lowering is proportional to the collision rate: a low collision rate makes the evaporation process excessively slow[32]. Finally, the evolution of the phase space density (PSD) and the atom number becomes:

$$\frac{\rho}{\rho_i} = \left(\frac{U_{0,i}}{U_0}\right)^{\frac{3(\eta'-4)}{2(\eta'-3)}} = \left(\frac{N_i}{N}\right)^{\eta'-4}, \tag{2.84}$$

where again i stands for "initial" and ρ and N give respectively the PSD and the remaining atom number after the trap has been lowered to the value U_0. The parameters in these equations are

[32]The collision rate itself is proportional to the scattering cross-section and the product of trap frequencies, and inversely proportional to the temperature, based on eq. (2.78). This is why one wants a tight enough trap and a large enough scattering length, and one can only use the evaporation process for an ultracold cloud; in other situations, evaporation will not be an efficient cooling method.

known or are under experimental control, so they can be used for numerical calculations of the evaporation result, which is essentially the magnitude of PSD increase and the fraction of the atoms that will remain at the end of evaporation.

2.6 Fundamentals of imaging and data analysis with ultracold atoms

The most widespread method for imaging ultracold clouds since the beginnings of BEC experiments has been absorption imaging [3, 13]. The basic purpose of absorption imaging is to quantitatively measure atom density in two dimensions, meaning that the third dimension, the line of sight, is automatically integrated along by the construction of the method and the way that the imaging beam is directed onto the camera. The geometrical distribution of this atom density can then be quantitatively analyzed in order to measure the important parameters for ultracold clouds, such as the total atom number, the BEC and thermal fractions, or the Fermi degeneracy parameter, the cloud temperature, and so on [13, 14]. As the first approximation[33], absorption imaging can be understood according to the Beer-Lambert law [98]:

$$\frac{dI(x,y,z)}{dz} = -n(x,y,z)\sigma_0 I(x,y,z), \tag{2.85}$$

where I denotes the intensity of the imaging laser beam, n is the atom density, and σ_0 is the scattering cross-section for the photons[34] of the imaging beam. There are a few important simplifying assumptions here: the cloud is supposed to be not very dense so that scattered photons are not reabsorbed, a significant portion of the beam passes the cloud without being scattered (again, relatively low density), and the imaging beam is assumed to be perfectly polarized and exactly on resonance. In addition, we assume that the probability of reemission in the direction of the imaging beam, and thus the camera, is negligible. The Beer-Lambert law differential eq. (2.85) suggests that the intensity of the imaging beam will decay exponentially according to [100]

$$I(x,y,z) = I_0(x,y)e^{-\sigma_0 \int_0^z n(x,y,z')dz'}, \tag{2.86}$$

with I_0 denoting the intensity of the imaging beam before the atomic cloud (so at location $z = 0$). We define the optical depth (od) of some object extending from 0 to z and having density

[33] One can also consider deviations from this elementary approximation. For example, one can consider how the equations are modified when the imaging light has a high intensity, which is shown in Ref. [98]. Imaging dense atomic clouds is discussed in Ref. [99]. However in some cases, it is possible to design the experimental sequence so that the measurement results do not depend on absolute atom numbers, but rather on relative atom numbers, for which precise atom number calibration is not needed. One then looks only at the ratios atom numbers as a function of some control parameter, and then the systematic imaging errors that arise from a simplified model should not affect the final conclusions.

[34] See Ref. [43] for an explanation of photon scattering cross-sections.

$n(x, y, z)$ as [99]

$$\mathrm{od}(x, y) \equiv \sigma_0 \int_0^z n(x, y, z')dz'. \tag{2.87}$$

Let us set the upper limit z at a location after the cloud, so that all photon scattering has already taken place there; in this case the integral covers the full cloud and there remains no dependence on z. Then, $I(x, y)$ will be used to denote the 2D intensity profile after the light has passed the atomic cloud, and $I_0(x, y)$ is the intensity profile before the beam has entered the cloud. Thus,

$$I(x, y) = I_0(x, y)e^{-\mathrm{od}(x,y)}, \tag{2.88}$$

$$\mathrm{od}_c(x, y) = -ln\left(\frac{I(x, y)}{I_0(x, y)}\right), \tag{2.89}$$

where od_c is the optical column density of the full atomic cloud [98].

Therefore, in order to measure the optical column density, we have to take the natural logarithm of the intensities before and after the cloud. Measuring after the cloud is easy; it is simply the beam on the camera after it has passed the cloud in the chamber. Since normally we cannot put a camera before the chamber, the way to get I_0 is to remove the atoms from the beam path and image on the same camera that is placed after the experimental chamber. This is easily done because shining the resonant imaging beam very quickly imparts a lot of kinetic energy to the atoms and blows them away (this is especially effective in blowing the atoms away because a cloud is often imaged after any trapping has been turned off). In a real imaging application, one also takes a third image, this time with the imaging beam off, in order to subtract the dark background. Let us recapitulate the procedure: an absorption imaging procedure will take 3 images: "RAW" by pulsing an imaging beam onto the atomic cloud (this measures $I(x, y)$), "BGR" by pulsing the same imaging beam around a millisecond after "RAW" (this measures $I_0(x, y)$), and finally "DARK" by taking a picture with the imaging beam off. The measured optical density is given by

$$\mathrm{od}_c^{(\mathrm{meas})}(x, y) = -ln\left(\frac{\mathrm{RAW}(x, y) - \mathrm{DARK}(x, y)}{\mathrm{BGR}(x, y) - \mathrm{DARK}(x, y)}\right). \tag{2.90}$$

In a practical imaging system, one sends a collimated imaging beam, ideally with a waist much larger than the atomic cloud width, but one clips that beam with an iris in order to send only the central part. In that manner one gets a more uniform illumination intensity, which is desirable, and one tries to minimize multiple reflections from the viewports crossing the imaging area and creating unwanted interference fringes. For the purposes of imaging system design, one views the shadow cast by the atoms in an analogous manner to light propagation. In other words, the image is formed by the part of the beam that has been scattered away by the atoms (a shadow), and it is transmitted and focused in the imaging system by the same geometrical optics laws that would be used if we were to use fluorescence for imaging; Ref. [98] contains a nice schematic of an absorption imaging system.

Finally, the integral $\int_0^z n(x,y,z')dz'$ is taken automatically by the imaging setup, because the imaging beam passes the full atomic cloud before reaching the camera. We can define the integrated 2D density by

$$n_{\text{2D}}(x,y) \equiv \int_0^z n(x,y,z')dz'. \tag{2.91}$$

This yields

$$n_{\text{2D}}(x,y) = \text{od}_c(x,y)/\sigma_0. \tag{2.92}$$

Since for a dipole-allowed transition at wavelength λ and a perfectly polarized beam, the on-resonance scattering cross-section is $\sigma_0 = \frac{3\lambda^2}{2\pi}$ [98], measuring the optical column density immediately gives the integrated 2D density of the atomic cloud. From now and until the end of this Section, we will investigate quantitatively which equations this $n_{\text{2D}}(x,y)$ obeys for different atomic clouds; that will be the fit equations for experimental data. Note that the total atom number in the cloud is obtained by 2D integration of the optical column density:

$$N_{\text{atoms}} = \frac{1}{\sigma_0} \iint_{-\infty}^{+\infty} \text{od}_c(x,y)dxdy, \tag{2.93}$$

and one can also consider 1D integrated densities of the form $n_{\text{1D}}(y) \equiv \int_{-\infty}^{+\infty} n_{\text{2D}}(x,y)dx$ for example.

In order to find the equations for $n_{\text{2D}}(x,y)$ under different experimental conditions, we will start by writing down the density profiles of a thermal gas and a BEC. For a BEC in the Thomas-Fermi regime in a harmonic trap we have, using eq. 43 from Ref. [13]:

$$n^{\text{BEC}}(\mathbf{r}) = n_0^{\text{BEC}} \max\left[1 - \sum_{i=1}^{3} \frac{r_i^2}{r_{i,\text{TF}}^2}, 0\right], \tag{2.94}$$

where n stands for gas density, n_0 is peak density in some sense, which will be a fitting parameter, r_i stands for the Cartesian components of the position vector $\mathbf{r}$, and finally $r_{i,\text{TF}}^2$ denotes the Thomas-Fermi (TF) radii along the coordinate axes. The max function simply returns the larger value of the two inputs separated by the comma. The Thomas-Fermi radius will determine the spatial extent of the BEC; if $r_i^2 > r_{i,\text{TF}}$, then the max function will yield 0 for density. The density function in eq. (2.94), however, is in three dimensions, but absorption imaging measures 2D density. We have seen that the imaging system integrates the signal along the imaging axis (let's take it to be z), so here we must integrate eq. 2.94 along the z-axis to get a theoretical expression for the expected density. Let us note that we are dealing with a piecewise-defined function due to the max, so we have to treat the integration carefully. The expression inside the maximum, when set to 0, defines an ellipsoid shell, and $1 - \sum_{i=1}^{3} \frac{r_i^2}{r_{i,\text{TF}}^2} = 0$ is the ellipsoid equation. This term in the max function becomes negative for locations outside the ellipsoid, in

which case the max always returns 0; we have seen that this implies zero BEC density outside the Thomas-Fermi radius. For our integration then, the ellipsoid surface defines the limits[35], which will become $z_\pm = \pm z_{\mathrm{TF}}\sqrt{1-\frac{x^2}{x_{\mathrm{TF}}^2}-\frac{y^2}{y_{\mathrm{TF}}^2}}$, where minus denotes the upper limit then and plus the lower one[36]. Then we get

$$\begin{aligned}\tilde{n}^{\mathrm{BEC}} &= n_0^{\mathrm{BEC}}\int_{z_+}^{z_-}\left(1-\frac{x^2}{x_{\mathrm{TF}}^2}-\frac{y^2}{y_{\mathrm{TF}}^2}-\frac{z^2}{z_{\mathrm{TF}}^2}\right)dz = \\ &= n_0^{\mathrm{BEC}}\left[1-\frac{x^2}{x_{\mathrm{TF}}^2}-\frac{y^2}{y_{\mathrm{TF}}^2}-\frac{z^3}{3z_{\mathrm{TF}}^2}\right]_{z_+}^{z_-} = \\ &= n_0^{\mathrm{BEC}}\frac{1}{3z_{\mathrm{TF}}^2}\left(z_{\mathrm{TF}}^3\left(1-\frac{x^2}{x_{\mathrm{TF}}^2}-\frac{y^2}{y_{\mathrm{TF}}^2}\right)^{3/2}+z_{\mathrm{TF}}^3\left(1-\frac{x^2}{x_{\mathrm{TF}}^2}-\frac{y^2}{y_{\mathrm{TF}}^2}\right)^{3/2}\right) = \\ &= n_0^{\mathrm{BEC}}\frac{2z_{\mathrm{TF}}^3}{3z_{\mathrm{TF}}^2}\left(1-\frac{x^2}{x_{\mathrm{TF}}^2}-\frac{y^2}{y_{\mathrm{TF}}^2}\right)^{3/2},\end{aligned} \tag{2.95}$$

where the tilde in $\tilde{n}$ denotes that it's a quantity in two dimensions. So the column-integrated atom density, which is the experimentally measured quantity, is

$$\tilde{n}^{\mathrm{BEC}} = \tilde{n}_0^{\mathrm{BEC}}\max\left[\left(1-\frac{x^2}{x_{\mathrm{TF}}^2}-\frac{y^2}{y_{\mathrm{TF}}^2}\right)^{3/2},0\right]. \tag{2.96}$$

The max function has reappeared because we have essentially projected an ellipsoid onto a plane, which means that the region where the BEC density is nonzero is now an ellipse. The prefactor $\tilde{n}_0^{\mathrm{BEC}}$ has absorbed the prefactors from the derivation, and it will be used as a fitting parameter[37]. In this way we have derived and understood eq. (44) (at least its condensate part) from Ref. [13]. For the purposes of fitting and presenting data, however, we may also be interested in a density profile integrated along one of the remaining two axes; in other words, we may want to get a 1D integrated expression, if we find it difficult to perform two-dimensional fitting and plotting.

Let us go ahead and integrate eq. 2.96, which is a bit more difficult due to power 3/2 in the expression. First of all, since the density is 0 outside the ellipse defined by $1-\frac{x^2}{x_{\mathrm{TF}}^2}-\frac{y^2}{y_{\mathrm{TF}}^2}=0$, the y-integration will have limits $y_\pm = \pm y_{\mathrm{TF}}\sqrt{1-(\frac{x}{x_{\mathrm{TF}}})^2}$. Consequently, we are looking for the

[35] One can take the limits of integration farther, but then anyway the integrand evaluates to 0 everywhere outside the ellipsoid. Taking the limits of integration on the ellipsoid surface is a good mathematical way to take care of this particular piecewise function.

[36] This is purely a matter of defining the plus and minus of the axis, switching the limits of integration just switched the sign of the integral, and we know that we must get a positive number, because a density cannot be negative.

[37] Note that actually $\tilde{n}_0^{\mathrm{BEC}} = n_0^{\mathrm{BEC}}\frac{2z_{\mathrm{TF}}^3}{3z_{\mathrm{TF}}^2} = \frac{2}{3}n_0^{\mathrm{BEC}}z_{\mathrm{TF}}$, which means that dimensions make sense, as they are supposed to. n_0^{BEC} has dimensions of [atoms/m^3], z_{TF} has dimensions of [m], and $\tilde{n}_0^{\mathrm{BEC}}$ has dimensions of [atoms/m^2], as expected.

integral

$$\int_{y_-}^{y_+} \left(1 - \frac{x^2}{x_{\mathrm{TF}}^2} - \frac{y^2}{y_{\mathrm{TF}}^2}\right)^{3/2} dy. \tag{2.97}$$

It can be evaluated using tables of indefinite integrals (for example, Ref. [101]), and it is

$$\frac{1}{4}y\left(\sqrt{1 - \frac{x^2}{x_{\mathrm{TF}}^2} - \frac{y^2}{y_{\mathrm{TF}}^2}}\right)^3 + \frac{3}{8}(1 - \frac{x^2}{x_{\mathrm{TF}}^2})y\left(\sqrt{1 - \frac{x^2}{x_{\mathrm{TF}}^2} - \frac{y^2}{y_{\mathrm{TF}}^2}}\right) + \\ + \frac{3}{8}\left(1 - \frac{x^2}{x_{\mathrm{TF}}^2}\right)^2 y_{\mathrm{TF}} \arcsin\left[y\sqrt{\frac{1/y_{\mathrm{TF}}^2}{1 - \frac{x^2}{x_{\mathrm{TF}}^2}}}\right]. \tag{2.98}$$

The last evaluation step is to plug in the integration limits for y. First of all, the $\arcsin$ argument evaluates to 1 and -1 at the integration limit, so the output will be $\pm\pi/2$. Plugging in the integration limits in the terms under the square root in the first and second terms of the sum will yield 0, as is expected based on the fact that those terms have the form of the ellipse equation and the integration limits are ellipse boundaries. Putting this all together, we arrive at the result

$$\int_{y_-}^{y_+} \left(1 - \frac{x^2}{x_{\mathrm{TF}}^2} - \frac{y^2}{y_{\mathrm{TF}}^2}\right)^{3/2} dy = \frac{3}{8}\pi y_{\mathrm{TF}}\left(1 - \frac{x^2}{x_{\mathrm{TF}}^2}\right)^2. \tag{2.99}$$

Therefore, the integrated 1D BEC density can be written as

$$\breve{n}^{\mathrm{BEC}} = \breve{n}_0^{\mathrm{BEC}} \max\left[\left(1 - \frac{x^2}{x_{\mathrm{TF}}^2}\right)^2, 0\right], \tag{2.100}$$

where the semicircle in $\breve{n}$ denotes that the corresponding quantity is in 1D and all prefactors have been absorbed into the constant $\breve{n}_0^{\mathrm{BEC}}$. Notice that the term $\left(1 - \sum_i \frac{r_i^2}{r_{i,\mathrm{TF}}^2}\right)$ (r_i being the general notation for the position coordinate) inside the max function in the density profile stays the same in 3D, 2D, and 1D, but its power increases by 1/2 after each integration step. In the end, we may want to determine the total atom number from the fitting parameters of this 1D density, namely $\breve{n}_0^{\mathrm{BEC}}$ and x_{TF}; we do that by taking the integral:

$$N_{\mathrm{BEC}} = \int_{-\infty}^{\infty} \breve{n}^{\mathrm{BEC}} = \breve{n}_0^{\mathrm{BEC}} \int_{-x_{\mathrm{TF}}}^{+x_{\mathrm{TF}}} (1 - \frac{x^2}{x_{\mathrm{TF}}^2})^2 = \\ = \breve{n}_0^{\mathrm{BEC}} \int_{-x_{\mathrm{TF}}}^{+x_{\mathrm{TF}}} (1 - 2\frac{x^2}{x_{\mathrm{TF}}^2} + \frac{x^4}{x_{\mathrm{TF}}^4}) = \breve{n}_0^{\mathrm{BEC}} \left[x - \frac{2}{3}\frac{x^3}{x_{\mathrm{TF}}^2} + \frac{1}{5}\frac{x^5}{x_{\mathrm{TF}}^4}\right]_{-x_{\mathrm{TF}}}^{+x_{\mathrm{TF}}} = \\ = \frac{16}{15}\breve{n}_0^{\mathrm{BEC}} x_{\mathrm{TF}}, \tag{2.101}$$

where N_{BEC} stands for the number of atoms in the BEC.

The equations above have been written for in-situ imaging, but the time-of-flight results can be obtained by simply replacing r_{TF} with $r_{\mathrm{TF}}(t)$ [13]. In other words, the functional form of all

the equations derived above will stay the same, but the Thomas-Fermi radius will evolve as a function of the time of flight t. As suggested in Ref. [102], if we assume a harmonic trapping potential which is changing in time, then any infinitesimally small volume of the condensate cloud will evolve according to

$$R_j(t) = \lambda_j(t) R_j(0), \tag{2.102}$$

where the subscript j stands for any Cartesian axis, and R is the coordinate of the small volume of the condensate along that axis. Therefore, if we take $R_j(0)$ to be the points located at the Thomas-Fermi radius, we will obtain the evolution of that radius. Assuming a sudden release from the trap at $t = 0$, which means that the trapping potential is set to 0 at that moment, the scaling factors $\lambda_j(t)$ obey a set of three coupled nonlinear differential equations [102]:

$$\frac{d^2\lambda_j(t)}{dt^2} = \frac{\omega_j^2(0)}{\lambda_j(t)\lambda_x(t)\lambda_y(t)\lambda_z(t)}, \tag{2.103}$$

where ω_j stands for the angular trap frequency before trap release, given in angular units. These differential equations can be solved numerically for any set of three trap frequencies, starting from the initial conditions for $\lambda_j(0) = 1$ because $R_j(t) = R_j(0)$ at $t = 0$, and setting $\frac{d\lambda_j(t)}{dt} = 0$ because the condensate is assumed to be initially at rest [102]. Notice though that the higher the $\omega_j(0)$, which corresponds to a more tightly confined axis, the faster the increase rate of the corresponding λ_j; this is the quantitative manifestation of the inversion of aspect ratio in a BEC time-of-flight measurement [3]. For the case of a cigar-shaped trap with a large aspect ratio, $\omega_z(0)/\omega_r(0) \ll 1$ (z is the longitudinal coordinate and r is the radial one), there is an approximate analytical solution:

$$\lambda_r(\omega_r(0)t) \approx \sqrt{1 + (\omega_r(0)t)^2}, \tag{2.104}$$

$$\lambda_z(\omega_r(0)t) \approx 1 + \epsilon^2 \left[\omega_r(0)t \arctan(\omega_r(0)t) - \ln(1 + (\omega_r(0)t)^2)\right], \tag{2.105}$$

where $\epsilon = \omega_z(0)/\omega_r(0) \ll 1$ is the measure of the trap aspect ratio.

Regarding the noncondensed fraction, we will immediately write down and discuss its 3D density after time of flight, which is given by eqs. (35) and (5.7) in Refs. [13] and [103] respectively[38]:

$$n^{\text{Bose}} = \frac{1}{\lambda_{\text{dB}}^3} \left(\prod_{i=1}^{3} \sqrt{\frac{1}{1 + (\omega_i t)^2}} \right) g_{3/2} \left[e^{\frac{\mu}{k_B T}} \left(\prod_{q=1}^{3} e^{-\left(\frac{r_q}{w_q(t)}\right)^2} \right) \right], \tag{2.106}$$

where $\lambda_{\text{dB}} = \sqrt{\frac{2\pi\hbar^2}{m k_B T}}$ is the de Broglie wavelength, m is the mass of the atom, the indices i and q stand for Cartesian components, the products are labeled by different indices just to emphasize that they both are taken independently, so each respective term is a product, ω_i denote the

[38] Notice a typo in Ref. [13]: there's division by $k_B T$ missing inside the exponential in eq. (35).

trap angular frequencies, and $w_q(t)$ stand for the widths of the cloud after time of flight t. The widths of the cloud are given by the relation $w_i(t) = \sqrt{\frac{2k_BT}{m\omega_i}}(1+\omega_i^2t^2)$. The function g is a polylogarithm, defined by the infinite series

$$g_s[x] = \sum_{k=1}^{\infty} \frac{x^k}{k^s}. \tag{2.107}$$

Let us note a few points about eq. (2.106). First of all, it holds for imaging a cloud in-situ too by simply setting $t = 0$. Secondly, the governing assumption in the time-of-flight derivation is that the non-condensed atoms do not interact during that time (that is called *ballistic expansion*); they purely move based on their momentum at the moment of trap release, without being affected by any other atoms in the cloud; this is an approximation, but usually a good one. Finally, this equation describes the density distribution of the atoms that are not in the trap ground state, with Bose-Einstein statistics being taken into account (that's why the subscript "Bose"); the atoms in the ground state are the BEC, which has been described above. In principle, this equation holds for bosons at any temperature; in practice, the effects of Bose-Einstein statistics only become noticeable in the density when the temperature is close to the BEC transition temperature.

Exactly as in the case of the BEC density, we must integrate the 3D thermal fraction density in order to get the equation for fitting that corresponds to the information that absorption imaging provides. Let us again take z to be the integration axis and we note that everything before the polylogarithm in eq. (2.106) is a constant with respect to z, so we only integrate the polylogarithm. Since it is an infinite sum, we in principle cannot simply integrate it term-by-term like we would do for a finite sum, because the convergence of the resulting expression is not guaranteed. However, we will not go into mathematical details and simply assume that in this case term-by-term integration does yield a converging sum. We explicitly write out a few terms of the infinite sum and integrate them in order to see the pattern that appears (we will, in the next few equations, not write $w_i(t)$ every time, but rather implicitly assume the t-dependence):

$$\begin{aligned} g_{3/2}\left[e^{\frac{\mu}{k_BT}}\left(\prod_{q=1}^{3} e^{-(\frac{r_i}{w_i})^2}\right)\right] = \\ = \frac{1}{1^{3/2}}e^{\frac{\mu}{k_BT}}e^{-(\frac{x}{w_x})^2}e^{-(\frac{y}{w_y})^2}e^{-(\frac{z}{w_z})^2} + \frac{1}{2^{3/2}}e^{\frac{2\mu}{k_BT}}e^{-2(\frac{x}{w_x})^2}e^{-2(\frac{y}{w_y})^2}e^{-2(\frac{z}{w_z})^2} + \\ + \frac{1}{3^{3/2}}e^{\frac{3\mu}{k_BT}}e^{-3(\frac{x}{w_x})^2}e^{-3(\frac{y}{w_y})^2}e^{-3(\frac{z}{w_z})^2} + \cdots \end{aligned} \tag{2.108}$$

We will be integrating along z, so only the exponential terms that contain z will go into the integral, the rest are constant prefactors. We will integrate from $-\infty$ to $+\infty$ because technically the thermal fraction distribution extends indefinitely (and it is not defined piecewise, like the

Thomas-Fermi one for BEC). Therefore, we will have integrals of the form

$$\int_{-\infty}^{\infty} e^{-k(\frac{z}{w_z})^2} = \frac{w_z}{\sqrt{k}}\sqrt{\pi}, \tag{2.109}$$

where the result is obtained by standard methods of Gaussian integration. Using this, we can write out the term-by-term integration procedure:

$$\begin{aligned}
&\int_{-\infty}^{\infty} g_{3/2}\left[e^{\frac{\mu}{k_BT}}\left(\prod_{q=1}^{3} e^{-(\frac{r_i}{w_i})^2}\right)\right] dz = \\
&= \frac{1}{1^{3/2}} e^{\frac{\mu}{k_BT}} e^{-(\frac{x}{w_x})^2} e^{-(\frac{y}{w_y})^2} \frac{w_z}{\sqrt{1}}\sqrt{\pi} + \frac{1}{2^{3/2}} e^{\frac{2\mu}{k_BT}} e^{-2(\frac{x}{w_x})^2} e^{-2(\frac{y}{w_y})^2} \frac{w_z}{\sqrt{2}}\sqrt{\pi} + \\
&+ \frac{1}{3^{3/2}} e^{\frac{3\mu}{k_BT}} e^{-3(\frac{x}{w_x})^2} e^{-3(\frac{y}{w_y})^2} \frac{w_z}{\sqrt{3}}\sqrt{\pi} + \cdots = \\
&= \frac{1}{1^2} e^{\frac{\mu}{k_BT}} e^{-(\frac{x}{w_x})^2} e^{-(\frac{y}{w_y})^2} w_z\sqrt{\pi} + \frac{1}{2^2} e^{\frac{2\mu}{k_BT}} e^{-2(\frac{x}{w_x})^2} e^{-2(\frac{y}{w_y})^2} w_z\sqrt{\pi} + \\
&+ \frac{1}{3^2} e^{\frac{3\mu}{k_BT}} e^{-3(\frac{x}{w_x})^2} e^{-3(\frac{y}{w_y})^2} w_z\sqrt{\pi} + \cdots = \\
&w_z\sqrt{\pi} g_2\left[e^{\frac{\mu}{k_BT}} e^{-(\frac{x}{w_x})^2} e^{-(\frac{y}{w_y})^2}\right],
\end{aligned} \tag{2.110}$$

where in the last step we have used the definition of a polylogarithm to collect the terms of the infinite sum. So then,

$$\tilde{n}^{\text{Bose}} = \frac{1}{\lambda_{\text{dB}}^3}\left(\prod_{i=1}^{3}\sqrt{\frac{1}{1+(\omega_i t)^2}}\right) w_z\sqrt{\pi} g_2\left[e^{\frac{\mu}{k_BT}} e^{-(\frac{x}{w_x})^2} e^{-(\frac{y}{w_y})^2}\right], \tag{2.111}$$

where the tilde again denotes a 2D density due to integration along one axis. In this way, we have derived eq. (5.10) from Ref. [103]. One can immediately take the next step and integrate along the y-axis if one wants the integrated 1D density, which can be easier to fit and plot. Performing exactly the same steps as in eqs. (2.108) and (2.110) we will get

$$\int_{-\infty}^{\infty} g_2\left[e^{\frac{\mu}{k_BT}} e^{-(\frac{x}{w_x})^2} e^{-(\frac{y}{w_y})^2}\right] dy = w_y\sqrt{\pi} g_{5/2}\left[e^{\frac{\mu}{k_BT}} e^{-(\frac{x}{w_x})^2}\right], \tag{2.112}$$

and then

$$\breve{n}^{\text{Bose}} = \frac{1}{\lambda_{\text{dB}}^3}\left(\prod_{i=1}^{3}\sqrt{\frac{1}{1+(\omega_i t)^2}}\right) w_z w_y \pi g_{5/2}\left[e^{\frac{\mu}{k_BT}} e^{-(\frac{x}{w_x})^2}\right], \tag{2.113}$$

where now the semicircle above n denotes that this is a 1D quantity. We can absorb all prefactors into a single constant in front and write down this equation as

$$\breve{n}^{\text{Bose}} = \breve{n}_0^{\text{Bose}} g_{5/2}\left[e^{\frac{\mu}{k_BT}} e^{-(\frac{x}{w_x})^2}\right], \tag{2.114}$$

where the fitting parameters become $\breve{n}_0^{\text{Bose}}$, w_x, and also the factor $\frac{\mu}{k_BT}$, which measures the

chemical potential in units of $k_B T$ (we note that this must be a small negative number close to the BEC phase transition). Finally, as in the case of the condensed fraction, we can integrate this equation in order to get an estimate of the total atom number, now in the thermal fraction, and based on the 1D fitting parameters. The result is

$$N_{\text{Bose}} = \int_{-\infty}^{\infty} \breve{n}^{\text{Bose}} dz = \breve{n}_0^{\text{Bose}} \sqrt{\pi} w_z g_3 \left[e^{\frac{\mu}{k_B T}} \right], \tag{2.115}$$

where the integration of the infinite series is performed in a term-by-term fashion as before, and N_{Bose} stands for the number of atoms in the thermal fraction, evaluated using the Bose-enhanced function.

To summarize, we have collected and explained the basic equations for analyzing ultracold bosonic clouds using absorption imaging. This is useful information on the one hand to understand in principle, and on the other hand to have as an immediate reference when one goes about fitting BEC images from a new ultracold gas machine.

Chapter 3

Theoretical basics of quantum gas microscopy with strontium

The machine described in this Thesis has been designed to have a quantum gas microscope functionality. Even though at the time of writing this functionality has not been yet experimentally demonstrated, the feasibility calculations have been done. Therefore, we would like to present a scheme for reliably detecting strontium atoms at the single-atom, single-site level in a strongly-correlated optical lattice. This involves two main parts. One is designing a cooling scheme so that enough photons can reach a CCD camera from a single atom before that atom has a high probability to jump to a different site or to leave the lattice. The other one is designing a suitable imaging system to have sufficient resolution and photon detection efficiency. In this Thesis we focus mainly on the first part and only briefly mention the second one, which is described in detail in a different Thesis [104].

3.1 Single-atom imaging

We have seen in Section 2.6 the classic method of measuring an ultracold sample, which is absorption imaging [13]. In early quantum gas experiments, absorption imaging was used to probe the momentum distribution of the gas, and the first evidence for both BEC and DFG was obtained in this manner. More recently, absorption imaging techniques have been developed to get high-resolution *in-situ* images of an ultracold gas [105]. However, it is very desirable to measure the occupation of individual lattice sites in a strongly-correlated 2D optical lattice, so to probe the lattice at a single-atom and single-site level. In the context of quantum simulation and Hubbard models of condensed matter physics, this would be equivalent to measuring the presence or absence of a valence electron at every individual atom. Such a measurement in condensed matter systems has not been performed and there exist no realistic ideas yet to be able to do it; in cold atom systems, on the other hand, single-atom single-site imaging has been achieved [106, 107, 108, 109, 110], and it is known as *quantum gas microscopy*. Recently, Yb quantum gas microscopes have been demonstrated [111, 112], and single Sr atoms were prepared and detected in optical tweezers [113, 114, 115], which is a precursor to quantum gas microscopy. A logical and immediate extension of this imaging method is single-site control of the internal state of the atoms, because an imaging system that has a high-enough resolution to resolve individual lattice sites can be used in reverse to focus the light to the spatial extent of an

individual lattice site because Maxwell's equations are defined in the same way forward and backward in time. Individual site addressing in a strongly-correlated lattice has already been demonstrated with a $95\,\%$ π-pulse fidelity between two hyperfine states of rubidium [116]. Let us note here that the blue transition in Sr at $461\,\mathrm{nm}$ makes our resolution task easier due to a lower associated diffraction limit compared to the first QGMs with Rb.

Since we are going to excite Sr atoms with resonant light in the microscope and then image them by collecting their fluorescent emission, we should carefully consider the momentum transfer from these resonant photons to the atoms. The photons can easily impart enough momentum to kick atoms out of their lattice sites. In fact, unless one specifically designs a cooling scheme and uses a deep optical lattice, the atoms will for sure move to a different site or leave the lattice before enough photons can be collected for their reliable identification. Therefore, the performance of a cooling and imaging scheme must be calculated before we attempt to build a QGM, and this is based on the specifics of the Sr electronic structure. With the available tools, mainly in terms of the achievable lattice depth and photon collection efficiency, any real scheme will likely have to be pushed to its limits in order to obtain good detection fidelity. A schematic representation of heating and cooling process is shown in Fig. 3.1; the reader can refer to that Figure to understand the explanations below.

3.1.1 The heating process

Each potential well of the optical lattice can be approximated as a harmonic potential, in which case "heating" refers to the increase in the average vibrational quantum number of the atom in that well. To understand why heating happens, consider that the blue transition in Sr, which is used for imaging, has $\frac{\Gamma}{2\pi} = 30.5\,\mathrm{MHz}$ (see Section 1.1 for the electronic level scheme of Sr and a short explanation of the transitions). A realistically achievable depth of a potential well in an optical lattice, on the other hand, is $\sim 10\,\mathrm{MHz}$ (in frequency units). Thus, the natural linewidth of the blue transition is greater than the well depth in which the atoms are confined. Since the harmonic oscillator level spacing in a potential well is much smaller that the well depth, it is clear that this level spacing is also much smaller than the transition linewidth. Therefore, it is impossible to have any frequency control over sideband and carrier excitations on this transition. The vibrational level in which the atom ends up after a scattering event is largely random, and in fact the natural linewidth is large enough to also excite the atom into the continuum instead of a bound state. Fortunately, wavefunction overlaps between the different vibrational states of a strongly confining potential well will favor absorption-emission cycles in which the level in the ground state does not change, which is the basis of the the Lamb-Dicke effect [117, 118]. However, heating will still occur, and our first job is to estimate its rate.

Let us outline the modeling approach for the heating. Each lattice site is viewed as an independent harmonic oscillator because the lattice is made deep to the point of negligible wavefunction overlap between adjacent sites and consequently almost no tunneling. The heating rate is then the rate at which the average harmonic oscillator occupation number is increasing at a lattice site. We take an atom starting in an arbitrary level n in $^1S_0$ and we assume that, due

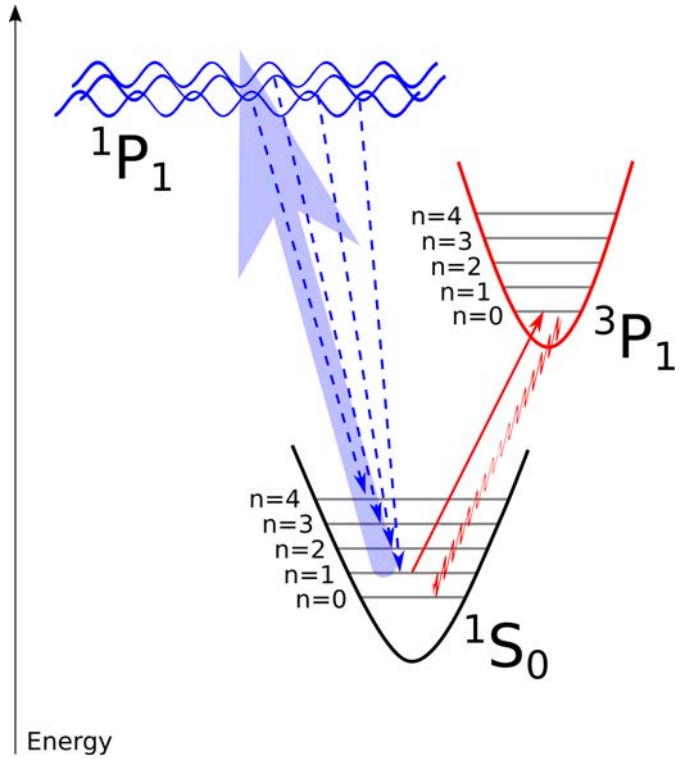

FIGURE 3.1: Schematic representation of the heating and cooling processes during quantum gas microscopy, as considered in our model. The $^1P_1$ state is assumed to be untrapped in the $1064\,\mathrm{nm}$ optical lattice and therefore it is represented by plane waves instead of a harmonic oscillator well. The large blue arrow represents excitation on the broad atomic transition, and the dashed arrows represent some of the possible decay processes back to the ground state. For the $^1S_0 - {}^3P_1$ sideband cooling transition, the solid arrow represents laser excitation and the squiggly line represents spontaneous emission. The energy axis is for illustration purposes only and is not drawn to scale.

to the fact that the blue transition is broader than the full lattice depth in $^1S_0$, a blue excitation takes it into the continuum. The atom in the electronically excited state could still end up in a vibrational bound state, but with such a linewidth we for sure expect some excitation into the continuum. Therefore, we take this slightly pessimistic scenario to see if the imaging approach still works, which would in the end attest to its robustness. According to standard quantum theory, a particle in the continuum (so, in the absence of a confining potential) has plane waves as its eigenstates of motion, and therefore excitation into the continuum means projecting the original wavefunction onto plane wave states; this corresponds to a Fourier transform [41]. In addition, since a photon is absorbed from the excitation beam, we must take the accompanying momentum boost of the atom into account, which is a shift in momentum space. We then let the new quantum state evolve for the duration of the $^1P_1$ state lifetime, and we finally project the result back onto the harmonic oscillator states, which corresponds to fluorescent emission[1]. This projection is done by first performing the inverse Fourier transform to get back the position

[1]Note that for simplicity, the boost due to photon emission is not taken into account here because it is zero on average; emission is equally probable in any direction.

space wavefunction, and then calculating the overlaps of the resulting wavepacket with the original harmonic oscillator wavefunctions in order to find the contribution of each level to the final state. In the end, we are interested in the average harmonic oscillator occupation number after an absorption-emission event.

This conceptual model can now be put on mathematical footing. For an arbitrary harmonic oscillator level n and its state vector $|\psi_n\rangle$, from which the atom is assumed to be excited by a blue photon, the Fourier transform corresponding to the projection onto the continuum states is given by

$$\psi_n(p) = \langle p|\psi_n\rangle = \frac{1}{\sqrt{2\pi\hbar}} \int_{-\infty}^{\infty} \psi_n(x) e^{-ipx/\hbar} dx, \tag{3.1}$$

where $\psi_n(x)$ is the position-space representation of $|\psi_n\rangle$ and p denotes momentum[2]. We would like to take the photon boost into account by performing the transformation $\psi_0(p) \mapsto \psi_0(p+\hbar k_{\mathrm{L}})$, where k_{L} is the laser k-vector. However, as these calculations are performed numerically using the fast Fourier transform (FFT) algorithm in *Numpy*[81], it is more convenient to use the frequency shift property of Fourier transforms:

$$\mathscr{F}\{e^{\pm i\omega_0 x}\psi(x)\} = X(\omega \mp \omega_0), \tag{3.2}$$

where $\mathscr{F}$ denotes the Fourier transform operation and X denotes the transformed function. In this way we can multiply the original wavefunction by the appropriate complex exponential before doing the FFT, and that results in a shift in momentum space. The boosted wavefunction can thus be written as

$$\psi_n(p + \hbar k_{\mathrm{L}}) = \frac{1}{\sqrt{2\pi\hbar}} \int_{-\infty}^{\infty} \psi_n(x) e^{-i\hbar k_{\mathrm{L}} x/\hbar} e^{-ipx/\hbar} dx, \tag{3.3}$$

and we notice the $\hbar k_{\mathrm{L}}$ factor in the exponential that corresponds to the momentum of the photon that does the boost. There is one detail to note regarding *Numpy's* FFT: the transformation is done using the multiplication factor e^{-ikx} under the integral, rather than $e^{-ipx/\hbar}$, as in the equations above. We can call this "transformation into k-space" rather than truly into momentum space, in which case the $\hbar$ under the square root in the prefactor should not be used[3]. The factor $\frac{1}{2\pi}$ is applied only in the inverse FFT (IFFT) in *Numpy* instead of being distributed with the square root, but for our purposes this does not matter, as we will always be doing the inverse transform

[2]Note that momentum eigenstates in the position representation are expressed as $|p\rangle = \frac{1}{\sqrt{2\pi\hbar}} e^{ipx/\hbar}$.

[3]Since the transformation back to the position representation is the inverse Fourier transform, the following identity must be shown to be true:

$$\psi_n(x) = \frac{1}{2\pi\hbar} \int_{-\infty}^{\infty} \int_{-\infty}^{\infty} \psi_n(\tilde{x}) e^{-ip\tilde{x}/\hbar} e^{ipx/\hbar} d\tilde{x} dp, \tag{3.4}$$

where tilde is only used to label x as the integration variable in the forward transform. Proving this identity means showing that the right-hand side evaluates to $\psi_n(x)$. The first step is the evaluation of

$$\int_{-\infty}^{\infty} e^{-ip\tilde{x}/\hbar} e^{ipx/\hbar} dp, \tag{3.5}$$

at the end. Let us define the wavefunction in k-space by

$$\psi_n(k) \equiv \int_{-\infty}^{\infty} \psi_n(x) e^{-ikx} dx, \tag{3.6}$$

which is the FFT formula in *Numpy*. In this way, whenever we perform calculations taking the photon boost into account, the boosted k-space wavefunction will be given by

$$\psi_n(k + k_{\mathrm{L}}) = \int_{-\infty}^{\infty} \psi_n(x) e^{-ik_{\mathrm{L}}x} e^{-ikx} dx, \tag{3.7}$$

numerically implemented as $\mathrm{FFT}\{\psi_n(x)e^{-i2\pi x/\lambda_{\mathrm{L}}}\}$. The form $\psi_n(k + k_{\mathrm{L}})$ for the boosted wavefunction makes sense because the expression $p = \hbar k$ holds for both light and atoms, and so we have simply omitted the constant factor $\hbar$. The time evolution in the excited state is modeled by applying the standard time evolution operator $U(\tau) = e^{iE\tau/\hbar}$ [15], where the energy, rather than the $\hat{H}$ operator, in the exponent implies that this particular form of the time evolution operator can only be applied in the eigenbasis of the Hamiltonian. Since we have taken the excited electronic state to be a free-particle plane-wave state for center of mass motion, which is precisely the eigenstate of the free particle Hamiltonian, the energy of each $\psi_n(k)$ is given by $E_k = \frac{(\hbar k)^2}{2M_{\mathrm{Sr}}}$. Consequently, the evolution operator for each $\psi_n(k)$ is given by $U_k(\tau) = e^{-i\frac{(\hbar k)^2\tau}{2M_{\mathrm{Sr}}\hbar}}$, and the value of τ should logically be the natural lifetime of the ${}^1P_1$ state, $\tau_{{}^1\mathrm{P}_1}$. Therefore in numerical calculations, we multiply the $\psi_n(k)$ states by this time evolution and take IFFT, which gives back the wavepacket in position space. This procedure can be written symbolically as

$$\psi_n^{\mathrm{evol}}(x) = \mathrm{IFFT}\{U_{k+k_{\mathrm{L}}}(\tau_{{}^1\mathrm{P}_1}) \cdot \mathrm{FFT}\{\psi_n(x)e^{-i2\pi x/\lambda_{\mathrm{L}}}\}\}, \tag{3.8}$$

where $\psi_n^{\mathrm{evol}}(x)$ denotes the wavefunction after the evolution that we described, n keeps track of the starting harmonic oscillator level, and the dot signifies that there is a vector with a list of k-values coming out of the FFT, which must be multiplied by the k-dependent diagonal time evolution matrix. After this procedure, we can get the coefficients

$$P_{mn} \equiv |c|^2 = \left| \int_{-\infty}^{\infty} \psi_m^*(x) \psi_n^{\mathrm{evol}}(x) dx \right|^2, \tag{3.9}$$

which denote the probabilities of an atom ending up in a vibrational state m after having been in the state n before the scattering event, and P stands for probability. These integrals can be rather easily evaluated numerically. We are particularly interested in the cases when $m > n$, which we interpret as heating in the lattice due to photon scattering.

which is done using the identity $\frac{1}{2\pi}\int_{-\infty}^{\infty} e^{-ik(x-\tilde{x})}dk = \delta(x - \tilde{x})$ [119]. We evaluate eq. (3.5) using a change of variables $q = p/\hbar,\ dp = \hbar dq$, and that will bring out a factor $\hbar$ in front, which will cancel the $\hbar$ in the denominator in eq. (3.4). In that way the right-hand side of eq. (3.4) will evaluate to $\psi_n(x)$. Consequently, if the exponent in the transformation is of the form e^{-ikx} rather than $e^{-ikx/\hbar}$, then there is no change of variables needed, and so $\frac{1}{\hbar}$ in front is not needed either.

It is also necessary to extend the model above to the case of multiple starting and final harmonic oscillator levels involved, which happens either due to the initial state being a statistical mixture already, or for sure due to scattering multiple photons during detection. In that case we must evaluate a total of N^2 of P_{mn} coefficients, where N denotes the total number of levels that we consider in a given calculation. It is convenient to cast these P_{mn} into matrix form:

$$\mathbf{P} = \begin{bmatrix} P_{00} & P_{01} & P_{02} & \cdots \\ P_{10} & P_{11} & P_{12} & \\ P_{20} & P_{21} & P_{22} & \\ \vdots & & & \end{bmatrix}. \tag{3.10}$$

By standard matrix multiplication rules and the definition of P_{mn}, we see that this matrix will transform any given vector of level occupation probabilities $\mathrm{p} = [p_0, p_1, p_2, \cdots]$ into a new vector of occupation probabilities after scattering one photon[4]. We can write this as $\mathrm{p}^{(1)} = \mathbf{P} \cdot \mathrm{p}$, where the superscript denotes the number of scattered photons. When the next photon is scattered, the vector $\mathrm{p}^{(1)}$ from the first step must be multiplied by the same $\mathbf{P}$, because we know that this matrix transforms an arbitrary vector of occupation probabilities into a new one after a scattering event. Thus, for two scattered photons, we obtain $\mathrm{p}^{(2)} = \mathbf{P} \cdot \mathrm{p}^{(1)} = \mathbf{P} \cdot \mathbf{P} \cdot \mathrm{p}$. In general, $\mathbf{P}$ must be raised to power q to obtain the level occupation probability distribution after scattering q photons. The equation:

$$\mathrm{p}^{(q)} = \mathbf{P}^q \cdot \mathrm{p} \tag{3.11}$$

summarizes our modeling approach. There is one more technical point to make: we perform the summation $p_{\text{total}} = \sum_{n=0}^{N-1} p_n$ and interpret it as the total probability of staying on a given site. If we observe that $p_{\text{total}} < 1$, it means that blue photons will kick atoms out of the lattice and reduce imaging fidelity[5].

These ideas can now be applied to evaluate the heating process in an experimentally relevant deep optical lattice of a quantum gas microscope. It will then later be compared to the possible sideband cooling rate with $689\,\mathrm{nm}$ light on the ${}^1S_0 - {}^3P_1$ transition. First of all, Fig. 3.2 shows an example of the original probability density, the Fourier transform, and the boosted Fourier transform corresponding to photon absorption for a harmonic oscillator level. This is a check to show that the frequency of the atom's de Broglie wave, which corresponds to momentum, indeed increases when it gets a kick from a blue photon; this is evident from subfigures (B) and (C) of Fig. 3.2. Performing the calculation procedure for a lattice beam of $5\,\mathrm{W}$ and a waist of $30\,\mu\mathrm{m}$, which corresponds to vibrational level gaps of about $350\,\mathrm{kHz}$ for the ${}^1S_0$ state atom in the low vibrational states (see Table 3.1 for ${}^1S_0$ AC polarizability, and the vibrational

[4]This rate equation model implies perfect decoherence. In other words, we do not take into account any the superposition states of vibrational levels and assume that the problem is fully described by assigning occupation probabilities to all vibrational states. This should be a reasonable assumption in the case of frequent spontaneous emission events, like in the problem at hand.

[5]This is because the number of levels accounted for in the problem is finite (it is also so in a real optical lattice), and the matrix $\mathbf{P}$ is truncated.

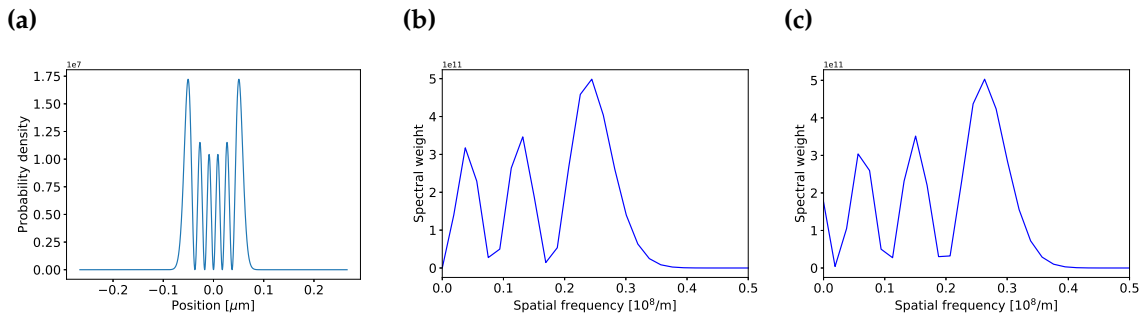

FIGURE 3.2: Example harmonic oscillator wavefunction ($n = 5$) (a) and its projection onto the continuum plane wave states before (b) and after (c) the boost due to photon absorption. All quantities are given as absolute squares, so subfigures (b) and (c) are spectra, and the spatial frequency refers to the atom's associated de Broglie wave.

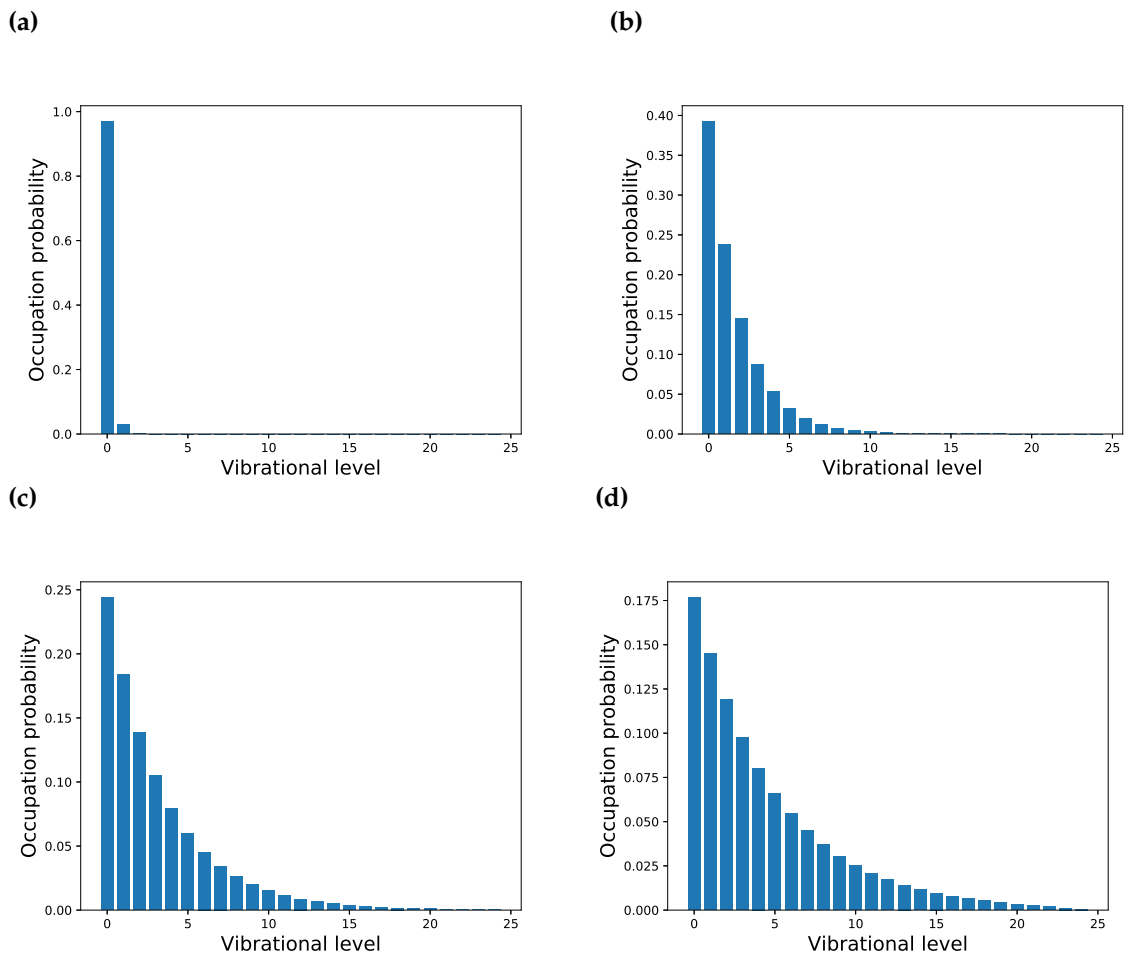

FIGURE 3.3: The harmonic oscillator level occupations for a lattice beam with $5\,\mathrm{W}$ of power focused to a $30\,\mu\mathrm{m}$ waist after scattering 1 photon (a), 50 photons (b), 100 photons (c), and 150 photons (d). The starting level is always $n = 0$.

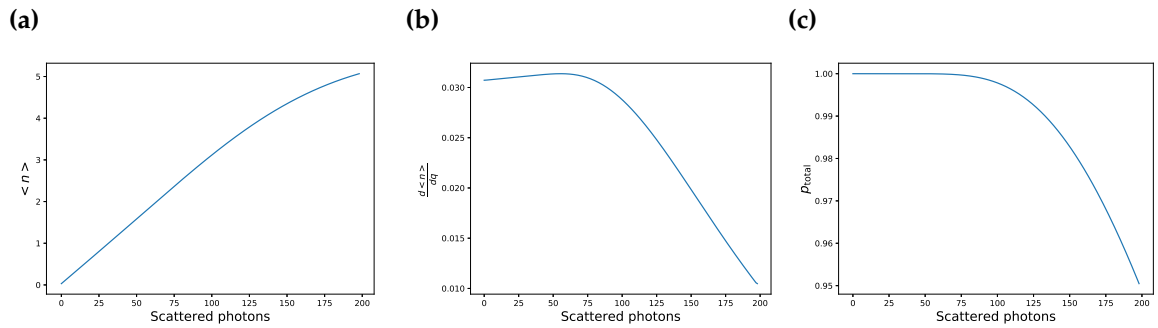

FIGURE 3.4: Average harmonic oscillator quantum number (a), calculated heating rate (b), and total probability of staying within the harmonic oscillator levels (c) for a lattice beam with 5 W of power focused to a 30 µm waist. The starting level is always taken to be $n = 0$.

level energies have been calculated numerically for a single well of a cosine wave lattice by modifying the *Python* script provided with Ref. [120]), we get the results shown in Fig. 3.3. That simulation is done for ^{87}Sr, but the result will not differ much for the other isotopes. For these parameters, $p_{\text{total}} = 0.998$ after scattering 100 photons, and $p_{\text{total}} = 0.983$ after scattering 150 photons. Since we have taken a total of 25 harmonic oscillator levels, and since we would not want the atoms to end up in highly excited vibrational states because then tunneling will increase, this suggests that scattering 100 photons is essentially the limit in the absence of a cooling mechanism. The collected fraction of photons in our objective is predicted to be about 5% due to the solid angle alone (see Subsection 3.2), and there are other losses on optical surfaces and filters, so 100 scattered photons are not enough for reliable atom identification. At the same time, this result suggests that with only moderate cooling we should be able to have enough photons for high-fidelity imaging, given an efficient low-noise camera.

We now formally define the heating rate r_{H} during imaging to be the rate of change of the average harmonic oscillator quantum number with the number of scattered blue photons, so $r_{\text{H}} = \frac{d\langle n\rangle}{dq}$, the angled brackets denoting the average. Fig. 3.4 shows the calculated plots of important quantities for heating in a 5 W, 30 µm-waist lattice that has been used as an example so far. There are a few important observations here. First of all, the heating rate is about 0.03 quanta/photon, which can be converted into rate per unit of time by using a scattering rate corresponding to the intensity of the imaging beam. Secondly, we notice that after scattering about 75 photons (in the non-cooled case as here), the probability of staying trapped starts dropping, and this corresponds to approximately $\langle n\rangle = 3$ according to part (A) of Fig. 3.4. It is essentially an evaporation process, where the atoms escape the trap with an increasing probability when they reach higher vibrational states, and so it looks like the average occupation number increases less, which signifies a lower heating rate. However, we do not want to enter this regime in microscope imaging, because atom loss means that the imaging fidelity immediately starts decreasing. Therefore, the cooling scheme and the scattering rate should be tuned so that $\langle n\rangle \leq 3$, otherwise atom losses would start appearing and reducing imaging fidelity. The crucial point is that now, having a realistic number for the heating rate, we can go

ahead and calculate the cooling rate, and then see how they can be made to balance each other in a steady state.

3.1.2 The cooling process and maximum permissible scattering rate

Given the presence of the $7.4\,\mathrm{kHz}$ $^1S_0 - {}^3P_1$ transition at $689\,\mathrm{nm}$ in Sr, a quite obvious cooling approach to consider is sideband cooling, which is regularly used in ion trap experiments [117, 121], and it has also been shown to work in optical tweezers with neutral atoms [122]. For the optical lattice considered in the heating calculations above, the vibrational level gaps ω are in the hundreds of kHz range for the low vibrational levels, so the sidebands are clearly separated on a $7.4\,\mathrm{kHz}$ transition. Taking $\omega = 2\pi\times\,350\,\mathrm{kHz}$ as an example, the Lamb-Dicke factor evaluates to $\eta = \frac{2\pi}{\lambda_\mathrm{L}}\sqrt{\frac{\hbar}{2M_\mathrm{Sr}\omega_\mathrm{HO}}} = 0.12$ [117, 118]. Even though we cannot truly claim that $\eta << 1$, we still expect photon emission with harmonic oscillator state change to be much less probable than the one without. The relative rate of the two processes can be expressed as $\frac{P_\mathrm{change}}{P_\mathrm{same}} \approx \eta^2 n$, where n denotes the harmonic oscillator level, and P denotes the probability of a fluorescent emission event with or without a change of a motional harmonic oscillator state respectively[6] [117]. Thus, a possible way to cool the atoms is to tune the $689\,\mathrm{nm}$ laser to the red sideband of the deep optical lattice, in this way letting the laser specifically drive the transition that removes one quantum of motional excitation from the system, and then to rely on the Lamb-Dicke factor to favor the process in which the motional state does not change during spontaneous emission. At the end of this cycle, the atom is back in the electronic ground state but one level down in the potential well. This is a cooling process, and it's the opposite of the heating described in the section above.

The modeling procedure for cooling follows Section IV of Ref. [117], and in particular eq. (118) there, which presents a rate equation approach. Briefly, we first need to calculate the scattering rate R_sc[7], given by eq. (2.2), but now the detuning will take into account the vibrational energy levels and the resulting sideband and carrier transitions. We will set $\Delta = -\omega_\mathrm{HO}$, which means that the laser drives the red sideband. Note one implicit assumption here: the harmonic oscillator frequencies are assumed to be the same in both the ground and the electronically excited states. This assumption is generally not true, but we still use it for computational simplicity, as long as the real difference is small. Using the same notation as in the heating calculation and letting p denote a vector of occupation probabilities of harmonic oscillator levels,

[6] In this case we only consider a possible level change by one unit, so the first blue or red sideband. The theory can be extended to changes by several units in one absorption-emission cycle, but they become suppressed by an additional η^2 multiplication factor for each next sideband.

[7] This is labeled $W(\Delta)$ in Ref. [117].

we can write down a rate equation for the time evolution of these probabilities in matrix form:

$$\frac{d}{dt}\begin{bmatrix} p_0 \\ p_1 \\ p_2 \\ \vdots \end{bmatrix} = \begin{bmatrix} R_{00} & R_{01} & 0 & \cdots \\ R_{10} & R_{11} & R_{12} & \\ 0 & R_{21} & R_{22} & \\ \vdots & & & \end{bmatrix} \begin{bmatrix} p_0 \\ p_1 \\ p_2 \\ \vdots \end{bmatrix}. \tag{3.12}$$

The matrix elements are given by the following expressions:

$$R_{nn} = -\eta^2 n \left[R_{\text{sc}}(-\omega_{\text{HO}}) + R_{\text{sc}}(0)\right] - \eta^2(n-1)\left[R_{\text{sc}}(-\omega_{\text{HO}}) + R_{\text{sc}}(-2\omega_{\text{HO}})\right], \tag{3.13}$$

$$R_{n,n+1} = \eta^2(n+1)\left[R_{\text{sc}}(-\omega_{\text{HO}}) + R_{\text{sc}}(0)\right], \tag{3.14}$$

$$R_{n,n-1} = \eta^2 n\left[R_{\text{sc}}(-\omega_{\text{HO}}) + R_{\text{sc}}(-2\omega_{\text{HO}})\right], \tag{3.15}$$

where as before η stands for the Lamb-Dicke factor, R_{nn} are the diagonal elements, $R_{n,n+1}$ are the elements just above the diagonal, and $R_{n,n-1}$ are the elements just below the diagonal. All the other matrix elements are 0[8]. This rate equation system can be solved to determine how fast the probabilities will approach p_0, for example, given a certain set of parameters such as η, laser power, etc.

Let us now estimate the cooling process with the same experimental optical lattice parameters as the ones we used for the heating described above. The $1064\,\text{nm}$ lattice is not magic for $^1S_0$ and $^3P_1$, but we can find the difference in vibrational frequency gaps for these two electronic states. Denoting the AC polarizabilities of $^1S_0$ and $^3P_1$ by $\alpha^{^1S_0}$ and $\alpha^{^3P_1}$, we get the relation [123]:

$$\frac{\omega_{\text{HO}}^{^1S_0}}{\omega_{\text{HO}}^{^3P_1}} = \sqrt{\frac{\alpha^{^1S_0}}{\alpha^{^3P_1}}}, \tag{3.16}$$

where ω_{HO} denotes the vibrational frequency gaps of the respective state. Carrying out the calculations shown in Section 3.1 of Ref. [123] (note possible typos there) gives the AC polarizabilities of the relevant electronic states, which are listed in Table 3.1. For the purposes of

State	Trap beam polarization	Polarizability [a.u.]
$^1S_0$	any	233.097
$^3P_1$ $m_J = 0$	circular	199.272
$^3P_1$ $m_J = 0$	linear	114.903
$^3P_1$ $m_J = \pm 1$	linear	199.272

TABLE 3.1: Some relevant values for Sr AC polarizabilities at $1064\,\text{nm}$

sideband cooling, we would like to be as insensitive to magnetic field fluctuations as possible, otherwise it will introduce stringent requirements on field stabilization. Therefore, in the case of

[8] The tridiagonal form comes from the fact that we consider only the carrier transition and the first blue and red sidebands. Each next sideband would add two additional diagonal lines.

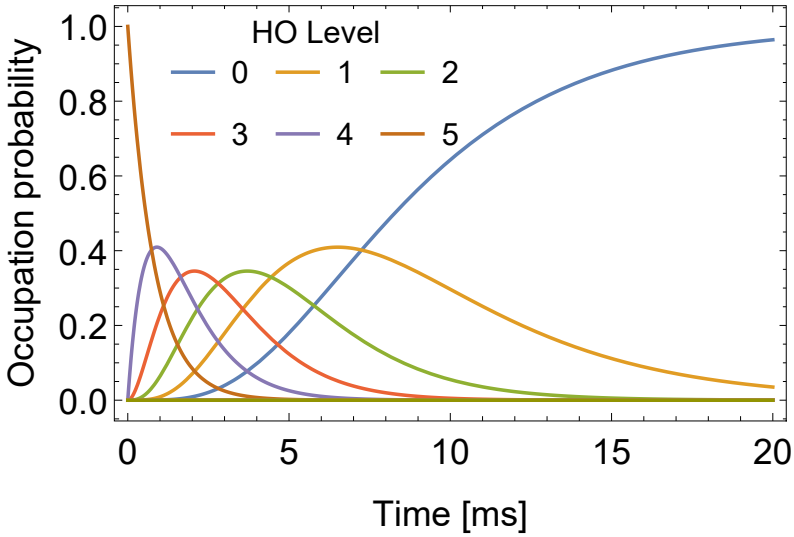

FIGURE 3.5: Evolution of the harmonic oscillator occupation probabilities in a lattice with 323 kHz vibrational frequency gaps while cooling on the -1st sideband.

bosons, we would like to use the $m_J = 0$ substate. The best choice for the optical lattice is then circularly polarized beams, in which case we find from eq. (3.16) that $\omega_{\text{HO}}^{^3P_1,\, m_J\,=\,0} = \omega_{\text{HO}}^{^1S_0}/1.08$. For the case of a 350 kHz oscillator gaps in $^1S_0$ considered above, this leads to 323 kHz oscillator gaps in $^3P_1$[9], and consequently $\eta = 0.122$ with 689 nm light. We will use these values for the cooling calculations, just because taking a smaller vibrational frequency gap and thus a larger η should give us the lower limit on cooling efficiency, and we will see if the cooling scheme still performs well. Fig. 3.5 shows the evolution of harmonic oscillator level occupation probabilities calculated using eq. (3.12) and starting in level 5 (so $p_5 = 1$ at $t = 0$). In this case cooling is done on the -1st sideband using the intensity of $2.5s_0$ of the $^1S_0 - {}^3P_1$ transition. As we can see, the atom is almost certainly in the ground state after 20 ms. Fig. 3.6 demonstrates the approach to the ground state for different intensities of the cooling light, using the same starting conditions. We notice that the rate of this approach saturates at a cooling light intensity of about $5s_0$. This behavior is reasonable, because cooling depends on spontaneous emission, and the fastest theoretically allowed rate of spontaneous emission is given by $\Gamma/2$ of the red transition. Raising the cooling laser intensity much above $5s_0$ will only drive Rabi oscillations, which do not lead to cooling; furthermore, it will cause unwanted sideband excitations by power broadening. Finally, we can estimate the evolution of the average level occupation and the cooling rate[10]. These results are shown in Fig. 3.7. We notice that the cooling rate decreases as the average harmonic oscillator level drops, which is also to be expected; in the extreme case of an atom being in the vibrational ground state, the cooling rate is 0, as it is impossible to decrease the average vibrational quantum number any further. Since we do not want to exceed $n = 3$ in

[9]We get a simple eq. (3.16) just because all other parameters drop out of the ratio: we are talking about the atoms cycling between the ground and the excited state inside the same optical dipole trap, so the parameters of beam power, waist, and atomic mass by definition stay the same and cancel out.

[10]The cooling rate will be defined as the rate of change of the average level occupation, so analogously to the heating rate.

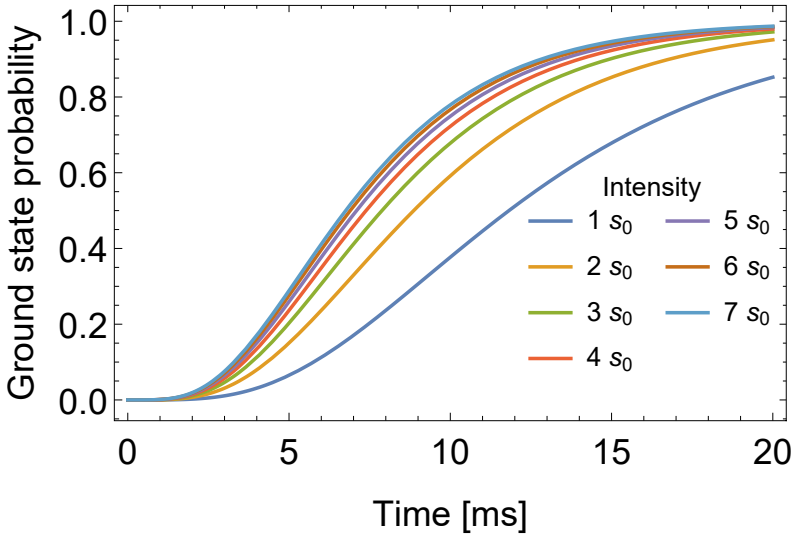

FIGURE 3.6: Approach to the ground state starting from state $n = 5$ in the same lattice as in Fig. 3.5 while cooling on the -1st sideband. Intensity refers to the red cooling beam.

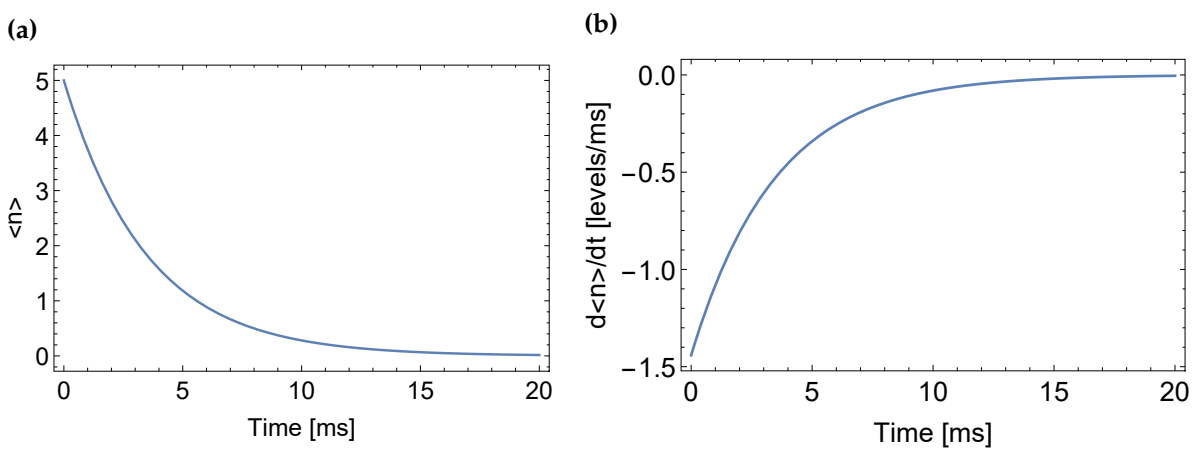

FIGURE 3.7: Evolution of the average vibrational quantum number (a) during the cooling process, and the cooling rate (b), which is the time-derivative of the quantum number, in a lattice with $323\,\text{kHz}$ vibrational frequency gaps, while cooling on the -1st sideband.

order to not cause losses (see the discussion of heating), we should look at the cooling rates for $\langle n \rangle = 3$, which, according to Fig. 3.7 (A), happens after about $3\,\mathrm{ms}$. Fig. 3.7 then shows that the best cooling rate after $3\,\mathrm{ms}$ is about -700 quanta/s[11].

We are now in position to compare heating and cooling rates, and to estimate the number of scattered photons per atom in the case where no atom loss is expected to occur. Based on Fig. 3.4 (B), the heating rate is below 0.035 levels/photon, and we take the inverse of that number to conclude that it takes on average 28 scattered blue photons for an atom to rise up by one vibrational level in this lattice. With the cooling rate being -700 quanta/s, it appears that the scattering rate for which cooling balances heating can be as high as 19600 photons/($\mathrm{s}\times$atom), and the equilibrium is still supposed to be below $\langle n \rangle = 3$. As the collection efficiency of the microscope objective is estimated to be about 5% by geometry (see Subsection 3.2), such a scattering rate suggests that 980 photons/($\mathrm{s}\times$atom) will enter the objective. Assuming rather poor lens and dichroic mirror coating performance, leading to a 60% transmission through the imaging system, and a camera quantum efficiency of 0.6 (it is generally higher for high-end EMCCD cameras), we expect 352 photons/($\mathrm{s}\times$atom) to be converted into photoelectrons on the CCD chip. This is a very large number for a modern scientific EMCCD camera[12], which can reach single photon counting performance. If we reduce the imaging time to 0.5 s and even assume a factor 5 worse performance in terms of scattering, we will still get around 35 photoelectrons per atom per image. This is expected to be well within the signal-to-noise ratio required for reliable atom identification.

3.2 Imaging resolution and the microscope objective

Section 3.1 focused completely on the question of obtaining a sufficient signal level from each Sr atom and keeping it pinned to one lattice site in the meantime. The second part of a working quantum gas microscope is a high-resolution microscope objective, which is the subject of this section. The goal is of course to spatially resolve the signal from each atom. Due to the nonzero wavelength of light and the diffraction phenomenon, any imaging system will have a finite resolution; object features smaller than that will be indiscernible in the image. If we consider fluorescence imaging and view the object as a pattern of points emitting light (which is a working approximation to any real object), then we would not be able to tell apart the two points that are closer than the resolution[13]. One commonly used resolution criterion is the Abbe

[11] The negative sign stands for the fact that it is a cooling process, so the average harmonic oscillator level decreases.

[12] Two common examples of such cameras are iXon Ultra 888 and iXon Ultra 897 from Andor Technology Ltd., Belfast, United Kingdom. Another possible supplier is Nüvü Camēras, Montreal, QC, Canada.

[13] There are methods, referred to as *superresolution imaging* [124], to image smaller features, but we will not be using them. One of their disadvantages is that they require multiple actual photo frames to reconstruct one image at higher resolution.

limit, given by [124]

$$d = \frac{\lambda}{2 \times \mathrm{NA}}, \qquad (3.17)$$
$$\mathrm{NA} = n \sin(\theta),$$

where λ is the wavelength of the imaging light, n is the refractive index of the medium, and NA is the *numerical aperture*. Since our object under study is the optical lattice and the points are the atoms at the individual sites, d must be at most as large as the optical lattice spacing, otherwise the resolution will not be enough to distinguish between occupied and unoccupied sites. We can slightly relax this limit because the knowledge of the lattice geometry makes image reconstruction possible, but the lattice spacing is still the general guideline for the resolution that must be achieved. The Abbe limit is the ideal scenario: the equation depends only on the wavelength and the numerical aperture, but it contains no details about the lenses of the imaging system. Thus, the Abbe limit is the *aberration-free* or *diffraction-limited* resolution, and since real lenses usually introduce aberrations, it becomes an engineering challenge to achieve such resolution in practice.

The approach to building a diffraction-limited system involves possibly using aspherical and achromatic lenses, which can be intrinsically aberration-free, and designing the objective so that the individual lenses compensate each other's aberrations. One should use a commercial optics design package for this job. In our case, the objective was designed by Dr. Georgios Siviloglou and by Ivo Knottnerus using the OSLO package[14] (extensive details about the design and the preliminary testing are given in Ivo's Master's thesis [104] and in this Reference [125]). One point to keep in mind while designing an objective is that adding more lenses makes it possible to better compensate for aberrations, but this also adds more surfaces, which will in turn cause increased loss of fluorescence photons, as no surface is perfectly transmissive, even with antireflection (AR) coating. For example, off-the-shelf AR-coated lenses[15] reflect $\approx 0.5\%$ of incoming light per surface. With the idealized assumption of no absorption or scattering, we get 99.5% of the light passing through each surface. A five-lens objective has 10 surfaces, so the fraction of the light passing through the objective is at most $0.995^{10} = 0.95$. This means that 5% of the signal is lost only on the lens coatings, and even more will be lost if we assume some finite absorption inside each lens, add more surfaces, or account for the fact that there is dust and some roughness of the optical surfaces, which leads to scattering. Furthermore, an objective with more lenses is practically more difficult to manufacture: aberrations can appear from imperfect lens placement itself. Consequently, it is desirable to use as few lenses as possible and to take advantage of software optimization to select and position these lenses in the way that would produce the best possible resolution. Our group produced and tested such a home-built objective [125].

[14] Acronym for Optics Software for Layout and Optimization, from Lambda Research Corporation, Littleton, MA, USA. Zemax, from Zemax LLC, Kirkland, WA, USA is another popular software tool for this purpose.

[15] LA-type planoconvex lenses from Thorlabs Inc., Newton, NJ, USA is one common example.

Chapter 4

Engineering basics for ultrahigh vacuum and electromagnets

Any work with quantum degenerate atomic gases requires a UHV environment. Furthermore, in the case of strontium and many other species that have been brought to quantum degeneracy, the MOT is loaded from an atomic beam and a Zeeman slower. Both the design of a UHV system and of the atomic beam itself require some modeling of gas flow in vacuum, and we would like to give a mathematical overview with the most relevant results and their applicability. In addition, water-cooled electromagnets capable of producing magnetic fields up to a few thousand Gauss are often a necessary tool; we would like to show the main ingredients for designing such magnets and for estimating their thermal performance.

4.1 Dynamics of gases and pumping in a vacuum system

4.1.1 Gas flow through thin tubes and atomic beam formation

A Sr atomic beam for our experiment is obtained by letting a hot gas in a reservoir pass through microtubes (see Section 5.1). The beam quality is determined by the flux and the angular spread of the effusing atoms: we would like to get as high a flux as possible for a given reservoir temperature, and as small an angular spread as possible. Let us also keep in mind that only the atoms moving sufficiently straight along the machine axis will be able to make it through the Zeeman slower. The combination flux and spread will determine the MOT loading speed, and that is beneficial to keep as short as possible for shorter experimental cycle times.

Flow dynamics through a thin tube are strongly influenced by the ratio between the mean free path (MFP) of atoms and the dimensions of the tube [126]. MFP is given by [127]

$$l_{\text{MFP}} = \frac{1}{\sqrt{2}\pi n \sigma^2}, \tag{4.1}$$

where n is the density of the atoms and σ is the effective atomic diameter, which determines collision rates. The density can be determined from the ideal gas law according to $n \equiv \frac{N}{V} = \frac{P}{k_B T}$, with N being the atom number, V the vessel volume, P the pressure, and T the absolute temperature. There are then two regimes to be distinguished: opaque and transparent, also called hydrodynamic and molecular flow. The transparent one is used when MFP is much larger

than tube length and tube diameter, and correspondingly the opaque one is used when MFP is on the same order or smaller than the tube dimensions [126]. We will see in Section 5.1 that our operating conditions do reach the point when MFP becomes close to tube length, in which case the system does start to approach the opaque regime. However, for mathematical simplicity and accepting a certain error, we will only treat the transparent regime. This regime is, in fact, a more desirable way of operating an atomic source.

Effusion from a hot reservoir through a thin tube effectively selects the atoms having momentum vectors pointing along the tube, with a small spread around that. This corresponds to collimating an atomic beam. The governing equations for total atom flux and angular spread in the transparent regime are given in Section III A of Ref. [126][1]. The flux equation is

$$\begin{aligned} \dot{N} &= \frac{1}{4} n \bar{v} \pi a^2 W, \\ W &\equiv \frac{8a/(3L)}{1 + 8a/(3L)}, \\ \bar{v} &= \frac{2}{\sqrt{\pi}} \sqrt{\frac{2k_B T}{M}}, \end{aligned} \tag{4.2}$$

where $\dot{N}$ denotes the flux in atoms/s, W is the Clausing factor, $\bar{v}$ is the mean atomic velocity inside the oven reservoir, and M is the atomic mass. The angular spread of the effusing atoms is given in a piecewise manner by:

$$\begin{aligned} f(\theta) &= \frac{2\cos(\theta)}{\pi} \left[(1 - W/2) R(p) + \frac{2}{3}(1 - W) \frac{1 - (1 - p^2)^{3/2}}{p} + \frac{W \cos(\theta)}{2} \right], \\ p &\equiv \frac{L \tan(\theta)}{2a}, \\ R(p) &\equiv \arccos(p) - p(1 - p^2)^{1/2} \end{aligned} \tag{4.3}$$

for $0 < \theta < \arctan(2a/L)$, and by

$$f(\theta) = \frac{1}{\pi} \frac{\cos^2(\theta)}{\sin(\theta)} \frac{8a}{3L}(1 - W) + \frac{w \cos(\theta)}{2} \tag{4.4}$$

for $\theta > \arctan(2a/L)$, where θ denotes the angle of the atomic momentum vector as measured form the central axis of the microtubes, and L and a denote the length and the inner diameter of the microtubes respectively [126]. Notice that $f(\theta) \equiv \frac{I(\theta)}{I(0)}$ where $I(\theta)$ is the flux intensity at angle θ in units of atoms/(s·steradian). Using these models, one can design and evaluate an atomic source for a particular quantum gas machine, something that we will show in Section 5.1.

[1] Since we work in the transparent regime, the equations ignore the possibility of atom-atom collisions inside the thin tubes. This approximation becomes better as the MFP increases.

4.1.2 Residual gases in an ultra-high vacuum environment

Let us now consider the flow and pressure of unwanted residual gases in a vacuum system, which in most cases should be minimized. Of the possible gas flow types listed in Table 3.1 of Ref. [127] (turbulent, laminar, supersonic, Knudsen, molecular), we are only interested in molecular flow for almost any application in ultracold atom machines. We need the governing equations for gas conductance and pumping. First of all, the conductance of a long cylindrical tube, expressed in m^3/s is given by [127]

$$C = \frac{1}{6}\sqrt{\frac{2\pi RT}{M_{\mathrm{mol}}}}\frac{d^3}{l}, \tag{4.5}$$

where d is the tube diameter, l is the tube length, $R \equiv 8.3145\frac{\mathrm{J}}{\mathrm{mol\,K}}$, T is the absolute temperature, and M_{mol} is the molar mass of the gas in $\mathrm{kg/mol}$. Such tubes are very common interconnects in vacuum chambers. Then, the flow rate at constant temperature though a tube between two reservoirs, which is a good approximation for residual gas flows between the sections of an ultracold atom machine, is given in units of $\mathrm{Pa\,m}^3/\mathrm{s}$ by [127]

$$Q = C\Delta P. \tag{4.6}$$

In this equation, C is the conductance from the equation above, and ΔP is the pressure difference between the reservoirs. These expressions can be used to calculate the performance and the vacuum quality produced by vacuum pumps, the effects of leaks and differential tubes. Given a certain gas inflow rate Q, which can be coming from a dirtier chamber through a differential tube, or from helium leaking through glass, for example, and a certain pumping rate S_p, expressed in m^3/s, we get [127]

$$P = \frac{Q}{S_p}, \tag{4.7}$$

P being the resulting equilibrium pressure in the vacuum chamber of interest.

For more realistic modeling, we need a few additional equations. First of all, the pumping speed listed in a pump specification sheet generally cannot be used directly because we must take into account the conductance of the tubes between the pump and the chamber in a given setup. The effective pumping speed S_{eff} at the vacuum chamber itself is then given by [127]

$$\frac{1}{S_{eff}} = \frac{1}{C_1} + \frac{1}{C_2} + \frac{1}{C_3} + \ldots, \tag{4.8}$$

where C_1, C_2, C_3, etc. are the conductances of the components in the path between the pump and the chamber[2]. Of course we try to make these conductances as large as possible. If there are

[2]In the case of a well-chosen titanium sublimation pump, $S_p \approx S_{eff}$ because titanium covers some of the walls of the vacuum chamber itself.

rectangular tubes in a UHV system, their conductance is calculated by [127]

$$C = \sqrt{\frac{2\pi RT}{M}} \frac{a^2 b^2}{(a+b)l} g, \tag{4.9}$$

where a, b, and l are height, width, and length of the tube, and g is the "form factor", which is approximately 0.5 as long as height and length are not too different. There can also be bends in the tubes; and if we consider a 90-degree kink, its conductance is given by [127]

$$C \approx \frac{1}{6} \sqrt{\frac{2\pi RT}{M}} \frac{d^3}{1+d}, \tag{4.10}$$

where d is the tube diameter. Now we have the tools to model common gas flows and pressures in a cold atom UHV system.

4.2 Fundamentals of electromagnet coil design

4.2.1 Generating magnetic fields

As we have seen in Section 2.2, a quantum gas experiment needs a source of magnetic field for MOT operation, but also for tuning magnetic substates in and out of resonance, and for accessing Feshbach resonances [36], for example. In this section, we will focus on the equations that can be used for designing the main electromagnet, the one which produces the largest magnetic field in our experiment (we will leave the discussion of the less sensitive and critical other magnets, like the Zeeman slower or compensation coils, to Chapter 5, where the details of the experimental apparatus are described). A practical way of generating a highly homogeneous magnetic field is to use two coaxially arranged coils of equal radius in what is known as *the Helmholtz configuration*. To understand this, consider two coaxial circular current-carrying loops of equal radius placed at some distance from each other. The along-the-axis field of each loop can be found by integrating the Biot-Savart law

$$B_z(z) = \frac{\mu_0}{4\pi} \frac{2\pi R^2 I}{((z-z_c)^2 + R^2)^{3/2}}, \tag{4.11}$$

where R stands for loop radius, z is the position along the central axis, z_c is the loop plane location, and I is the running current. In this section's discussions, we will take z to be the central axis of any loops and coils. The total magnetic field is always the sum of the magnetic fields produced by each source separately, so the field of two current loops is

$$B_{z,\text{total}}(z) = \frac{\mu_0}{4\pi} \frac{2\pi R^2 I}{((z-z_{c1})^2 + R^2)^{3/2}} + \frac{\mu_0}{4\pi} \frac{2\pi R^2 I}{((z-z_{c2})^2 + R^2)^{3/2}}, \tag{4.12}$$

where z_{c1} and z_{c2} are the central plane locations of the respective loops. We can now assume that the current runs in the same circulation sense in both loops, denote the distance between

them by D_l, and write down the resulting equation for the along-the-axis magnetic field:

$$B_{z,\text{total}}(z) = \frac{\mu_0}{4\pi}\frac{2\pi R^2 I}{((z+D_l/2)^2+R^2)^{3/2}} + \frac{\mu_0}{4\pi}\frac{2\pi R^2 I}{((z-D_l/2)^2+R^2)^{3/2}}. \tag{4.13}$$

The term $D_l/2$ expression arises from the fact that the plane $z = 0$ is taken to lie midway between the loops, and so one loop is in the positive half-volume, the other one is in the negative one. Consider now the along-the-axis field midway between the two loops, so at $z = 0$; this normally corresponds to the center of the chamber, and this is the place where the ultracold gas sample is trapped. If one evaluates the derivatives of B_z with respect to z at $z = 0$ and sets $D_l = R$, one will find that the first, second, and third derivatives vanish[3]. This condition, $D_l = R$, defines the Helmholtz configuration, and it gives a very homogeneous magnetic field because that field depends on position at most to fourth order at the expected sample location. A real coil consisting of multiple loops has a finite spatial extent, so both its position and radius cannot be defined in a simple way like those of an infinitely thin loop; there is no simple formula for the Helmholtz configuration then, but a similar maximally homogeneous field configuration exists and can be found by numerical optimization.

Let us now consider some specific details for real electromagnets in cold atom machines. First of all, for MOT operation, magnetic traps, and some experiments, we require a field gradient rather than a homogeneous field at the sample. However, this is easy to achieve by running the current in the top and bottom coils of the electromagnet in the opposite sense of circulation (mathematically it means taking I with different signs in the two terms of the sum in eq. (4.13)): the result is a quadrupole field, where $|\mathbf{B}| = 0$ at the center, and from there it grows in all directions. Secondly, a design process will generally benefit from field calculations not only along the central axis, but in all space. One way to do this is to directly integrate the Biot-Savart law for an arbitrary coil configuration, but programming such a calculation requires heavy numerical work, mesh generation, etc. The option that we chose to use is based on the closed-form expressions that give the field in all space for a thin circular current loop, and then representing the shape of a real coil as an integral over such thin loops. These closed form

[3]The fact that all odd derivatives vanish results from symmetry: B_z is eq. (4.13) is an even function, so all its odd-numbered derivatives are odd functions, and they must thus be 0 at $z = 0$. The fact that the second derivative is 0 at $z = 0$ can be shown by an explicit calculation and it specifically relies on having $D_l = R$.

expressions are given in Ref. [128], and in cylindrical coordinates they are

$$B_\rho = \frac{Cz}{2\alpha^2\beta\rho}\left[(\alpha^2+\rho^2+z^2)E(k^2)-\alpha^2K(k^2)\right], \tag{4.14}$$

$$B_z = \frac{C}{2\alpha^2\beta}\left[(\alpha^2+\rho^2+z^2)E(k^2)+\alpha^2K(k^2)\right], \tag{4.15}$$

$$\alpha^2 \equiv a^2+\rho^2+z^2-2a\rho,$$
$$\beta^2 \equiv a^2+\rho^2+z^2+2a\rho,$$
$$k^2 \equiv 1-\frac{\alpha^2}{\beta^2},$$
$$C \equiv \frac{\mu_0 I}{\pi}.$$

Here, z denotes the vertical position, the loop is assumed to lie in the place $z=0$, ρ is the radial position, a is the loop radius, and the functions K and E denote the complete elliptic integrals of the first and second kind [129], which are available as compiled functions in numerical packages such as *Numpy* or $Mathematica$. We work with the version in cylindrical coordinates because, up to the error due to layer changes in the winding procedure (see Section 5.4), the main electromagnets in machines like ours are cylindrically-shaped. Eqs. (4.14) and (4.15) can now be used for practical electromagnet design. We would also like to mention that there exists an efficient computational package called *Radia* [130] (*Mathematica* plugin) for more general Biot-Savart law calculations in different geometries; we used it for some calculations and verifications.

4.2.2 Water cooling of electromagnets

High-current electromagnets in an ultracold atom experiment often experience substantial Ohmic heating, and that energy needs to be efficiently dissipated in order to not overheat the magnet. Water cooling is a good method for this purpose, because we can use hollow copper tubes to wind the coil, and cool it from inside. The electrical power dissipated in a coil is given by $P = VI = I^2R$, where P, V, I, and R are power, voltage, current, and resistance. We assume that heat exchange occurs only with the water flowing inside; the calculation of convective heat exchange through air is difficult, and air cooling is usually much less efficient anyway.

Let us summarize the main equations for water cooling simulations. The steady-state flow of water through the coil will limit the coil's temperature increase to [131]

$$\Delta T = \frac{P}{\rho_w C f}, \tag{4.16}$$

where ΔT is the difference between the water temperature and the steady-state coil temperature with a constantly flowing current, P is the dissipated electrical power, ρ_w is water density, C is water heat capacity, and f is the flow rate. Estimating the pump pressure that can achieve this flow rate is more difficult and error-prone, because it requires solving complicated fluid

dynamics that takes into account the shape of the water duct and fluid friction. However, one simplified approach is to relate flow rate and pump pressure according to the Darcy-Weisbach equation [132, 133, 134]

$$\Delta p = f \frac{L}{D_h} \frac{\rho_w v^2}{2} \tag{4.17}$$

where f is the Darcy friction factor, L is the length of the duct, D_h is the hydraulic diameter of the duct (the actual diameter for a circular pipe, and corresponding expressions for other shapes [133]), and v is water velocity in the pipe. For a relevant case of a square hollow tube, the hydraulic diameter is simply given by $D_h = a$, where a is the side length [133]. The only unknown parameter now is the Darcy friction factor f. In the case of turbulent flow, with $Re > 4000$, Re denoting the Reynolds number, it is given implicitly by the Colebrook-White equation [134]:

$$\frac{1}{\sqrt{f}} = -2 \log_{10} \left(\frac{k_s}{3.7 D_h} + \frac{2.51}{Re\sqrt{f}} \right), \tag{4.18}$$

where Re is the Reynolds number and k_s is the average roughness height of the tube wall. For a copper tube, $k_s = 0.002\,\mathrm{mm}$ [134]. This equation can be solved numerically for f. For laminar flow ($Re < 2100$ [134]), we have $f = \frac{64}{Re}$ [133, 134]. In the intermediate regime, when $2100 < Re < 4000$, the fluid dynamics are complicated and closed-form equations do not exist; we must simply assume that the reality is expected to be somewhere between the laminar and the turbulent regime predictions. Thus, we can now calculate the steady-state temperature increase for a given value of dissipated electrical power, or find the required pump pressure to limit ΔT to a desired value, which are the main tasks in designing a cooling scheme for a high-power electromagnet.

Chapter 5

Experimental apparatus

The most fundamental ingredients of an ultracold atomic gas machine are a chamber that can support ultrahigh vacuum (see Section 1.2 for a short discussion) and windows (termed "viewports") for accessing the sample with laser beams. The sizes, locations, and other properties of these ingredients must be well-thought-out during the design stage and they must be built with care because any deficiencies cannot be corrected without opening the vacuum chamber, which is a very slow process. In this chapter, we will describe the design and construction of our new vacuum apparatus for strontium. We will pay attention to making the machine not only work, but also be convenient and reconfigurable in order to meet future needs. Let us keep in mind that such machines are built for 10-15 years of operation, and one cannot predict well what research directions will be relevant so far in the future.

General design ideas

We chose to make a three-chamber vacuum system, with gate valves[1] in place to close off the two side chambers and another gate valve for closing off the oven section. The three chambers are: 1) the main chamber; 2) the microscope chamber; 3) the glass cell. The main chamber[2] is the place where the atoms are collected immediately after the Zeeman slower, where the MOTs are made, where quantum gases or optical tweezers can be made and investigated in some experiments, or from which the ultracold gas in a dipole trap can be transported to either side chamber. The microscope chamber is a dedicated steel chamber where the high-resolution objective can be installed (see Chapter 3 and Section 5.7). The objective somewhat restricts optical access in the main chamber, and the entire experiment achieves greater flexibility with a dedicated microscope chamber. The glass cell is currently installed on the side opposite to the microscope, and it can be used for experiments where laser beams need to be put at almost arbitrary angles (not limited by viewport geometry), or where the eddy currents that necessarily arise in a steel chamber need to be avoided.

The gate valves are installed at the critical locations so that we can open certain sections in a planned or an emergency case and modify or repair them without exposing the main chamber to air. Gate valves separate the side chambers so that they can be replaced. A gate valve separates the oven section so that we can open and refill the strontium oven, or add a different chemical

[1] All-metal construction with pneumatic actuators, from VAT Vakuumventile AG, Haag, Switzerland.
[2] The steel components are made of 316LN ESR type stainless steel.

element. There is the fourth gate valve between the main chamber and the back section of the machine because the back section contains a heated sapphire window that may need to be replaced if it gets coated with strontium.

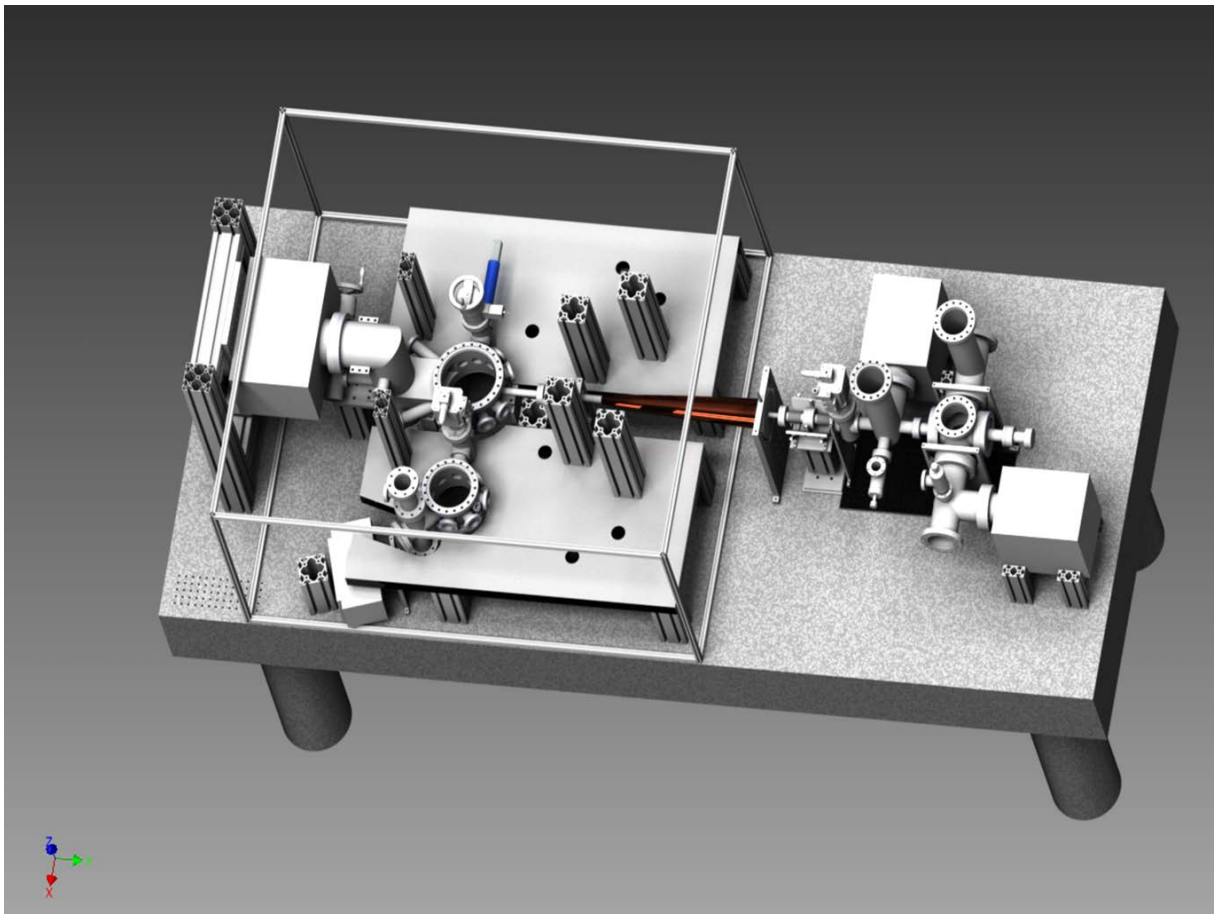

FIGURE 5.1: Three-dimensional rendering of the machine's CAD design (made with the *Autodesk Inventor* suite). The rendering shows the UHV system and the support structure mounted on an optical table. All laser beam optics are omitted (The vacuum system design and the CAD drawings are work of Dr. Georgios Siviloglou).

We decided to load the Sr MOT using a Zeeman slower because this is how Sr machines have been conventionally operated, both in our group and in other groups [37, 123]. In addition, such a design envisions the possibility of adding any alkali species in the future. Production of quantum gas mixtures is an important capability that is available in a current and a former machine from our group [37, 52]. We do note that a Zeeman slower, makes the machine significantly larger, taking up more than 1/3 of the length, and a strontium loading procedure from a compact two-dimensional MOT has recently been reported [135]. However such a scheme would require multiple independent 2D MOT sources for multi-species operation.

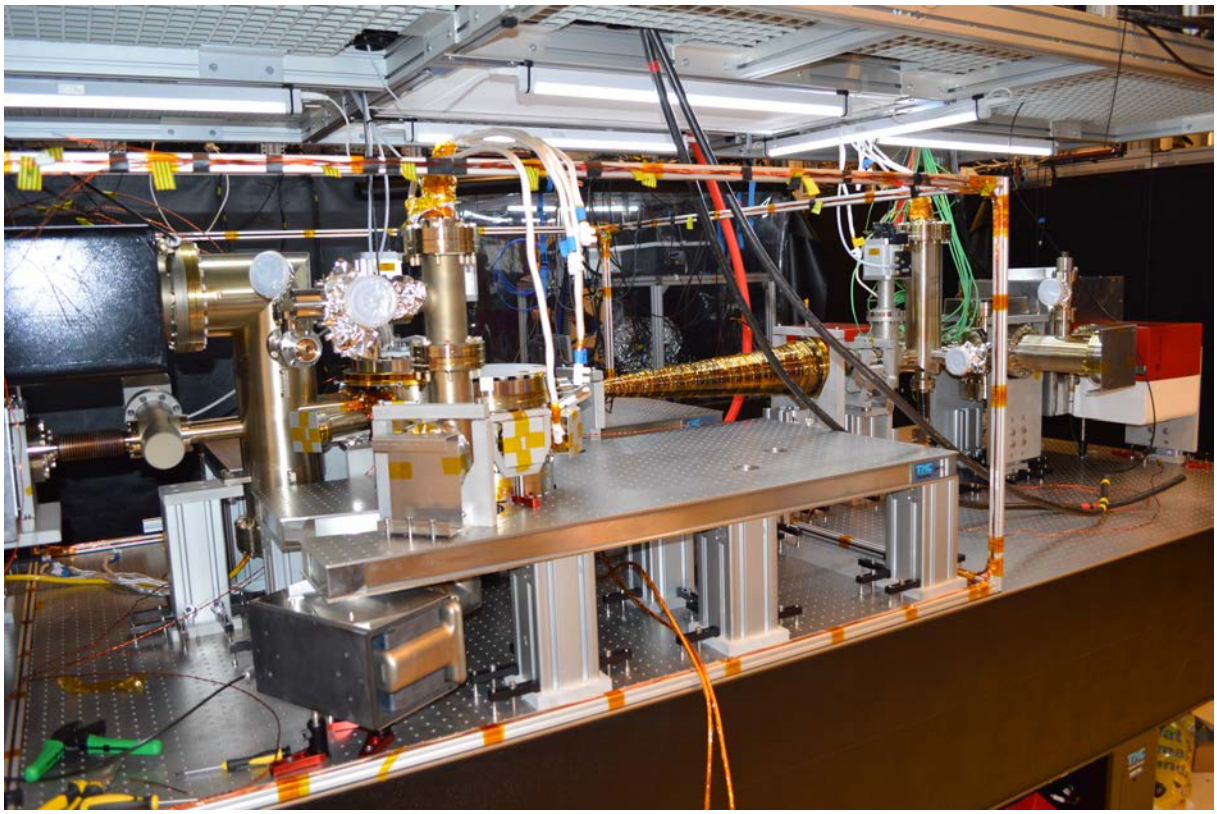

FIGURE 5.2: Fully constructed and baked Sr machine UHV system. Additional optics breadboards and Earth compensation cage coils are also shown here.

Fig. 5.1 shows the CAD rendering of the vacuum system and Fig. 5.2 is a picture of the constructed vacuum system before the installation of any optics. We deliberately show the machine without the optics because the optics can be installed, removed, and exchanged quickly depending on particular experimental needs, while vacuum system modifications are generally not possible or very lengthy. Let us now go part by part and describe this particular apparatus in detail, as well as the considerations that can be useful for building other quantum gas machines.

5.1 Strontium source

The atoms for the experiment are obtained by sublimation from a heated chunk of Sr metal in a hollow oven reservoir. We loaded the oven with $25\,\mathrm{g}$ of a natural sample[3], which has the isotopic abundances listed in Table 5.1 [136]. These abundances are all sufficiently high to work with any isotope by only adjusting the MOT loading time (longer loading for less abundant ones) and the relevant laser frequencies. The atomic oven itself is a hollow tube reservoir held at about $550\,^{\circ}\mathrm{C}$, sealed off at one end and having a set of microtubes pointing towards the Zeeman slower at the other end, similar to the design described in Ref. [137]. Note that at this operating temperature, one must use nickel gaskets instead of the standard copper gaskets for ConFlat

[3]Thermo Fischer (Kandel) GmbH, Karlsruhe, Germany

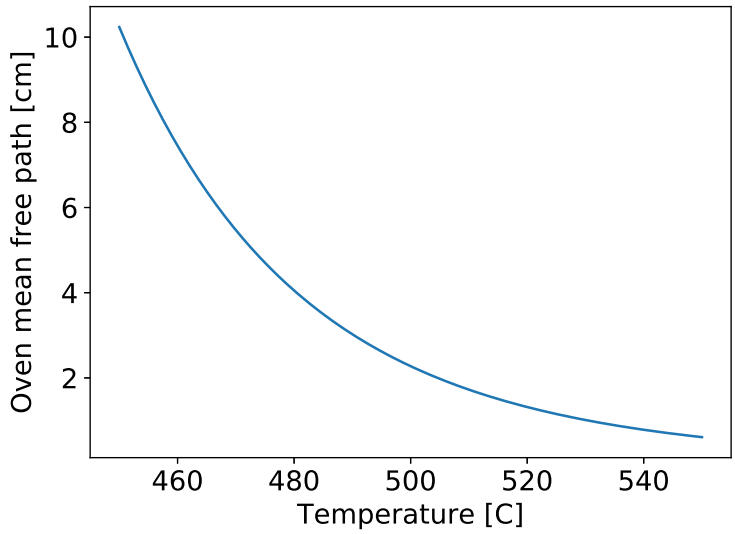

FIGURE 5.3: Calculated mean free path in the oven reservoir.

Isotope	Abundance [%]
^{84}Sr (boson)	0.56
^{86}Sr (boson)	9.86
^{87}Sr (fermion)	7.00
^{88}Sr (boson)	82.58

TABLE 5.1: Abundances of stable Sr isotopes

(CF) flange connections. Fig. 5.4 shows a rendering of the oven flange and a close-up picture of the microtubes held in a triangular cutout in the middle of the flange.

At $550\,^{\circ}\mathrm{C}$, the reservoir is filled with strontium vapor at the pressure of $2.27\,\mathrm{Pa}$. In general, the partial pressure of Sr vapor, P_{Sr}, is described in the relevant temperature range by the following empirical equation [138][4]:

$$\log_{10}\frac{P_{\mathrm{Sr}}}{1\,\mathrm{Pa}} = -\frac{7628}{T/(1\,\mathrm{K})} + 7.498 + \log_{10} 133.322, \tag{5.1}$$

where T is the absolute temperature of the Sr sample (the last term in the sum comes from conversion from mmHg to Pa). Sr is known to have the effective atomic diameter $\sigma = 4.3\,\text{Å}$ [140]. The values of the effective atomic diameter, as well as the vapor pressure and temperature, from which the density can be calculated by the ideal gas law, can be put into eq. (4.1) to obtain the MFP in the oven reservoir. The MFP is plotted in Fig. 5.3, and it is a function of only temperature for a given atom, as pressure and density are in a one-to-one relation with the absolute temperature. Our microtubes have length $L = 8\,\mathrm{mm}$ and inside hole radius $a \approx 55\,\mu\mathrm{m}$

[4]We have converted the units of the result in Ref. [138] into SI units. The pressure is converted from mmHg to Pa according to $1\,\mathrm{mmHg} = 133.322\,\mathrm{Pa}$ [139].

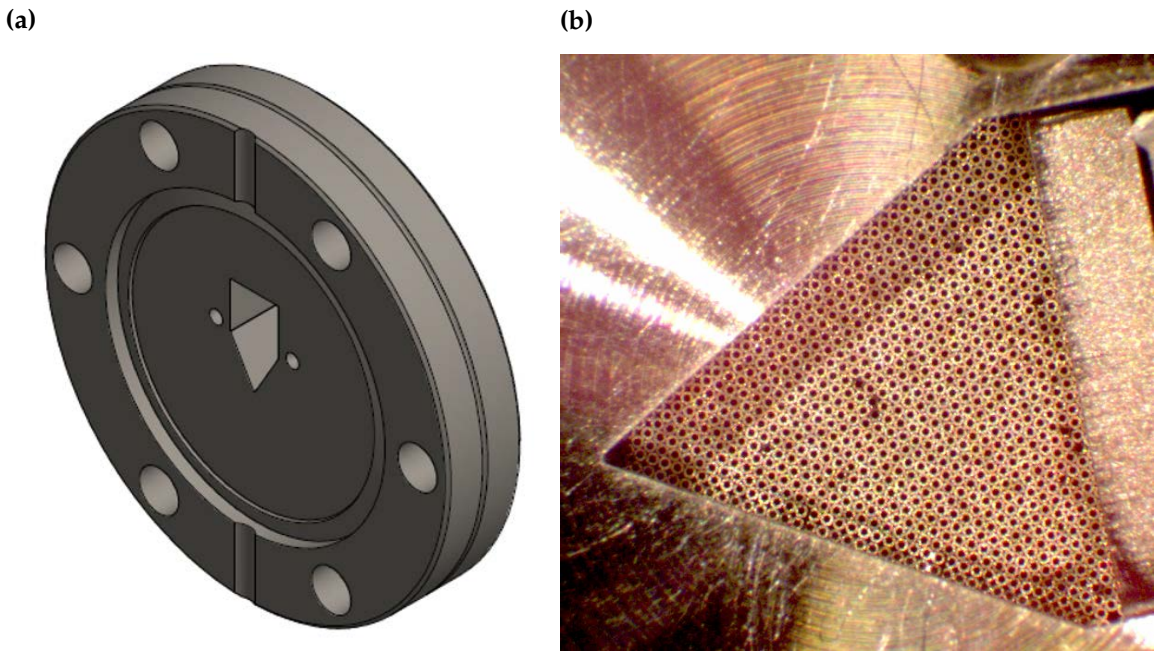

FIGURE 5.4: CAD rendering of the Sr oven flange (a) and a detailed view of the oven microtubes (b). The triangular cutout in the middle in subfigure (a) is the place where the microtubes are loaded. The bar on the right in subfigure (b) is the holder that presses the microtubes down. Flange design: Shayne Bennetts. Flange construction and microtube placement: Sergey Pyatchenkov and the University's Mechanical workshop).

(the outside radius is $95\,\mu\mathrm{m}$). At the normal oven temperature, the MFP is much larger than the microtube diameter, but it approaches the microtube length. However, as the temperature is lowered, the mean free path quickly starts to exceed the microtube length, which corresponds to the transparent mode, and which justifies our simplification and treatment of the problem only in the transparent regime, as described in Subsection 4.1.1. Fig. 5.5 shows the total flux and the angular spread of the effusing atoms, calculated according to eqs. (4.3) and (4.4) respectively. The values for atomic flux are given per microtube, so in order to estimate the total flux in our machine, we will have to multiply the result by approximately 600, which is the number of microtubes in our oven. Regarding the angular spread, we see that about 1/5 to 1/10 of the atom flux is at 5° or more from the central axis. Transverse cooling is used to reduce this angle and the velocity component perpendicular to the line of flight as much as possible and thus to improve the flux into the main chamber. Note that if the density in the oven reservoir or the length of the microtubes become larger, we will get more and more into the opaque regime. In that case atom-atom collisions will become more probable, which we logically expect to lead to reduced flux and increased angular spread. If more accurate predictions are needed, analysis of the opaque regime can be done using the further discussions in Ref. [126]. Alternatively, one can do a Monte Carlo simulation. Practically speaking, due to atom-atom collision effects, we cannot simply keep increasing the oven temperature and hope to get a correspondingly higher atom flux for a given microtube size. The angular spread will also increase, which will reduce

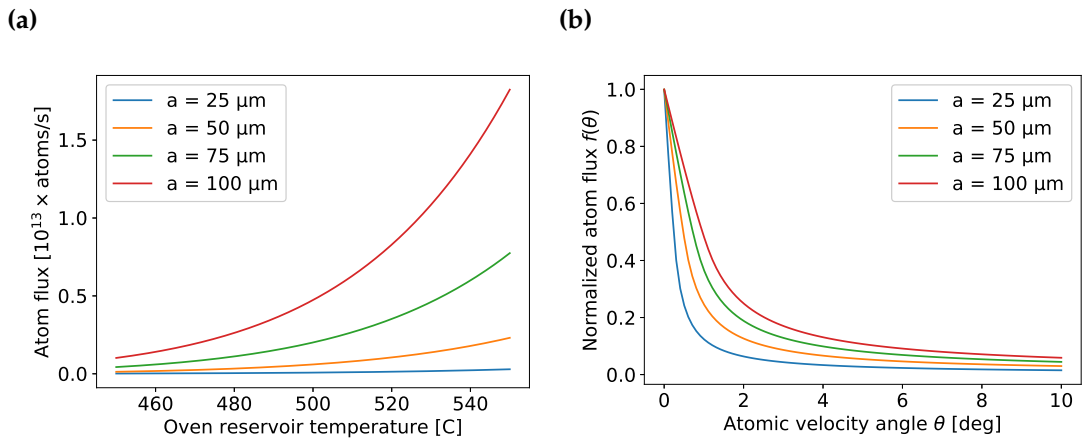

FIGURE 5.5: Performance of the oven in terms of atom flux and effusion angles. Subfigure (a) shows the atom flux through a single microtube with $L = 1\,\mathrm{cm}$ for different inner radii a. Subfigure (b) shows the angles of the effusing atoms' velocity vectors with respect to the axis of the microtubes for $L = 1\,\mathrm{cm}$, $T = 550\,°\mathrm{C}$.

the fraction of usable flux. That is one of the reasons why we do not go above $550\,°\mathrm{C}$ in our oven temperature.

5.2 Transverse cooling

Fig. 5.5 shows that there is a trade-off between Sr flux from the source and atomic beam collimation quality: the narrower the oven microtubes, the more highly collimated the atomic beam, but also the lower the flux. Therefore, it is necessary to make a compromise and to accept a finite amount of angular spread and perpendicular (commonly called "transverse") velocity in the emerging atomic beam for the sake of achieving an acceptable overall flux. We can partly compensate for this spread and improve the collimation by shining light from the sides and decelerating the atoms in the perpendicular direction; this is known as transverse cooling (TC) (see Section 1.2 for the overall context). This is a very useful step because the atomic beam must pass through a long and narrow ZS tube, and even a small velocity in the perpendicular direction will result in the atoms hitting ZS walls and being lost. The governing equations for TC are given in Section 2.3. While it is possible to operate the machine without TC, having it working improves our MOT loading.

We have a dedicated TC chamber with 6" viewports[5] giving vertical and horizontal optical access. Fig. 5.6 shows the cross-shaped TC chamber with the viewport flanges on left and right, top and bottom, blanked off for the high-temperature bake[6]. The large viewports are good for passing long elliptical beams, which increases the interaction time between the cooling light

[5] All flange-mounted viewports on the machine are from Demaco Holland BV, Noord-Scharwoude, the Netherlands. The glass is laser-grade fused silica, and they have broadband antireflection (AR) coating on both sides, transmissive in the $461\,\mathrm{nm}$-$1064\,\mathrm{nm}$ wavelength range.

[6] The atomic oven reservoir is at the front in this picture, it is attached to the TC chamber so that the effusing atoms enter it directly

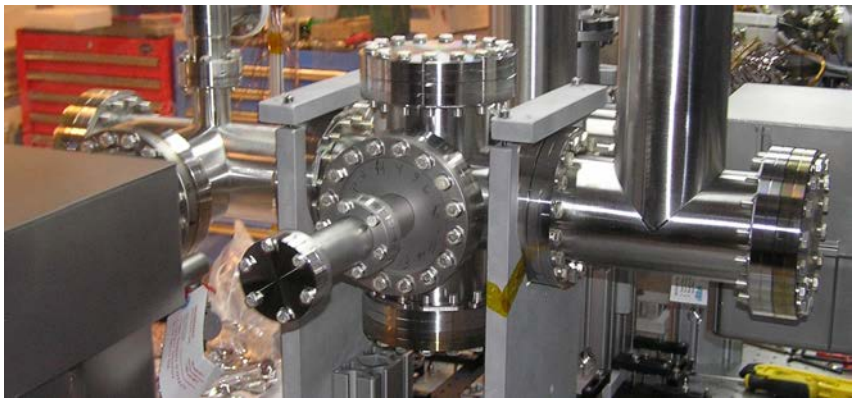

FIGURE 5.6: The TC chamber, shown here mounted in its final supporting structure, before the high-temperature bake with viewport flanges closed off with steel blanks.

and atoms. There are also differential pumping tubes (see Section 5.11) before and after this chamber; they allow us to achieve a cleaner vacuum in the main chamber by isolating it better from the oven, which has a much higher pressure than what is acceptable for quantum gas experiments. There is a wobble stick[7] after the TC chamber, which is a steel rod on a mechanical UHV feedthrough; we need it in order to be able to block the incoming Sr beam when we are not operating the machine and in this way to not cover the gate valve or the back window with Sr (note that the oven is always kept hot, so we cannot stop the flux by shutting down the oven).

In order to design a beam configuration for efficient transverse cooling, we need to calculate a favorable cooling beam shape, given a certain available total laser power. "Favorable" in this context will mean the one that reduces the transverse spread as much as possible, starting from the velocity angle distributions in Fig. 5.5, with the absolute speed given by the Maxwell-Boltzmann distribution in Fig. 5.10. One can imagine two extreme options for beam configurations: one can make small-waist beams with correspondingly high intensity, which will interact with the atoms for only a short time, but with a higher photon scattering rate[8]; alternatively, one can make long-waist beams, which will have lower peak intensity, but will interact with the atoms for a longer time. The optimal transverse cooling will happen somewhere between the two extremes, and the challenge is to approximately find that optimum for a given transition, atomic mass, and laser power. Fig. 5.7 shows the results of a one-dimensional simulation of the TC process (see Section 2.3 for the relevant equations). Laser detuning from resonance has been chosen based on the previous experience in our group [37]. The figure of merit here is taken to be transverse velocity after having passed the TC region, which is a reasonable way to look at this problem: for a given atomic beam produced by the oven, the smaller the transverse velocity after TC, the better chance of actually making it through the ZS tube without hitting the walls. The simulation tells us first of all that short beams are not a good idea; the long axis of the ellipse should have a waist of about $15\,\mathrm{mm}$; further increasing the waist makes the beam less convenient to work with,

[7] Type WBL-275 from Nor-Cal Products, Inc., Yreka, CA, USA.

[8] Remember that the atoms are moving along the machine at around $500\,\mathrm{m/s}$ in the TC section, so they will fly across this beam quickly.

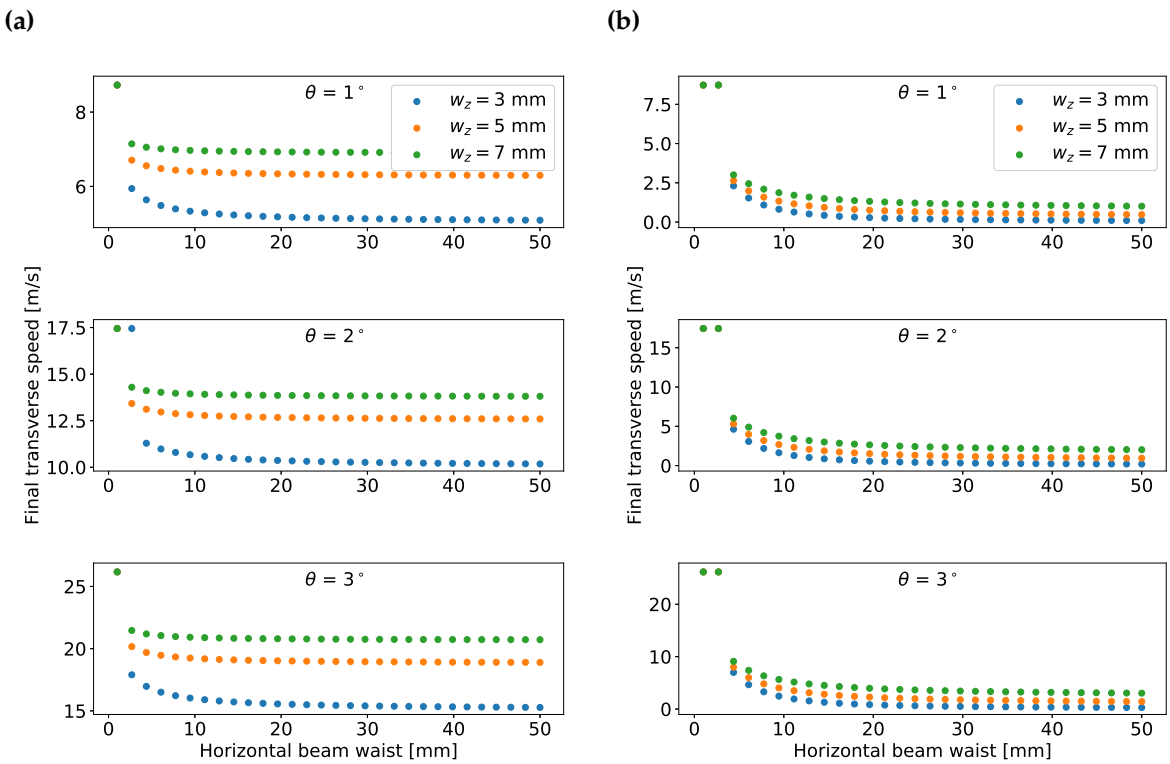

FIGURE 5.7: Calculated ^{84}Sr transverse velocity after the TC stage for different effusion angles θ, shown for $3\,\mathrm{mW}$ of total cooling beam power (a) and for $30\,\mathrm{mW}$ of total cooling beam power (b). The TC beam is assumed to be an elliptical Gaussian TEM00 mode, with the horizontal waist (long axis of the ellipse, along the line of flight of the atoms) given on the x-axis and the vertical waist (short axis of the ellipse) given in the legend. Laser frequency detuning is assumed to be $-\Gamma/2$ from the $461\,\mathrm{nm}$ transition, and the speed of the effusing atoms is assumed to be $500\,\mathrm{m/s}$.

but it doesn't lead to any improvements. Secondly, the simulation tells us that making the beam larger vertically makes TC less efficient, which sounds reasonable because a given laser power is spread over a larger beam. This is, however, an artifact of a one-dimensional simulation, in which we assume that the atoms are flying perfectly along the long axis of the ellipse; a full simulation would need to be made in two dimensions, with the horizontal and vertical beams crossing and the interaction region being an ellipsoid. Our simulation is made fast and simple in order to provide rough guidance, which we then supplement with basic thinking about our beam configuration. Since the calculation tells us that changing the vertical waist does not dramatically change TC efficiency, that waist should be made to roughly coincide with the vertical size of the atomic beam from the oven in order to address the largest fraction of atoms. The exact same logic holds for the vertical TC beam; at this speed, the deflection due to gravity inside the TC chamber is negligible. The final insight based on this simulation and our chamber geometry is that since a longer interaction region is beneficial, we can effectively "recycle" laser power by sending the beam through the TC chamber twice in a Π-shaped configuration and retroreflecting it on the same side where it comes from. Assuming that the amount of scattered photons is negligible at each passage (this is a reasonable assumption, the gas is very dilute, the main loss occurs on the viewports themselves), we double the interaction region for free in this way. This beam configuration is used for both the horizontal and the vertical TC beams, and their estimated waists are respectively $8.4\,\mathrm{mm}$ and $2.7\,\mathrm{mm}$ for the long horizontal and the short vertical axes of the ellipse[9] (the lengths refer to the standard ellipse notation in terms of the semi-major and semi-minor axis and are expressed in the $1/e^2$ sense in intensity). Fig. 5.8 shows the fluorescence of the atomic beam inside the TC section when the ZS beam is on (in this case the TC beams themselves are off).

[9]These waists have not been measured, these are estimations based on the telescope lenses and the mode field diameter of the optical fiber that delivers this light to the machine table.

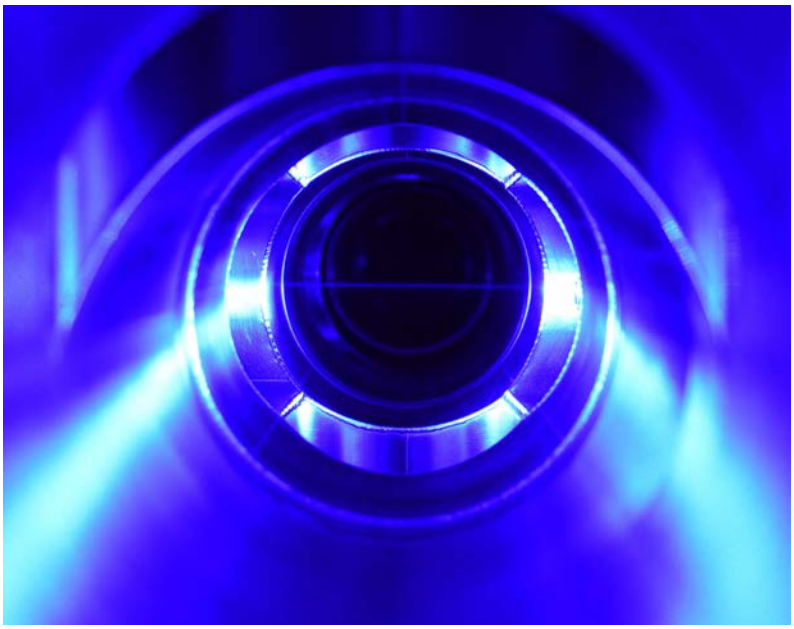

FIGURE 5.8: Fluorescence of the Sr atomic beam (thin blue line in the middle) inside the TC chamber when the ZS laser is on. In this case, the TC beams are off.

Even though we did not quantitatively measure the atom number in the blue MOT with and without TC beams on, mainly because there is no possibility to perform blue MOT absorption imaging, we visually noticed an increase in blue MOT intensity depending on the presence or absence of TC. This is especially important when working with ^{84}Sr and ^{87}Sr, whose natural abundance in the case of ^{84}Sr and relatively inefficient cooling in the case of ^{87}Sr require the maximum possible flux.

5.3 The Zeeman slower

The Zeeman slower is the first crucial laser cooling stage in our machine, which is designed to slow down the atomic beam from about $500\,\mathrm{m/s}$ to about $20\,\mathrm{m/s}$. Integrating the Maxwell-Boltzmann distribution for Sr at the oven's operating temperature, we obtain 63.5% of the atoms at or below $500\,\mathrm{m/s}$; this is the fraction that is expected to be slowed down. Expressed in terms of the Maxwell-Boltzmann distribution, this corresponds to cooling the gas from $550\,^{\circ}\mathrm{C}$ to approximately $2\,\mathrm{K}$ (Fig. 5.10).

The slower is a tube-shaped section with copper wire wound around it to act as an electromagnet, and it consists of two parts: the long main part and the short so-called "spin-flip" part. Its place in the general scheme of the apparatus is described in Section 1.2, and the theory of its operation is explained in Section 2.3. The main part is shown in Fig. 5.9, while the spin-flip part is a tube that is directly welded to the main chamber. Let us take a moment to understand the reasons for these names and to find out why the ZS is built in this particular manner. As we have seen in Section 2.2, the laser frequency as seen in the reference frame of the atoms depends on the Doppler shift. As the atoms are being slowed down, the magnitude of the Doppler shift

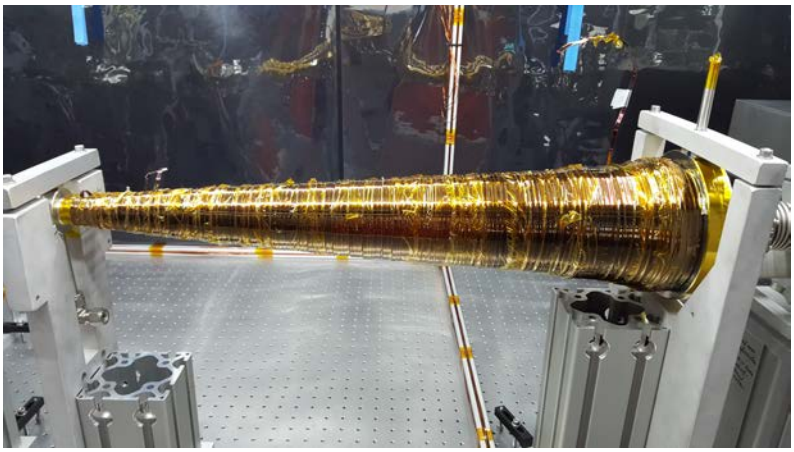

FIGURE 5.9: Long section of the Zeeman slower, shown in its normal support structure.

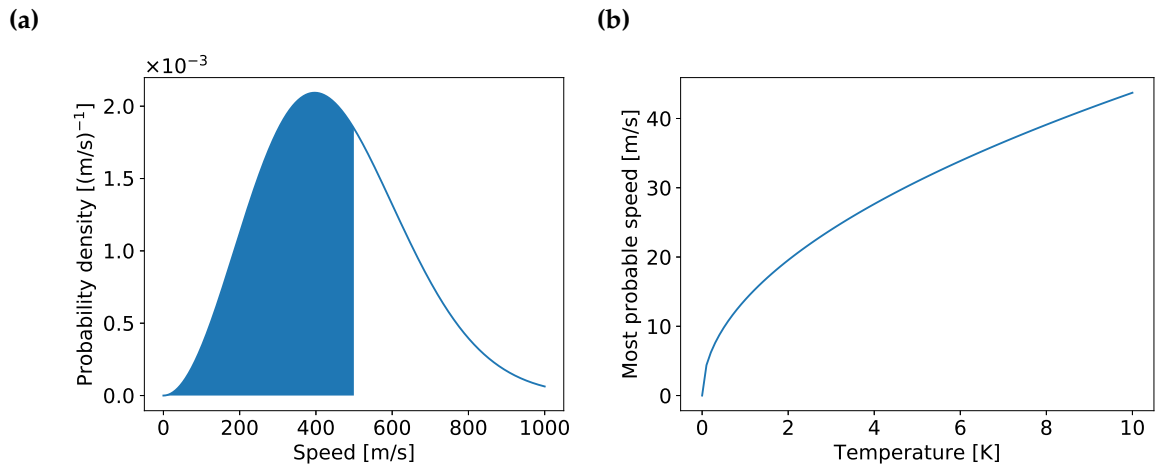

FIGURE 5.10: Maxwell-Boltzmann distribution plots for ^{87}Sr at different temperatures. Subfigure (a) shows the probability distribution for the speed of atoms assuming a temperature of $550\,^{\circ}\mathrm{C}$. Subfigure (b) shows atom speeds and corresponding temperatures at the exit of the ZS.

changes, which would rather quickly bring them out of resonance with the laser and render the further slowing process inefficient. One option would be to change the laser frequency to match the Doppler shift, but this would slow the atoms in a pulsed manner, whereby only some small volume of atoms would be slowed at once, and everything behind and ahead of it inside the ZS tube would be non-resonant and not slowed down. We take a different approach: we design a magnetic field configuration that compensates the Doppler shift at each location. Consider for now the bosonic isotopes of Sr: using different **B**-field strengths, we can shift $m_J = \pm 1$ substates of $^1P_1$ by different amounts, without affecting the $^1S_0$ state, which is nonmagnetic, and thus change the blue cooling transition frequency. The need for different field strengths is the reason for the conically-shaped electromagnet around the ZS tube, with the **B**-field, and consequently the quantization axis, pointing along the tube. Furthermore, since we are addressing $m_J = \pm 1$, the ZS beam is circularly polarized. Which one of the two possible circular polarizations is used

in principle does not matter, it is only determined by the **B**-field direction, which is given by the sense of current circulation.

The next logical question is: what should the laser frequency be? In other words, the laser should be resonant with the atoms moving at which velocity? The answer to this question will explain why there are two parts, and what the origin of the "spin-flip" term is. An apparently simple option is to say that the frequency should be the bare transition frequency, so resonant with the slow atoms at the end of the slowing process. This can be done, and then the electromagnet compensates the Doppler shift along the way, up to the end, where the velocity is minimal and the Doppler shift is small. However, we must remember that the atoms exiting the ZS are captured in the MOT, and the ZS beam shines from the back of the machine, through the MOT location, and into the ZS tube. Consequently, such an approach would mean that the ZS beam is resonant with the atoms in the MOT, and it would be essentially destroying the MOT. This is where the "spin-flip" idea comes in: we make the laser resonant with the atoms at some larger velocity, let's say $200\,\mathrm{m/s}$, as in our case. The beam is thus red-detuned by $434\,\mathrm{MHz}$ from the bare transition. This immediately avoids the problem of MOT destruction; the ZS beam is not resonant with the almost stationary atoms in the MOT. So we now have the following picture: the atoms effusing from the oven are too fast to be resonant with the ZS beam, the laser beam is blue-shifted too much in the atoms' reference frame, and this is compensated by the electromagnet (shown in Fig. 5.9), which Zeeman-shifts the transition towards the blue. When the atoms are slowed down to $200\,\mathrm{m/s}$, they get in resonance with the laser, and this is spatially where the first electromagnet ends. Then they pass vacuum bellows and enter the short ZS section. Now as the atoms are slowed further, the Doppler shift is too small to compensate for the laser's red detuning, so we must do that again with the magnetic field, but now the magnetic field must reduce the transition frequency. One could imagine switching the laser polarization to address the other m_J; that state's energy would be decreasing in an increasing magnetic field. However this would require running the ZS in some kind of a pulsed manner during MOT loading, or applying two beams with opposite circular polarization, and would by definition be less efficient. We take a different approach: we will flip the sign of the magnetic field by running the current in the opposite sense of circulation in the spin-flip section. The result is equivalent to having the laser beam of the opposite circular polarization and it leads to addressing the m_J state that is decreasing in energy with rising magnetic field (rising in terms of absolute value). We have, speaking with serious abuse of notation, "flipped the spin", the "spin" here actually referring to m_J and not m_S. Now we can again compensate the detuning by increasing the absolute value of the magnetic field along the line of flight, and finish the slowing process. This spin-flip section has the **B**-field maximum at the end, and that field extends into the main chamber. It has to be eventually compensated in order to null the undesirable magnetic field bias from the ZS at the location of the trapped sample; this will necessitate one of the coils described in Section 5.5. Fig. 5.11 schematically shows the two ZS sections with the directions of the magnetic field, the atom path, and the light path.

The discussion above has focused on bosonic Sr, where the $^1P_1$ state has no hyperfine

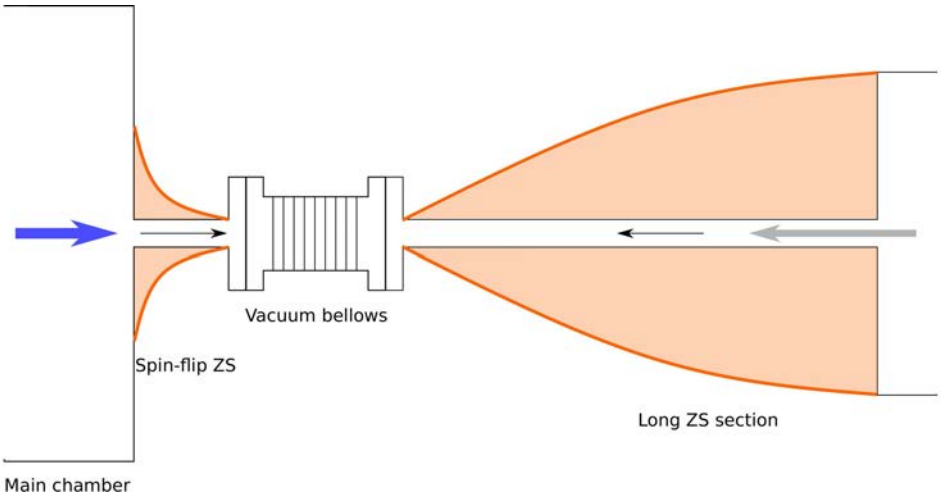

FIGURE 5.11: Schematic representation of the ZS. The thin black arrows show the direction of the magnetic field in the respective sections, the gray arrow denotes the atomic beam, and the blue arrow denotes the circularly-polarized ZS laser beam. The orange sections stand for the copper wire windings of the electromagnets.

structure, but the same ZS has to also work for ^{87}Sr, which does have hyperfine structure. However, this essentially happens for free because the hyperfine splittings in $^1P_1$ are small; the frequency gaps $F' = 7/2 - F' = 11/2$ and $F' = 11/2 - F' = 9/2$ are $43\,\mathrm{MHz}$ and $17\,\mathrm{MHz}$ respectively [21], which is approximately the same as the $30.5\,\mathrm{MHz}$ linewidth of the $^1S_0 - {}^1P_1$ transition linewidth itself, and it is a lot less than the red laser detuning that is used, for example. Therefore, we ignore that hyperfine structure in the design process and calculate ZS parameters only for bosons for the sake of simplicity. The performance for ^{87}Sr is not expected to be very different.

We now need to calculate a magnetic field configuration for an efficient ZS process and then find the appropriate shape of the coil. Note here an important point that frequently comes up in design jobs: finding truly optimal configurations for things like magnets, beam shapes, etc. is a computationally difficult task. The reason is that it's an inverse problem with non-unique solutions. Consider this: if we are given a coil and asked to calculate its magnetic field, we can in the simplest approach numerically integrate the Biot-Savart law and find the field; that is a simple calculation and we also know that this field is unique. However, if we are asked to find a coil to produce a certain desired field, we do not have an immediate equation to integrate, and even worse, there is in general an infinite number of coil configurations that will do the job well enough. That's what makes this inverse problem difficult. We have to make some design choices and try them by calculating the resulting field. Based on the simulation results, we can modify our design and recalculate, until we are satisfied with the outcome. Making good design choices is the art of engineering.

The ZS magnet is designed to achieve constant acceleration along the ZS tube, assuming constant laser power. This is done for computational and conceptual simplicity; it is not the optimal slower, but it does the job. The design recipe is then the following: first, we find the

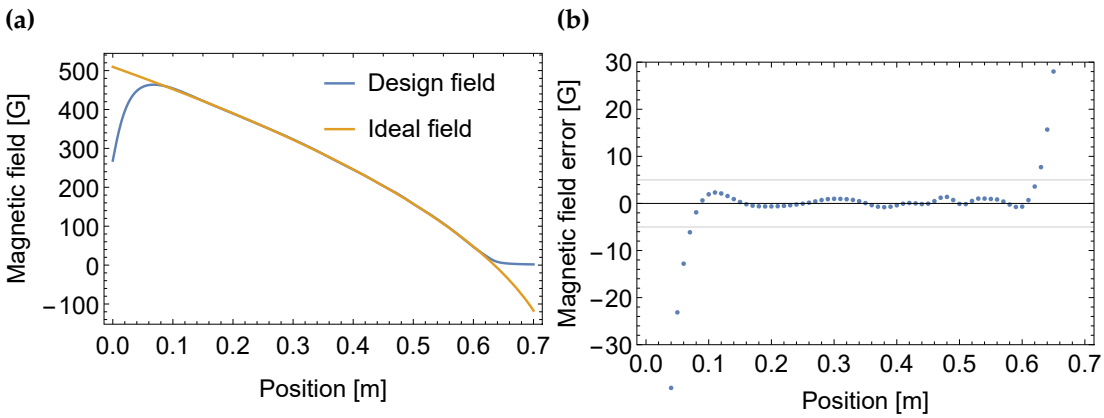

FIGURE 5.12: Calculated Long ZS magnetic field (a) and ZS field error (b), assuming constant acceleration value for the atoms. These particular plots are for ^{88}Sr, but the differences for the other isotopes are small. We assume $\eta_{ZS} = 0.2$. The design field refers to what our chosen wire configuration is computed to produce, whereas the ideal field refers to what would be necessary based on the equations of motion for the atoms. The error refers to the difference between the design and the ideal field. The horizontal dashed lines denote $\pm\,5\,\mathrm{G}$.

ideal magnetic field for constant acceleration, using completely classical analysis (it is eq. (2.30) applied separately to the long and spin-flip parts); next, we try to guess the configuration of wires that will produce such a field and we numerically calculate the field from that presumed wire configuration to see how it deviates from the ideal case; afterwards, we add or remove some wires in different places, recalculate, and repeat this procedure many times until the deviation from the ideal field is small. Figs. 5.12 and 5.13 show the ideal field, the expected coil field, and the difference between the two, which is the field error, for both sections of the ZS. The factor η_{ZS}, mentioned in the captions, is the one that appeared already in Section 2.3: it sets the required value of acceleration in the ZS as a fraction of theoretical upper limit of acceleration on the atomic transition at hand[10]. This is important for two reasons. First of all, the maximum acceleration cannot be achieved in practice because it's the infinite-intensity limit. Secondly, and less obviously, a low η_{ZS} makes the ZS process robust: if there are errors in the magnetic field and at some point along the flight path, the atoms are not slowed efficiently, and they will leave the slowing cycle and be lost because the magnetic field further along cannot compensate for the greater remaining Doppler shift. However if we design the magnet for a smaller acceleration than is actually produced, then even if the resonance condition at some points is not met as expected, the stronger slowing force further along is enough so that even a slightly detuned interaction can slow the atoms sufficiently so that they stay in the cooling cycle. The downside of this is the need for a longer ZS because less acceleration means a longer path to reach the same final speed. We accept this downside because if we required a larger acceleration than is achievable given the laser power and magnetic field errors, that problem cannot be corrected in any easy way afterwards, apart from lowering the magnetic field globally without changing its

[10]The ideal **B**-field profile is calculated using a from $a = \eta_{ZS} a_{max}$.

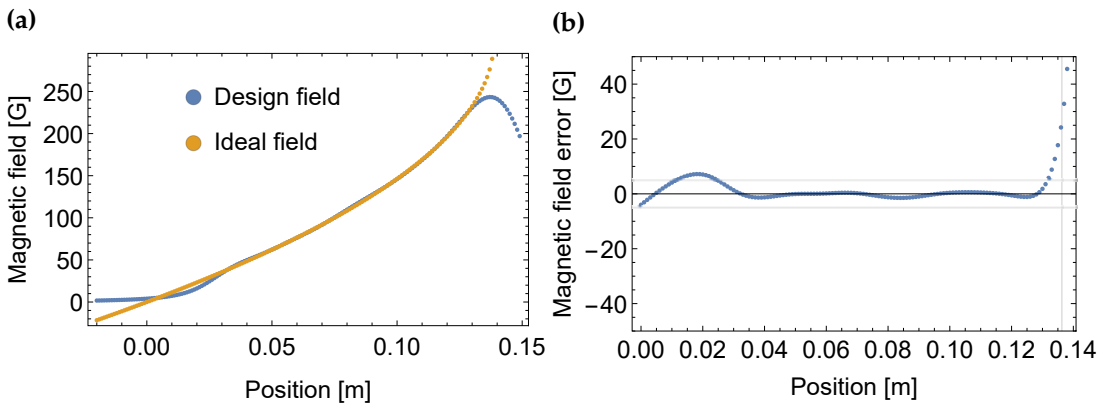

FIGURE 5.13: Calculated spin flip ZS magnetic field (a) and its error (b), assuming constant acceleration value for the atoms. These particular plots are for ^{88}Sr, but the differences for the other isotopes are small. We assume here $\eta_{ZS} = 0.153$. The meaning of the design and ideal field, and the field error, is identical to that in Fig. 5.12. The origin of the horizontal axis corresponds to the beginning of the spin flip ZS coil (at the side close to the long ZS). The horizontal dashed lines in (b) denote $\pm\,5\,\mathrm{G}$. The vertical dashed line in (b) denotes the beginning of the main chamber.

profile, which makes the ZS inefficient.

We measured the magnetic field inside the spin-flip part of the Zeeman slower in order to compare it to simulations and also to evaluate the residual field at the position of the atoms, which needs to be compensated (see Section 5.5). The measurement results and the fit with equation

$$B_z = C\frac{R^2}{(z^2+R^2)^{3/2}},$$

which is a simple model for the magnetic field of a current loop, with C and R left as fitting parameters, are shown in Fig. 5.14. From this fit we expect about $2.5\,\mathrm{G}$ of along-the-axis residual field at $100\,\mathrm{mm}$ of axial distance from the coil, which corresponds to the center of the main chamber, where the MOT resides. As the MOT (see Section 7.1) is centered at the zero point of a quadrupole magnetic field and would be shifted away from the chamber center by this residual field, we have to provide compensation to bring the quadrupole zero crossing to the original position created by the main magnet; this can be easily done with the ZS compensation coil (see Section 5.5)[11]. The calculated final speed of the atoms for the measured magnetic field in the spin-flip section is plotted in Fig. 5.15 for different starting velocities as a function of the laser intensity, given in units of the blue transition's saturation intensity[12]. The plot shows that the atoms entering at high velocity or seeing low light intensity will be lost from the cooling cycle and exit the ZS at high speed, but for higher light intensities, the atoms are cooled efficiently, even when they are slightly faster than the expected entry speed. Consequently, we expect the ZS to produce a flux of atoms entering the main chamber at about $20\,\mathrm{m/s}$, which is within the

[11]The spin-flip ZS magnets and the ZS compensation coil are ramped to zero after the blue MOT stage. They are off during the red MOT and evaporative cooling.

[12]We assume here that the long ZS part works according to its design specifications and produces atoms at about $200\,\mathrm{m/s}$ at the entry into the spin-flip portion.

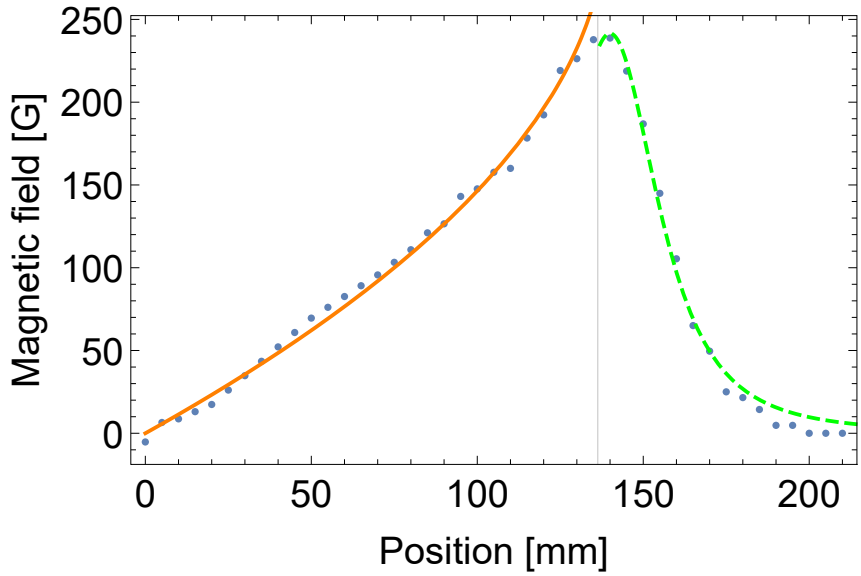

FIGURE 5.14: Measured along-the-axis magnetic field of the spin-flip ZS (blue dots), together with the fit of the ideal calculated field inside the tube (solid orange line) and the fitted residual field in the main chamber (dashed green line). The vertical gray line denotes the end of the ZS tube and the beginning of the main chamber. We note that this is a summed result of two measurements, with each individual measurement performed with one of the two coils on (see main text).

capture velocity of the blue MOT. We note that we did not measure the magnetic field inside the long ZS and we trust the simulation in order to not risk putting oil traces into the ZS tube while manipulating the magnetic sensor. The fact that the short ZS works according to design specifications gives us confidence that the same is the case with the long ZS, because they were designed and made very similarly.

The ZS coils are constructed in two stages. First of all, the long ZS steel tube is designed and manufactured as two concentric pipes so that water can flow in the channel between the inner and the outer one and provide cooling. In permanent operation, water cooling is necessary because we expect the long ZS coil to dissipate about 73 W of power. For the winding procedure itself, the flanges on both sides are closed off with blanks and the coil is wound on a lathe using enameled copper wire with dimensions 1.15 mm by 4.67 mm. Each winding run is started at the thin end of the magnet, it proceeds towards the large disk (see Fig. 5.9), which serves as the physical limit and support for the layer change, and then back as many turns as necessary towards the thin end, at which point the wire is cut off. Then the next run is started closer to the thick end and done in the same way, and so on, until the entire coil is finished. This method produces the required conical shape. The number of wire turns belonging each layer, counted along the long ZS tube, and listed starting from the innermost layer and proceeding to the outermost one, is given the following: {134, 132, 129, 127, 125, 123, 121, 119, 116, 114, 112, 107, 105, 104, 102, 96, 94, 91, 89, 84, 81, 77, 75, 72, 68, 64, 62, 56, 53, 49, 44, 42, 36, 32, 30, 26, 24, 22, 21, 14, 11, 10, 9, 8, 7, 6, 5, 4}.

The spin-flip part is made in a similar way, but it is wound by hand on the mounted chamber.

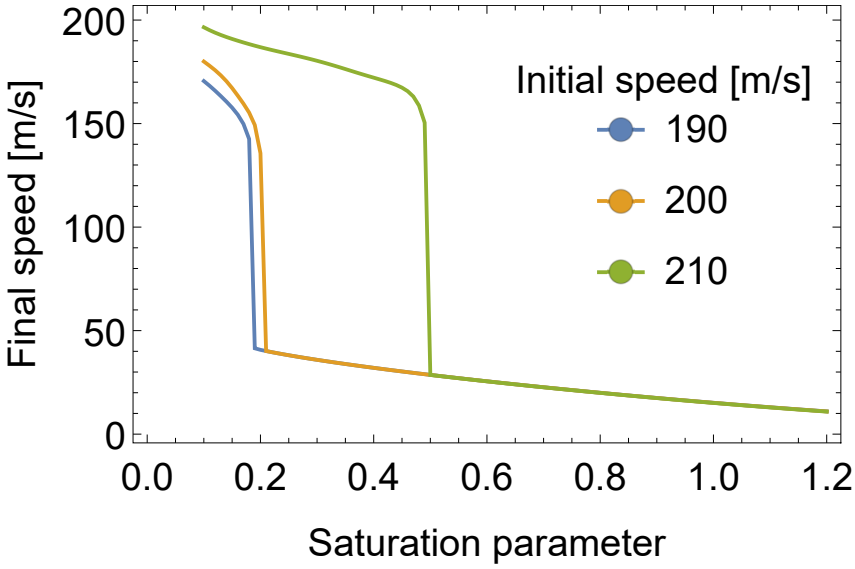

FIGURE 5.15: Calculated final speed of the atoms at the end of the spin-flip ZS, shown for different values of the speed upon entering the spin-flip ZS.

In fact, since the ideal field must increase sharply close to the end of this section (so, the main chamber body), we chose to make this coil in two parts: one is made with the same wire as the long ZS, and in addition, there are 8 turns of $6\,\mathrm{mm}$-diameter round hollow-copper wire for what we call the "high-current" section. The number of turns of the thin wire, listed in the same manner as for the long ZS above, is the following: {22, 21, 16, 12, 10, 6, 4, 2}. We note that since the hollow-copper wire is water-cooled from the inside, we can safely run up to $200\,\mathrm{A}$ of current through it, which allows us to achieve that final steep increase in the magnetic field, all the while making this entire spin-flip section compact, its length being only $13\,\mathrm{cm}$.

The design current for the optimal magnetic field is $4.7\,\mathrm{A}$ in the long ZS, $10\,\mathrm{A}$ in the thin wire part of the spin-flip section, and $110\,\mathrm{A}$ in the high-current part. In the course of experimental optimization we found that the best results are achieved with $5\,\mathrm{A}$, $7\,\mathrm{A}$, $82\,\mathrm{A}$ in each of the sections respectively. The normal operating power in the ZS laser beam is around $32\,\mathrm{mW}$.

5.4 The main electromagnet

When designing an electromagnet for a particular application, there are in principle two options to consider for achieving a given magnetic field strength: one can either use many coil turns and little current, or a high current and few turns. The version with few turns and a high current is safer and more versatile. One then needs less voltage per Gauss of field (good for human safety), and, very importantly, coil self-inductance is lower. Since ultracold atom experiments may require fast magnetic field switching, it is imperative to aim for low self-inductance, otherwise such switching may become difficult or impossible. The field strength is proportional to the number of turns, whereas the inductance is proportional to the number of turns squared [141], which speaks in favor of the high-current approach. This is the way we built our main magnet,

and the design goal then is to find the position and the number of turns that can produce the strongest and most homogeneous field, and that can be efficiently water-cooled with our existing pump. Numerical calculations are performed to predict the necessary current values and the expected temperature increase of the coil.

(a) **(b)**

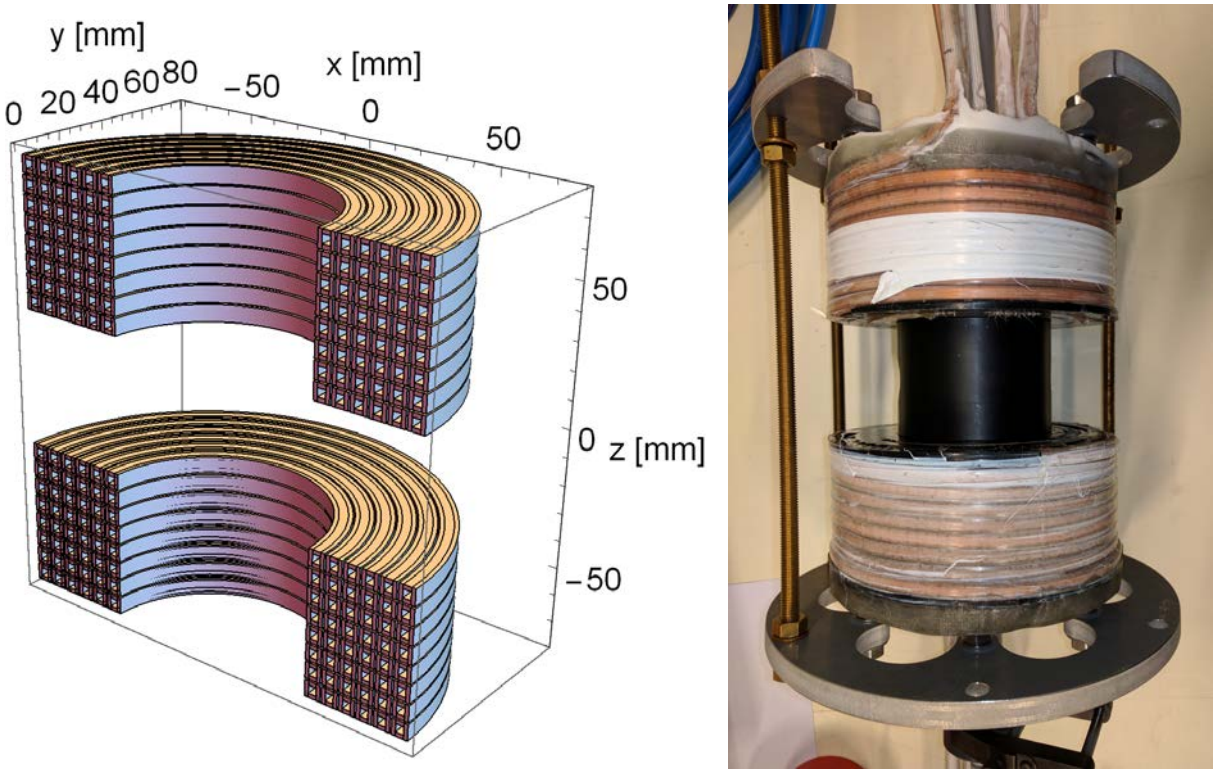

FIGURE 5.16: Main magnet design and manufactured result. The 3D rendered cross-section is shown in subfigure (a) and the assembled magnet with its aluminum holders is shown in subfigure (b). Those aluminum holders are then mounted directly onto the reentrant window flange with M6 bolts.

We chose to make the main electromagnet out of annealed square hollow copper wire, 6 mm-wide on the outside and 3 mm-wide on the inside[13]. A 3D rendering of the coil cross-section and the assembled coil are shown in Fig. 5.16. The coils are made to have the largest possible diameter permitted by the reentrant window, but without coming too close to risk rubbing against the steel. This gives the largest possible magnetic field per unit of electric current. Since the full magnet consists of two separate coils, top and bottom, it can be operated in the bias configuration (meaning a homogeneous field at the center of the chamber), or in the quadrupole configuration (field gradient at the center of the chamber); the particular configuration is set using an H-bridge circuit[14]. The electrical connections of the coils to the power supply[15] and the

[13]CW008A, from Cole & Swallow Materials Ltd, Berkshire, UK.
[14]The H-bridge is made with mechanical relays Kilovac EV200HAANA, rated for 500 A, from TE Connectivity Ltd., Schaffhausen, Switzerland.
[15]TDK Lambda ZUP 6-132 from TDK Corporation, Tokyo, Japan.

H-bridge are shown in Fig. 5.17[16]. Each of the two individual coils has 8 turns in the vertical

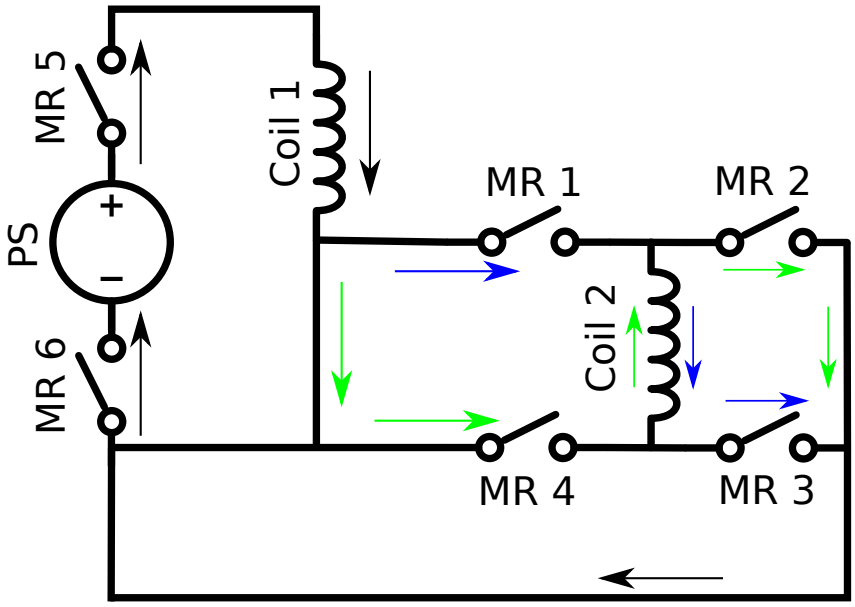

FIGURE 5.17: Main electromagnet power connection and H-bridge. Coil 1 and 2 represent the top and bottom coils, "PS" stands for "power supply", and "MR" stands for "mechanical relay". MR 1 - MR 4 make up the H-bridge, which switches the direction of the current in Coil 2, and this switches the magnet from the bias to the quadrupole configuration; the current direction in Coil 1 is unchanged. In case of quadrupole configuration, MR 1 and MR 3 are conducting while MR 2 and MR 4 are open, while the opposite is the case in the bias configuration. The black arrows denote the current path common to both configurations, the blue ones show the current path only in the quadrupole configuration, and the green ones show the path only in the bias configuration. MR 5 and MR 6 are used to galvanically isolate the main power supply when an additional small current power supply is needed.

direction and 6 turns in the horizontal direction, wound as three barrels of 2 turns horizontally and 8 turns vertically. The reason for this geometry is that layer changes must happen at the bottom, as there is no place to lead the wire to the outside at the bottom of the reentrant windows. The three barrels are made to have different diameters in order to fit one around the next. The wire leads are electrically connected appropriately to each other and to the power supply outside the reentrant window space. The expected magnetic field of such a pair of coils is shown in Fig. 5.18. We note that this calculation is a slight approximation in the sense that the actual windings are not perfectly circular, they are a spiral due to the need for layer changes. Note also the difference between subfigures (b) and (c): as we expect, the quadrupole field is two times stronger along the central axis than in the central plane, and its sign changes. As the plots are shown in $\mathrm{G/A}$, we can say that, for example, the current of about $300\,\mathrm{A}$ will achieve a field of about $1000\,\mathrm{G}$. With sufficient water cooling, the coil is definitely capable of sustaining such a current. We would like to mention as well that since the electrical connections among the barrels are made about $1\,\mathrm{m}$ away from the coil, the barrels can easily be connected each to a different power supply, which adds magnetic field control versatility.

[16]This figure is produced using the Electrical symbols library for vector graphics [142].

The coils are wound on a lathe, using epoxy as the glue that holds their mechanical integrity and provides the means for mounting them onto the vacuum chamber. Each barrel is made of 3 continuous pieces of square copper wire, 8 turns of inner layer first, then layer change, and then the outer layer on top of the inner one. Before winding, the square copper wire is insulated with fiberglass sleeving[17]. It is then soaked in epoxy[18] and wound while wet. The surfaces of the lathe have to be covered with Teflon, otherwise epoxy will stick to them. The coils are only removed from the lathe when the epoxy has completely cured. At the top, a layer of epoxy, approximately $2\,\mathrm{cm}$ thick, is added after the winding has been finished, and that can be seen as the greyish layer above the top coil and below the bottom one, immediately above and below the copper wire in Fig. 5.16b[19]. M8 bolts with large heads and threads pointing away from the coil are embedded in this layer. They allow us to attach aluminum holders (the disks with cutouts on the top and bottom coils, as shown in Fig. 5.16b; the one on the top coil has its cutout facing the front) to the coils, and these holders in turn have M6 holes that can be used to attach the coils directly to the reentrant window flange. Only the cured epoxy provides the connection between the aluminum holder and the copper wires, which is acceptable, epoxy is strong enough for this task. For the final manufactured coils, the inner diameter is $71\,\mathrm{mm}$, the outer diameter is $147\,\mathrm{mm}$ and the distance between the bottom surfaces of the coils is calculated to be about $61\,\mathrm{mm}$[20].

We subsequently measured resistances and inductances, and the magnetic field[21] of the manufactured coils outside the machine. The resistances for the full top and bottom coils are $15.9\,\mathrm{m\Omega}$ and $17.7\,\mathrm{m\Omega}$ respectively, and the measured inductances are $170.5\,\mu\mathrm{H}$ and $170.8\,\mu\mathrm{H}$ respectively. Fig. 5.19 shows measurement results for the bias configuration at different currents, normalized in order to present them independently of the actual current values used for the tests. We note that the measured field strength is slightly smaller than the theoretically predicted one, most likely due to the layer change happening at the bottom of each coil, where it is closest to the measurement point and has the strongest effect on the magnetic field. However, the deviation from the calculated value is only 5%, so this is not a problem for us; it only means that we would need 5% more current to reach a given magnetic field value.

The last part of coil design is water cooling, where we have to calculate and test the increase in coil temperature as a function of the running current. Using eq. (4.16) and assuming that the current is flowing constantly and thus causing constant Ohmic heating, we can determine the required cooling water flow rate through the coil in order to ensure that the equilibrium coil temperature is not higher than a certain value above water temperature. Then, for a continuous copper wire of a given length, we can determine the required pressure drop in order to achieve

[17] Corsil sheath from Tisstech, Bourg Argental, France.

[18] Epoxy resin L and Hardener EPH 161 from R&G Faserverbundwerkstoffe GmbH, Waldenbuch, Germany.

[19] Note that when soaked in epoxy, the fiberglass sheath becomes transparent

[20] This distance cannot be measured directly on the machine, it is calculated based on coil dimensions and the known size of the main chamber

[21] Measurements are done with the magnetometer GM08 from Hirst Magnetic Instruments Ltd., Falmouth, UK.

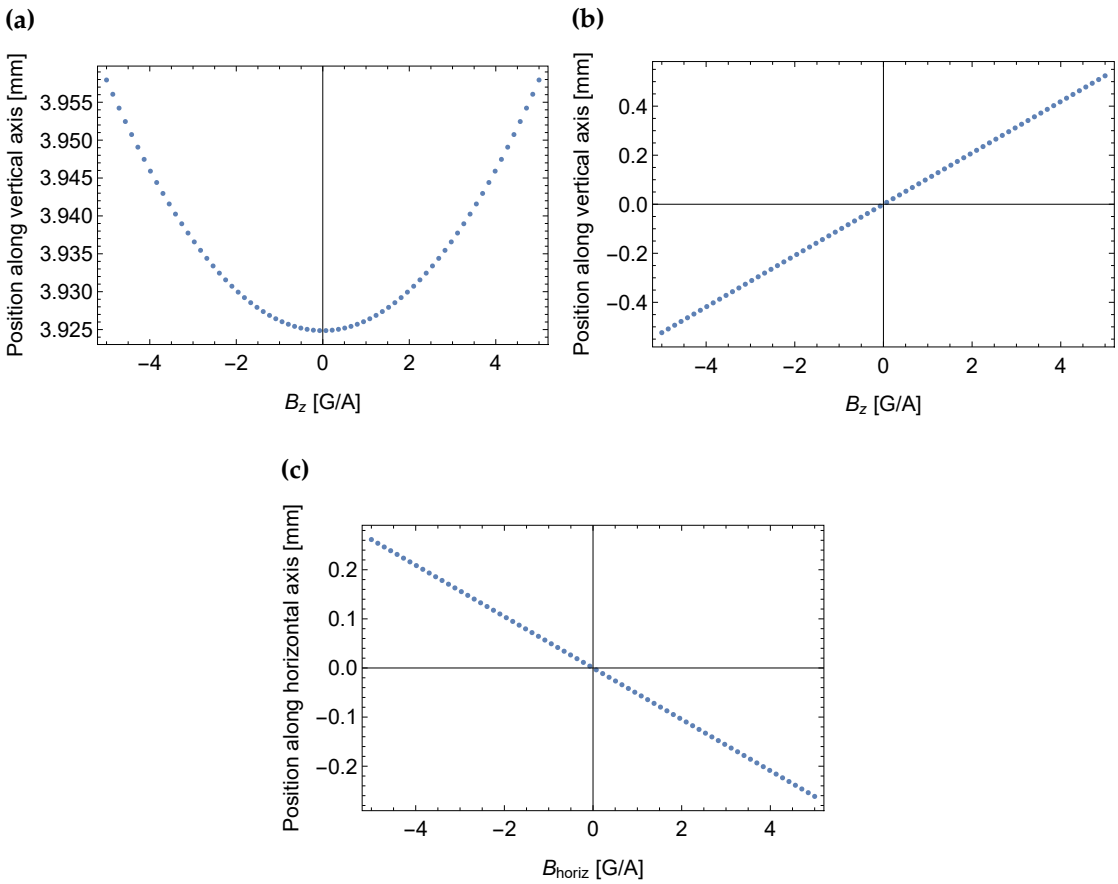

FIGURE 5.18: Calculated magnetic fields of the main magnet. Axial magnetic field in the bias field configuration, along the vertical axis (a); Axial magnetic field in the quadrupole configuration, along the vertical axis (b); horizontal magnetic field in the quadrupole configuration, along a horizontal axis (c).

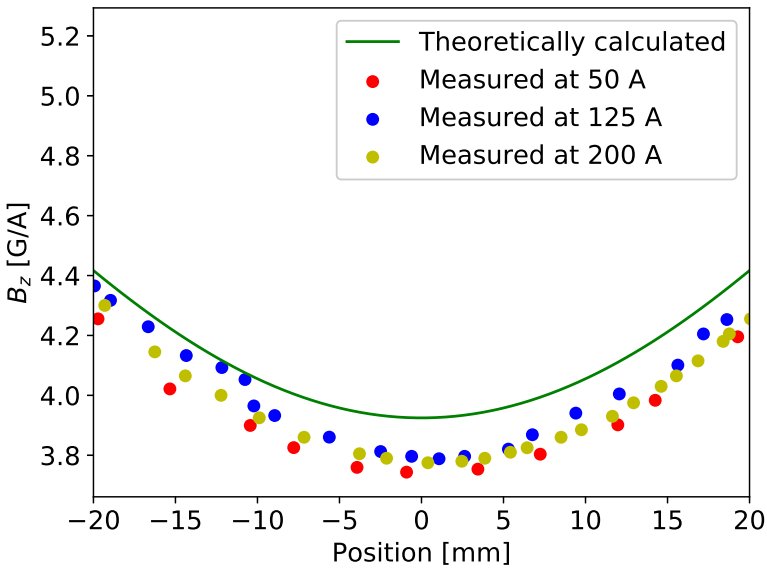

FIGURE 5.19: Comparison between the measured and calculated magnetic fields of the main coil. The measured fields are normalized in order to make the results independent of the current used.

that flow by eq. (4.17). These results are plotted in Fig. 5.20[22]. We performed very rough tests of cooling performance by using tap water from the building, which has approximately $4\,\mathrm{bar}$ of pressure, and we measured the flow rate through each barrel of the coil and the equilibrium temperature increase for different values of the current. With the water flow of about $0.85\,\mathrm{L/min}$ per barrel we got a temperature rise of $2\,^{\circ}\mathrm{C}$ at $200\,\mathrm{A}$. With the flow rate somewhere in the range between $0.35\,\mathrm{L/s}$ to $0.4\,\mathrm{L/min}$ per barrel the temperature increase was $4.5\,^{\circ}\mathrm{C}$. Consequently, the calculations in Fig. 5.20 underestimate the required flow rate, but in practical terms this is not a problem, because the observed temperature increases are safe and manageable for the coil[23]. The existing water chiller and pump in the lab[24] provide a pressure of approximately $4\,\mathrm{bar}$, which is expected to be enough to safely operate the coil up to $400\,\mathrm{A}$; that corresponds to $1.52\,\mathrm{kG}$ in bias configuration and a $410\,\mathrm{G/cm}$ gradient along the vertical axis in the quadrupole configuration. When the coil is mounted on the machine, water connections to it are made with Swagelok brass unions[25], making sure that all unions located above the optical table are copper-to-copper

[22]The kinks in the pump pressure plot come from the fact that the full simulations must be performed in three hydrodynamic regimes: laminar flow, intermediate regime, and turbulent flow; however, the intermediate regime does not have good analytical equations (see Section 4.2.2 for details). For the simplicity of plotting, we artificially extend the laminar flow regime up to the Reynolds number of 4000, but we keep in mind that the results close to the kink on its left side are not valid, because it is not laminar flow anymore. That does not matter because we are mainly interested in pressures of 3-4 bar anyway, which is in the turbulent regime.

[23]A good question is what is assumed to be safe and manageable. First of all, safe operation means that the coil should never approach the temperature where its epoxy becomes malleable, which, for this particular epoxy, is specified to be $70\,^{\circ}\mathrm{C}$. Secondly, it can happen that temperature changes of the coil slightly affect its geometric shape due to expansion and contraction, which in turn affects magnetic field precision. This consideration highly depends on the field stability requirements for the particular experiment that one tries to do.

[24]Manufactured by van der Heijden Labortechnik GmbH, Dörentrup, Germany.

[25]Swagelok Company, Solon, OH, USA.

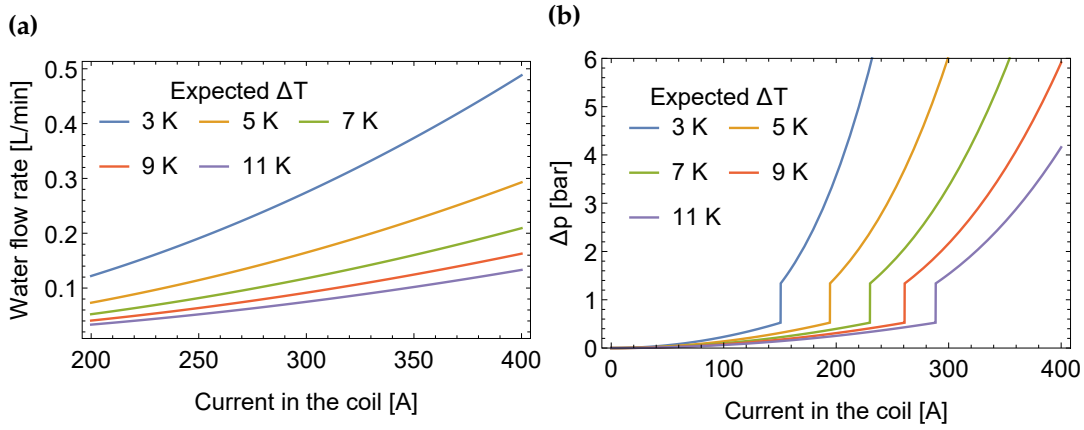

FIGURE 5.20: Expected cooling performance for a 6 mm outside and 3 mm inside square hollow copper wire. ΔT denotes the equilibrium state increase in temperature in the case of a constantly running current, compared to the case of no current. Subfigure (a) shows the water flow required to limit the temperature increase of the wire to below a given ΔT. Subfigure (b) shows the required pump pressure to limit ΔT below a given value in a 10 m wire.

rather than copper-to-plastic for leak safety reasons. The connections from the water distribution manifold to individual barrels are always made in parallel in order to decrease the required pressure drop for a certain flow rate, and there is always a piece of plastic tubing between the manifold and each copper connection to the coil in order to provide electrical insulation. This main coil design is operating normally and it gives us experimental versatility for current and future work. We note that there are multiple thermal switches glued with Kapton tape on top and at the bottom of the main magnet coils. These thermal switches are all connected in series among each other and then connected to the interlock port of the power supply. If the temperature of at least one of them exceeds the threshold of 45 °C, it changes from a conductive state to a high-impedance state, which makes the entire series loop non-conductive, and which in turn triggers the power supply interlock and stops the current to the main coil. This is a protection mechanism against coil overheating, and note that the threshold is set rather far below the 70 °C deflection temperature of the epoxy used to construct the coils[26].

5.5 Additional electromagnet coils

Apart from the main magnet, which is meant to produce the MOT field, possibly Feshbach resonance fields [36], and any strong fields necessary in particular experiments, an ultracold gas machine needs weak coils along different axes for residual field compensation, or, alternatively, as a quick and easy source of small magnetic fields. In our case, those are the Earth field compensation cage coils, the ZS compensation coil, the vertical compensation coils, and the horizontal viewport coils. All of these coils are hand-wound with thin circular enameled copper

[26]See the datasheets for epoxy resin L and Hardener EPH 161 from R&G Faserverbundwerkstoffe GmbH, Waldenbuch, Germany.

	H x W x S [cm]	Measured **B**-field [mG/A]
x-axis	78 x 165 x 150	36
y-axis	78 x 150 x 165	32
z-axis	150 x 165 x 78	151

TABLE 5.2: Sizes and measured magnetic fields of the Earth compensation coils. H, W, and S stand for height, width, and separation distance between the coils, respectively.

wire and are designed to be operated with no more than 10 A of current[27]. They are all driven by commercial adjustable linear power supplies[28], controlled by an analog signal from the control system (see Section 5.14). Just like on the main coils, there are thermal switches for different limiting temperatures placed in various places on the compensation coils to prevent overheating.

The Earth field compensation coils are three large pairs of rectangular coils along the x, y, and z axes. Their main purpose is to compensate the Earth magnetic field, and also other small stray magnetic fields, such as those coming from the ion pump magnets. Each single coil has 10 turns of wire. The sizes and the measured magnetic fields of these coils are listed in Table 5.2.

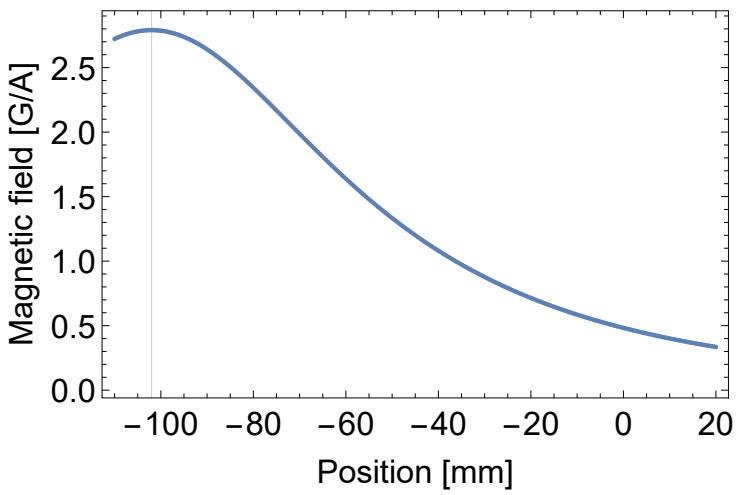

FIGURE 5.21: Calculated along-the-axis magnetic field produced by the ZS compensation coil. The thin vertical gridline shows the position of the coil, and the center of the main chamber is assumed to be at 0.

The ZS compensation coil is wound on the large rectangular duct leading from the main chamber to a large ion pump and it serves to null the residual magnetic field of the spin-flip ZS at the position of the atoms. It has approximately 30 turns of wire. Its calculated magnetic field is shown in Fig. 5.21 (along-the-axis component of the field). This coil is also eventually used for fine adjustment of the final red MOT position (see Sections 1.2 and 7.2 for information about the red MOT). Its predicted strength is approximately 0.5 G/A. This means that in order

[27] Pulses of larger current are possible, but any continuous operation with a larger current must be tested carefully while monitoring coil temperature.

[28] Type EA-PS for different voltages and currents, depending on the coil, all from EA Elektro-Automatik GmbH & Co.KG, Viersen, Germany.

to compensate roughly 2.5 G from the spin-flip ZS, we would need to run 5 A, which is easily achievable.

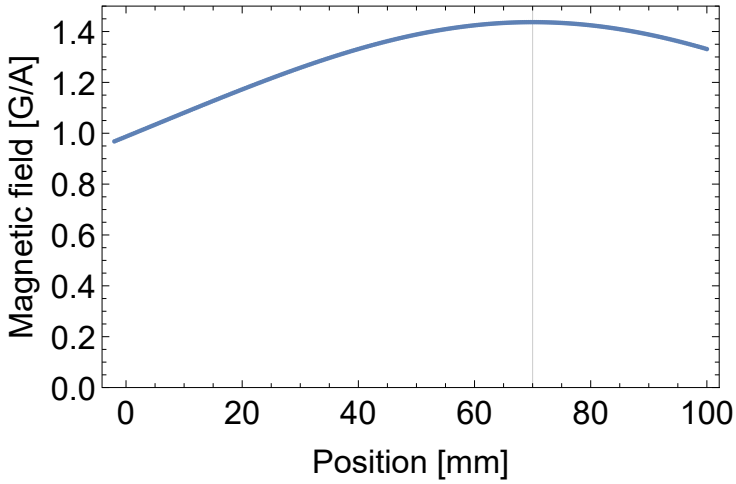

FIGURE 5.22: Calculated along-the-axis magnetic field of the inner vertical compensation coil (so this is the vertical axis one the machine). The thin gridline shows the position of the coil, assuming that the center of the chamber is at 0.

The vertical compensation coils are two circular coils wound one on the outside of the other in an aluminum holding ring, approximately 26 cm in diameter, that is mounted on the large top flange of the main chamber. The ring sits about 7 cm above the center of the chamber, and the coils are made from circular enameled copper wire, very similar to the one used for Earth field compensation coils. The inner coil has 5 turns and the outer one has 30 turns. The purpose of these vertical coils is to quickly make small bias fields, and so there are two possibilities in terms of speed and strength of magnetic field generation: the fastest option with the inner coil, and the higher field option with the outer coil. The calculated magnetic field of the outer coil is plotted in Fig. 5.22, and the strength at the center is expected to be around 1 G/A. We note that these coils do not produce a uniform vertical field at the center of the chamber because there is no corresponding set on the bottom viewport due to geometric constraints; the field is slanted with respect to the vertical at all positions away from the central axis, and it is also variable in space, even to first order in position. However, this is a small effect because these coils are designed to be used in the last stages of the MOT and with quantum gases or optical tweezers. As the spatial extent of those samples is on the order of micrometers, it is much smaller than the size of the coils, and so the spatial nonuniformity of the magnetic field across the sample can generally be neglected. The outer coil is used for vertically moving the red MOT in the optical tweezer experiments, for example (see Chapter 9).

The last set of compensation coils consists of three pairs of small coils wound on the viewports of the main chamber. They are designed to produce bias or quadrupole fields along the axes in the horizontal plane. Since the main magnet and the vertical compensation coils are oriented vertically, we wanted to also have the possibility to produce a horizontal magnetic field and to set the quantization axis in the horizontal direction, if necessary. At the center of the chamber,

they are expected to produce a bias field of about $1.5\,\mathrm{G}$ per $10\,\mathrm{A}$. Note that $10\,\mathrm{A}$ is about the maximum safe continuous operation current for these coils, and operation at any larger current should first be closely monitored by observing the temperature increase In essence, the Earth field compensation coils could take the function of these small coils, but due to their large size, those coils produce stray magnetic fields for other ultracold Sr machines in our group, which becomes problematic if their values are changed during our experimental sequence. Therefore, using small coils closer to the chamber is better.

5.6 The main chamber

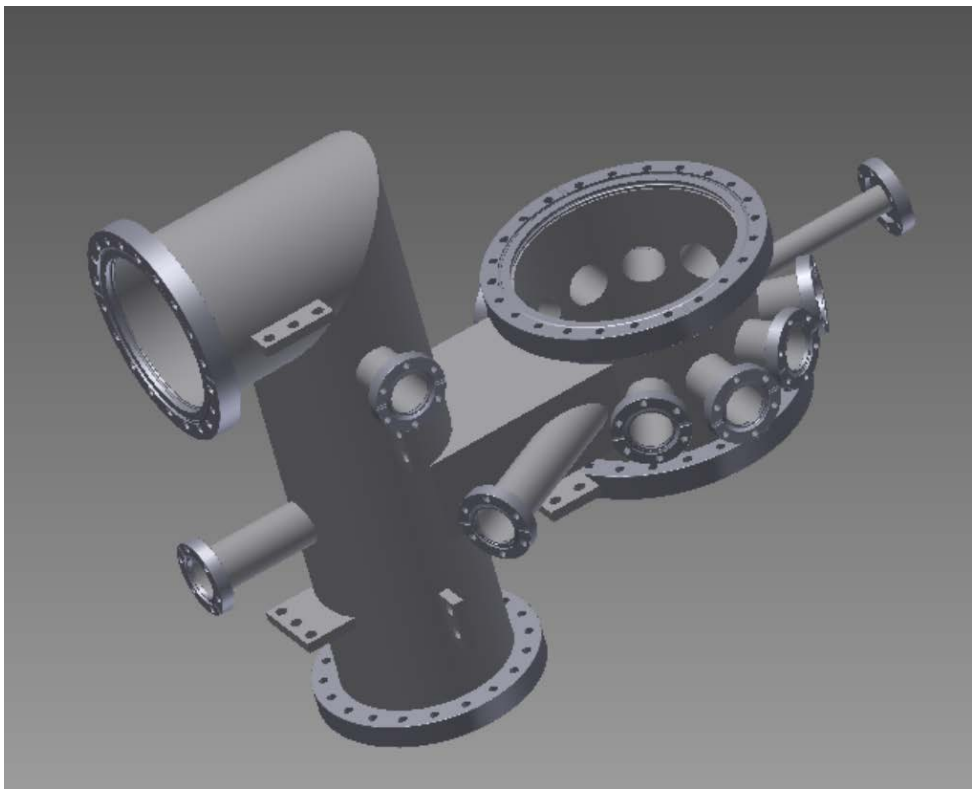

FIGURE 5.23: 3D CAD rendering of the main chamber, together with a large chimney for high conductance towards the ion pump and a welded tube on the right, where the spin-flip ZS magnet is wound (see Section 5.3) (The CAD design and rendering is work of Dr. Georgios Siviloglou).

Since the blue and red MOTs must be made in the main chamber, as well as the first quantum gases, optical tweezers, and possible future experiments, which we cannot envision at the design stage, we put effort into designing it to be as flexible and versatile as possible. It is a cylindrical steel chamber, $20\,\mathrm{cm}$ in diameter on the inside. Optical access is provided by viewports on top and bottom and a total of 10 viewports on the sides, all located at angles $\pi/6$ from each other. The front and back openings of the main chamber lead to the ZS and the back window respectively. A 3D CAD rendering of the main chamber is shown in Fig. 5.23, and a photo of it as delivered from the manufacturer is in Fig. 5.24. There are in principle three main options for

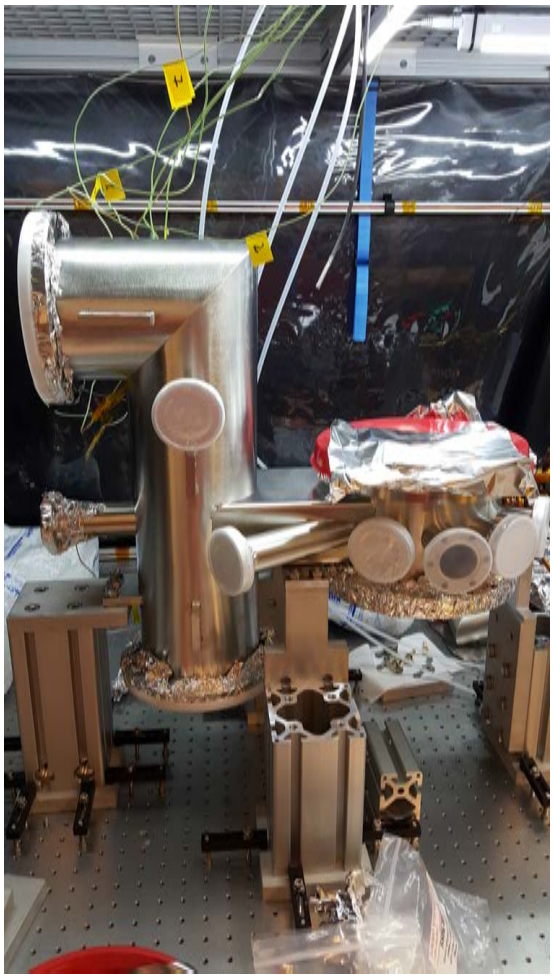

FIGURE 5.24: The main chamber of the machine as delivered from the manufacturer, shown here with its supports.

the main chamber in an ultracold quantum gas experiment: it is either a steel chamber, like in our case, or a large glass cell with a size comparable to that of a steel chamber, like in another experiment in our group [37], or a small glass cell. Since we wanted to have side chambers too, a steel chamber is essentially the only option because a glass cell with four orthogonal vacuum connections would be difficult and expensive to manufacture, and also very fragile.

In order to be able to have viewports as close as possible to the atoms for eventual high-resolution imaging and also to put the main electromagnet close to the atoms, we decided to use reentrant windows. It is a good option for steel chambers, as it allows one to essentially recover the space that would be otherwise lost due to CF flanges. The top and bottom viewports are attached by the manufacturer directly to the reentrant windows with glass-to-metal vacuum seals. They are $50\,\mathrm{mm}$ in diameter, $3.18\,\mathrm{mm}$ thick, and the separation between the inside surfaces is designed to be approximately $38\,\mathrm{mm}$. In addition, all side viewports are part of CF40 2.75" ($69.85\,\mathrm{mm}$) viewport flanges. Their glass is $35.56\,\mathrm{mm}$ in diameter.

All glass on the main chamber is fused silica[29] and the viewports are AR-coated with the

[29] Type Corning HPFS 7980

dielectric coatings optimized for the wavelength range of 450-800 nm and 1064 nm at 0° angle of incidence. The AR coatings help minimize the approximately 4 % power reflections that would occur at each interface between glass and air or vacuum (see Fresnel equations in Ref. [87], for example). It is worthwhile to aim for as little undesirable reflections as possible for several reasons: first of all, the beams entering the chamber could be affected by interference fringes from multiple reflections inside the viewport glass; secondly, there would be more power loss, which can become a problem when laser power is scarce; thirdly, for high-power infrared beams used for optical dipole traps and lattices, a 4 % reflection is already dangerous for humans. With any AR coating, there is always a tradeoff between the passband in terms of wavelengths, and the residual level of stray reflection. In other words, if one wants to have AR performance over a broad range of wavelengths, such as the entire visible spectrum, the residual reflection will be about 0.5 %, and conversely if one wants to have 0.01 % residual reflection, the passband of wavelengths will be narrow. We must make do with more residual reflection for the sake of a broad passband because Sr has important laser transitions at 461 nm, 689 nm, 671 nm, 698 nm, 497 nm, plus there are dipole trap and optical lattice wavelengths of 532 nm, 813 nm, 1064 nm, and we should also envision a possible use of other elements in this machine.

5.7 The quantum gas microscope chamber

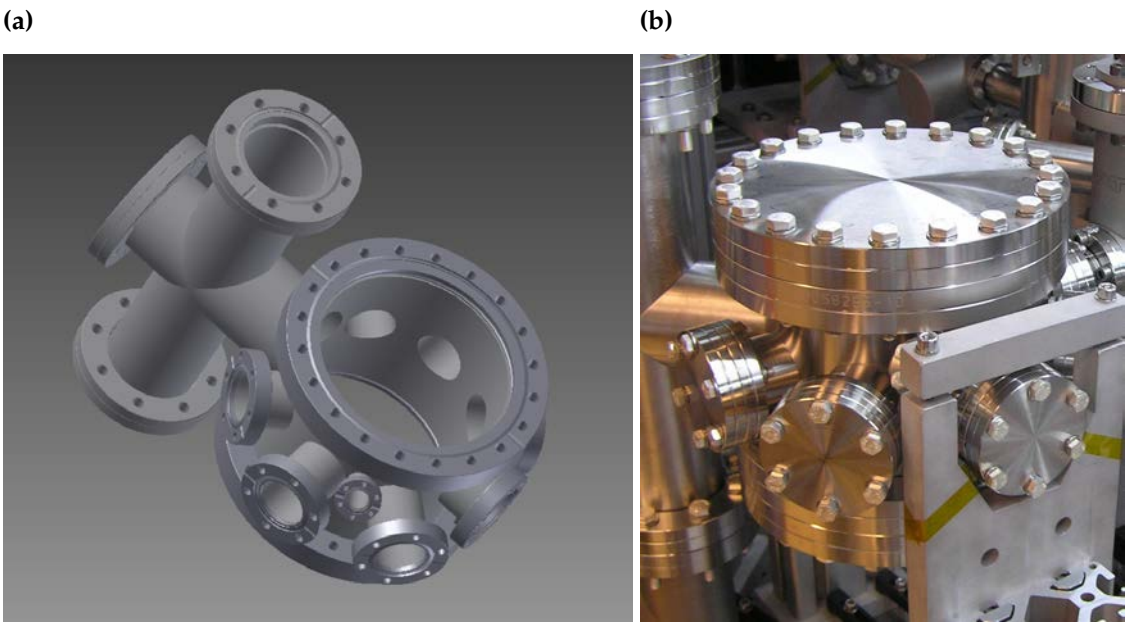

FIGURE 5.25: The quantum gas microscope chamber CAD rendering (a), and its photo (b). The CAD shows also the tube for an ion pump and a TiSub pump connection on the left. The photo shows the chamber as it is built into the full machine, with the viewport and the reentrant window flanges closed off for a bake. Chamber design and CAD renderings: Dr. Georgios Siviloglou.

The machine is envisioned to have quantum gas microscope functionality for Sr, which means having an imaging system able to resolve single-atom occupations in a strongly-correlated

optical lattice [106, 107]. As explained in Chapter 3, this requires a resolution of approximately $600\,\mathrm{nm}$ and a correspondingly large NA. Therefore, we must get as close as possible to the atoms and this will fully block optical access to one vertical viewport. In order to not compromise the flexibility of our machine, we designed a separate chamber to house the microscope. In this manner we were able to place the vertical viewports closer to the atoms, to not worry about the MOT beams a ready-made ultracold gas will be transported there from the main chamber, and to put a highly-reflective coating for $1064\,\mathrm{nm}$ on the inside surface of the bottom viewport so that a high-power IR beam never enters the microscope objective. The vertical axis of the optical lattice is then made by retroreflecting an IR beam directly on the inside surface of the bottom viewport, whereas the other two lattice axes will be made either with retroreflected beams using mirrors outside the vacuum system, or with pairs of counterpropagating beams.

The microscope chamber resembles very much the main chamber, but has a smaller size (see Fig. 5.25). It is cylindrical, having an inner diameter of $14.8\,\mathrm{cm}$ and reentrant windows on top and bottom. The top and bottom viewports are $50\,\mathrm{mm}$ in diameter and are connected directly to the reentrant window steel, just like in the main chamber. Their glass is exactly the same as in the main chamber reentrant viewports (see Section 5.6), and the gap between the inner surfaces of the top and bottom viewports is designed to be about $20\,\mathrm{mm}$. This allows us to get closer to the atoms without moving the atoms away from the center of the chamber, and to achieve a higher NA with the objective. There are 6 side viewports, not counting the entrance from the main chamber and the optical transport viewport opposite to it. The side viewports here are the same as the ones in the main chamber. Apart from the highly-reflective coating for $1064\,\mathrm{nm}$ on the inner surface of the bottom viewport, as mentioned before, all other coatings are the same as on the main chamber viewports.

As we have mentioned, ultracold samples must be moved from the main chamber into the microscope, which requires an optical transport system. The viewport opposite to the entrance from the main chamber is reserved for this purpose. We have envisioned using a pair of tunable focus lenses[30] for this purpose in order to avoid the vibrations and the costs of a mechanical translation stage [143]. The transport system has already been built and shown to work outside the machine by Ivo Knottnerus, but it has not been installed yet.

5.8 The glass cell

One can envision experiments in which a steel chamber may not be a good option and where one would benefit from having a sample in a glass cell. The existence of eddy currents in steel, the limited optical access through the viewports, the inherent large distance between the side viewports and the atomic sample, and the difficulty in installing powerful electromagnets are some of the possible problems of steel chambers. Therefore, with an outlook towards future experiments, we installed a quartz glass cell[31] on the side of the main chamber opposite to the

[30] Model EL-10-30-NIR-LD from Optotune Switzerland AG, Dietikon, Switzerland.
[31] UHV glass cell from Hellma Analytics, Kruibeke, Belgium.

microscope chamber. It is a simple rectangular glass cell, without optical coatings. The length is $8\,\mathrm{cm}$, the inner size is $20\,\mathrm{mm}$ on the side, and the glass is $5\,\mathrm{mm}$ think. We envision transporting samples into this glass cell in exactly the same manner as into the microscope. It is also possible to close the corresponding gate valve and replace the glass cell with a more specialized chamber, if need arises. As with other components, experimental flexibility has been the guiding idea in the design.

5.9 Permanent vacuum pumps

We want to create as good a vacuum as possible in the machine in order to limit Sr atom collisions with background gases, which would kick Sr out of the MOT, or a quantum gas, or a tweezer, and thus limit the lifetime and the range of experiments that can be done. We use standard UHV techniques and UHV-certified materials, but the leak rate into the chamber can never be exactly zero. This is because there are always residual gases inside the materials and on the chamber walls that can be gradually released, CF flange connections cannot be perfectly leak-tight, and helium slowly diffuses through glass. Consequently, if we are to stably maintain UHV inside the chamber, we need to permanently pump so that the residual leaks are in equilibrium with the pumping rate. The two standard pump types for UHV systems are titanium sublimation pumps and ion pumps[32]. We use both on the machine, they are an integral part of the vacuum system construction and are in constant operation.

The titanium sublimation pumps (TiSub) have a much higher pumping speed than the ion pumps, but only the ion pumps can remove noble gases from the system [144]. This, in fact, is the reason for using both, otherwise TiSubs would be sufficient; if one calculates their pumping speed for a reasonable area covered with titanium, one obtains values of tens of thousands of liters per second for hydrogen and water, for example, compared to one or a few hundred $\mathrm{L/s}$ for an ion pump [145]. We have four units of each type in the machine: a $150\,\mathrm{L/s}$ ion pump[33] and a TiSub[34] at the TC chamber, an equivalent pair after the differential tube between the TC chamber and the ZS, a $300\,\mathrm{L/s}$ ion pump and a TiSub serving the main chamber and a $55\,\mathrm{L/s}$ ion pump and a TiSub serving the quantum gas microscope chamber. There are two important points to keep in mind when installing and operating TiSubs and ion pumps. One is that the TiSubs should be installed inside a large tube so that titanium can cover as much surface area as possible, but there must be no line of sight from the titanium filaments to viewports or any objects that could be damaged by electrical short circuits; titanium is a metal, so it can cover viewports, and it's a conductor, so it will short everything it lands on[35]. The other point is that the pumps should in general have as large and straight ducts as possible leading towards them

[32] Machines that work with ultracold metastable helium use permanently running turbomolecular pumps because helium cannot be very efficiently pumped with any other techniques.

[33] All ion pumps are of Starcell type from Duniway Stockroom Corp., Fremont, CA, USA.

[34] All TiSubs are of type ST22 with 3 titanium filaments inside, from Vacgen Ltd., Hailsham, UK.

[35] An important point for cold atom experiment vacuum systems: there should never be a line of sight from a TiSub to an ion pump, otherwise it will possibly short-circuit the ion pump and render it inoperable.

for the most efficient pumping (see Section 4.1 for a discussion of the equations and parameters governing gas flow in a UHV system).

5.10 Support structure

A large and complex vacuum system, like ours, consists of multiple sections of different size and shape, which have to be held together in precisely aligned positions and without applying excessive stress to CF flange connections. Consequently, part of the vacuum system design is the design of an appropriate support structure to safely mount the machine on an optical table. In our case, the support structure consists of square ($10\,\mathrm{cm}$ x $10\,\mathrm{cm}$) and rectangular ($10\,\mathrm{cm}$ x $5\,\mathrm{cm}$) aluminum profiles[36] with custom heights to match the appropriate vacuum parts. Each profile sits on a water-cut aluminum base[37], which is then attached to the optical table with standard clamps[38] and M6 screws. These structures appear in the picture in Fig. 5.24. Sometimes we need to support particular individual flanges, in which case we require a shape that can match and clamp a disk. That support is provided by custom-designed water-cut pieces, such as the one shown in Fig. 5.25 at the bottom right. There are small steel blocks (shims) between the water-cut support and the flange itself. The aluminum pieces are then held on the sides of the profiles using special inserts and M8 bolts.

5.11 Miscellaneous vacuum parts

We would like to mention the roles of several other vacuum parts used in different sections of the machine. One important part is a differential tube, which is simply a long steel tube used to establish a pressure difference between the two chambers that are being independently pumped. We have two such differential tubes in the machine: one immediately after the TC section, and the second one inside the bellows connecting the entire oven and TC unit to the ZS. The differential tube immediately after the TC section has an inner diameter of $8\,\mathrm{mm}$ and a length of $190\,\mathrm{mm}$, whereas the one in the bellows is $7\,\mathrm{mm}$ in diameter and $160\,\mathrm{mm}$ long. Let us estimate the pressure difference established by these tubes. Consider the second tube and assume for simplicity that it would directly connect the ion and TiSub pump section after the TC with the main chamber (in other words, we will ignore the role of the ZS, which in itself acts like a long differential pumping tube). Assume also that we are mainly interested in pumping He: the point is that most other residual gases, like nitrogen and water, are captured by the much more efficient TiSubs, but He is not, due to its inertness. So then using eqs. (4.6) and (4.7), we can write $\Delta P = \frac{S_\mathrm{p}}{C} P_i$, where P_i is the pressure in the chamber of interest, S_p is the pumping speed of the pump servicing the chamber of interest, C is the conductance of the tube connecting the chamber of interest to some other reservoir that has less critical vacuum requirements and thus a higher pressure, and ΔP is the pressure difference between the chamber of interest and

[36] item Industrietechnik GmbH, Solingen, Germany.
[37] Made by Watersnijtechniek Rijssen, Rijssen, The Netherlands.
[38] CL2, from Thorlabs Inc., Newton, NJ, USA.

that other reservoir. We first use eq. (4.5) to calculate C for ^{4}He at room temperature passing through the differential tube in the bellows; that evaluates to $7 \times 10^{-4}\,\mathrm{m}^3/\,\mathrm{sec}$. The pumping speed of the ion pump servicing our main chamber is $300\,\mathrm{L/s}$. If we require an excellent vacuum in the main chamber, for example the residual pressure $P_i = 1 \times 10^{-11}\,\mathrm{mbar}$, then it implies that $\Delta P = 4.2 \times 10^{-9}\,\mathrm{mbar}$, according to the equation above. Consequently, the permissible pressure in the chamber before the differential tube is $4.21 \times 10^{-9}\,\mathrm{mbar}$, which is much easier to achieve and maintain than $1 \times 10^{-11}\,\mathrm{mbar}$. This shows the usefulness of differential tubes in separating the cleanest and most important parts of a UHV system from the ones where vacuum quality requirements are less critical.

A large vacuum system generally cannot be assembled only with rigid connections between all sections. To give one basic example, the oven flange with its microtubes needs to be carefully aligned to the ZS tube direction. The microtube alignment should not rely purely on manufacturing tolerances for perpendicular placement of the flanges, and furthermore, flange tightening itself can introduce small angles that become important in a long flight path. Such tasks require mechanical flexibility and post-construction alignment of one vacuum piece with respect to another, which is made possible by vacuum bellows[39]. We installed three such bellows. The first one is between the TC section and the long ZS, and it was used to align the microtubes to the ZS path. The next one is between the long and short ZS; it was not actively used, and it is there simply to avoid a very long tube with multiple rigid connections, which could introduce mechanical stresses and pose a leak risk. The final one separates the main chamber from the sapphire back window section, and it is there for safety in case part of the back window accidentally gets coated with Sr, in which case it can be moved and adjusted with respect to the ZS flight path, and an uncoated part can be used. Furthermore, we used welded bellows[40] between the main chamber and each of the two side chambers. Welded bellows are very flexible components which transmit mechanical vibrations very poorly. Consequently, they are used in those locations because of the presence of pneumatic gate valves, which create mechanical shocks that could otherwise damage the glass cell or misalign the microscope objective.

Another important element in the case of a Sr machine is a heated sapphire window. The reason is that the ZS laser beam must enter from the back, against the path of the atomic beam, and this means that the atoms which are not slowed in the ZS (this is a large part of the incoming atomic beam) would de deposited on the back window and rather quickly make it non-transparent and render the ZS inoperable. A way to avoid coating that window is to constantly keep it hot, at about $170\,^\circ\mathrm{C}$ in our case. This simply makes the evaporation rate from the surface of the back window much higher than from the adjacent steel parts that are kept at room temperature, so in equilibrium the atoms end up on the steel chamber walls. However, a standard viewport cannot be heated up that much, so we use a sapphire one for this purpose[41].

[39] The formal name for them is "hydraulically formed bellows", and we always use the CF-flanged version. One possible supplier is Kurt J. Lesker Co Ltd, Hastings, United Kingdom.

[40] Also called "flex metal bellows"; Kurt J. Lesker Co Ltd, Hastings, United Kingdom is one of the common suppliers.

[41] Another point that can become important is the fact that sapphire is less chemically reactive than a standard glass viewport. This will play a role when a reactive atomic species is used, such as lithium.

The surrounding thermally insulating box is briefly described in Section 5.12.

In addition, we installed radiofrequency antennas in the main and microscope chambers with an outlook towards driving m_F substate transitions in the $^3P_2$ state of ^{87}Sr, for example (see Chapter 8 for $^3P_2$ state spectroscopy). Furthermore, an alkali element can be added to the machine later, and in that case these antennas can drive m_F substate transitions in that element as well (see Ref. [146] for an example with Li). The main chamber antenna consists of two rectangularly shaped single turns of copper wire, approximately $165\,\mathrm{mm}$ by $19\,\mathrm{mm}$, and separated by about $45\,\mathrm{mm}$. These rectangles are oriented in the vertical plane, on the two sides of the chamber center. The copper is insulated from the steel chamber body with Macor beads, and connected to the outside with UHV electrical feedthroughs. Macor is a common UHV-compatible machinable ceramic insulator[42]. It can be made into beads that can be threaded onto a copper wire, which is very convenient for our application. It must be kept in mind that Macor requires a mild bake at $150\,^\circ\mathrm{C}$ before being installed. The field strength produced by this antenna, with a dc current running through it, is predicted to be about $0.17\,\mathrm{G/A}$. We note that when the antenna is eventually operated with a radiofrequency drive, the amplitude of its generated magnetic field at the chamber center will be given by the amplitude of the current oscillating inside its conductor according to the same $\mathrm{G/A}$ conversion as in the dc case. This is because the antenna is located much closer to the sample than the wavelength of any radio wave that it will produce. The antenna in the microscope chamber is similar, but smaller in order to fit into the smaller space between the viewports.

Finally, there are two more essential components in a UHV system: gaskets, and bolts with nuts for attachments. The gaskets are either standard copper, if they connect two regular steel pieces (like an ion pump or a gate valve to a tube or chamber), or silver-plated annealed copper, which is softer and which is used for connecting viewport flanges, or nickel, which are only used in the oven flanges because they must safely operate up to about $650\,^\circ\mathrm{C}$. All bolts are stainless steel and silver plated[43], which makes them easily removable after bakes. The nuts are always plate nuts, which connect to two bolts at the same time and which are thus convenient to work with; one does not need to apply counter-torque while tightening and releasing them as the connection to two screws keeps them from rotating. Another important technicality is that during tightening at the construction stage, we leave a gap of about $0.1\,\mathrm{mm}$ to $0.15\,\mathrm{mm}$ between the flange bodies. In this way, the flanges can be tightened further in case a leak appears later during machine operation, which actually happened once in our case and we did seal the leak by tightening the bolts more and thus using that gap. If the flanges are tightened metal-to-metal right away, no further tightening can be done later and so this relatively easy method of leak repairs is not available.

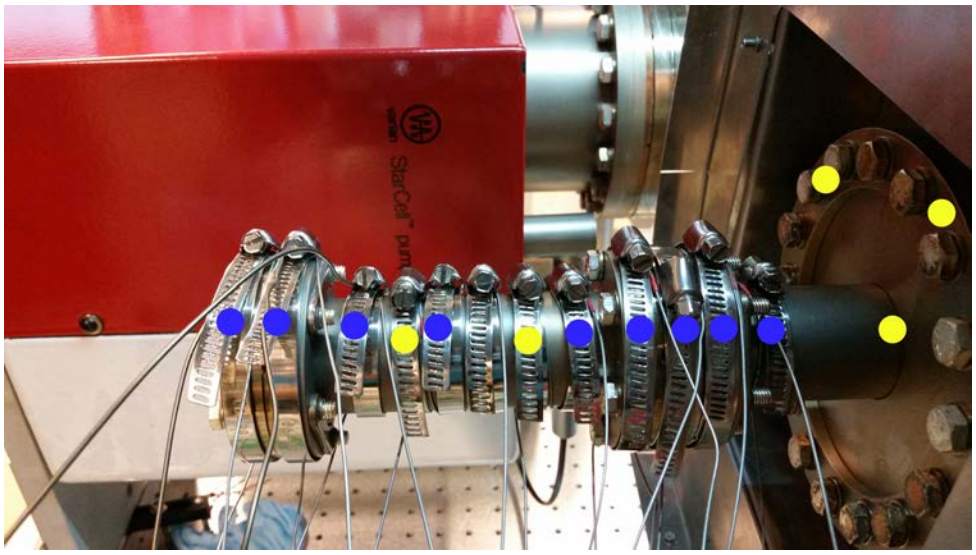

FIGURE 5.26: The oven section with attached Thermocoax heaters and thermocouples. Blue circles indicate the locations of Thermocoax heaters, yellow circles indicate the locations of thermocouples.

5.12 Local heating and heat insulation boxes

We have already seen that there are two places in the machine, the oven and the sapphire back window, which must be kept locally hot during normal operation. Good thermal insulation is necessary there in order to ensure temperature stability on the optical table and the safety of the vacuum connections and the sapphire window in case of a power outage, for example. The design and construction of the thermally insulating boxes will be presented in the PhD thesis of Sergey Pyatchenkov, and we will limit outselves here to a short summary.

The oven is heated with 9 strips of Thermocoax wire[44] connected in four independent groups, and driven by four adjustable switching power supplies[45] in order to be able to control the temperature of different oven sections independently. This is needed to set up temperature differences in the oven section and to make sure that the flange with the microtubes is the hottest point, otherwise the microtubes can get clogged. The temperature is monitored at the hot points with special coated thermocouples[46] and at the colder points with simple home-made thermocouples[47]. The hot part is then thermally insulated with several layers of Superwool blanket[48] and enclosed in an aluminum box. Fig. 5.26 shows the oven section with the attached heaters and thermocouples, clamped to the vacuum tubes with steel rings.

[42] One possible supplier is Corning Incorporated, Corning, NY, USA.
[43] All silver-plated screws, washers, and plate nuts are from Duniway Stockroom Corporation, Fremont, CA, USA.
[44] Type 1509 from Thermocoax, Suresnes, France.
[45] Types Voltcraft LSP-1165 and LRP 1205 from Conrad Electronic SE, Hirschau, Germany.
[46] NiCr-Ni mineral-insulated thermocouple (Mantel-Thermoelement) from JUMO GmbH & Co. KG, Fulda, Germany.
[47] Made with K type thermocouple wire from Omega Engineering Inc., Norwalk, CT, USA.
[48] Morgan Thermal Ceramics, Morgan Advanced Materials, Berkshire, United Kingdom.

FIGURE 5.27: The back window flange with its attached heating ring. The black steel tube protects the viewport from Superwool dust and and glass windows inside are used to avoid direct contact of room-temperature air with the hot window.

The back window is heated with an appropriately-sized heating ring[49], driven by a Variac autotransformer powered from the 230 V mains. Large fitted copper blocks around the back window flange and the heater act as heat buffers that prevent a fast drop in temperature in case of power failure. The insulation is again done with Superwool in an aluminum box. Fig. 5.27 shows the back window flange with the attached heating ring. Both the oven and the back window heating power are connected to an uninterruptible power supply so that the temperature does not drop fast in case of a power outage.

5.13 Vacuum system construction and baking procedures

We have seen that UHV is a necessary requirement for experiments with quantum-degenerate gases. In fact, with an outlook towards future experiments, one can say that the better the vacuum is, the more capable and future-proof the machine is. Higher vacuum increases atom lifetime in a quantum gas, optical lattice, or an optical tweezer sample; the higher the lifetime, the larger the pool of possible experiments is. The biggest unfortunate consequence of stringent vacuum requirements is the need to bake a new machine twice. Some of the other difficulties are:

- All vacuum parts must be cleaned thoroughly with purified ethanol[50] before being mounted; the knife edges must be cleaned very well and be free of any residue.

[49] Band heaters from Omega Engineering Inc. Norwalk, CT, USA.
[50] Alcohol Absolutus, 99.8% ethanol from Koninklijke Nedalco B.V., Bergen op Zoom, Netherlands.

- There should be no ethanol traces left on vacuum parts when mounting them.
- Care must be taken to only work in clean and powder-free latex or nitrile gloves, and to not touch any vacuum surfaces with bare skin.
- Care must be taken to not allow any oil residue to land on vacuum surfaces (this means thoroughly cleaning any pieces that come from the mechanical workshop).
- Small vacuum pieces must be sonicated in ethanol.
- All ConFlat (CF) flanges, especially the large and vertically mounted ones, must be initially put together carefully without hitting the knife edge. Any hits can damage the knife edge and make lengthy and expensive repairs or replacements necessary (damaged knife edges will for sure lead to leaks).
- All CF flanges must be tightened in an appropriate star-pattern (see the instructions in the manufacturers' manuals and websites, they differ depending on the flange).
- The entire vacuum system must be thoroughly leak-checked by blowing helium at all vacuum connections and observing the signal on a residual gas analyzer (RGA) mounted somewhere on the vacuum system, usually on a working turbomolecular pump (turbo).
- Apart from the fact that the support structure must hold the vacuum system without applying excessive stress to the flanges in normal operation, it must also not apply excessive stress during bakes, when parts expand and contract; we supported large and heavy pieces, like ion pumps, with stiff springs during bakes in order to make sure that the flange is the only point of rigid connection.

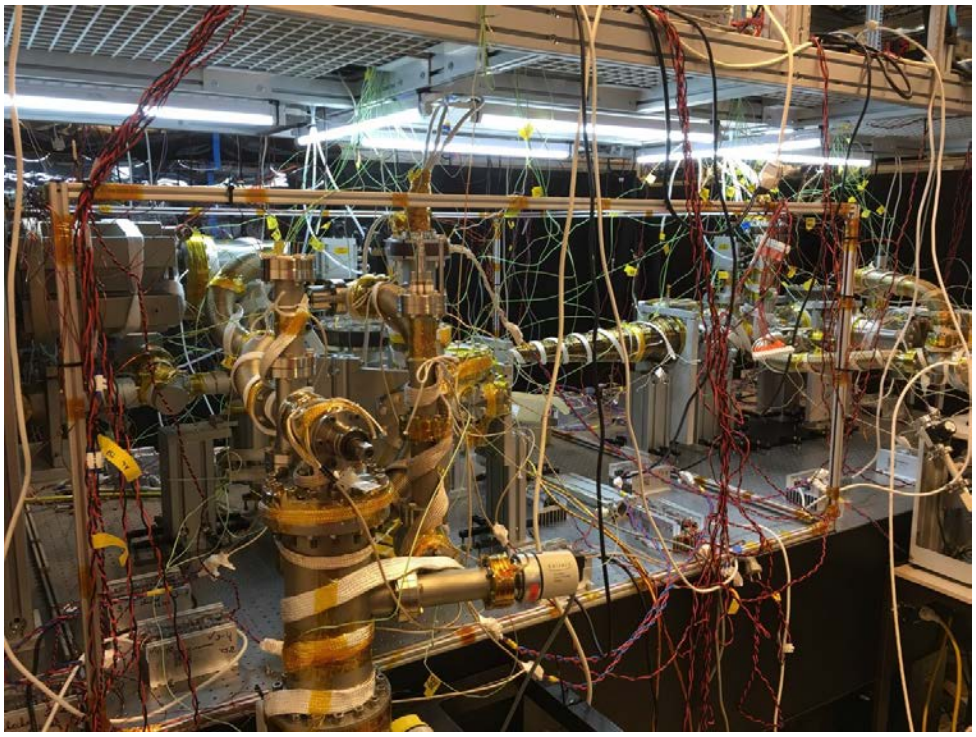

FIGURE 5.28: The vacuum system right before a bake, with heating tapes and thermocouples attached. It is not wrapped with aluminum foil yet.

After the full assembly, the vacuum system is first pumped down with external pump stations consisting of a prepump, a turbomolecular (turbo) pump, and a residual gas analyzer (RGA). It is important to note that the connections to the pump stations must always have an angle valve[51], otherwise it will be impossible to close the vacuum. After the bake is completed and the vacuum quality is acceptable, the angle valve is closed when the turbo is still fully running. Only with the closed angle valve can the turbo be turned off.

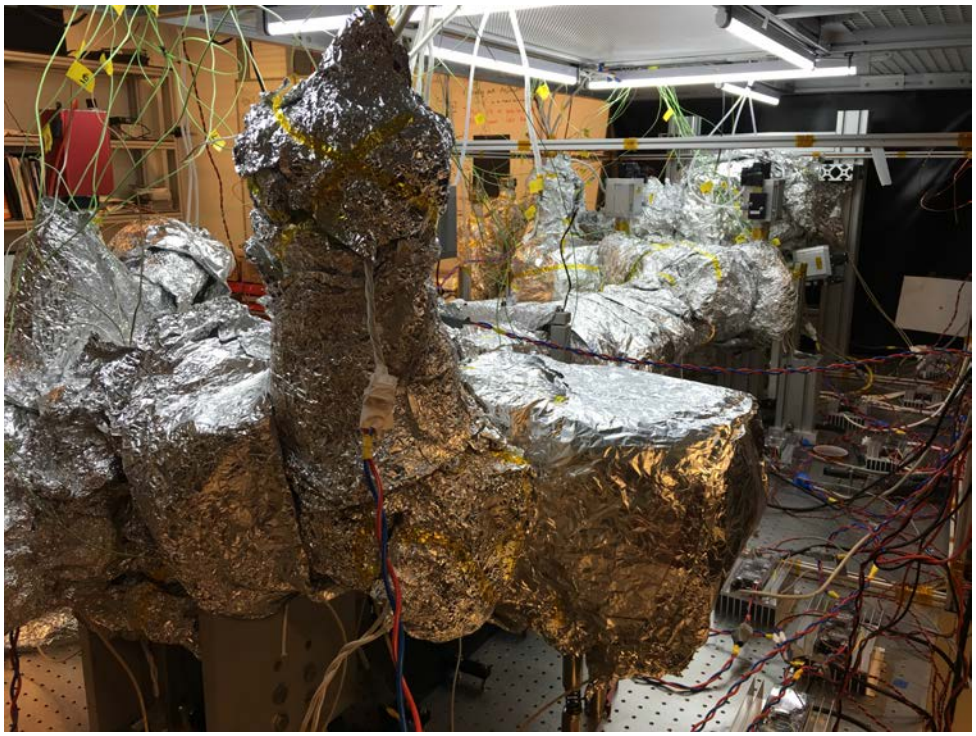

FIGURE 5.29: The vacuum system during a bake, with aluminum foil heat insulation covering the heating tapes.

Before the bake, the turbos on their own should be able to achieve a pressure below $1 \times 10^{-7}\,\mathrm{mbar}$. After that, the vacuum chamber must be wrapped with heating tapes[52], appropriately sized heating rings[53] must be placed on some of the flanges, many thermocouples[54] must be attached under the heating tapes for reliable temperature monitoring (note that thermocouples can easily fail during a bake), and then the chamber must be wrapped with very thoroughly crumpled thin aluminum foil in multiple layers for thermal insulation. After that has been done, one can start baking. We used the guideline that the temperature should not increase by more than $10\,°\mathrm{C/h}$ for the high-temperature bake when there are no glass viewports present, and by more than $3\,°\mathrm{C/h}$ in the final low-temperature bake with the glass viewports on[55]. Fig. 5.28 shows the machine before the high-temperature bake, with heatings bands

[51] Model 54132-GE02 "Easy-close" all-metal angle valve from VAT Vakuumventile AG, Haag, Switzerland.
[52] STH Series, various powers and lengths, from Omega Engineering Inc., Norwalk, CT, USA.
[53] Also from Omega Engineering Inc., just like the heating tapes.
[54] K type thermocouple wire from Omega Engineering Inc., Norwalk, CT, USA.
[55] It is possible that the heating and cooling rate can be higher. The values given here have a large safety margin.

and thermocouples mounted, and Fig. 5.29 shows the wrapped aluminum foil. We constantly monitor the pressure at the entrance to the turbo with a cold and hot cathode gauge [147] during the bake. The point in time when to stop the bake is estimated by observing or fitting an exponential to the dropping values of the chamber pressure; the bake is stopped when the decrease in pressure has passed the time of rapid decrease and is predicted to drop only slowly for any further baking.

Regarding the reasons for these bakes, we should mention that hydrogen [148] and water vapor are the main residual gas pollutants in a UHV system, and they are removed by baking. Hydrogen is dissolved in newly-manufactured steel and it slowly diffuses and outgasses from the steel surface, creating a high background pressure [148, 149]. A way to avoid that is to heat up the entire chamber to approximately $350\,^{\circ}\mathrm{C}$ for about two weeks, while constantly pumping it with turbos. The heat exponentially speeds up hydrogen diffusion out of steel and the turbos remove that hydrogen, so there is a lot less of it left still inside and it then creates a lot less background pressure during normal machine operation [148, 149]. Of course all viewport optical coatings and glass seals would get damaged when heated to $350\,^{\circ}\mathrm{C}$, so there is no glass on the chamber during this bake; all viewport and reentrant window locations are closed off with blank steel flanges. Such a bake is done only once for a brand-new chamber. When it is finished, the chamber must be opened to air again for all viewports to be installed. During that time, water vapor from ambient air sticks to the inside steel surfaces, and it would be another source of outgassing and high background pressure. In order to avoid that, we perform a cooler bake, heating up the entire chamber to about $150\,^{\circ}\mathrm{C}$ for about a week, now with all the glass on. Here again, heat speeds up desorption rate of water vapor from the steel walls, and the working turbos remove that vapor. Importantly, the lower temperature of this bake is safe for viewports and coatings (this may not be true for all viewports and all coatings, and the manufacturers' specifications all the parts used in a particular setup should always be checked beforehand). This second "water" bake is a big reason why ultracold atom machines are difficult and time-consuming to construct: one must make sure all necessary components for all future experiments are installed at the construction stage before this bake. If one wants to open the vacuum chamber for any reason later, or if there are leaks or accidents, one will have to repeat the "water" bake, which would involve removing all optics around, wrapping the whole machine with heatings bands and aluminum foil, and it would take months.

One has to pay special attention to the support structure during the high-temperature bake, otherwise one can approach the forging temperature of aluminum [150]. In that case the support structure will lose its rigidity, leading to uncontrolled movements of the vacuum parts and misaligning them, producing leaks, or even rendering some parts unusable. Practically, it means that one should leave the support structure exposed to ambient air as much as possible and avoid placing any heating tapes or aluminum foil on it.

5.14 Electronics for the experiment

An ultracold atom experiment requires an extensive and precisely timed system of electronic control and signal generation in order to change AOM frequencies and power, coil currents, close and open shutters, trigger cameras, and possibly to send RF pulses to the atoms or even to control the lasers themselves. We use the electronic system developed originally by Florian Schreck and Todd Meyrath, and subsequently modified in order to add upgrades or new functionality. The hardware is described online [151], and we will here summarize the fundamental ideas that should allow one to understand the governing logic of the system.

5.14.1 The National Instruments card and the bus system

The experimental control hardware starts with an NI 6534 card[56] connected to the PCI slot of the computer motherboard. The card continuously reads a timed command sequence from a ring buffer in main memory. The buffer is continuously refilled, enabling sequences of arbitrary duration. This sequence then gets sent out to all the electronics downstream, timed by an external clock running at approximately $2\,\mathrm{MHz}$. It is important to note that the output of the NI 6534 is purely digital; any required analog signals must be produced by digital-to-analog (DAC) converter cards and direct digital synthesizers (DDS) downstream on the experiment.

All the control electronics after the NI card are home-built. The first stage along the line is a set of identical cards (known as *drivers for bus*) whose main components are digital magnetocouplers: they separate control computer ground and signal lines from the ground and signal lines of experiment's electronics, as well as the grounds of different optical tables from each other. We note that this first set of cards requires $5\,\mathrm{V}$ power input, which is used to relay the control signals downstream. From that point, the signal travels to what is known as *subbuses*; these are the boards that decode the first layer of addresses and generate the *strobe* pulse (see below). After the subbuses, the signal travels to the final output cards, each of which has a specialized function on the experiment. There is a simple bus driver card on each rack (known as *driver for rack*), which basically provides a way to conveniently plug in power for the output cards themselves, amplifies the bus signal, and converts from the rack external to the rack internal flat ribbon cable format.

The control system transmits signals in a parallel manner, using either 50-wire or 64-wire flat ribbon cables[57]. Each subbus has a 3-bit address, meaning that there can be at most 8 of them in the system, and this address is transmitted by a small auxiliary ribbon cable extending only from the drivers for bus to the subbuses. The main cables carry 25 signal lines: 16 data lines, 8 address lines, and the strobe. Each output card has thus an 8-bit address, which is decoded on the card itself: all cards after a given subbus receive the same data, but they only act on it if the transmitted address matches the one that they had been manually given with a set of dip switches. In this way, each subbus can in principle drive up to 256 output cards. Furthermore

[56] National Instruments Corporation, Austin, TX, USA.

[57] Flat ribbon cable (Flachbandkabel) AWG 28-50G ot AWG 28-64G from reichelt elektronik GmbH & Co. KG, Sande, Germany.

we note that each clock cycle of the NI card can transmit at most a 16-bit data word. This sets the limit on the timing resolution of the commands that can be sent to the devices. The card outputs are updated at the rising edge of the strobe pulse, which has been generated by the subbus if its address matched. The system is modular and its components can easily be upgraded in the future. This includes replacing the link between the computer and the output racks with Ethernet or serial connections, or adding new types of output cards.

5.14.2 Output cards

Here is a good place to list and briefly describe the electronic output cards that are used in our experiment and that would be applicable to many cold atom experiments. The high-power (up to $2.5\,\mathrm{W}$) electromagnetic waves in the hundreds of MHz range (RF signals) required to drive AOMs are generated by direct digital synthesizer (DDS)[58] cards and then amplified by separate RF amplifiers. We also use 4-output DAC cards, which can generate analog signals in the range of -$10\,\mathrm{V}$ to +$10\,\mathrm{V}$ with 16-bit resolution, 8-output digital output cards, which generate 0 and $5\,\mathrm{V}$ outputs for things like hardware triggers, and specialized digital output cards that can drive servo motors for moving shutters. Two other cards, which are technically not part of the control system, but which are nevertheless crucial, are the clock generator and the clock splitter. The reason is that the DDS can only synthesize a given frequency if it has an input clock signal at a certain precisely set higher frequency, and in fact the quality of DDS frequency synthesis can never exceed the quality of the reference clock signal. For that reason one should always try to obtain a stable clock signal to feed the DDSs. We get it initially from a Rb atomic clock, which produces a $10\,\mathrm{MHz}$ reference signal. However that frequency is too low for the DDSs, so that signal is translated in frequency to either $300\,\mathrm{MHz}$ or $1.2\,\mathrm{GHz}$, depending on the DDS, by our separate clock generator that uses the phase-locked loop (PLL) technique. We would like to only use a single clock generator for all DDSs in the experiment, so its signal is subsequently split and amplified by the clock splitter cards. We note an important point here: since the clock signal for all DDSs in the experiment comes from the same reference, there is phase coherence between all of their outputs and one has to keep that in mind as a possible feature or a bug if one tries to drive a single AOM from multiple DDS cards.

[58] AD9852 and AD9858, from Analog Devices, Norwood, MA, USA.

Chapter 6

Laser systems

Once we have built the UHV system, which is the appropriate environment for ultracold atom experiments and for many other experiments in the broader area of atomic physics, we need to also prepare lasers, which are the tools for atom manipulation and measurement. There exists currently a wide range of laser systems, so it is worthwhile to put our ones in the general context. First of all, our lasers are of continuous-wave type (CW), meaning that their output power ideally does not fluctuate in time, unlike that of pulsed laser systems, which produce consecutive electromagnetic pulses. Secondly, we use single-mode frequency-stabilized lasers in most cases because we need to address atomic resonances, which are very narrow on the scale of optical frequencies[1]*. Finally, apart from the infrared far-off-resonant optical traps, we use diode lasers, in some cases with tapered amplifiers and frequency doubling, and we work at relatively low optical powers, powers above a few hundred* mW *being rare. Exceptions to all those statements do occur, but these considerations hold for most work in the field of ultracold atoms, and definitely for our experiment. This chapter will describe the design, construction, and use of the laser systems in our apparatus.*

Outline of the laser systems

As we have seen in Section 1.1, a useful method for laser cooling of Sr to quantum degeneracy requires light at 461 nm (blue), 689 nm (red), a repumper at 497 nm, and a high-power dipole trap at 1064 nm (IR). We design and construct the laser systems to conveniently work with different Sr isotopes. The blue and red master oscillators are located in the adjacent lab and are locked to spectroscopy cells on the respective lines in ^{88}Sr. The corresponding lines in the other isotopes are a few hundred MHz to around 1 GHz away, so we bridge such frequency gaps with acousto-optic modulator (AOM) cascades[2]. Injection-locked slave lasers are then used as the sources of all blue and red beams [152]. The IR system is derived from a commercial source[3] and its power splitting system is set such that we immediately have ports for dipole trap beams (see Sections 7.3 and 7.4), an optical transport beam (this is necessary for a quantum gas microscope, see Chapter 3), and optical lattice beams (they are not in use yet). In addition, there is a master

[1] Consider a laser with 1 kHz linewidth, not a particularly narrow laser, operating at 689 nm, so with red light. Then its absolute frequency is about 435 THz and since its linewidth is assumed to be 1 kHz, the fractional uncertainty is $\frac{1*10^3}{435*10^{12}} \approx 2 \times 10^{-12}$, which is already a very high relative stability.

[2] All AOMs in our laser systems are from Gooch & Housego PLC, Ilminster, United Kingdom.

[3] Type ALS-1064-50-I from Azur Light Systems, Pessac, France.

oscillator at 671 nm[4] locked to an optical cavity; its frequency can be conveniently shifted with an AOM by several hundred MHz, which is useful for wide spectroscopy scans of the $^1S_0$ - $^3P_2$ transition (see Chapter 8). The 671 nm laser system is also foreseen for clock-level locking to an ultrastable cavity[5]. We take a moment here to note the importance of laser system stability for a quantum gas experiment: not only is the obvious problem of delocking detrimental, whereby an experiment must be interrupted to relock the lasers, but also the injection lock quality itself must be optimized. We realized that slight drifts of the slave lasers, even when they don't fully delock, cause major variation in atom numbers. Consequently, reliable operation of the laser systems, achieved with both passive stability and possibly active automatic feedback measures, is an important criterion for the efficiency of data collection in experiments such as ours.

6.1 The blue laser system

The 461 nm (blue) laser system provides light for the first stages of Sr laser cooling and trapping, which are TC, ZS, and blue MOT, as well as for absorption and fluorescence imaging. Blue laser cooling benefits from the largest possible power, and ZS, for example, needs tens of mW of power (this comes from the result of the calculations that led to Fig. 5.15, a similar calculation for the long ZS, and the fact that $I_{\text{sat}} = 43\,\text{mW/cm}^2$ for the blue transition [21]). Therefore, sources had to be chosen that can provide many tens of mW of power per beam or, alternatively, hundreds of mW of total output power in a single beam. A few years ago, the only option was a frequency-doubled laser system based on an amplified 922 nm beam; this is still our spectroscopy-locked master laser [37]. Recently, however, laser diodes at 461 nm appeared on the market[6], which we decided to use. They make a frequency-doubling setup unnecessary, which saves cost and space. Their disadvantages, however, are poor spatial mode quality and difficulty and instability of injection locking. For example, it is difficult to achieve more than a 50% coupling efficiency of blue diode output into a single-more fiber (the coupling efficiency of the red laser diodes, mentioned in subsection 6.2 can routinely reach above 70%). Regarding random delocking events, with five slave lasers on the setup, it is difficult to keep them all locked for more than an hour on average. Manual relocking takes about 1-2 min, depending on which particular slave laser it is. This situation occurs with almost daily checks of the injection fiber path alignment (the slave diodes of the red laser system, subsection 6.2, do not need any servicing for several weeks at a time). One can possibly introduce an auto-relock system for the blue slave lasers [154], but in that case it would be better to have an independent Fabry-Perot cavity for checking single-mode operation of each diode (see footnote in subsection 6.2 for

[4] Toptica DL Pro from Toptica Photonics AG, Graefelfing, Germany.

[5] ATF 6300, 50 mm spherical Fabry-Perot cavity with a specified finesse of 250000 at 698 nm and a similar finesse at 671 nm from Stable Laser Systems, Boulder, CO, USA. Ref. [153] provides technical details about this kind of optical cavities.

[6] NDB4216 from Nichia Corporation, Tokushima, Japan.

Isotope	$^1P_1$ resonance [MHz]
^{84}Sr (boson)	- 270.8
^{86}Sr (boson)	- 124.8
^{87}Sr (fermion)	- 46.5
^{88}Sr (boson)	0

TABLE 6.1: Resonance frequencies of the $^1S_0 - {}^1P_1$ transition in stable isotopes of Sr, given as a frequency offset from this resonance in ^{88}Sr.

details), and to not have one slave diode injecting the next one[7]. Neither of those conditions was true on our experiment, and for that reason we found it difficult to make an auto-relock system work reliably. Overall, the unreliability of the laser diodes makes the blue system the least stable one and the most maintenance-intensive one on our experiment.

The full details of this laser system will be described in the PhD thesis of Sergey Pyatchenkov, and here we limit the discussion to the main features of power distribution and frequency shifting. There is a total of five slave lasers; two are used essentially to amplify the incoming frequency-stabilized light and to provide enough power, after AOMs[8], to injection-lock the other three slave lasers. The AOMs make the necessary detunings, starting from the ^{88}Sr resonance. TC, ZS, and blue MOT each get a dedicated slave laser for the maximum possible power delivery to the machine. We on purpose installed the respective frequency-shifting AOMs before the injection (meaning, we already inject with the frequency we want, instead of detuning the output beam) to lose as little power as possible. The downside of this approach is that the light can only be turned off with shutters, which are at best $1\,\mathrm{ms}$-precise, and we cannot, for example, perform absorption imaging of the blue MOT for this reason. However, this is an acceptable trade-off given the output power of the available blue laser diodes. Table 6.1 shows the resonance frequencies of the $^1S_0 - {}^1P_1$ transition in stable Sr isotopes with respect to the ^{88}Sr value.

6.2 The red laser system

The $689\,\mathrm{nm}$ (red) laser system provides cooling light for the narrow-line MOT, and it can also be used for relatively narrow-linewidth spectroscopy on the $7.4\,\mathrm{kHz}$ transition, optical Stern-Gerlach separation [155], optical pumping, photoassociation to molecules [156], etc. As the saturation intensity of the $^1S_0 - {}^3P_1$ transition is about $3\,\mu\mathrm{W/cm^2}$ [22], the power requirements for laser beams are low (so frequency stability is a much more difficult criterion to fulfill than output power). This system is built according to the following guiding principles:

- the lasers should reliably stay locked,

[7] Having one slave diode inject the next one makes automatic lock detection and optimization algorithm more difficult, because one has to consider that some slave can delock due to its own fault, or due to its injection source getting delocked.

[8] Each first-order diffraction passage through an AOM is 50-80% efficient, depending on AOM frequency. Thus if one makes a double-pass configuration, the round-trip efficiency will range between 25-64%.

- all isotopes and all hyperfine states of ^{87}Sr should be accessible,
- switching between isotopes should be simple and fast, and
- the system should be configurable to add more beams if necessary.

The red master oscillator is an ECDL in Littrow configuration[9], locked to an optical cavity for linewidth reduction by the PHD technique and using a commercial fast PID loop[10] [157, 158]. The cavity is build with two concave mirrors with a $25\,\mathrm{cm}$ radius of curvature, glued to a Zerodur spacer; the resulting finesse is about 16000 and the free spectral range is $1.5\,\mathrm{GHz}$ [157]. The cavity assembly is mounted in a vacuum can. One of the mirrors is on a piezo actuator to tune the cavity resonance frequency. The stabilized laser linewidth is estimated to be approximately $2\,\mathrm{kHz}$ [157], which is narrow enough to work with the $7.4\,\mathrm{kHz}$ atomic transition. In addition to linewidth reduction, we must also lock the master oscillator in absolute frequency to the $^1S_0 - {}^3P_1$ transition in Sr. The error signal for this lock is obtained from Doppler-free spectroscopy of ^{88}Sr in a steel cell at $550\,^\circ\mathrm{C}$, it is then processed with a lock-in amplifier[11], and this feedback loop is closed by acting on the piezo-mounted cavity mirror and thus tuning the resonance frequency set point for the fast lock. In this way, the linewidth reduction is a fast lock (high-bandwidth feedback acting on the current and the grating of the ECDL), while the absolute frequency lock to Sr spectroscopy is a slow one (low-bandwidth feedback); the fast lock then continuously follows the slow lock. The master oscillator is locked $80\,\mathrm{MHz}$ above in absolute frequency from the $^1S_0 - {}^3P_1$ transition in ^{88}Sr, and a few hundred µW of master laser light arrives at our laser table through an optical fiber to be used as seed light for injection locking.

All the necessary $689\,\mathrm{nm}$ beams for our experiment are currently generated by four home-made diode slave lasers, each one of which can provide up to $35\,\mathrm{mW}$ of output power. The laser diodes are of the same type as in the master oscillator. Each diode is actively temperature-stabilized with a PI feedback loop circuit designed at the Institute of Quantum Optics and Quantum Information (IQOQI) in Innsbruck, Austria. The temperature sensor is a $10\,\mathrm{k\Omega}$ negative temperature coefficient thermistor[12] and the actuator is a Peltier module[13]. The current source circuit for the diode can provide up to $500\,\mathrm{mA}$, which is enough for any of the diode lasers in use. These laser diodes appear to be stable and reliable, they run single-mode even without injection-locking light, they can be easily injected with a few 10 µW of seed light, they do not delock at all on a typical day of operation, the injection fiber path has to be checked and alignment has to be improved only once per three weeks to once per month, and the diodes have been running for about two years without any noticeable power degradation.

The basic layout of a slave laser unit is shown in Fig. 6.1[14]. Each unit requires an optical

[9] Diode type HL6738MG from Opnext Japan Inc., Nagano, Japan.
[10] FALC 110 from Toptica Photonics AG, Graefelfing, Germany.
[11] Model SR830 DSP from Stanford Research Systems.
[12] Type B57863S0103+040 from EPCOS AG, Munich, Germany.
[13] Type ET-131-10-13-S from European Thermodynamics Ltd, Leicestershire, United Kingdom.
[14] This figure and other figures in this Thesis that involve optical components were made using the Optical components library for Inkscape [159].

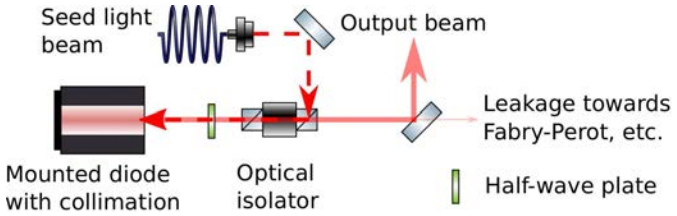

FIGURE 6.1: Basic slave laser unit layout. The collimating lenses are all inside the housing mount. The dashed line denotes the injection beam. The mirror after the isolator is polished on the back.

isolator[15] in order to avoid uncontrolled optical feedback by reflections from the surfaces in the beam path. Our isolators provide more than 30 dB of isolation against the reverse beam and typically transmit about 92% of incoming light. The injection beam is fed through the second PBS of the isolator. Several tens of µW of leakage light are accessed through a polished mirror[16] and sent to a scanning Fabry-Perot interferometer[17] for injection lock monitoring. The first slave, termed S0R, is injected with master laser light, and it feeds the power distribution system and the AOM frequency shifting cascade. S0R itself does not directly deliver any light to the machine table.

The power distribution system and the AOM frequency shifting cascade are designed so that the red laser system can address a mixture of ^{87}Sr with any boson, or, alternatively, up to all three bosons together in a single experiment. Even though we have not worked with mixtures yet, it is an important option to have, and furthermore, the flexibility of this design allowed us to already use an independent spectroscopy beam or an optical Stern-Gerlach beam while working with ^{87}Sr, which requires two different frequencies (see Section 7.2). The cascade tunes the light frequency to the $^1S_0 - {}^3P_1$ transition value for each of the four Sr isotopes and to the three hyperfine states in ^{87}Sr $^3P_1$. The schematic of the distribution system and the AOMs is shown in Fig. 6.2 and the AOM models and frequencies are listed in Table 6.2. Apart from the AOMs, some other important elements in this frequency shifting and distribution cascade are polarizing beamsplitters[18] (PBSs, or simply cubes), half- and quarter-wave plates[19] and plano-convex lenses[20].

The light at the frequency appropriate for each isotope is then used to inject one of the other three slaves, S1R, S2R, or S3R. We transport the light from the output ports of the frequency shifting cascade to the input injection ports of the other slaves with polarization-maintaining

[15]Type FI-680-5SV from Qioptiq Photonics GmbH & Co. KG, Göttingen, Germany.

[16]This can be replaced with a PBS.

[17]Model FPI 100 from Toptica Photonics AG, Graefelfing, Germany. The basic idea of its operation is that one of its mirrors is being continuously scanned across the free spectral range, and we observe the transmission on the photodiode behind the optical resonator. If the laser has a single frequency mode, there will only be a single peak within a free spectral range.

[18]Thin film polarizers of type G335715000 from Qioptiq Photonics GmbH & Co. KG, Göttingen, Germany (for high extinction ratio) or BPS Cube 12.7x12.7x12.7mm at 660-710 nm from Casix Inc. Fuzhou, PRC. (as a cheaper option with lower extinction ratio).

[19]Types 2-CPW-ZO-L/2-0689 and 2-CPW-ZO-L/2-0689 from UAB Altechna, Vilnius, Lithuania.

[20]Made of N-BK7 glass, 1" diameter, B-coated from Thorlabs Inc., Newton, NJ, USA, or alternatively with a similar bandwidth AR-coating from Casix Inc, Fuzhou, PRC.

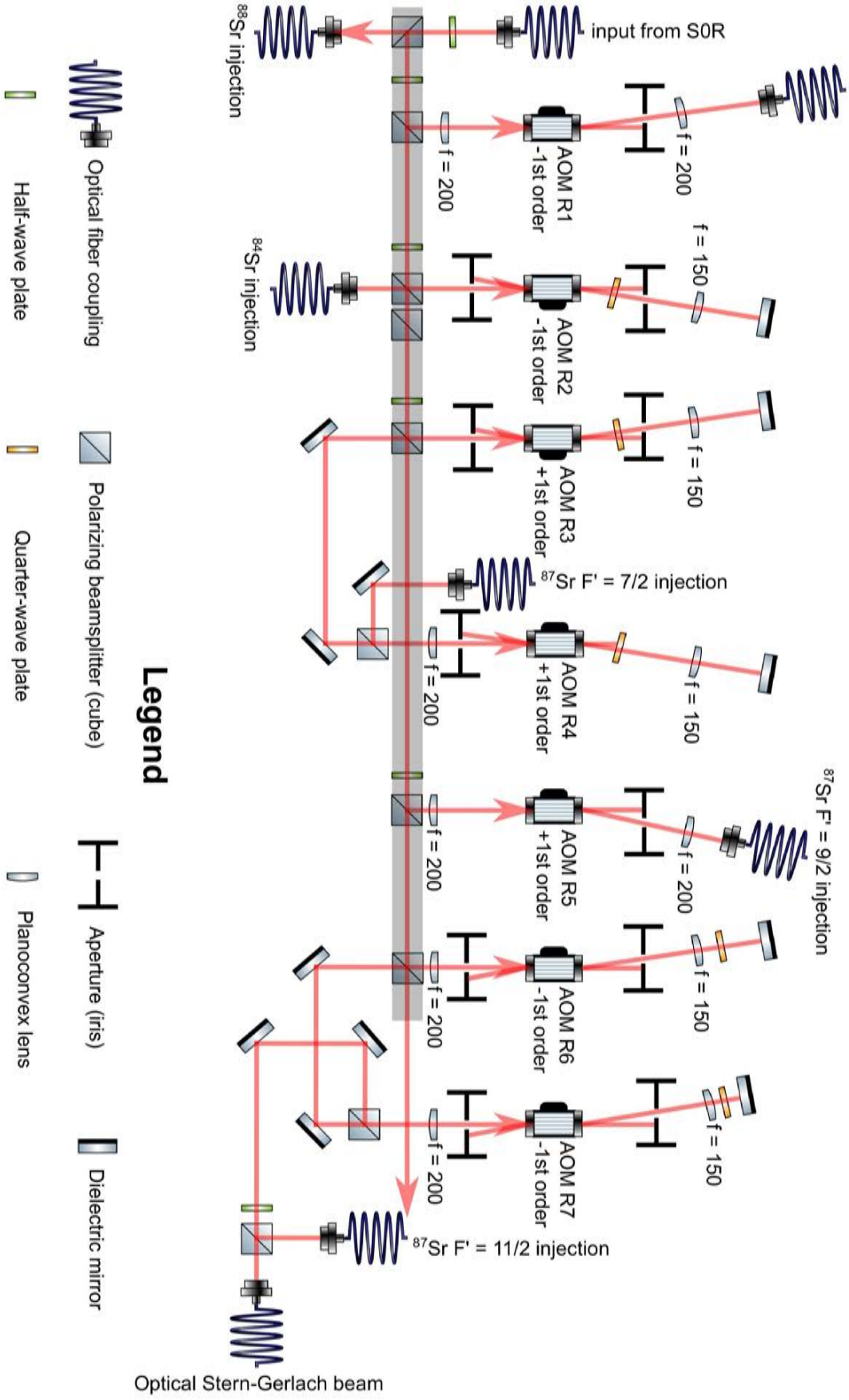

FIGURE 6.2: The red distribution system diagram. The mirrors required to inject fibers and guide beams have been mostly omitted for illustration clarity. The cubes within the shaded area are all placed on kinematic mounts (type KM100PM/M from Thorlabs Inc. Newton, NJ, USA). See main text for all relevant part numbers and the list of AOM frequencies.

	Model number	AOM Frequency [MHz]
AOM R1	AOMO 3200-121	163.81
AOM R2	AOMO 3200-125	175.75
AOM R3	AOMO 3200-125	256
AOM R4	AOMO 3350-199	420
AOM R5	AOMO 3200-121	221.7
AOM R6	AOMO 3200-121	210.5
AOM R7	AOMO 3350-199	410.2

TABLE 6.2: AOM model numbers and frequencies in use in the red AOM frequency shifting cascade. The diffraction order and the designation of single-pass or double-pass configuration is shown in Fig. 6.2. All AOMs are from Gooch&Housego.

single-mode optical fibers[21]. In this way, exchanging the isotope involves possibly redistributing power in the cascade by turning the waveplates, and then exchanging the seed beam fiber for a particular slave laser and relocking it. This procedure can be done in an hour, which is convenient and flexible. There is an AOM[22] running in -1st diffraction order at a frequency close to $80\,\text{MHz}$ as the first element in the output beam path of S1R, S2R, and S3R in order to compensate for the $+80\,\text{MHz}$ lock offset of the master laser, to set an appropriate detuning for the MOT or red spectroscopy (this is why it is not necessarily exactly -$80\,\text{MHz}$, because that would be precisely the resonance frequency), to tune or quickly turn off the beam power, and to create a comb of frequencies that is required at the initial stages of the red MOT (see Section 7.2).

We finally need a way to combine two or three laser beams at almost the same frequency and in the same state of polarization into an optical fiber that will deliver the light to the machine table. For reasons of optical access, it is convenient to have these beams share the same path through the main chamber when they correspond to the MOT and the stirring beams for ^{87}Sr, for example (Section 7.2), or when one deals with MOT light for different isotopes in a mixture. As the frequency is too close for dichroic mirrors to be used and the same polarization state does not allow us to use PBSs, a good working approach is an optical multiplexer [37]. It is an arrangement of four 50/50 reflection/transmission non-polarizing beamsplitters[23], which, in an ideal scenario, recombines three input beams into four output beams with each output beam having an equal power contribution from the input beams, and without loss of power[24]. The multiplexer is schematically shown in Fig. 6.3. Let us note some important features of multiplexer alignment. First of all, the 50/50 beamsplitter plates are mounted rigidly. Assume now, without loss of generality, that we have used the output fiber injection degrees of freedom to align the input "in 1" for maximal coupling into all "out" fibers. It turns out in that case, possibly not immediately intuitively, that we only need two movable mirrors (the same as for doing any normal beam walk) on each of the remaining inputs ("in 2" and "in 3") to align them

[21] Fiber type P3-630PM-FC-2 - PM from Thorlabs Inc., Newton, NJ, USA. All collimators in the red system are of type 60FC-4-A4.5S-02 from Schäfter+Kirchhoff GmbH, Hamburg, Germany.

[22] Model AOMO 3080-120 from Gooch&Housego.

[23] Single wavelength beamsplitter plates from Casix Inc., Fuzhou, PRC.

[24] In reality, equal power conditions are violated because real beamsplitters are not exactly 50/50, but rather they split the power unequally into the reflection and transmission ports.

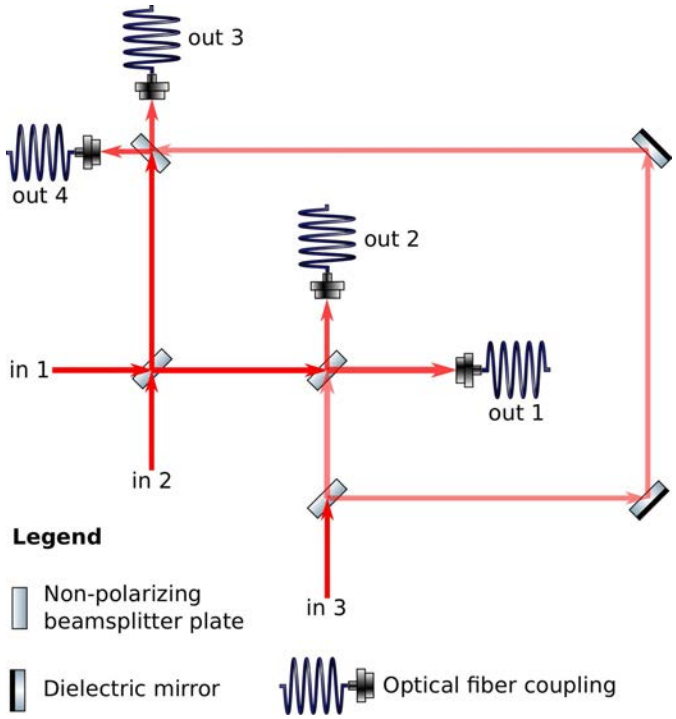

FIGURE 6.3: Red multiplexer layout. The mirrors required for beam alignment and fiber injection are omitted (see main text). Note that in the case of ideal 50/50 beamsplitters, each output port gets 75% of each input beam power. The details of reflection and refraction at each beamsplitter are omitted here and are shown in Fig. 6.4.

to all four output fibers. This is based on Fresnel's equations for reflection and refraction at interfaces and is shown schematically for one beamsplitter in Fig. 6.4. We see from that Figure that whatever path the "blue" beam follows (that is, we have used the output fiber adjustment to match its path and fiber-couple it), we can always use two mirrors in the "green" beam before the beamsplitter to overlap its transmission with the reflection of the "blue" beam; this will inject the transmitted "green" beam part into the same fibers where the reflected "blue" beam part is injected. However, this will automatically overlap the reflection of the "green" beam with the transmission of the "blue" one due to the angles of reflection and refraction. The same scenario will happen on all other beamsplitters. This means that, back in Fig. 6.3, if we have overlapped the transmission of "in 2" with the reflection of "in 1" at the first beamsplitter, these beams are copropagating thereafter and will be injected into the same fibers. This is very useful because it greatly reduces the number of alignment mirrors needed to couple three independent beams into four fibers and makes the multiplexer alignment procedure manageable.

6.3 The IR system

The infrared (IR) laser system at 1064 nm is required to make the ODT for trapping and evaporatively cooling Sr to quantum degeneracy (Sections 1.1 and 7.3), as well as for the future operation of optical lattices [103, 59]. The technical requirements for ODT beams are rudimentary: they are

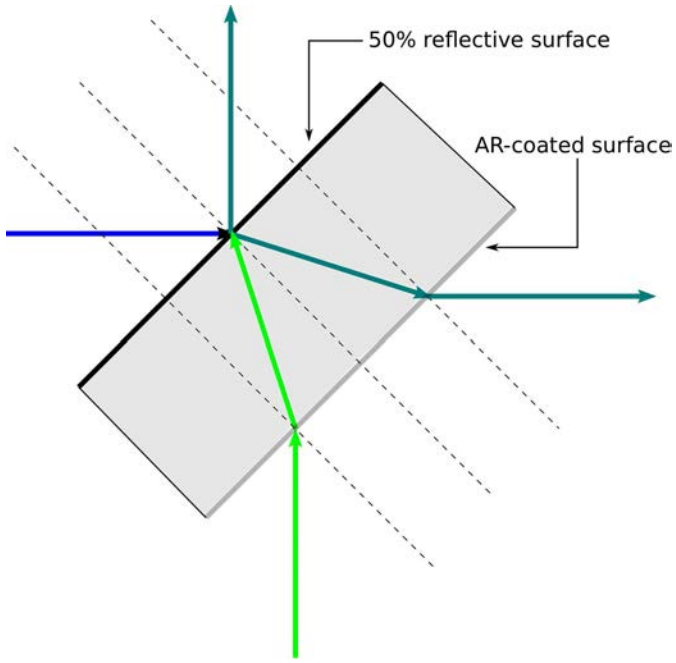

FIGURE 6.4: Reflection and refraction at each non-polarizing 50/50 beamsplitter plate. The basic working principle of these plates is the presence of one partly-reflective surface and one AR coated surface. The light blue and the green arrows schematically represent the beams coming in from two directions, and the mixture of colors represents the reflected and transmitted beams with 50% of contribution from each original beam.

simply far off-resonant high-power beams. Given the dynamical polarizability of Sr at $1064\,\mathrm{nm}$ (see Section 2.4), each of the two ODT beams normally has a couple of watts of power, the exact value being determined by their waists. The linewidth and the wavelength of the laser are irrelevant for the ODT; the wavelength can differ by several nm, because the polarizability of the ${}^1S_0$ state depends very weakly on wavelength around $1064\,\mathrm{nm}$. The only real ODT requirement is a relatively stable output power, at least without high-frequency noise; low-frequency fluctuations can be easily compensated by active feedback onto an AOM. The technical requirements for optical lattice beams are more stringent. Here, in addition to power stability, one requires a relatively narrow linewidth, so that the coherence length of the laser, given by $L_{\mathrm{coh}} = \frac{c_0}{\pi \Delta\nu_{1064}}$ [160], is much larger than any optical lattice beam paths. The output polarization should also be stable, because one normally puts polarizing elements into the optical lattice path, and laser polarization noise would then translate into power noise. However, a lattice still does not require absolute frequency locking to any atomic reference[25].

Since the ODT and the optical lattice do not require a specific atom-dependent wavelength and frequency locking, one can use a common and well-developed gain medium to generate such light. Therefore, commercial turnkey and nearly one-size-fits-all high-power laser systems for atomic physics and many other kinds of experiments are available. One such common gain

[25]Unless one is trying to use a magic wavelength optical lattice, which is not the case in most experimental work with ultracold atoms in optical lattices.

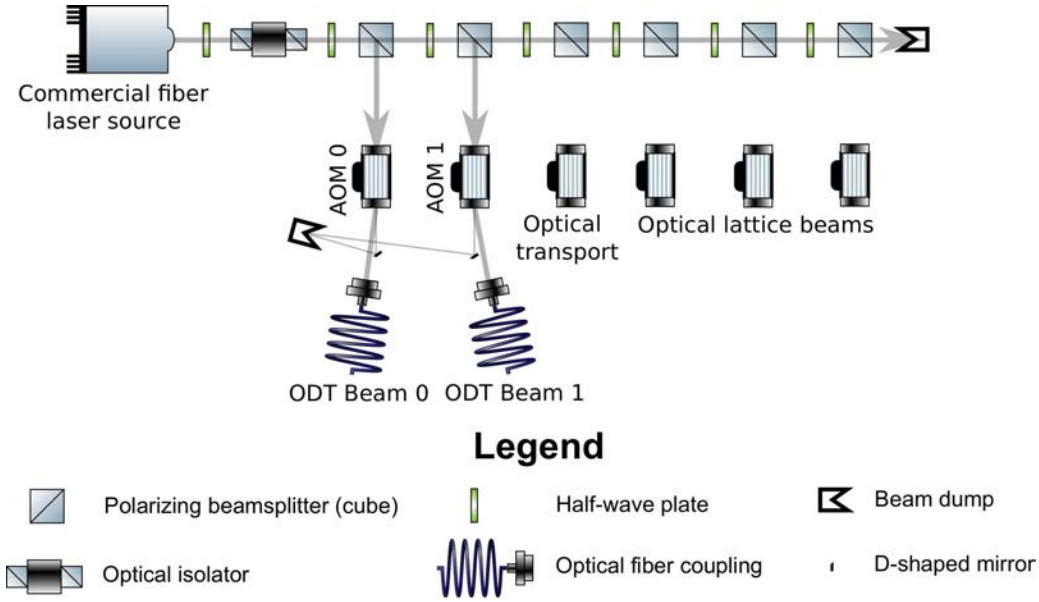

FIGURE 6.5: IR system schematic. Notice the dedicated paths for the optical transport and lattice beams. All PBSs are on kinematic mounts and are used as a degree of freedom for AOM alignment. The alignment mirrors used in the system have been omitted for illustration clarity.

medium is Nd:YAG, which emits around $1064\,\mathrm{nm}$; this is the reason for the widespread use of this wavelength. We use a commercial laser for the IR system, and it is specified to reach up to $50\,\mathrm{W}$ of output power with a linewidth $\Delta\nu_{1064} = 50\,\mathrm{kHz}$. This power is sufficient for both the ODT and an optical lattice, and the linewidth corresponds to $L_{\mathrm{coh}} = 1.9\,\mathrm{km}$, definitely sufficient for making an optical lattice with beam paths of at most several meters. The use of such a turnkey laser makes the IR system at $1064\,\mathrm{nm}$ the simplest one on the setup, because it requires only power distribution with waveplates and PBSs, and trivial frequency shifting with AOMs. However, there are two points to pay particular attention to while working with the IR system: the beams are invisible[26] and often high-power, which is a potential danger to humans, equipment, and a possible fire hazard.

Currently, the IR distribution system is providing the two beams for the crossed ODT, but it has been immediately set up to also give an optical transport beam and three lattice beams with minimal realignment. The schematic of the IR distribution is shown in Fig. 6.5. One important point to note is that all elements, so mirrors[27], waveplates, PBSs[28], AOMs[29], the optical isolator, optical fibers, must be rated for high-power beams. All beams that are not coupled into the fibers must terminate on beam dumps, which can be either air-cooled or water-cooled, depending on the amount of incoming power and the permissible amount of heating. It is also a good idea to

[26]During alignment procedures, IR beams can only be viewed with special phosphorescence cards or an IR viewer, such as IRV2-2000 from Newport Corporation, Irvine, CA, USA, for example.

[27]UVFS quartz laser line mirrors, type 1-OS-2-0254-5-[1PR45] from UAB Altechna, Vilnius, Lithuania for round mirrors and the same properties and manufacturer for the D-shaped ones.

[28]Optically contacted PBS, type 2-HPCB-C-0125 from UAB Altechna, Vilnius, Lithuania.

[29]High-power IR AOMs, Model AOMO 3080-194 from Gooch&Housego.

FIGURE 6.6: IR system enclosure. The large white tube is for air supply from the HEPA filter, and the thin copper tubes are water ducts for the water-cooled beam dumps (Design of Dr. Georgios Siviloglou).

put a diverging lens before the beam dump in order to spread the power over a larger area. In addition, due to the high intensity involved, dust on any optical surface can burn and cause damage, and for this reason the distribution system is enclosed in an anodized aluminum box with air supply coming directly from a HEPA filter at a slightly elevated pressure, shown in Fig. 6.6.

We note that in the future, some of the waveplates in the power distribution line can be replaced with motorized ones in order to adjust the power dynamically during an experimental cycle. This can be relevant for the quantum gas microscope, for example, because the ODT beams and the transport beam are not required when the deep microscope lattice is in operation; in this way, optical power can be consecutively used for two tasks. Furthermore, we note that it is possible to frequency-double this $1064\,\mathrm{nm}$ light to obtain a few W of $532\,\mathrm{nm}$ light, which can be useful for optical tweezer work or optical lattices with a smaller lattice period. This can be done in a simple way with a single-pass frequency doubling crystal[30].

[30]One option is a PPLN crystal from Covesion Ltd., Hampshire, United Kingdom.

Chapter 7

Production of strontium quantum gases

The major milestone in the construction of a new ultracold quantum gas machine is the demonstration of Bose-Einstein condensation and Fermi degeneracy. Supplemented by atom lifetime measurements, these results show that the vacuum quality is sufficiently good, the atom flux is high enough, the near-resonant cooling steps work, the dipole traps are focused and aligned well, and the evaporation process works. Furthermore, it is the starting point for most further experiments with ultracold gases. In this chapter we will show the procedures needed to achieve quantum-degenerate samples and present their basic analysis.

Brief look at the experimental sequence in the main chamber

We have seen a general and brief description of our ultracold gas machine in Section 1.2, and let us now focus on the experimental steps that happen in the main chamber (see Section 5.6 for its design information). TC and ZS are relatively simple and are essentially not different in Sr compared to the alkali atoms, for example. The peculiarities of Sr start becoming important at the MOT stage.

Due to the presence of two easily accessible optical cooling transitions from the ground state with very different linewidths (see the level scheme in Fig. 1.1), we use two MOTs in a sequence. The initial "blue MOT", operating on the broad $^1S_0 - {}^1P_1$ transition, allows us to efficiently capture atoms from the ZS. The details of the upper state decay process are such that the atoms eventually end up in a metastable state that can be held in a magnetic trap that is automatically created by the MOT quadrupole field [37]. After having collected enough atoms, we repump them back to the ground state and transfer them into a "red" MOT, which operates on a $7.4\,\mathrm{kHz}$-wide transition. Notice that based on the natural linewidths, the Doppler temperature [27] of the blue MOT is $730\,\mu\mathrm{K}$, and the Doppler temperature of the red MOT is below $1\,\mu\mathrm{K}$; in fact, the red transition is so narrow that its Doppler temperature is lower than its recoil temperature [27], so technically cooling to its Doppler limit is impossible. The red MOT leads to a very high phase space density (PSD), and, very importantly, the narrow linewidth of the red transition enables laser cooling inside the ODT itself in order to achieve very favorable starting conditions for evaporation [161]. After the red MOT beams have been ramped off, evaporative cooling is performed by lowering the ODT beam power. Due to a high starting PSD, the fraction of the atoms that escape during evaporation is much smaller than in the case of alkali quantum gases, for example. Quantum gas samples are generally characterized by absorption imaging

after release from the ODT (see Chapter 2); we can also perform experiments inside the ODT; a particular important example of Sr narrow-line spectroscopy in an ODT is described in Chapter 8. Alternatively, the ultracold sample from the main chamber ODT can be optically transported to one of the side chambers of the machine (see Sections 5.7 and 5.8).

7.1 The blue MOT, metastable reservoir and repumping

According to Fig. 5.15 in Section 5.3, the atoms exiting the ZS are expected to be moving at 20 to 30 $\mathrm{m/s}$; the broad blue transition is appropriate to use at this stage. The blue MOT is a standard three-dimensional MOT with all retroreflected beams crossing at right angles. The frequency is set to $30\,\mathrm{MHz}$ (it is approximately 1Γ) below resonance, and the beam powers and waists[1] are listed in Table 7.1. The quadrupole field gradient along the axis of the coils (vertical

Path	**Total power** [mW]	**Beam waist** [mm]
"corridor"	10	12.3
"wall"	10	12.3
vertical	4	5.8

TABLE 7.1: Powers and waists of the blue MOT beams. The names "corridor" and "wall" refer to the viewport locations where the two horizontal beams enter the chamber on the incoming side. The values for the waists are according to design and lens specifications, not direct measurements.

direction) is normally $50\,\mathrm{G/cm}$. This MOT is technically simple to set up and achieve, as long as one keeps in mind two important points: one must ensure the correct polarization of the MOT beams, and stable blue master and slave laser locking are crucial. Regarding the first point, note that the standard dielectric mirrors used in an optical setup scramble any kind of polarization, apart from linear, in unpredictable ways upon reflection, and this becomes critically important in the case of a MOT, which requires circularly polarized beams. The way to deal with this is to measure the polarization[2] right before the beam enters or right after it exits the vacuum chamber[3], and to set the polarization to the desired value by rotating a quarter-wave plate upstream, while watching the polarimeter reading. Once the polarization is set, it is not modified afterwards (up to possibly slight adjustments while the MOT is operating in order to maximize the signal, but always keeping a record of the original waveplate positions to be able to recover those). As for the second point, blue slave laser lock instability turns out to be the biggest reason for atom number fluctuations between experimental runs. As an aside, we would

[1] These waists are calculated based on fiber mode field diameter and collimating and expanding optics, rather than a direct measurement.

[2] We used polarization analyzer Model SK010PA-UVIS from Schäfter & Kirchhoff GmbH, Hamburg, Germany for this purpose.

[3] If there is no space on the optical table to install a polarimeter and do the measurement, one can always reflect a sample of the incoming MOT beam with a silver mirror. One has to only keep in mind that a silver mirror flips the sense of circular polarization. A good way to measure the retroreflected beam polarization is by reflecting a sample with a silver mirror.

like to mention that the Sr blue MOT can be seen directly with the eyes in real time, which is not true for the red MOT. Refs. [37, 162] describe more details of the blue MOT operation in Sr.

The blue $^1S_0 - {}^1P_1$ transition is not a completely closed one in Sr; there is a decay channel from $^1P_1$ first into the $5s4d^1D_2$ state, from which the atoms further decay into the $^3P_2$ and $^3P_1$ states with a branching ratio $^3P_2$:$^3P_1$ = 1:2 [21, 161, 163]. The decay probability into the $^1D_2$ state is a subject of debate[4], but it is at a level of once per a few 10000 scattering events on the blue transition. The $^3P_2$ state is magnetic, and so its low-field-seeking substates can be immediately trapped at the minimum of the MOT quadrupole magnetic field. In this manner, the continuous operation of the blue MOT is filling up the quadrupole trap with atoms in the metastable $^3P_2$ state; we call it the *metastable reservoir* [37]. In fact, we are explicitly using here for the first time the metastability of one of the Sr excited states (see Section 1.1 for a general discussion in the context of Sr properties). There are two points to note here. First of all, one can immediately ask how a simple quadrupole trap can collect cold atoms, because there exist the highly detrimental nonadiabatic spin flip losses (Majorana spin flips) [165]. Our trap is actually continuously losing atoms to this process, but the loading rate is higher than this loss rate, so the atom number in the trap grows, at least until density-dependent losses start to dominate. Furthermore, we are not cooling the gas to ultralow temperatures in this trap and so the density of the atoms at the centre of the trap remains low, which makes the spin flip losses less pronounced. The second question to ask is why does it not appear to be highly detrimental that the atoms in the excited states tend to collide inelastically and thus leave the trap. The solution to this problem is a low density: the metastable reservoir is large and has a lower density than the MOT itself; the probability of any two-body decay process decreases quadratically with decreasing density [166]. Thus, it is reasonable to collect atoms in the $^3P_2$ state in a quadrupole magnetic field. However, these atoms must be brought back to the ground state in order to do further experimental steps (red MOT, ODT, evaporative cooling); this process is called *repumping*. Following the previously developed techniques in our group, we repump by illuminating the center of the main chamber with a few hundred µW of $497\,\mathrm{nm}$ (green) light resonant with the $^3P_2 - {}^3D_2$ transition [37, 167] for approximately $150\,\mathrm{ms}$[5]. This green beam is overlapped with the ZS beam on a dichroic mirror at the optical fiber input on the laser table. Therefore, the green beam shares the fiber with the ZS beam and has nearly the same beam path and beam shape as the ZS beam inside the vacuum system. The green beam parameters are rather forgiving and are optimized by imaging the atoms immediately after the repump flash and maximizing their number, or alternatively, by directly maximizing the number of atoms in the red MOT. In addition, the polarization of the repump beam is irrelevant. After the repump flash we are left with a cloud of ground-state atoms at a temperature of several mK, a lot colder than the atoms exiting the ZS. This cloud is ready to be loaded into the red MOT.

[4]There are essentially two reported values for that decay probability: about 1/20000 [113] and about 1/50000 [21, 164]. We did not attempt to measure it ourselves, so we cannot comment on which value is closer to reality.

[5]The $497\,\mathrm{nm}$ light is produced in the adjacent lab using a frequency-doubling system that consists of a laser diode and a tapered amplifier at $994\,\mathrm{nm}$, and then a bow-tie doubling cavity from Toptica Photonics AG, Graefelfing, Germany. See Ref. [37] for more information.

7.2 The red MOT

The Sr red MOT allows us to cool a cloud from approximately $1\,\mathrm{mK}$ to around $1\,\mu\mathrm{K}$ or even less, when the steps are well-optimized. We will see in a simulation below (Fig. 7.5) that, given a cloud at $1\,\mu\mathrm{K}$ in a dipole trap with commonly achievable trap frequencies, one has to evaporate only about 20% of the atoms to reach quantum degeneracy. The ability to achieve such a low-temperature MOT is a fortunate consequence of the narrow ${}^1S_0 - {}^3P_1$ transition linewidth in Sr.

The red MOT consists of two stages: we call the first one the "broadband red MOT" and the second one the "single-frequency red MOT". Consider eq. (2.32), which leads to two main conclusions in the case of a narrow transition (small Γ): first of all, the maximum achievable force on the atoms in the MOT is low; secondly, the atoms will scatter photons only in a small region of the magnetic field or in a small velocity class, otherwise the Zeeman and Doppler shifts quickly take the transition out of resonance with the cooling laser. Addressing the atoms at different field positions or velocities requires different frequency detunings. The broadband red MOT is the answer to this challenge and it simply means that its beams contain multiple frequency components. Eq. (2.32) is applicable for a single frequency MOT beam; if there are multiple frequency components, the term on the right-hand side becomes a sum with different Δ'_L. As the atoms are being cooled, we keep reducing the number of frequency components in the red MOT beams, shifting them closer to the free-space resonance, and reduce the beam power. The cloud gets progressively colder and eventually reaches about $1\,\mu\mathrm{K}$. In the end, only a single frequency component in the red beam is left, which is good for trapping and cooling at the final low temperature.

It is worthwhile to explain how a set of multiple frequencies is produced for the broadband red MOT. The main point is that the red MOT beams each pass an AOM before being sent through the multiplexer (see Section 6.2) and then being injected into the fibers that take the light from the laser table to the optical table. We can program a radiofrequency (RF) generator[6] to apply a time-varying RF frequency to these AOMs, and viewed with a Fourier transform, this time-varying signal will result in a spectrum containing multiple frequencies. To see this, let us first consider a simple oscillating signal, written in the form

$$s(t) = \cos(\omega t + \theta_0); \tag{7.1}$$

we know from elementary physics that this is a wave with a constant angular frequency ω and a phase offset θ_0 from some chosen reference. The term in parentheses can be labeled as $\Theta(t)$, and it is the generalized time-dependent phase; the instantaneous angular frequency of a wave is the time-derivative of that phase, $\omega(t) = d\Theta(t)/dt$ [168, 169]. We can for simplicity set $\theta_0 = 0$ above (that only fixes the phase offset, which is not important here because we will only be working with a single source of waves, no interference involved) and add a time-dependent term to the

[6] This is a DDS in our case, see Section 5.14.

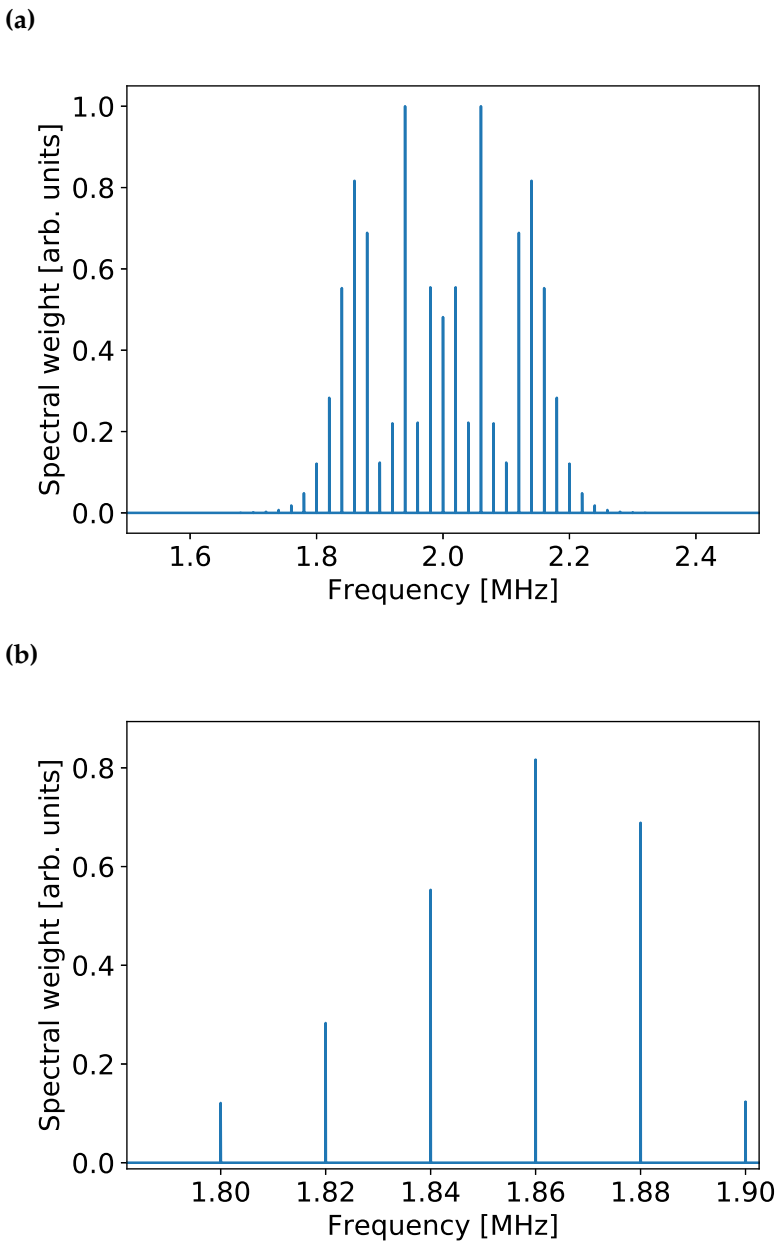

FIGURE 7.1: Numerically calculated (FFT) spectrum of a sinusoidal wave with triangle-wave frequency modulation: the full spectrum (a) and the zoomed-in part showing individual line separation (b). In this case $\omega_c = 2\pi \times 2\,\mathrm{MHz}$, $a_f = 2\pi \times 0.2\,\mathrm{MHz}$, $\omega_m = 2\pi \times 20\,\mathrm{kHz}$; eq. (7.4) has been used. The values of a_f and ω_m are the realistic experimental parameters that can be used at a red MOT stage. The value of ω_c is chosen for computational convenience, in order to not evaluate the integral in eq. (7.4) and to not perform the Fast Fourier Transform for a very large number of points. A higher value of ω_c will only shift the point around which the spectrum is centered. The apparent gaps in spectral weights are numerical artifacts.

generalized phase, thus getting

$$s(t) = \cos(\Theta(t));\ \Theta(t) \equiv \omega_c t + \theta(t), \tag{7.2}$$

where ω_c stands for central frequency. The instantaneous angular frequency of $s(t)$ is $\omega(t) = d\Theta(t)/dt = \omega_c + d\theta(t)/dt$. In the red MOT in our experiment, DDS produces a time-variation of RF frequency in the shape of a triangular wave in frequency space, centered at ω_c. This requires that $d\theta/dt = A_m \mathrm{Tr}_{\omega_m}(t)$, where $\mathrm{Tr}_{\omega_m}(t)$ denotes a triangular wave of unit amplitude centered around 0 (meaning, it is oscillating between the values -1 and 1) and having angular frequency ω_m; A_m is the modulation amplitude. This implies that

$$\theta(t) = \int_0^t A_m \mathrm{Tr}_{\omega_m}(\tau) d\tau. \tag{7.3}$$

We can now write the driving RF field for out AOMs at the red MOT stage:

$$d_{\text{AOM, RF}}(t) = \cos\left(\omega_c t + \int_0^t A_m \mathrm{Tr}_{\omega_m}(\tau) d\tau\right), \tag{7.4}$$

where d stands for "drive" and ω_c denotes the central frequency around which the RF is swept in a triangular pattern. We can numerically integrate the triangular wave part in eq. (7.4) and then perform the FFT to find the spectrum. A particular example of such a spectrum, for an experimental set of parameters (with the exception of central frequency, which is, however, only a constant shift along the frequency axis), is shown in Fig. 7.1 (evaluated in *Numpy* [81]). We note the important points: the spectrum is centered around ω_c, one obtains a comb of lines separated by ω_m, and the spectrum extends to $\pm A_m$ from ω_c. This is a general rule of what happens during such frequency modulation and it produces the kind of a multifrequency beam that we need. Since the optical frequency of the diffracted beam is the incoming laser frequency plus or minus[7] the applied RF frequency, the diffracted MOT beam will also have the frequency content described by eq. (7.4) and depicted in Fig. 7.1. Note that there are some apparent numerical artifacts in that spectrum (the spectral weights of the different frequency components not being uniform close to the middle of the spectrum); they are most likely due to coarse-graining and not taking a fine enough numerical grid, in order to avoid a long computation time. If a more precise result is desired, one can perform a longer calculation, possibly on a cluster, using a much finer grid. Table 7.2 gives an example of the experimental red MOT frequencies used in evaporations to ^{84}Sr BEC.

The frequencies listed in Table 7.2 are not the only possible option, and the broadband red MOT frequencies and powers have to be experimentally optimized depending on the isotope, MOT beam size and total power, for example. One can regard those values as a starting point, around which one can look for improvements, if necessary. The beam powers for each step can be rather quickly optimized by trial and error, starting from the condition that initially each frequency component of the broadband red MOT should have an intensity of about 2-3 I_{sat} and then in the later steps that value should be getting progressively lower. The optimization is done based on the measured atom number and temperature. Ref. [37] provides more details on the red MOT as it was done on a different machine in our group.

[7] This depends on whether the $+1^{\text{st}}$ or the -1st diffraction order is used.

Step	Detuning [kHz]	Comb spacing [kHz]	Ramp time [ms]	Duration [ms]
Capture	-150 to -3000	20	n/a	150
I	-150 to -1150	20	150	200
II	-40 to -500	20	150	200
III	-20	n/a	175	50
IV	0	n/a	120	n/a

TABLE 7.2: Red MOT laser frequency parameters and ramp times for ^{84}Sr BEC production. Since the broadband red MOT consists of multiple frequency components (see main text), we give them here as the range of detunings and the gap between equally spaced frequencies within that range of detunings. The values of detunings are referenced to the free-space resonance. The cases when the comb spacing is not applicable (n/a) refers to single-frequency operation. The ramp time refers to the time in which the frequency (and power) is ramped from the step to reach the values needed in the given step. The duration of the last step is irrelevant because in that step the MOT beams are being turned off.

The last step of the red MOT, which is not a MOT procedure anymore, but rather a clever use of the red transition, is in-trap cooling. The ODT is switched on during the red MOT sequence, and at the end of this sequence, the sample is already held by the ODT. At that point the MOT beam intensity can be made much lower than what would be necessary to levitate the atoms against gravity, because the ODT does that job [161, 37]. One only uses very weak red cooling beams to take advantage of the narrow line and push the sample temperature down as much as possible. The differential AC Stark shift in the ODT blue-shifts the $^1S_0 - {}^3P_1$ transition, and so we put the red beams at the frequency of the free-space resonance or even above it; these beams, however are still red-detuned with respect to the light-shifted transition frequency inside the ODT.

The red MOT procedure in the ^{87}Sr isotope is very different from the classic alkali-atom MOTs not only due to the narrow transition, but also due to the particular hyperfine structure of ^{87}Sr. First of all, we note that the red MOT beam for ^{87}Sr addresses the $F = 9/2 \rightarrow F' = 11/2$ transition (prime denotes the upper state). Since the $^1S_0$ state has $J = 0$ orbital angular momentum, the magnitude of the m_F substate Zeeman shift in the quadrupole magnetic field of the MOT is set by the value of the nuclear magneton. In contract, the upper electronic state involved, $^3P_1$, has $J = 1$, and so its Zeeman shift is determined by the much larger Bohr magneton. The outcome is that at a given red detuning, a σ^- beam, for example, will be trapping for some of the $m_F < 0$ substates, but actually repulsive for some other ones [37]. Some other substates will simply not feel any restoring MOT force and also be lost from the trap. This is an unfavorable situation which would lead to a very low MOT atom number, because one always starts with an m_F state mixture in the red MOT. The key ingredient that makes the ^{87}Sr red MOT work and limits the losses is the fact that the Clebsch-Gordan coefficients for different $m_F \rightarrow m'_F$ transitions on average turn out to be favorable for trapping (see Ref. [37] for details). However, in order to make the best use of this, we have to randomize the m_F substates in $^1S_0$ faster than the time it would take them to escape the MOT region, and this is done by using

stirring beams. These beams are overlapped with the MOT beams still on the laser table and get delivered to the machine through the same fibers. They are red-detuned from resonance by the same amount as the MOT beams, but the main difference is that for the stirring beams, the resonance refers to the $F = 9/2 \rightarrow F' = 9/2$ transition, unlike the $F = 9/2 \rightarrow F' = 11/2$ MOT transition [37]. Refs. [37, 170] provide more details. Recently an interesting way of creating a fermionic Sr MOT without stirring beams was demonstrated by James Thompson's group at JILA [171].

7.3 Strontium in an optical dipole trap and evaporative cooling: simulation results

The last step on the way to Sr quantum gases is an ODT made with the IR laser system described in Section 6.3. We can use the results from Section 2.4 to evaluate the potential energy landscape for different waists and powers, and then to estimate the expected evaporation process. We will not be concerned much with the optimization of trap loading dynamics from the red MOT because we initially do not need a highly optimized loading process, as long as we have enough atoms to evaporate to a clearly measurable quantum gas. A simple consideration that the trap size should be comparable to the red MOT size in the last step, together with experimental trial and error, is sufficient. In case a more rigorous calculation is needed, Refs. [172] and [173] provide more details for general ODT loading procedures, and Ref. [174] specifically describes work with Sr. The goal of this section is to estimate the relevant parameter that can be good starting points for optimization and further improvement on the machine.

Eq. (2.42) allows us to estimate the optical potential for a single-beam trap and also to see the effect of gravity in the vertical direction. The results of these calculations for the ground state of Sr are shown in Fig. 7.2, where the trap depth is found numerically by subtracting the energy at the bottom of the central dimple from the energy maximum on its left. A beam waist of around $70\,\mu\mathrm{m}$ allows us to achieve a trap depth of a few tens of µK with a few watts of laser power, which is readily available from a $1064\,\mathrm{nm}$ laser system (see Section 6.3). In the actual experimental configuration, the trap should be deeper because it is a crossed dipole trap, and so the powers of both beams should be added (that is not accounted for in the calculation for Fig. 7.2). On the other hand, imperfections in the focus position and greater-than-expected focus spot size will reduce the trap depth. Those things are best to fine-tune experimentally, and this result gives us a general guide. A rough measurement of the ODT beam waists based on the measured trap frequencies is given in Subsection 7.5.4. Fig. 7.3 shows an absorption image of a single beam of our dipole trap, loaded from the red MOT.

The trap frequencies for a crossed ODT with different powers and waist sizes can be predicted using eqs. (2.51) and (2.63). We assume here that both crossing beams significantly contribute only in the case of the radial direction for both beams; and we neglect the contribution of a beam in its longitudinal direction. The calculated trap frequencies, assuming beams of equal waist size and equal power, are shown in Fig. 7.4; the x-axis is labeled in terms of power per beam.

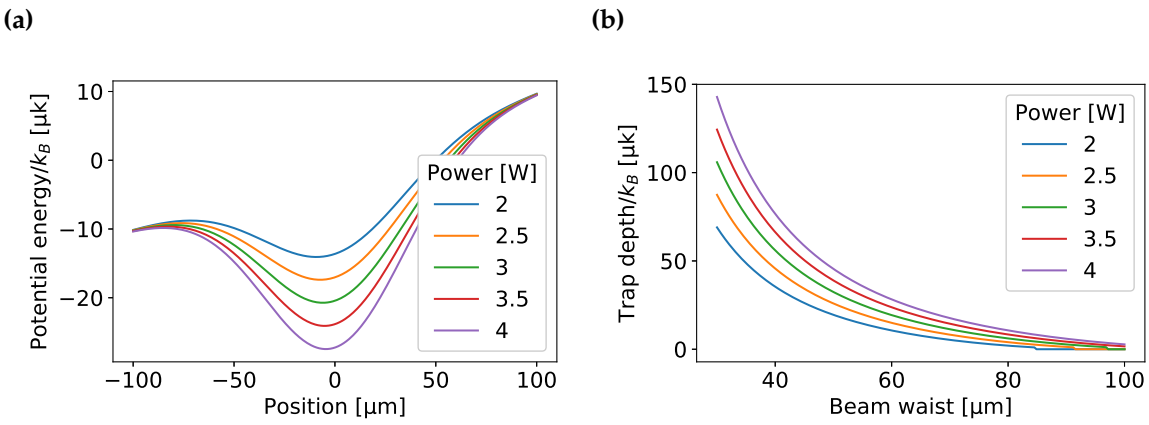

FIGURE 7.2: Shape (a) and depth (a) of a single-beam horizontal ODT for ^{84}Sr in $^1S_0$ state, in the vertical direction. Each curve represents a different ODT beam power. Notice the linear tilt due to gravity in (a). The trap depth is defined as the energy difference between the bottom of the central dimple and the maximum point on the left side of it in (a).

Notice that the trap frequency is expected to be in the range of 200 Hz - 400 Hz (expressed in linear units), which is the value that can be used, for example, to predict the peak PSD before evaporation, and thus to estimate the necessary amount of evaporation. The trap frequencies have been subsequently measured experimentally using a BEC sample and they are reported in subsection 7.5.4.

It is helpful to numerically estimate the evaporation procedure and to get a handle on the parameters to start from on the path to quantum gases. The PSD of ^{84}Sr at the end of the red MOT can be as high as 0.1, and it has been reported to reach even 0.3 after in-trap cooling and dipole trap loading [161]. We will see in section 7.4 that we get an estimated peak PSD = 0.7 before evaporation, which is very large. Let us take a tenfold safety margin and assume a starting PSD = 0.07. The PSD for the BEC phase transition in a harmonic trap is 1.202 [175, 176][8]. In the notation of eq. (2.84), we require $\frac{\rho}{\rho_i} \approx 20$ for the BEC transition. The temperature of the sample loaded into the ODT is about 1.5 μK, and we can load in excess of 2 million atoms into the crossed dipole trap. This, together with the trap frequencies, will be the parameters to use in the equations from Section 2.5. Fig. 7.5 shows the evolution of the PSD and the atom number as the trap power is being lowered, calculated according to eq. (2.84). We label the plots by the value of η, which is the ratio between the trap depth and the thermal energy of the sample, defined in eq. (2.80). Experimentally, the values of η between 5 and 10 are reasonable: $\eta < 5$ would lead to not enough time for rethermalization and $\eta > 10$ would make evaporation very slow and thus make undesirable loss processes dominate. We see that for $\eta \geq 7$, a decrease in power by a factor of 15 already increases the PSD by a factor greater than 20, which should lead to quantum degeneracy in our experiment. Notice that one keeps about 20% of the atoms from the original sample, which is a large number when one talks about the fractions of atoms

[8] A different well-known PSD value for a BEC phase transition is 2.612, but that one is derived for the case of a uniform box potential [175], which is not our case.

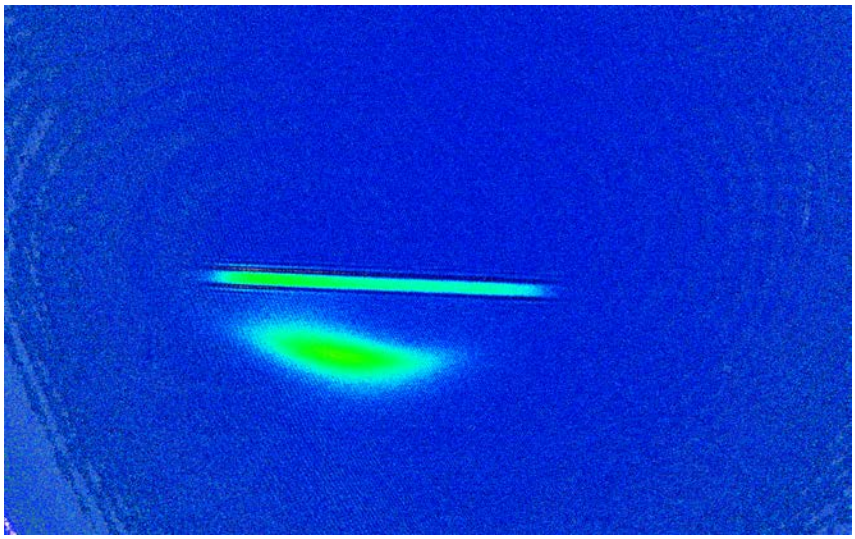

FIGURE 7.3: Loaded single beam of the dipole trap, with the remaining atoms in free fall after the red MOT has been turned off.

remaining and being evaporated away: this is the consequence of starting with a high PSD. An estimate of the timing for the evaporation towards BEC is shown in Fig. 7.6. From experience, we know that η should be somewhere between 5 and 10, and the timing of the evaporation ramp is calculated under the assumption that η should stay constant throughout the procedure, as mentioned in Ref. [95]. The condition of constant η is possibly not satisfied in the experiment because of the heating and loss processes that are not a direct consequence of the evaporation ramp shape, but this simulation is meant to serve as a general guideline. From its result we see that 3-4 s of evaporation should be required to reach a factor of 15 drop of power, which, as explained in Fig. 7.5 and the text that belongs to it, should be enough to achieve quantum degeneracy. In actual experiments, we do not necessarily perform evaporation exactly like in this simulation: we can, for example, reduce the power of one beam of the crossed ODT and keep the other one at a constant value. However, those things can be optimized on the machine.

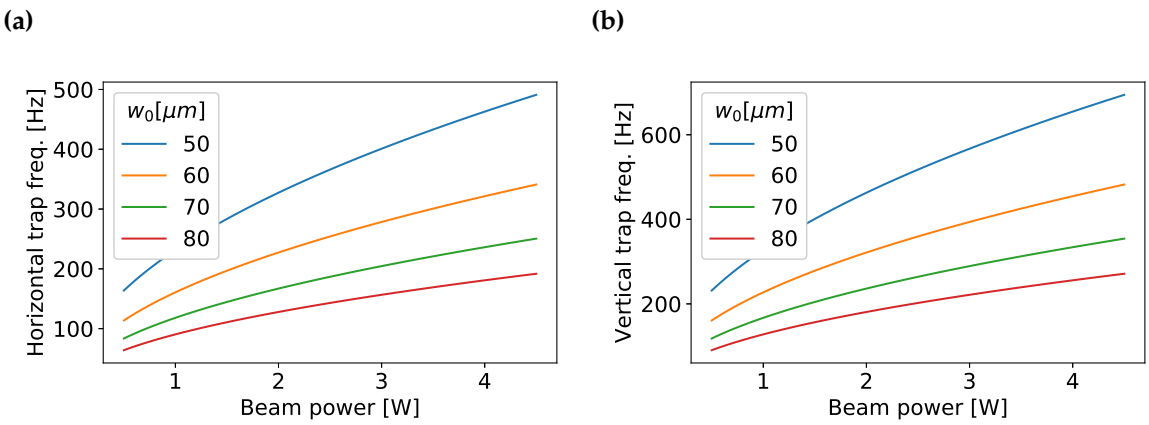

FIGURE 7.4: Calculated trap frequency for ^{84}Sr in $^1S_0$ state in a crossed ODT. Subfigure (a) shows the result for the horizontal direction (strongly confining for only one beam); subfigure (b) shows the result for the vertical direction (strongly confining for both beams). The waists w_0 and the powers of both beams are taken to be equal.

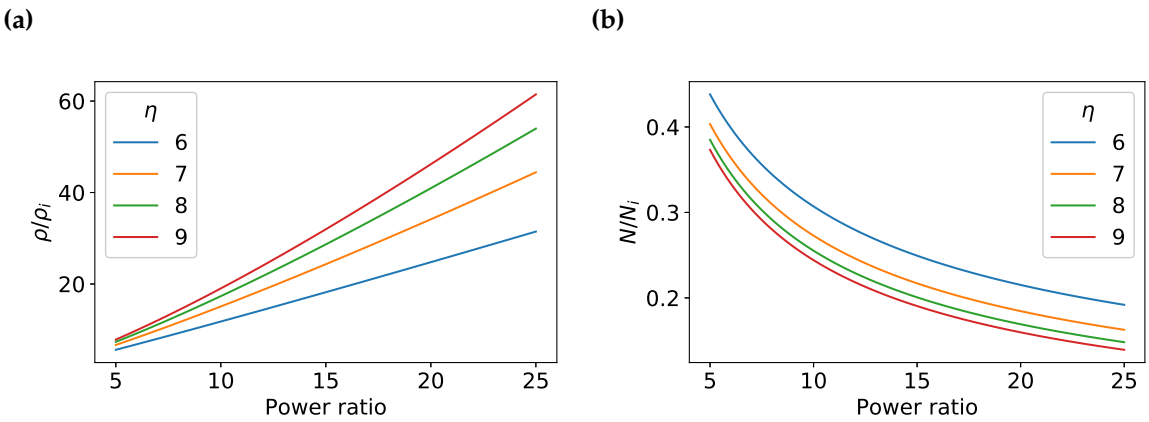

FIGURE 7.5: Calculated evaporation results in an ODT using eq. (2.84), where η is defined in eq. (2.80). The increase in PSD as a ratio with the respect to the initial PSD (a), and the fraction of remaining atoms (b) are shown for a crossed ODT. The power ratio denotes the factor by which both beams are weaker at the end of evaporation (we assume that the trap depth decrease in both beams occurs at the same rate). Note that for Sr in the $^1S_0$ state in a crossed ODT ($1064\,\mathrm{nm}$) with two beams of equal power and having waists of $70\,\mu\mathrm{m}$, $\eta = 6$ corresponds to $660\,\mathrm{mW}$ per beam and $\eta = 9$ corresponds to $1\,\mathrm{W}$ per beam.

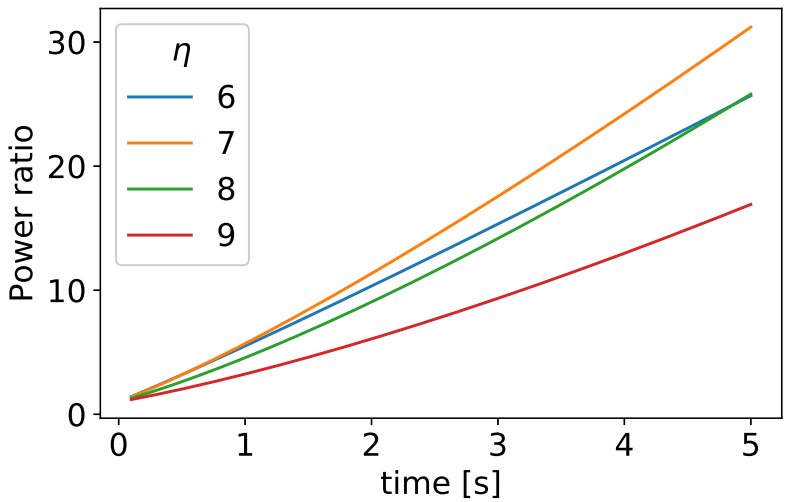

FIGURE 7.6: Calculation of the timing for the last steps of the evaporation sequence using eqs. (2.82) and (2.83). Here, the crossed ODT beams are both assumed to have a waist $w_0 = 70\,\mu\mathrm{m}$ and a 1:4 relation in power. The starting power of the stronger beam is $1.25\,\mathrm{W}$ and the "Power ratio" has the same meaning as in Fig. 7.5. The initial atom number is assumed to be 2×10^6 and the initial sample temperature is set at $1.5\,\mu\mathrm{K}$. Note that by construction of the theory, the evaporation ramp is calculated under the requirement that η be kept constant in time. Power ratio of 15 is the threshold for quantum degeneracy in this parameter regime (see main text).

7.4 Simple evaporation of ^{84}Sr to BEC

The final, far off-resonant, stage of BEC production starts with loading the ODT with a ^{84}Sr sample from the red MOT. IR Beam 0 and IR Beam 1 (see Fig. 6.5) are ramped up to $3.6\,\mathrm{W}$ and $2\,\mathrm{W}$ respectively within $50\,\mathrm{ms}$ during the multifrequency red MOT stage in order to create a potential well where the atoms will be collected as they are being cooled. We emphasize again that a very important step at the end of the red MOT for Sr is in-trap cooling: when the sample has been loaded into the dipole trap, the MOT beams do not have to hold atoms against gravity anymore, so their power can be gradually reduced to zero and their detuning can be brought closer to resonance, taking full advantage of the $^1\mathrm{S}_0 - {}^3\mathrm{P}_1$ linewidth. Unlike evaporation, this cooling step removes thermal energy without losing the atoms (see Refs. [23, 24] for particularly innovative uses of this technique). Fig. 7.7 shows a time-of-flight (TOF) absorption image of a ^{84}Sr cloud in the ODT after MOT and in-trap cooling but before evaporation. Since this gas is not yet very close to the critical temperature for quantum degeneracy, we fit it with a 2D Gaussian [177], and, based on the integral under the 2D surface and the scattering cross-section, we estimate the atom number to be about 2.8 million. We can then find the temperature of the cloud using the long TOF approximation, which results in the following expression for the temperature (eq. 5.15 in Reference [103]):

$$T \approx \frac{M_{\mathrm{Sr}} w(t)^2}{2 k_B t^2} \tag{7.5}$$

where M_{Sr} denotes the atomic mass of Sr, t is the TOF, and $w(t)$ is the $1/e$ width of the fit to cloud. The cloud temperature evaluates to $1.6\,\mu\mathrm{K}$. Since the cloud is in a harmonic trap, its peak phase space density (PSD) can be calculated as (see eq. 3.7 in Ref. [176] and Ref. [178])

$$\rho = N \omega_{\mathrm{HO},x} \omega_{\mathrm{HO},y} \omega_{\mathrm{HO},z} \left(\frac{\hbar}{k_B T} \right)^3 , \tag{7.6}$$

where N is the total atom number, $\omega_{\mathrm{HO},x}$ denotes the trap frequency in the x direction, and the notation is analogous for the y and z directions, and T is the cloud temperature. The $1/e^2$ waists of the ODT beams are approximately $70\,\mu\mathrm{m}$ (see subsection 7.5.4), and so using the powers of IR Beam 0 and IR Beam 1 given above and eq. (2.51) we can calculate the radial trap frequencies for ^{84}Sr in these ODT beams to be $\omega_{\mathrm{HO,IR\ beam\ 0}} = 1.4 \times 10^3\,\mathrm{rad/s}$, $\omega_{\mathrm{HO,IR\ beam\ 1}} = 1.0 \times 10^3\,\mathrm{rad/s}$. Those are the trap frequencies in the horizontal directions, and since the vertical direction is strongly confining for both beams, its trap frequency has to be calculated using eq. (2.60), and it evaluates to $1.7 \times 10^3\,\mathrm{rad/s}$. Putting all these values in eq. (7.6), we find the peak PSD of this sample to be 0.7. If one assumes an uncertainty of $10\,\mu\mathrm{m}$ in ODT beam waist (see subsection 7.5.4) and takes this to be the dominant uncertainty peak PSD calculation, then this lead to the peak PSD being given with the following error bars: $0.7^{+1.2}_{-0.4}$. In any case, this is a large number, but still compatible with the phase-space density of 0.3 that was reached in our group's earlier work with Sr at this stage in the experimental sequence [161]. However, one possible effect

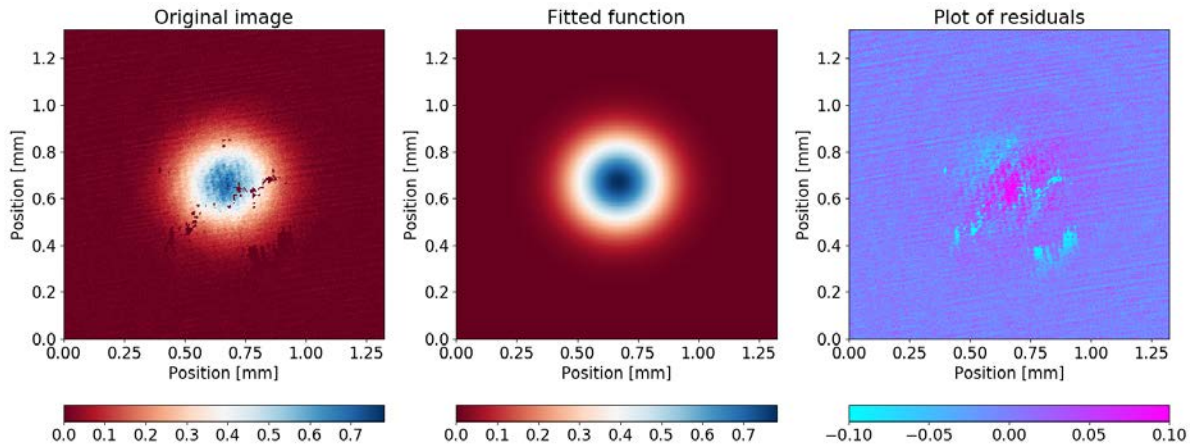

FIGURE 7.7: Absorption image of a ^{84}Sr thermal cloud in the ODT prior to evaporation, after 15 ms TOF. The color bars are given in units of optical density. Atom number is about 2.8 million, cloud temperature is 1.6 µK, peak PSD ≈ 0.7.

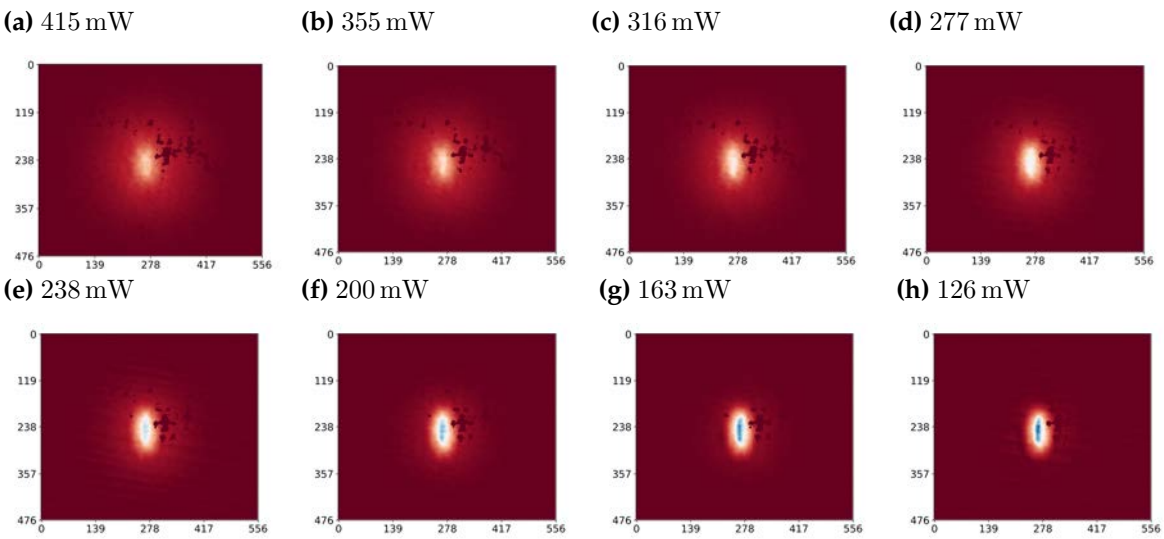

FIGURE 7.8: Absorption images of ^{84}Sr cloud at different stages of evaporation, after 15 ms TOF. Axes are labeled im µm. The labels above each image give the final power of IR Beam 1; that of IR Beam 0 is 2.9 W.

that could make the calculation here give a larger result that what the PSD really is is thermal lensing: when a high-power laser beam, like the one at the ODT loading stage, passes through glass elements, thermal lensing can make its waist larger than the waist when rather low power is used, and in this case, beam waist determination by BEC trap oscillations was done in a lower-power beam (see subsection 7.5.4).

The evaporation sequence itself permits multiple power ramp options and configurations, depending on what one's goals are. For example, one approach is a two-step sequence which separates a initial rampdown of the ODT beams to the point where BEC starts forming, and then the next step is the rampdown to the point of maximal BEC fraction, where the steps are

performed at different rates (expressed in W/s). In the first step, after the atoms have been loaded into the ODT and all near-resonant beams have been switched off[9], both IR beams are ramped down linearly in power within 3.5 s to 573 mW and 415 mW. In the second step, which lasts 1.5 s, IR Beam 0 is ramped linearly up to about 2.9 W, while IR Beam 1 is ramped down to different final values, and the resulting cloud is imaged in time of flight. The one beam is ramped up in order to provide stronger confinement in one direction and thus to create a cloud aspect ratio different from 1, even though both beams are circular and have approximately equal waists; aspect ratio inversion in TOF is then a telltale sign of a BEC. Fig. 7.8 shows the cloud after the evaporation, imaged after 15 ms TOF; the individual figures are labeled by the final IR Beam 1 power. If we roughly assume, based on Fig. 7.8, that the thermal fraction is small after maximal evaporation, then we can estimate the number of atoms in the BEC from the integrated total optical density to be about 600000. This is probably an overestimate, and part of this number is still the thermal fraction. More measurements, in a different ramp sequence, together with more accurate analysis, are presented in the next section.

7.5 Analysis of BECs

We will now present basic analysis of the BECs made in the new machine. This is necessary for future optimization, and we would also like to make quantitative statements about the achieved results. In particular, we will show how the BEC fraction grows with deeper evaporation, demonstrate the inversion of aspect ratio, analyze ODT loading and lifetime, and determine the ODT trap frequency.

7.5.1 BEC fraction growth

BEC fraction growth, and thus evaporation dynamics, is analyzed by stopping evaporation at different points and imaging the resulting atomic cloud. We know that the lower the final ODT potential is, meaning the more hot atoms spilled from the ODT, the purer the resulting BEC will be. However, the total atom number then will also be smaller, and at some point the ODT will be too weak to hold the cloud against gravity and the entire sample will be lost. It is thus valuable to find the point where the BEC is pure enough and has a large enough number of atoms for further experiments.

For the purpose of BEC growth analysis, the evaporation sequence steps are modified compared to Section 7.4. This also lends support to the statement that there is more than one possible evaporation procedure. In this case, after having loaded the ODT at 3.6 W and 2 W in the beams, the power is reduced to 2.9 W in IR Beam 0 and to different values in IR Beam 1 in a single linear ramp of 3 s, and then held at the final values for 1 s. The ODT is then switched off to release the atoms and the cloud is imaged after a TOF. This is conceptually the simplest approach

[9] It is important to note here that one must take the best possible precautions to prevent any leakage resonant light from reaching the atomic sample. In practice, we block the near-resonant beams with mechanical shutters on the laser table; only turning off the respective AOMs lets too much leakage light through.

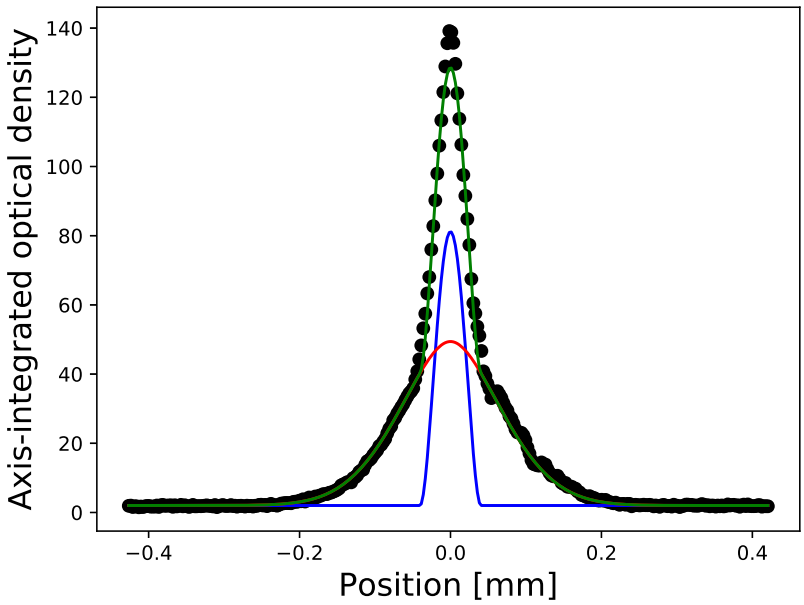

FIGURE 7.9: Bimodal 1D fit, using the sum of eqs. (2.100) and (2.114), to a partly condensed cloud after TOF. The absorption image is integrated along the less-confined axis of the ODT. Black dots denote the data, blue line is eq. (2.100), red line is eq. (2.114), and green line is the sum of the two equations, all evaluated with the best fit parameters.

to evaporation because it involves only a single linear ramp in power and some waiting time at the end for the thermalization process to finish.

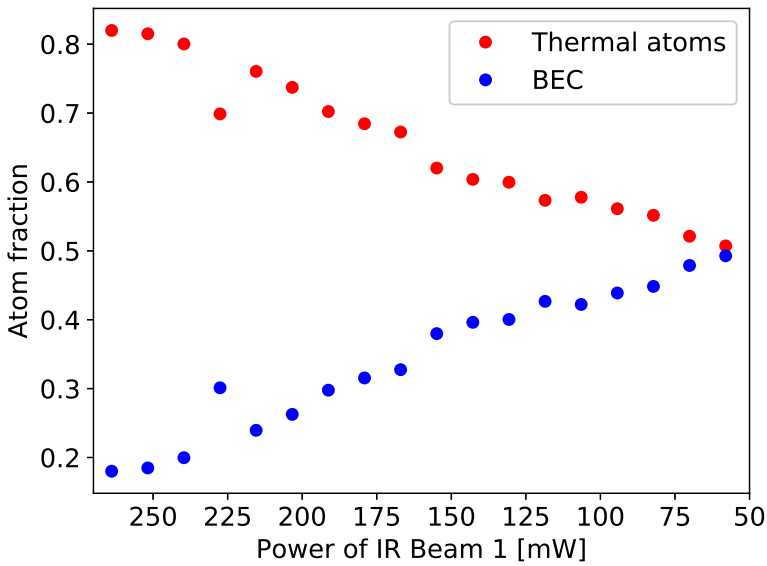

FIGURE 7.10: BEC and thermal gas fractions extracted from the fits of the type shown in Fig. 7.9.

Fitting TOF images of partly condensed clouds and extracting information from those fits in a reliable manner is a difficult topic, where there are no universally accepted models [13]. One option is to fit with the sum of eqs. 2.100 and 2.114 because we expect a bimodal distribution, as suggested in eq. (43) of Reference [13]; for simplicity, we fit the integrated 1D profile instead of a 2D fit with a polylogarithm, and we do not demand that $\mu = 0$ but rather leave it as a fitting parameter limited to small negative values. The result of such fitting for one example of a partly condensed cloud is shown in Fig. 7.9. For comparison, a full 2D fit to a cloud at the beginning and at the end of evaporation using a sum of the Thomas-Fermi profile and a Gaussian is shown in Fig. 7.11. This method is an approximation which ignores Bose-enhancement of the thermal cloud [167]. The relative atom numbers in the BEC and thermal fraction can be evaluated using

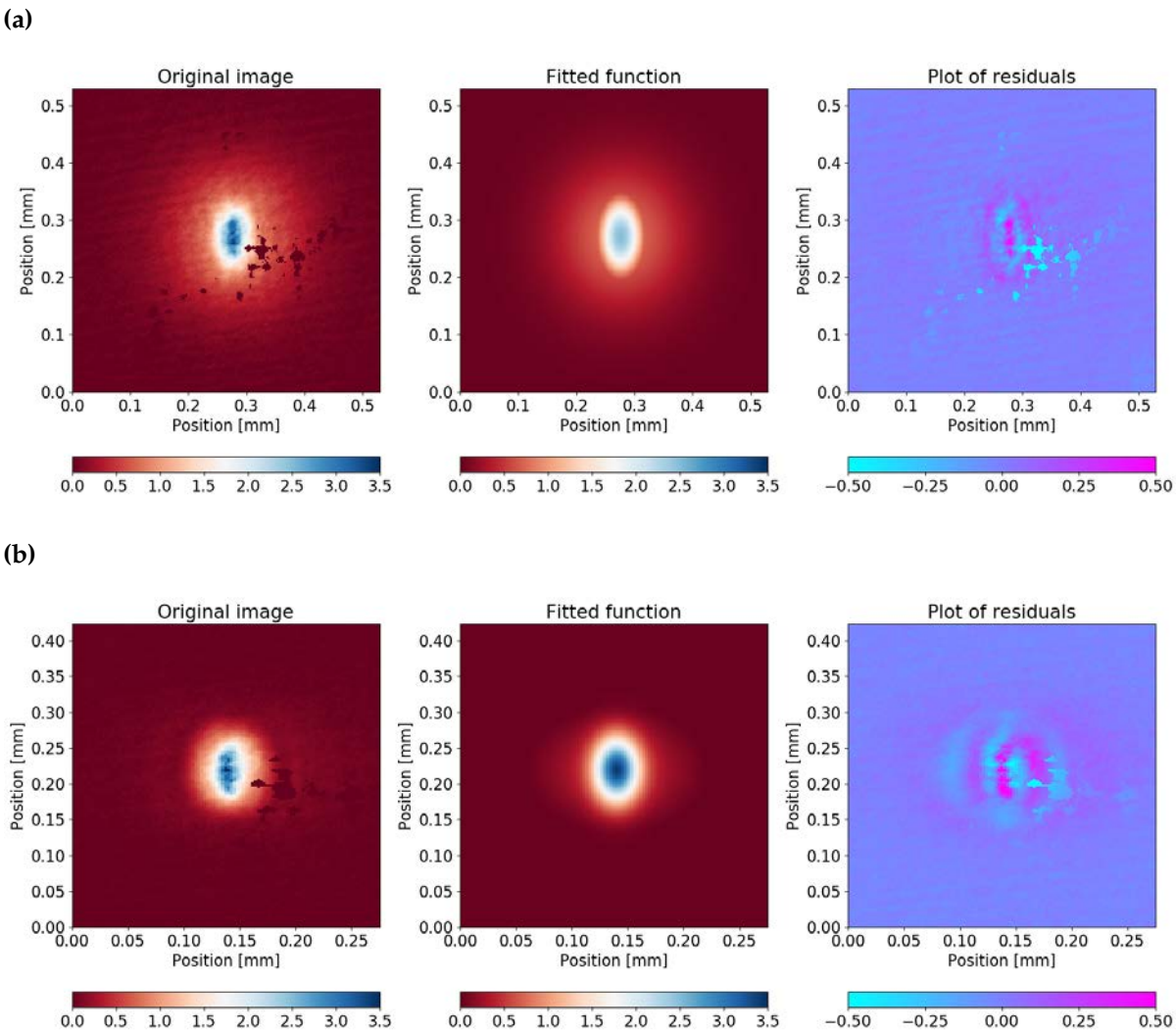

FIGURE 7.11: Absorption images and 2D fits to the optical density profiles at the beginning (a) and at the end (b) of BEC formation. The fitting function is a sum of the Thomas-Fermi distribution and a Gaussian [167]. The color bars are given in units of optical density. Notice the broad pedestal of thermal atoms at the beginning of BEC formation.

eqs. 2.101 and 2.115, and calculated according to $f_{\mathrm{BEC}} = \frac{N_{\mathrm{BEC}}}{N_{\mathrm{BEC}}+N_{\mathrm{Bose}}}$ and $f_{\mathrm{Bose}} = \frac{N_{\mathrm{Bose}}}{N_{\mathrm{BEC}}+N_{\mathrm{Bose}}}$, where f stands for "fraction" and "Bose" has again the meaning of Bose-enhanced thermal fraction[10]. The result of this calculation is shown in Fig. 7.10. We will note as a remark here that given $2.9\,\mathrm{W}$ of IR Beam 0 power and $75\,\mathrm{mW}$ of IR Beam 1 power, which is close to the maximum BEC fraction based on Fig. 7.10, 250000 atoms in the BEC, as shown later in Fig. 7.14, and the crossed ODT with beams of $70\,\mu\mathrm{m}$ waist, we expect the Thomas-Fermi radius to be approximately $27\,\mu\mathrm{m}$ in the horizontal direction across IR Beam 1, and approximately $4\,\mu\mathrm{m}$ in the vertical direction, the calculation being based on Ref. [13][11]. The length of the cloud in the vertical direction cannot actually be resolved with our imaging system (in the sense that the length of the object projected onto a single pixel is about the same as the Thomas-Fermi radius in the vertical direction), but its expansion will be more rapid in a series of TOF images and will thus lead to the observation of the inversion of aspect radio (see the next subsection).

A more recent analysis suggests that one cannot ignore the interactions: the BEC has a higher density than the thermal cloud, and the repulsive atom-atom interaction pushes thermal atoms out of the BEC area [179]. Consequently, we can fit the center peak of the cloud absorption image with a pure 2D Thomas-Fermi profile, and assume that all atoms in that peak are BEC; we then get the BEC fraction by integrating the entire optical density in the image and comparing it to the integral under the Thomas-Fermi peak [179]. This is another extreme approximation because in reality there will be some thermal atoms in the central region after the time of flight, but if it is acceptable for ^{87}Rb, with a scattering length of about $100a_0$ [180], then it is even better for ^{84}Sr with a scattering length of $124a_0$ [37] and thus stronger atom-atom repulsion. The reasoning is that the BEC has the highest density at the center of the trap, and so the thermal atoms will be mostly expelled from that region by repulsive atom-atom interaction. Fig. 7.12 shows the growth of BEC fraction with increasing amount of evaporation as evaluated by this second method and using 2D fits with only a Thomas-Fermi profile. This suggests that the evaporation procedure yields a 60% BEC fraction. The analysis with 2D fits also gives similar results for the BEC fraction as the one with 1D fits (Fig. 7.10), although the BEC fraction evaluated with 2D fits is approximately 10% higher. In these particular evaporation sequences we evidently did not optimize either the amount of evaporation, in which case the remaining thermal fraction is relatively high, or the holding time after evaporation, in which case heating causes atoms to enter the thermal fraction; otherwise, the BEC fraction could have been even higher.

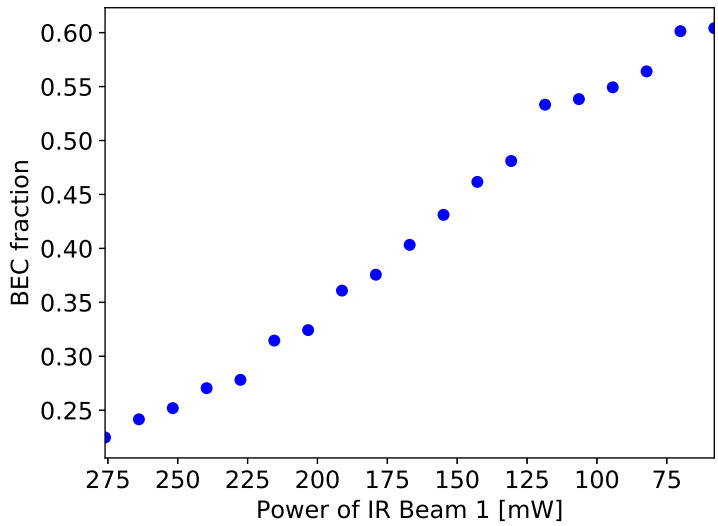

FIGURE 7.12: BEC fraction at different evaporation endpoints, as determined by fitting a pure 2D Thomas-Fermi profile to the center peak and dividing by the total integrated optical density of the cloud [179].

7.5.2 Inversion of aspect ratio

One of the clearest ways to show the existence of a BEC in a system is the inversion of the cloud aspect ratio in time of flight. This was already noticed by the authors of the first BEC papers [3, 8]. The theoretical description of this phenomenon is given in review papers [11, 13] and books [182, 175]. The main idea is that time-of-flight expansion converts the momentum of a given atom to position in an image. Since for a thermal gas, the momentum distribution is isotropic in momenta, the absorption image after a sufficiently long time of flight will be circular[12], no matter what the original trap shape was. On the other hand, for a BEC in a trap in the Thomas-Fermi limit, the kinetic energy term in the Hamiltonian can be neglected in comparison to the mean-field potential energy due to atom-atom interactions [11]. The counterbalancing of that mean-field energy by the harmonic potential confinement creates the Thomas-Fermi density profile. However when the confinement is removed, the atom-atom repulsion gets converted to kinetic energy, and in particular, the gradient of the mean-field potential acts as a repulsive force. Since that gradient in the direction of the tighter confinement is larger, the atoms will accelerate more and spread faster in that direction. This is how the shorter, and thus tighter, axis of the

[10]We use optical density for this evaluation rather than real atom density. The outcome of plugging optical densities into eqs. 2.101 and 2.115 will be a quantity proportional to the atom number. However this is fine, as we are interested in ratios of atom numbers, so the proportionality factor drops out.

[11]The relevant expressions are the chemical potential μ, $\mu^{5/2} = \frac{15\hbar^2 M_{\mathrm{Sr}}^{1/2}}{2^{5/2}} N_0 \omega_{\mathrm{HO},x}\omega_{\mathrm{HO},y}\omega_{\mathrm{HO},z} a$, where N_0 is the total number of atoms in the BEC and a is the scattering length, and $\mu = \frac{1}{2} M_{\mathrm{Sr}} \omega_{\mathrm{HO},i} r_{i,\mathrm{TF}}^2$, where i stands for one of the Cartesian directions, and so then $r_{i,\mathrm{TF}}$ is the Thomas-Fermi radius measured in that direction [13]. Based on the measured data, the first equation can be solved for μ, and then the Thomas-Fermi radius can be calculated from that.

[12]To put it in a more general way, the distribution of atoms will be spherical in space, which results in a circular absorption image. See Section 2.6 for the basics of ultracold cloud absorption imaging.

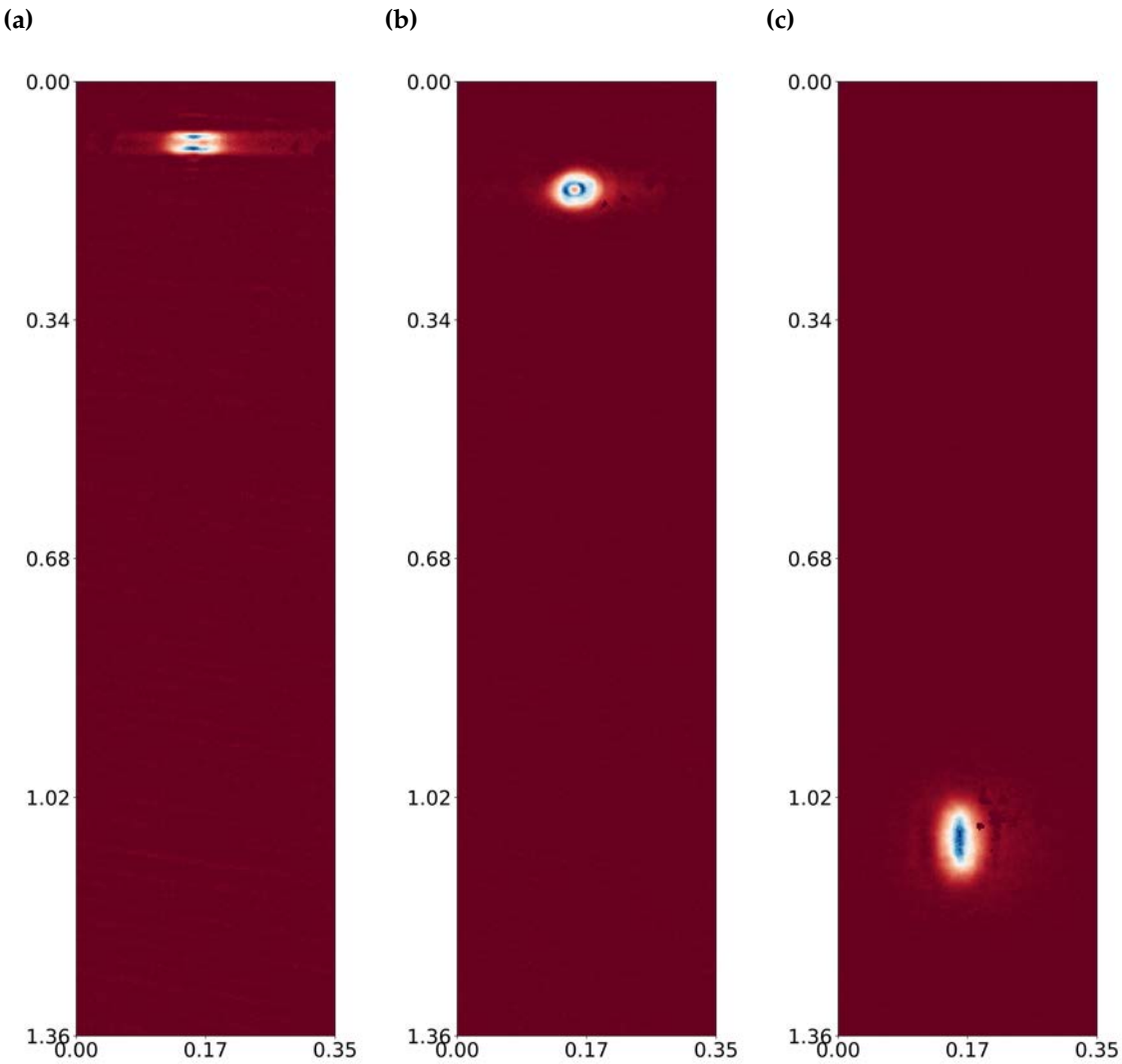

FIGURE 7.13: Inversion of aspect ratio in a BEC after ODT release. The captions under each subfigure refer to the time of flight: 1 ms (a), 4 ms (b), 15 ms (c). The axes are labeled in units of mm. The distortions in the images corresponding to short times of flight (a) and (b) are possibly due to scattering and lens aberrations, as described in Ref. [181]. Our imaging system was not optimized for *in situ* or short TOF images of a BEC, when the density is high; most of the imaging was done after a longer TOF, after the gas had expanded.

original cloud becomes longer than the original long axis in the course of the time of flight, and that is known as the *inversion of aspect ratio*[13] (see Section 2.6 for a discussion of BEC sample evolution after TOF). An experimental demonstration of this in our experiment is shown in Fig. 7.13, and this is a telltale sign of a BEC [3, 8].

[13]"Aspect ratio" is a fancy way of expressing the ratio between the length and the radius of a cylindrically-symmetric object.

7.5.3 Dipole trap loading and BEC lifetime

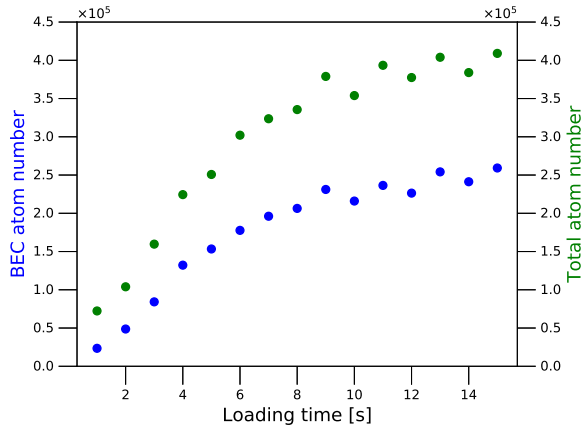

FIGURE 7.14: Final BEC atom number (blue) and total atom number (green) shown for different atom loading times.

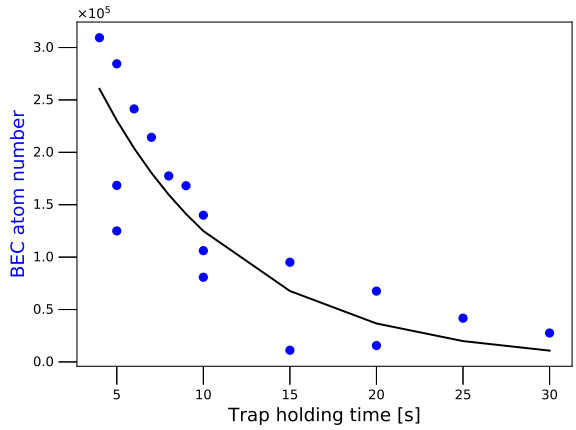

FIGURE 7.15: BEC atom number evolution with holding time in the dipole trap. Black line is an exponential fit.

Two other important measurements to do in a new quantum gas machine are BEC growth as a function of loading time and BEC lifetime. Figs. 7.14 and 7.15 show their results, where the atom number has been determined using the pure TF peak fits as described at the end of Subsection 7.5.1. The measured BEC lifetime, based on the exponential fit in Fig. 7.15, is 8 s. We also notice that the loaded atom number saturates at 10 s. This possibly happens due to background gas collisions in vacuum, or due to loss processes in the magnetic reservoir (see Section 7.1 for magnetic reservoir description), or else due to saturation of dipole trap loading from the red MOT.

7.5.4 Dipole trap frequency measurement

A BEC is also a useful and reliable tool for characterizing the harmonic potential in which atoms are trapped, be it a magnetic trap like in the early years of quantum-degenerate gases or in work with metastable He*, or an ODT, like in many modern experiments. In fact, condensate oscillations inside traps were the subject of early fundamental studies of BECs and a testing ground for theoretical descriptions of quantum gases [183, 184, 102, 185, 186]. A rigorous theoretical derivation of condensate dynamics inside a trap requires the techniques of quantum many-body physics. However, the end results in the case of low-energy excitations in commonly-used harmonic traps are simple. For example, if the center-of-mass oscillations of the condensate are excited by some form of trap perturbation, the fundamental mode of these oscillations happens precisely at the trap frequency in each oscillation direction [186]. The center of mass dynamics of the cloud are effectively described by the second-order differential equation for a classical harmonic oscillator, with $\omega_{\mathrm{COM}} = \omega_{\mathrm{HO}}$, where "COM" stands for "center-of-mass"; ω_{HO} is discussed in Section 2.4. Consequently, a measurement of the BEC oscillation frequency

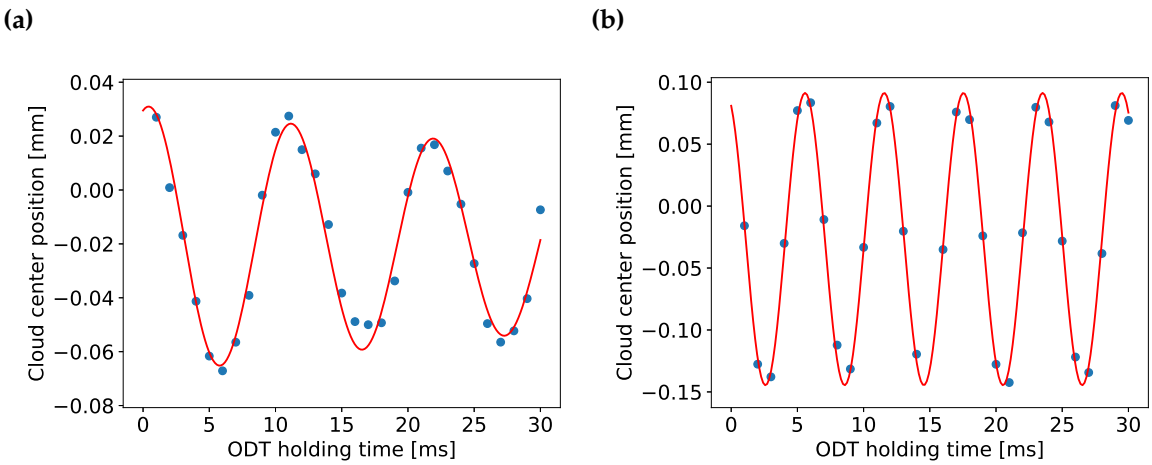

FIGURE 7.16: Examples of ODT trap frequency measurements. The blue dots correspond to the vertical position of the center of the cloud, as fitted with a 2D Gaussian in raw absorption images, and the red line is a fit with a damped sinusoid (a) and a pure sinusoid (b). Subfigure (a) corresponds to $310\,\mathrm{mW}$ in IR Beam 0 and $306\,\mathrm{mW}$ in IR Beam 1, and Subfigure (b) corresponds to $1.52\,\mathrm{W}$ in IR Beam 0 and $306\,\mathrm{mW}$ in IR Beam 1.

immediately yields the trap frequency, which is the single parameter that characterizes a harmonic trap[14].

The easiest BEC center-of-mass oscillation to excite in our case is the vertical one; it can be excited directly by gravity. The horizontal ones require some horizontal force on the atoms, which is difficult for bosonic Sr as the $^1S_0$ ground state is nonmagnetic, and so the horizontal force cannot be caused by a magnetic field ramp, for example. We excited vertical oscillations by suddenly (within microseconds) switching one of the ODT beams to a low power, which makes the trap weaker, waiting for $1\,\mathrm{ms}$ so that the BEC can sag downwards by gravity, and then suddenly switching that ODT beam back to the original power, which causes an upward force on the cloud towards the original equilibrium position[15]. We finally let the cloud evolve in the ODT for a variable amount of time (we will call this "holding time"), after which the trap was abruptly switched off, and the atoms were imaged after a fixed TOF. In this way, the linear momentum in the vertical direction at the point when the ODT is switched off translates into the vertical position of the cloud because no forces other than gravity are acting during the TOF. Finding the center position of the cloud in a series of images and then fitting it as a function of holding time yields the trap oscillation period. The sudden up-and-down kick with which oscillations are excited is the driving term in the second-order differential equation describing the damped driven harmonic oscillator. Such a driving term consists of many frequency components in the Fourier domain, but mathematical results suggest the oscillations will persist only at the mode frequency, meaning the harmonic oscillator frequency, the non-resonant frequencies being

[14]Of course a realistic optical or magnetic trap is not exactly harmonic, so the actual functional form of the potential is necessary for its full characterization. However, if we assume that the gas is cold enough to occupy only the deep part of the potential, then the trap frequencies in the three cartesian directions fully describe a given trap.

[15]Fast control of beam power is done by fast adjustments of the RF drive power to an AOM.

quickly damped as transients. This reasoning justifies the use of such a sudden excitation to measure the mode frequency.

Example results of trap frequency measurements are presented in Fig. 7.16, and such measurements can also be used to calibrate the ODT beam waist. Under the assumption of circularly-symmetric Gaussian TEM00 beams, this only requires the knowledge of the total power, which is easy to measure. The two parts of Fig. 7.16 show the different trap frequencies that result from varying ODT beam powers. The cloud center position data are extracted by fitting a 2D Gaussian function to the BEC optical density image. Even though an appropriate fit to a BEC image would be a sum of a Thomas-Fermi distribution and a Bose-enhanced thermal fraction, we choose to use a Gaussian for the sake of simplicity: any approximation that adequately captures the cloud center is already sufficient here, regardless of the validity of the underlying model. The fit of the BEC center-of-mass position as a function of holding time is then done either with a damped sinusoid, like in Fig. 7.16 (a), or with a pure sinusoid, like in Fig. 7.16 (b). From this result we note that the weaker ODT appears to have more damping than a stiffer one. In the particular case of Fig. 7.16, the measured trap frequencies are $93.1(7)\,\mathrm{Hz}$ in subfigure (a), and $167.2(3)\,\mathrm{Hz}$ in subfigure (b). As the powers in both ODT beams are known, and the assumption of circular Gaussian beams should hold[16], Eq. (2.63) can be used to write down a system of algebraic equations and solve for the beam waists. We thus obtain

$$2\pi \times 93.1\,\mathrm{Hz} = \sqrt{\frac{4}{M_{^{84}\mathrm{Sr}}}\alpha^{1064\,\mathrm{nm}}_{^1S_0} Z_0 \left(\frac{0.310\,\mathrm{W}}{\pi w^4_{\text{IR Beam 0}}} + \frac{0.306\,\mathrm{W}}{\pi w^4_{\text{IR Beam 1}}}\right)}, \tag{7.7}$$

$$2\pi \times 167.2\,\mathrm{Hz} = \sqrt{\frac{4}{M_{^{84}\mathrm{Sr}}}\alpha^{1064\,\mathrm{nm}}_{^1S_0} Z_0 \left(\frac{1.52\,\mathrm{W}}{\pi w^4_{\text{IR Beam 0}}} + \frac{0.306\,\mathrm{W}}{\pi w^4_{\text{IR Beam 1}}}\right)}. \tag{7.8}$$

From these particular values we obtain $w_{\text{IR Beam 0}} = 67\,\mu\mathrm{m}$ and $w_{\text{IR Beam 1}} = 72\,\mu\mathrm{m}$. However, using other pairs of IR beam powers and measured trap frequencies, we arrive at the values of w that have a spread of about $10\,\mu\mathrm{m}$. Therefore, this particular measurement of the beam waists is only an estimate. If a more reliable value is required, it should be measured by systematically taking data points at multiple values of both beam powers, and then fitting to obtain w. In addition, taking gravitational sagging into account in the model should also improve the accuracy.

[16] These beams are delivered to the vacuum chamber through single-mode polarization-maintaining optical fibers, collimators, and only spherical optics.

Chapter 8

The frequency of the ultranarrow $^1S_0$ - $^3P_2$ transition in ^{87}Sr

This chapter has been published as Phys. Rev. A **99**, 052503 (2019).

8.1 Introduction

Atoms with two valence electrons, such as the alkaline-earth metals or ytterbium, possess ultra-narrow intercombination transitions from their singlet ground state to metastable triplet states. The $^1S_0$ - $^3P_0$ transition, which connects two states that are free of electronic magnetic moment, is used as frequency reference in optical atomic clocks [1] and is of interest for quantum simulation [187, 188, 189, 190, 191], computation [30, 192, 193], and gravitational wave detection [194, 195, 196]. The $^1S_0$ - $^3P_2$ transition is equally narrow [18], but it connects the ground state to an excited state with electronic magnetic moment. This property has enabled high-resolution imaging of an Yb quantum gas in a magnetic field gradient [197, 198], a method that could also provide selective access to qubits in a quantum computer [30, 192]. Isotopes with nuclear spin exhibit hyperfine structure in the $^3P_2$ state, which will make it possible to induce nuclear spin state specific ac Stark shifts and Raman couplings using the $^1S_0$ - $^3P_2$ transition. This property might allow the creation of artificial gauge fields that are significantly less hampered by off-resonant scattering of photons or collisions between metastable state atoms compared to schemes exploiting broader transitions [199, 200, 201, 202, 203] or using metastable atoms [204, 190, 188]. Ultracold mixtures containing $^3P_2$ atoms have been obtained from quantum gases of ground state atoms by excitation on the $^1S_0$ - $^3P_2$ transition, leading to the discovery of Feshbach resonances between Yb $^1S_0$ and $^3P_2$ atoms [38]. These resonances are interesting for quantum information processing [30, 192, 193], are predicted to show signatures of quantum chaos [205] and have been exploited to form Feshbach molecules [206, 207]. Also mixtures of ^{3}P$_2$ Yb with Li have been created [208, 209] and their collisional stability investigated [210, 211, 212, 213, 214]. The $^1S_0$ - $^3P_2$ transition might also be useful to create quantum gases with quadrupole interactions [215, 216, 217, 218, 219].

Many of these applications require quantum degenerate gases and so far three two-valence-electron elements have been cooled to quantum degeneracy: Yb [26], Ca [25], and Sr [167]. The frequency of the $^1S_0$ - $^3P_2$ transition is only well known for Yb. Strontium has properties that

significantly distinguish it from Yb, offering different opportunities. It enables higher phase space densities directly by laser cooling, which makes it possible to create quantum gases with large atom number or with high repetition rate [161]. Its fermionic isotope ^{87}Sr has a nuclear spin of 9/2, which should enable better Pomeranchuck cooling [220, 221] or larger synthetic dimensions [34]. In order to combine these favorable properties with the possibilities offered by the $^1S_0$ - $^3P_2$ transition, the frequency of this transition needs to be determined to at least the MHz level.

In this article we report the measurement of the ultra-narrow ^{87}Sr $^1S_0$ - $^3P_2$ transition by direct optical excitation. We perform loss spectroscopy of an ultracold strontium sample and determine the resonance frequency by comparison to four spectral lines of molecular iodine, which serves as a natural and documented reference. The iodine lines are identified by comparing a gigahertz-wide iodine spectrum around the Sr lines with the spectra calculated by the IODINESPEC5 software [222]. The accuracy of the measurement is limited by the uncertainty in iodine transition frequencies, whereas the precision is limited by frequency drifts of an optical resonator used for spectroscopy laser stabilization. The relative frequency between the Sr transition and specific iodine lines is obtained with an accuracy of $0.5\,\mathrm{MHz}$ and the absolute frequency is limited by the iodine line accuracy of $30\,\mathrm{MHz}$. These measurements open the door to using the Sr $^1S_0$ - $^3P_2$ transition for important applications, such as the creation of artificial gauge fields or quantum computation.

This article has the following structure: Sec. 8.2 describes the spectroscopy laser system, the iodine spectroscopy setup, and Sr sample preparation; Sec. 8.3 introduces relevant Sr transitions, presents initial coarse and final precise determination of the $^1S_0$ - $^3P_2$ transition frequency and analyzes the measurement error. Conclusions are given in Sec. 8.4.

8.2 Experimental details

8.2.1 $^1S_0$ - $^3P_2$ spectroscopy laser setup

Light for the spectroscopy of Sr and iodine is produced by an external cavity diode laser (ECDL; wavelength: $671\,\mathrm{nm}$; power: $24\,\mathrm{mW}$; diode: Toptica LD-0670-0035-AR-1), see Fig. 8.1. The ECDL is locked to an optical resonator by the Pound-Drever-Hall (PDH) method [158]. The resonator uses a Zerodur spacer, is length-tunable by two piezos that compensate each other's thermal expansion [37], and is kept under vacuum, with the vacuum chamber placed inside a thermally insulating box. A frequency shift of $550\,\mathrm{MHz}$ to $850\,\mathrm{MHz}$ is introduced by an acousto-optic modulator (AOM) between the ECDL and the light used for locking. Spectroscopy scans are performed by slowly varying the AOM frequency so that the lock follows. The feedback loop uses a fast proportional-integral-differential (PID) controller (Toptica FALC 110), providing feedback of $1.9\,\mathrm{MHz}$ bandwidth to the ECDL current and $10\,\mathrm{kHz}$ bandwidth to the ECDL grating. Based on the error signal, we estimate the laser linewidth to be at most $85\,\mathrm{kHz}$. The light is sent through polarization-maintaining single-mode optical fibers to the Sr sample and to the iodine spectroscopy setup. The absolute frequency of the spectroscopy laser can be obtained with

a wavemeter (Toptica HighFinesse WSU-30, accuracy of 30 MHz) calibrated to the frequency of the 7.4 kHz-wide $^1S_0$ - $^3P_1$ transition of ^{88}Sr, known to within 10 kHz [223]. The calibration laser's absolute frequency is determined by spectroscopy of a Sr Bose-Einstein condensate to better than 50 kHz and its frequency stability is better than 10 kHz, as verified by successful operation of a $^1S_0$ - $^3P_1$ line magneto-optical trap (MOT). The wavemeter calibration is done each day immediately before the data collection runs using the designated calibration port of the wavemeter.

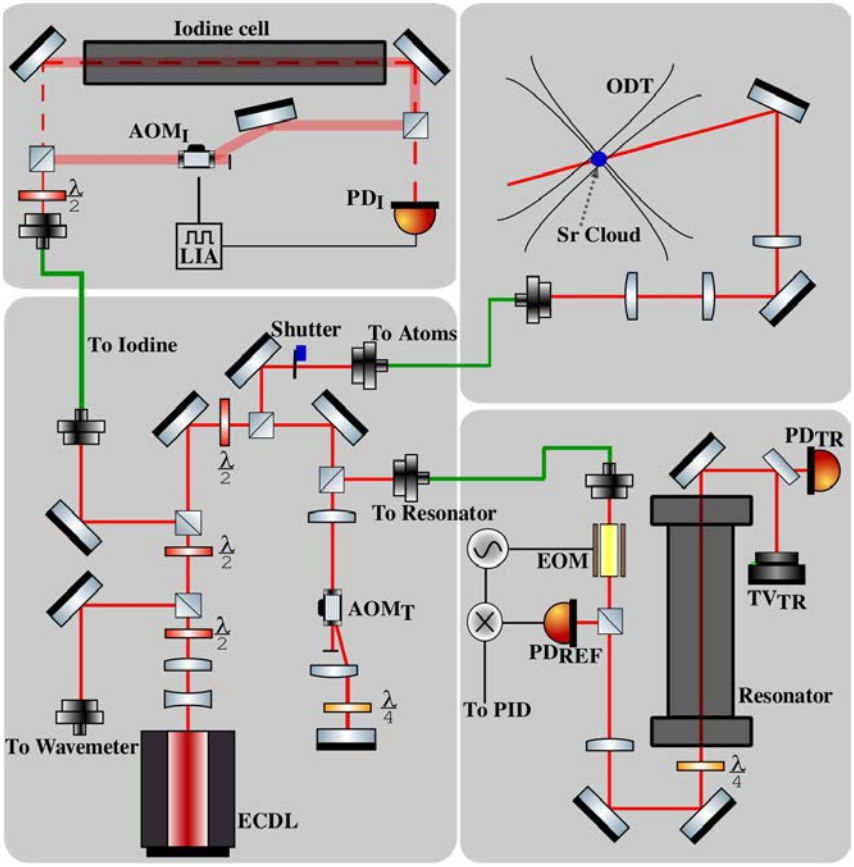

FIGURE 8.1: Scheme of the spectroscopy setup. The light of an extended cavity diode laser (ECDL) is distributed to a wavemeter, an optical resonator, an iodine spectroscopy setup, and Sr samples in an optical dipole trap (ODT). The laser frequency is stabilized to a mode of an optical resonator. Acousto-optic modulator AOM$_T$ introduces a controlled offset between the laser light and the resonator mode and is used to perform spectroscopy scans. To lock the light to the resonator the Pound-Drever-Hall method is used, for which an electro-optic modulator (EOM) creates sidebands on the light sent to the resonator and photodiode PD$_{REF}$ measures the light intensity reflected from it. The light transmitted through the resonator is analyzed by TV camera TV$_{TR}$ and photodiode PD$_{TR}$. The laser frequency can be referenced to iodine lines using the iodine spectroscopy setup, consisting of an iodine vapor cell, AOM$_I$, PD$_I$, and a lock-in amplifier (LIA).

8.2.2 Iodine spectroscopy setup

Spectra of iodine molecule vapor (natural sample, essentially 100% $^{127}I_2$ [136]) contained in a heated quartz cell are recorded using Doppler-free saturated absorption spectroscopy [224, 225]. We will now briefly describe the I_2 spectroscopy setup, see Fig 8.1. The quartz cell is $60\,\mathrm{cm}$ long and kept at approximately $530\,^\circ\mathrm{C}$ (not stabilized by feedback) in order to populate the higher vibrational levels of the iodine molecule [225]. A cold finger, stabilized at $20.0(3)\,^\circ\mathrm{C}$, is used to set the iodine partial pressure. The collimated spectroscopy beam entering the setup (waist $0.7\,\mathrm{mm}$, power $5\,\mathrm{mW}$) is split into a pump and a probe beam. The probe beam (power $0.5\,\mathrm{mW}$) is sent through the cell onto a photodiode that records the spectroscopy signal. The pump beam is frequency shifted by acousto-optic modulator $\mathrm{AOM_I}$, after which it has approximately $3\,\mathrm{mW}$ of power, and gets sent through the iodine cell in a counterpropagating manner with respect to the probe[1]. We enhance the weak Doppler-free signal by lock-in detection. We use $\mathrm{AOM_I}$ to chop the pump beam at $50\,\mathrm{kHz}$ (square wave) and we demodulate the detected probe signal at that frequency on a lock-in amplifier (EG & G Instruments Model 7265) using a time constant of $100\,\mathrm{ms}$. A few things are worth mentioning about this approach: first of all, the lock-in method is necessary, because the bare Lamb dips in the Doppler spectrum are too weak to be seen directly with the available power; secondly, the method is quite forgiving in terms of the chopping frequency, and in particular, the chopping frequency can be increased if one wants to reduce the time constant of the lock-in for faster scans, at the expense of signal-to-noise[2]; thirdly, the method is forgiving to slight misalignment in the overlap of the pump and probe beams, imperfect collimation of the beams, and slight power fluctuations of pump and probe.

8.2.3 Strontium sample preparation and spectroscopy principle

Spectroscopy of the Sr $^1S_0$ - $^3P_2$ transition is done on an ultracold cloud of ^{87}Sr in an equal mixture of all nuclear spin states contained in an optical dipole trap (ODT). The ODT consists of two horizontally propagating, linearly-polarized $1064\,\mathrm{nm}$ beams crossing at right angles and having waists of approximately $70\,\mu\mathrm{m}$ and $60\,\mu\mathrm{m}$ and powers of $2.2\,\mathrm{W}$ and $1.2\,\mathrm{W}$; the beams have a $160\,\mathrm{MHz}$ frequency difference in order to avoid mutual interference. To prepare the sample, a magneto-optical trap is loaded from a Zeeman-slowed atomic beam and then transferred into the ODT using the techniques described in Ref. [161]. We obtain a cloud of 2×10^5 Sr atoms at $730\,\mathrm{nK}$, which has a $1/e$-width of $\sim25\,\mu\mathrm{m}$ in the vertical direction and $\sim38\,\mu\mathrm{m}$ in the horizontal direction. We reduce the residual magnetic field to less than $30\,\mathrm{mG}$ at the location of the atomic cloud. The Sr spectroscopy beam is focused to a waist of about $60\,\mu\mathrm{m}$ at the sample position. Spectroscopy is performed time sequentially and measures frequency dependent loss of ground state atoms. A sample is prepared, exposed to spectroscopy light,

[1] $\mathrm{AOM_I}$ introduces the frequency shift of approximately $\nu_{\mathrm{AOM_I}}/2 = 35\,\mathrm{MHz}$ between the frequency of the iodine transition under study $\nu_{\mathrm{I_2}}$ and the frequency of the spectroscopy beam entering the setup ν_{spec}: $\nu_{\mathrm{I_2}} = \nu_{\mathrm{spec}} - \nu_{\mathrm{AOM_I}}/2$.

[2] The chopping frequency cannot be much larger than roughly one linewidth of the transition that one tries to observe [226].

which leads to atom loss, and the remaining ground-state atom number is detected by absorption imaging on the $^1S_0$ - $^1P_1$ transition.

8.3 Determination of the $^1S_0$ - $^3P_2$ transition frequency

Strontium levels and transitions that are relevant for this work are shown in Fig. 8.2. The transitions $^1S_0 - {}^3P_{0,2}$ are dipole forbidden in isotopes with pure spin-orbit (LS) coupling because of spin and total angular momentum selection rules [48]. A small dipole matrix element can be induced by mixing of the $^3P_{0,2}$ states with $^1P_1$ through the application of a magnetic field or through hyperfine coupling in the case of ^{87}Sr, the only stable Sr isotope with nuclear spin. For the bosonic ^{88}Sr the observation of the $^1S_0$ - $^3P_0$ clock transition has been reported with an external mixing field as low as 13 G [19, 227]. Most Sr optical lattice clocks use fermionic Sr in order to exploit hyperfine mixing to enable the clock transition.

In this work we use fermionic ^{87}Sr, which allows dipole transitions between $^1S_0$ $(F = 9/2)$ and $^3P_2$ $(F' = \{7/2, 9/2, 11/2\})$ with a linewidth of approximately $1\,\mathrm{mHz}$ by hyperfine mixing [18]. The transitions $^1S_0$ $(F = 9/2) - {}^3P_2$ $(F' = \{5/2, 13/2\})$ have $\Delta F = \pm 2$ and the ground and excited states have opposite parity, which makes them dipole forbidden. They are however still accessible as magnetic quadrupole transitions (M2) [228] and we observe the $^1S_0$ $(F = 9/2) - {}^3P_2$ $(F' = 5/2)$ transition.

We determine the $^1S_0$ - $^3P_2$ transition frequency in two steps. The first step, described in Sec. 8.3.1, determines the transition indirectly to within $\sim$100 MHz. This is sufficiently precise to find the transition with direct spectroscopy, see Sec. 8.3.2. In Sec. 8.3.3 we discuss the error of our measurement.

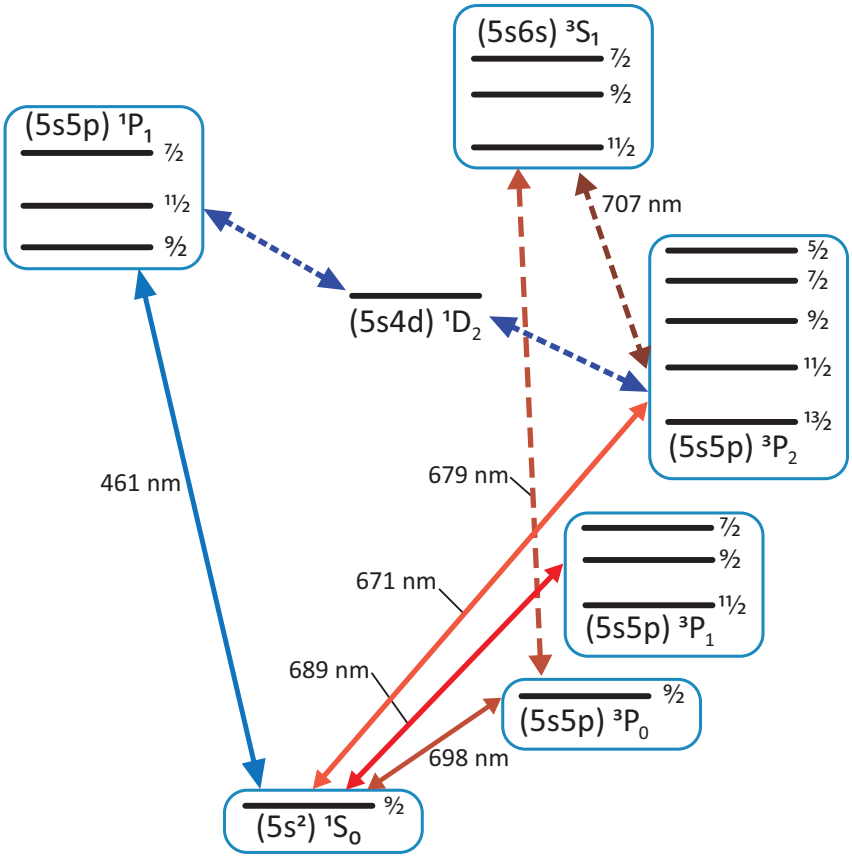

FIGURE 8.2: Level scheme of the low-lying electronic states of ^{87}Sr. The transitions at 461 nm and 689 nm are used for MOTs, the transitions at 679 nm and 707 nm are repump transitions, the one at 698 nm is the clock line, and the transition at 671 nm is the $^1S_0$ - $^3P_2$ line whose frequency we measure in this work. The hyperfine structure of the $^1D_2$ is neglected because it is irrelevant for this work.

8.3.1 Coarse, indirect determination

The $^1S_0$ - $^3P_2$ transition frequency has only been measured for the most abundant isotope ^{88}Sr with an accuracy of 120 MHz [229]. The ^{87}Sr $^1S_0$ - $^3P_2$ transition frequencies can be estimated by adding the ^{87}Sr $^3S_2$ hyperfine shifts, which have been determined by radiofrequency spectroscopy in hot Sr [230], and the isotope shift. Here we assume that the $^1S_0$ - $^3P_2$ isotope shift is the same as the measured $^1S_0$ - $^3P_0$ and $^1S_0$ - $^3P_1$ isotope shifts [231, 232, 233], which are both within 1 MHz of $f_{88} - f_{87} = 62$ MHz. We verify the estimated transition frequency by performing a simple, coarse and indirect frequency determination. We determine $f(^1S_0$ - $^3P_2)$ using conservation of energy: we measure $f(^3P_2$ - $^3S_1)$ and use the well-known transition frequencies $f(^1S_0$ - $^3P_0)$ and $f(^3P_0$ - $^3S_1)$ [234] to calculate $f(^1S_0$ - $^3P_2)$ (see Fig. 8.2). The $^3P_2$ - $^3S_1$ transition is dipole allowed, which makes it much broader and easier to find than the doubly forbidden millihertz-linewidth $^1S_0$ - $^3P_2$ transition. Similar schemes were used to determine the Sr $^1S_0$ - $^3P_0$ transition [234] and the Yb $^1S_0$ - $^3P_2$ transition [235].

To determine $f(^3P_2$ - $^3S_1)$ we use reservoir spectroscopy [236]. This technique relies on the fact that atoms in the $^1S_0$ - $^1P_1$ MOT cycle can decay through the $^1D_2$ state into the metastable

and magnetic $^3P_2$ state, the low field seeking m_F substates of which are captured in the magnetic quadrupole field of the MOT. These atoms can be pumped back into the MOT cycle with light on a transition from the $^3P_2$ state to some higher-lying state that has a high chance of decaying into the ground state. We use the $^3S_1$ state as the higher-lying state, from which atoms decay to the ground state through the short-lived $^3P_1$ state. The $^3P_2$ - $^3S_1$ transition corresponds to a repump laser operating around $707\,\mathrm{nm}$. Thus, when the repump laser is tuned to a resonance, the $^3P_2$ atoms from the magnetically trapped reservoir are quickly brought back into the $^1S_0$ - $^1P_1$ MOT cycle, rapidly increasing the number of ground-state atoms and causing a MOT fluorescence flash. There are nine repump resonances due to the number of hyperfine states in both $^3P_2$ and $^3S_1$, but we do not need to measure all of those transitions to determine $f(^3P_2$ - $^3S_1)$.

We observe three $^3P_2$ - $^3S_1$ repump resonances, which we can attribute to specific transitions between hyperfine states in the $^3P_2$ and $^3S_1$ manifolds using knowledge of the $^3P_2$ hyperfine structure [230], knowledge of the $^3S_1$ hyperfine structure [234], and selection rules. The absolute frequencies of these transitions are obtained with the wavemeter that is also part of the $^1S_0$ - $^3P_2$ spectroscopy setup. These measurements, combined with the known transition frequencies $f(^1S_0$ - $^3P_0)$ and $f(^3P_0$ - $^3S_1)$ [234], provides estimates of the individual transition frequencies $f[^1S_0\ (F=9/2) - {}^3P_2\ (F'=\{7/2, 9/2, 11/2\})]$. This determination has an accuracy of $\sim$100 MHz and confirms the estimated transition frequencies. Using this good starting point we now expect to find the transitions quickly in a direct spectroscopy search.

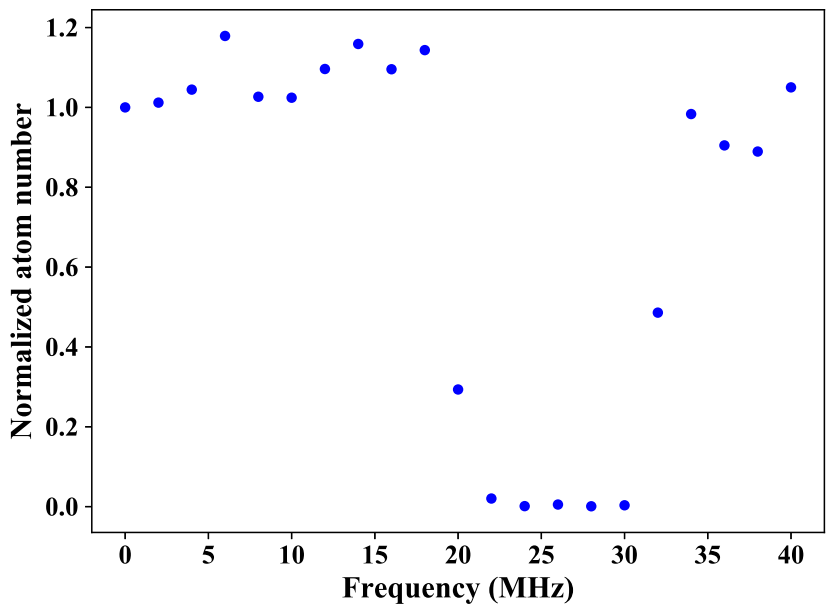

FIGURE 8.3: Spectrum of the $^1S_0\ (F=9/2) - {}^3P_2\ (F'=11/2)$ transition broadened by using a large Rabi frequency (spectroscopy laser power of $4.5\,\mathrm{mW}$). The zero of the frequency axis is chosen arbitrarily.

8.3.2 Precise, direct determination

We perform direct spectroscopy of the $^1S_0$ - $^3P_2$ transitions using Sr samples in an ODT. When the spectroscopy laser is tuned into resonance, ground-state atoms are excited to the metastable $^3P_2$ state. Atoms in this state are transparent to the $^1S_0$ - $^1P_1$ absorption imaging beam and furthermore likely lost by inelastic collisions [237]. To find a resonance we measure the fraction of $^1S_0$ atoms remaining in the ODT as a function of spectroscopy laser frequency, while keeping other parameters, such as illumination time and laser power, constant. During the first search for the transition we use the full power of the spectroscopy beam ($4.5\,\mathrm{mW}$). We repeatedly prepare Sr samples and use each to scan a $1\,\mathrm{MHz}$ frequency interval over $1\,\mathrm{s}$. An example for the resulting spectrum is shown in Fig. 8.3 and determines all $^1S_0$ - $^3P_2$ transitions to within $10\,\mathrm{MHz}$, using the known $^3P_2$ hyperfine splittings.

F'	Frequency [MHz]	FWHM linewidth [MHz]
$7/2$	$446\,648\,769(30)$	0.52(4)
$9/2$	$446\,647\,793(30)$	0.74(3)
$11/2$	$446\,646\,618(30)$	0.69(8)

TABLE 8.1: Frequencies and measured linewidths of the $^1S_0 - {}^3P_2$ transition to three different hyperfine states in the $^3P_2$ manifold. The frequencies are determined using a wavemeter, whereas the full-width half-maximum (FWHM) linewidths are obtained from Gaussian fits to the spectroscopy signals shown in Fig. 8.4.

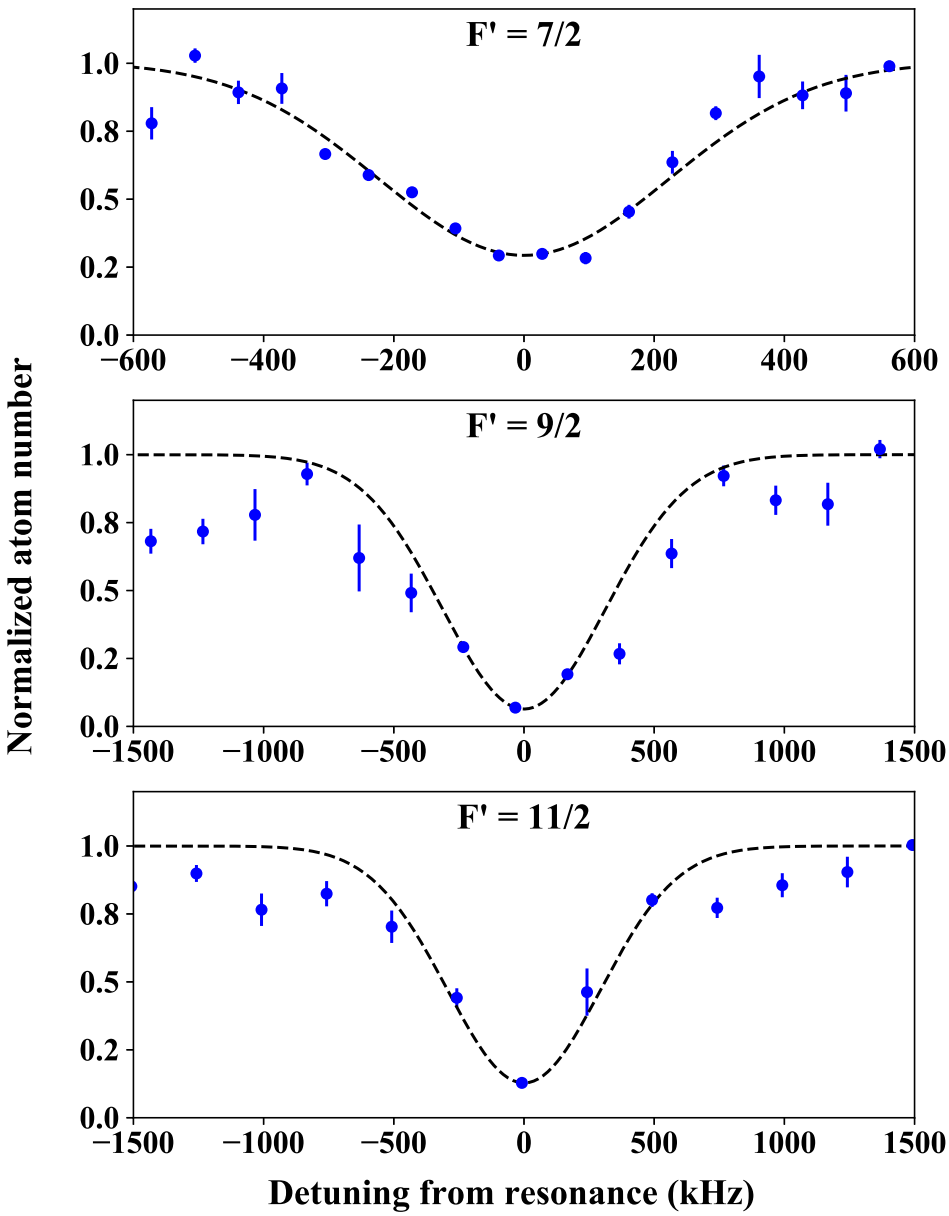

FIGURE 8.4: High-resolution spectra of the $^1S_0$ - $^3P_2$ ($F' = \{7/2, 9/2, 11/2\}$) transition in ^{87}Sr measured by atom loss spectroscopy in an ODT using low spectroscopy beam power ($0.45\,\mathrm{mW}$). The atom numbers are normalized to the ones far away from any spectroscopy signal. The error bars represent the standard error of five measurements per data point.

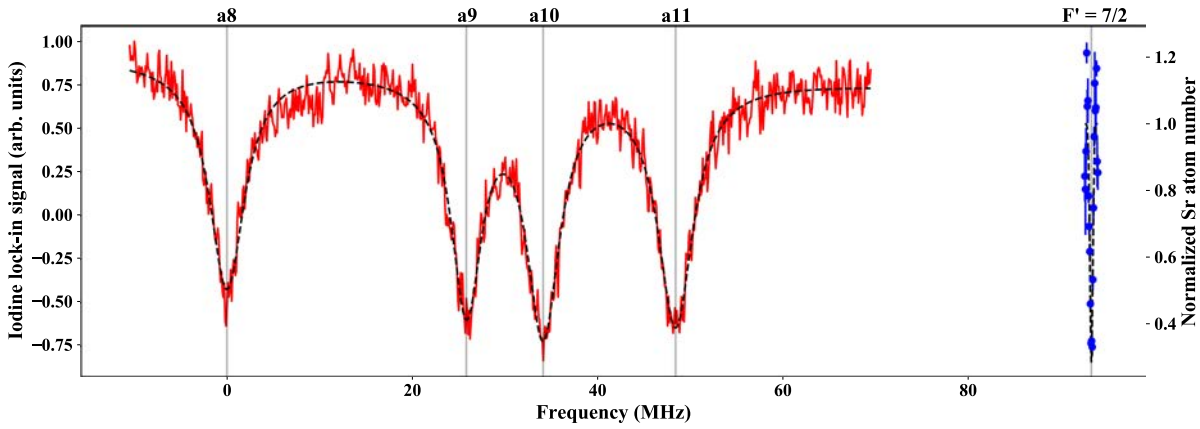

FIGURE 8.5: (Color online) Combined spectrum of the ^{87}Sr ^{1}S$_0$ − ^{3}P$_2$ (F′ = 7/2) line and iodine lines {a8, a9, a10, a11}. The red line is iodine data, the blue circles are ^{87}Sr data, the black dashed lines are the fits to the respective spectra (multiple Lorentzian for iodine and Gaussian for ^{87}Sr). The center of each fitted spectral line is marked with a vertical gray line and labeled on top. The center of the a8 line is chosen as the zero of the frequency axis.

In order to determine the transition frequency with more precision we zoom in on the detected broad spectroscopy signals by recording spectra with $0.45\,\mathrm{mW}$ of spectroscopy laser power and reduced frequency interval and illumination time per sample. The narrowest spectroscopy signals for $F' = \{7/2, 9/2, 11/2\}$ are shown in Fig. 8.4 together with Gaussian fits, the parameters of which are summarized in Table 8.1. The values of the transition frequencies measured with the wavemeter are also reported in Table 8.1, and the uncertainty is dominated by wavemeter inaccuracy.

Next we determine the frequency difference between four iodine transitions and the ^{87}Sr $^1S_0$ $(F = 9/2) - {}^3P_2$ $(F' = 7/2)$ transition. This allows us to determine the frequency of the Sr transition with the accuracy of the known iodine transition frequencies, which currently is the same as the accuracy of the wavemeter ($30\,\mathrm{MHz}$), but can be improved in the future with iodine spectroscopy alone [225]. More importantly the accuracy of the frequency difference ($0.5\,\mathrm{MHz}$) is much higher than the accuracy of the absolute frequency, which makes it possible to find the Sr transition with simple iodine spectroscopy and to lock the Sr laser to iodine lines.

The $F' = 7/2$ state is used for iodine comparison because it is within the spectroscopy AOM tuning range of the strong iodine transitions $(J' - J'' = 32 - 33)(\nu' - \nu'' = 9 - 9)$ {a8, a9, a10, a11}[3]. The frequencies corresponding to the other hyperfine states in the $^3P_2$ manifold can be found by using this frequency and the known $^3P_2$ hyperfine splittings [230]. Figure 8.5 presents an example of a recorded iodine spectrum (scan time 1.5 minutes), fitted with Lorentzians, combined with the Sr spectrum, fitted with a Gaussian. In order to estimate the drift of the spectroscopy laser, we record four iodine spectra within a 2.5 hour interval that encompasses the ^{87}Sr $^1S_0$ $(F = 9/2) - {}^3P_2$ $(F' = 7/2)$ frequency measurement. The maximum change of the relative frequency between the iodine laser and the iodine lines is $250\,\mathrm{kHz}$. Since the iodine line frequency is expected to change much less than that we attribute this frequency shift mainly to the lock of the spectroscopy laser to the reference cavity. Table 8.2 lists the fitted central frequency values of the iodine transitions, where each value is an averaged result from the fits to four measured spectra. Using the a8 frequency calculated by IODINESPEC5 we obtain $446\,648\,775(30)\,\mathrm{MHz}$ for the ^{87}Sr $^1S_0$ $(F = 9/2) - {}^3P_2$ $(F' = 7/2)$ transition frequency, which is consistent with the frequency determined by the wavemeter.

The frequency of the $^1S_0 - {}^3P_2$ $(F' = 5/2, 13/2)$ M2 transitions can be determined from the previous measurement and the $^3P_2$ hyperfine splittings. Guided by this calculation we observe the $^1S_0$ - $^3P_2$ $(F' = 5/2)$ transition by direct optical excitation. Since it is an M2 transition it is expected to be much weaker than the HFM-E1 lines, and we indeed must use about 10 times larger intensity and a 20 times longer illumination time to induce observable atom loss on this transition compared to the case of the dipole transitions. Fig. 8.6 shows a spectrum of this line recorded with a spectroscopy beam power of $4.5\,\mathrm{mW}$ and an illumination time of $10\,\mathrm{s}$.

Based on our measurement of the $^1S_0 - {}^3P_2$ transition and the previously reported results for the $^1S_0 - {}^3P_1$ and $^3P_1 - {}^3S_1$ transition frequencies and hyperfine splittings of all mentioned

[3]Here, J'' and ν'' denote the lower rotational and vibrational levels respectively, and J', ν' denote the upper level. The symbols {a8, a9, a10, a11} label the hyperfine states [222]. The common designation for these rovibrational transitions is P(33) (9-9).

Transition	frequency (MHz)
a8	0.00(3)
a9	25.88(3)
a10	34.17(5)
a11	48.39(4)
$^1S_0 - {}^3P_2$ $(F' = 7/2)$	93.27(25)

TABLE 8.2: Measured frequencies of the iodine transitions {a8, a9, a10, a11} within the manifold P(33) (9-9) and the $^1S_0 - {}^3P_2$ $(F' = 7/2)$ transition frequency. The frequencies are reported with respect to the measured frequency of the a8 transition. The iodine transition frequencies are given for our conditions of the iodine cell (see text) and are shifted by $-100(15)$ kHz with respect to iodine lines at zero pressure and temperature. The error of the Sr transition is dominated by drifts of the reference resonator.

states [234, 230], we can also give a more accurate value for the $^3P_2(F = 7/2) - {}^3S_1(F' = 7/2)$ repumping transition frequency, which evaluates to $423\,914\,969(30)$ MHz. The corresponding values involving any other hyperfine states can be easily calculated from the known hyperfine splittings [234, 230].

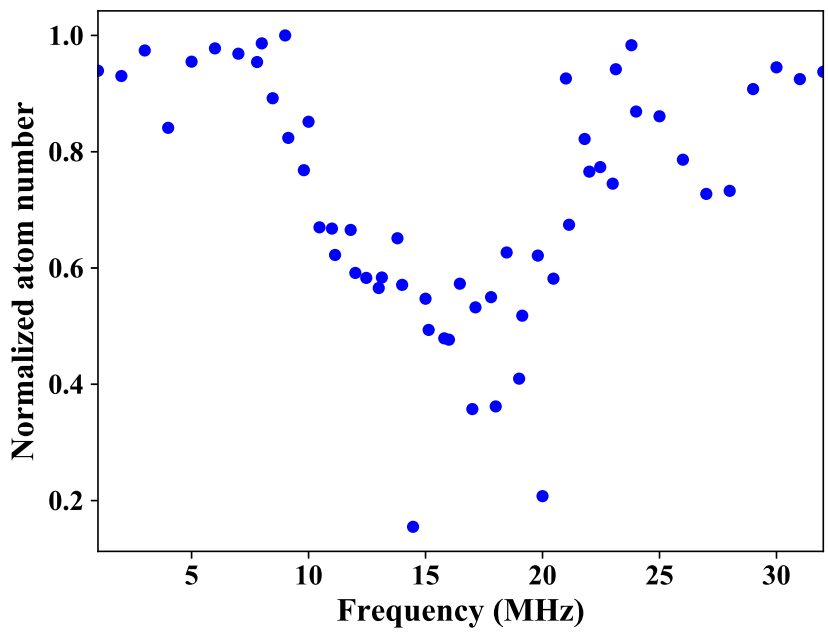

FIGURE 8.6: Spectrum of the $^1S_0$ $(F = 9/2) - {}^3P_2$ $(F' = 5/2)$ M2 transition with a spectroscopy beam power of $4.5\,\mathrm{mW}$. The zero of the frequency axis is chosen arbitrarily.

8.3.3 Error analysis

We measure absolute frequencies in two ways, using the wavemeter or using iodine lines as reference [222]. Both methods have an uncertainty of $30\,\mathrm{MHz}$, which dominates all other sources of error. We also determine the relative frequency between the Sr transitions and the iodine lines. The error in the relative frequency is much smaller than the absolute error and will be discussed in the following.

The error in the relative frequency measurement has statistical and systematic components. Statistical errors arise from the drifts of the Fabry-Perot resonator to which the laser is locked, from errors in the fits used to determine the center of spectral lines, and from iodine line shifts by iodine temperature and pressure changes[4] [238]. Systematic errors are the collisional shifts of the iodine lines, which effectively move our frequency reference point from its literature value [238], and the ac Stark shift of the Sr transitions by the dipole trap light.

The dominant contribution to the statistical error comes from changes of the cavity resonance to which the spectroscopy laser is locked while the measurements are performed. This error is estimated by recording iodine spectra several times before, during, and after the one-hour timespan during which the Sr spectra are recorded, and then analyzing the drift of the relative frequency between the cavity resonance and the iodine lines. We assume that the iodine lines do not change significantly over this timespan (the validity of that assumption will be analyzed below), therefore the drift is due to changes of the resonator frequency. The maximum drift we observe is $250\,\mathrm{kHz}$.

Errors also originate from pressure and temperature shifts of the iodine lines. Compared to a zero temperature and pressure gas the iodine lines are shifted by $\delta f_{I_2} = \alpha_S P_{\mathrm{I}_2} T^{-7/10}$ at pressure P and temperature T, where $\alpha_S = -400(60)\,\mathrm{kHz\,K^{7/10}/Pa}$ is an empirically determined proportionality constant [238]. P_{I_2} is set by the cold finger temperature, and the relevant iodine vapor pressure equation is given in Ref. [225], whereas T is set by the iodine cell body temperature. Statistical errors arise from uncertainties in P and T. The cold finger temperature uncertainty of $0.3\,\mathrm{K}$ translates into a pressure uncertainty below $1\,\mathrm{Pa}$. The body temperature has an uncertainty below $20\,\mathrm{K}$. These uncertainties lead to a statistical error of $3\,\mathrm{kHz}$ in the iodine line frequency. The systematic shift of the iodine lines is $\delta f_{I_2} = -100(15)\,\mathrm{kHz}$, where the dominant contribution to the error arises from uncertainties in α_S. The values reported in Table 8.2 are given in presence of this shift.

Another source of error is the light shift induced on the Sr transition by the ODT. We obtain an upper limit for this shift by recording spectra using ODT depths up to a factor two higher or lower than the depth used usually. We do not observe a correlation of the transition frequency with the ODT depth, which we attribute to drifts of the reference resonator during the few hours that we spent to record this data. We conclude that the light shifts are at most as large as the resonator drifts of $250\,\mathrm{kHz}$, which is consistent with a calculation using the Sr transition strengths of [78]. Adding statistical and systematic errors we arrive at a total error of $0.5\,\mathrm{MHz}$.

[4] The AOM frequency uncertainty is negligible compared to other error sources as it is driven by a direct digital synthesizer synchronized to a rubidium atomic clock.

The Sr spectroscopy lines are broadened by ODT light shifts, the Doppler effect, Zeeman shifts of the unresolved m_F levels, and collisional effects.

8.4 Conclusion

We have determined the frequency of the ^{87}Sr $^1S_0 - {}^3P_2$ transition with an accuracy of $30\,\mathrm{MHz}$ and the frequency difference of that transition to molecular iodine lines with an accuracy of $0.5\,\mathrm{MHz}$. This knowledge enables the use of simple iodine spectroscopy to find the ^{87}Sr $^1S_0 - {}^3P_2$ transition frequency or to lock a Sr $^1S_0 - {}^3P_2$ laser. Our work prepares the use of this Sr transition for applications, such as quantum simulation or computation.

8.5 Acknowledgements

We thank Jan Matthijssen for technical assistance in the early stages of the project, H. Knöckel, B. Bodermann, and E. Tiemann for the software IODINESPEC5 [222], R. Gerritsma and his group (University of Amsterdam) for giving us access to their Toptica HighFinesse WSU-30 wavemeter, and W. Ubachs and his group (VU University, Amsterdam) for providing us with the iodine cell for spectroscopy and R. Spreeuw for discussions. This project has received funding from the European Research Council (ERC) under the European Union's Seventh Framework Programme (FP7/2007-2013) (Grant agreement No. 615117 QuantStro). We thank the Netherlands Organisation for Scientific Research (NWO) for funding through Vici Grant No. 680-47-619 and Gravitation Grant No. 024.003.037, Quantum Software Consortium. G. S. thanks the European Commission for Marie Skłodowska-Curie Grant SYMULGAS, No. 661171. C.-C. C. thanks the Ministry of Education of the Republic of China (Taiwan) for a MOE Technologies Incubation Scholarship.

Chapter 9

Outlook

The new machine for producing and studying quantum gases of strontium is now ready and tested, and the first scientific result, the measurement of the $^1S_0$ - $^3P_2$ transition frequency in ^{87}Sr, has been obtained. We can look into the future and consider what further scientific questions can be investigated with this tool. There are multiple interesting directions: strontium provides many opportunities, as we saw in the introductory Section 1.1, and fortunately the machine is reconfigurable and future-proof even to the point of adding a new atomic species. Let us outline a few of these directions.

First of all, the microscope objective designed by Ivo Knottnerus [104] should make it possible to project a pattern of highly-focused beams, with expected sub-micron focus waists, onto the red MOT, and thus capture atoms in such tight optical dipole traps, which are known as *optical tweezers*. The big point here is that one can load single atoms into the tweezers [65]. The pattern of tweezers is generated either by imaging a spatial light modulator pattern onto the atoms[1], or by converting the deflection angles from an acousto-optic modulator or an acousto-optic deflector, into a different beam focus position. In both cases, the high resolution and thus the high focusing power of the microscope objective must be used. The tweezer approach in general gives a high degree of control over the number of atoms, the positions of these atoms, and the tweezers can be moved and merged. This research field has been developing for years and has achieved several important milestones, such as sideband-resolved cooling of a single atom to the tweezer ground state [239], producing nearly arbitrary three-dimensional patterns of single atoms [240], and creating a single molecule out of two individual atoms in a controlled manner [241]. However, the majority of the progress with optical tweezers has been achieved with alkali atoms. We can now learn how to use the tools developed with alkali atoms and adapt them to strontium, which provides unique opportunities due to its two-electron structure and the presence of metastable states and corresponding ultranarrow transitions (Section 1.1). This is an ongoing project in our team. In fact optical tweezers with strontium is a new territory, with the first publications appearing only in 2018 [113, 114][2]. There exists a very recent proposal for a quantum computation and quantum simulation scheme using alkaline-earth atoms in

[1]Note that if the objective can be used to image atoms onto the image plane, then it can be equivalently used to project the pattern that is already in the image plane onto the atoms. Such a pattern can be generated by a spatial light modulator.

[2]The first tweezers with ytterbium, another two-electron atom that is used for quantum gas experiments, have also been reported in 2018 [242].

tweezers [243]. One therefore does not expect a dearth of scientific opportunities when one has a system of optical tweezers with Sr. Furthermore, looking even further, one can think of exciting Sr atoms to Rydberg states inside the tweezers and making use of the very long range of Rydberg interactions to induce coupling between the atoms, even when the individual tweezers are separated by microns and tunneling processes are essentially completely non-existent; this is mentioned in Ref. [243] as well.

The introductory part of Chapter 8 mentions several other future directions that would directly benefit from Sr properties. The immediate ones in terms of the technology already largely present on the machine, and the ones that will open up further opportunities if implemented successfully, are the search for Feshbach resonances between the $^1S_0$ and $^3P_2$ states [38] and m_F-selective Raman coupling in the ground state hyperfine manifold by using the m_F substates of $^3P_2$ as the intermediate levels, which would be useful to create artificial gauge fields. These Raman coupling experiments will immediately use the results of the spectroscopy work described in Chapter 8 and will also provide an impetus to further develop the $671\,\mathrm{nm}$ laser system that was used in that work. In turn, predicting the implications of a successful observation of the Feshbach resonances with the excited state, or of the development of such Raman coupling, is difficult precisely because this opens up large research areas. Let us only mention that such a combination can lead to experimental observations of artificial gauge fields in the presence of interactions, which is one of the major goals in the field of ultracold atoms.

With the milestones that are required for a new quantum gas setup completed and the first measurement finished, the experiment is ready to keep exploring. The setup design is flexible enough to facilitate new developments. Having this in mind, we are justified to hope and expect that this new strontium experiment can make significant contributions to quantum simulation with ultracold atomic gases.

Samenvatting

In dit proefschrift worden het ontwerp en de realisatie van de nieuwe opstelling voor kwantumgassen van strontium gepresenteerd, samen met de eerste experimenten die gedaan zijn op deze opstelling, die is gebouwd tussen 2014-2017 aan de Universiteit van Amsterdam. Het resultaat is een flexibel apparaat, dat geschikt en handig is voor meerdere experimenten, inclusief enkele die niet voorzien waren bij het initiële ontwerpen van de opstelling.

De inleiding geeft een overzicht van de nuttige eigenschappen van strontium en van de belangrijkste onderdelen van een kwantumgas-apparaat in het algemeen, en het in dit proefschrift omgeschreven apparaat in het bijzonder. De belangrijkste reden waarom strontium een goede keuze is in dit soort experimenten zijn de twee aanwezige valentie-elektronen, die tot verschillende types optische overgangen leiden, namelijk dipool-toegestane overgangen, smalle dipool-verboden overgangen, en ultrasmalle dubbel verboden overgangen. Hierdoor is strontium een geschikt systeem voor laserkoeling, wat precisie-spectroscopie en atoomklok-experimenten mogelijk maakt en leidt tot de aanwezigheid van metastabiele toestanden, die nuttig kunnen zijn voor bijvoorbeeld kwantumgas-microscopie of twee-foton Raman-overgangen. Met het oog op al deze eigenschappen van strontium werd de opstelling voor verschillende toepassingen tegelijk ontworpen, daarom zijn er drie experimentele vacuümkamers aan elkaar geschakeld. De hoofdkamer is bedoeld voor de magnetooptische val (MOT) en voor verdampingskoeling tot een kwantumgas. Daarnaast zijn er twee zijkamers: één ervan is bedoeld voor de toekomstige kwantumgas-microscoop en de andere is een glas-cel voor experimenten die moeilijk of onmogelijk zijn in een metalen kamer.

In hoofdstuk 1 worden fundamentele theorieën uitgelegd die nodig zijn om de verschillende stappen van laserkoeling en de analyse van kwantum-ontaarde gassen te begrijpen. De belangrijkste vergelijkingen worden uitgelegd voor optische melasse, de Zeeman-afremmer, de magnetooptische val, ac-Stark-niveauverschuivingen in een optische dipoolval (ODT), en de verdampingskoeling. Uiteindelijk wordt ook de basis van het afbeelden van ultrakoude wolken met behulp van absorptie van licht uitgelegd. Het hoofdstuk eindigt met een herleiding van de formules die kunnen worden gebruikt voor het fitten van koude thermische wolken, wolken dichtbij het punt van Bose-Einstein condensatie en bijna pure Bose-Einstein condensaten. Met behulp van deze fits is het mogelijk om de eigenschappen zoals de dichtheid van het gas, de temperatuur of de fractie van een Bose-Einstein condensaat te evalueren.

In hoofdstuk 2 worden de relevante theorie en berekeningen gepresenteerd die van pas komen bij microscopie van strontium met een resolutie van enkele atomen en enkele roosterpunten in een optisch rooster waarin wisselwerkingen een belangrijke rol spelen. Deze techniek wordt kwantumgas-microscopie genoemd. De conclusie is dat fluorescentie-microscopie waarbij

de brede 461 nm overgang wordt gebruikt, met gelijktijdige zijbandkoeling op de smalle 689 nm overgang, zou moeten leiden tot een voldoende aantal verzamelde fotonen om de bezetting van enkele roosterpunten met goede zekerheid waar te nemen. Hiervoor is een goed ontworpen objectief met hoge numerieke apertuur (NA) nodig. Het blijkt echter niet nodig te zijn om optische elementen in het vacuüm te plaatsen als het objectief dicht genoeg bij de venster van de microscoop-kamer kan worden geplaatst.

Hoofdstuk 3 beschrijft twee thema's op het gebied van machinebouw die belangrijk zijn voor de bouw van een kwantumgas-apparaat, namelijk gasstroming in ultrahoog vacuüm (UHV) en het ontwerpen van elektromagneten. In het eerste deel worden de vergelijkingen gepresenteerd die kunnen worden gebruikt om de verwachte achtergronddruk in een vacuümsysteem te berekenen op basis van pompsnelheiden en de achterblijvende instromingen vanuit bijvoorbeeld een minder schone kamer of door diffusie van helium door de vensters van de kamers. In het tweede deel van het hoofdstuk wordt getoond hoe elektromagneten die een behoorlijk hoog magneetveld produceren kunnen worden gemaakt. Deze spoelen worden efficiënt met water afgekoeld, zodat een stroom van enige honderden A kan worden gebruikt. Dat leidt tot een hoog magneetveld en een lage inductie, wat praktisch is wanneer snelle schakeling nodig is.

Hoofdstuk 4 presenteert het ontwerp en de bouw van het apparaat zelf. De kamers en de belangrijke onderdelen worden in aparte secties beschreven, met de relevante berekeningen voor ons geval, schema's, foto's, leveranciers voor de meeste onderdelen en de relevante aanmerkingen om rekening mee te houden voor de bouw van bijna elk ultrahoog-vacuüm systeem voor atoomfysica.

Hoofdstuk 5 beschrijft de lasersystemen in ons experiment. Er zijn drie hoofdsystemen: één voor 461 nm om de brede overgang aan te slaan, één voor 689 nm om de smalle overgang aan te slaan en het 1064 nm systeem voor optische dipoolvallen, het toekomstige optische rooster en het optische transport tussen de kamers. De leidende beginselen voor het ontwerp van deze lasersystemen zijn uitgelegd, met bijbehorende diagrammen van hun samenstellingen. Het hoofdpunt is dat voor de lasers op zichtbare golflengtes gebruik gemaakt wordt van versterking van licht vanuit een gelockte master laser met behulp van injection-gelockte slave lasers. Dat levert voldoende vermogen op. Het infrarode systeem heeft geen absolute frequentie-locking nodig en daardoor is het mogelijk om een gemakkelijk verkrijgbaar commercieel hoog-vermogen lasersysteem te gebruiken.

In hoofdstuk 6 wordt uitgelegd welke experimentele stappen in onze hoofdkamer nodig zijn om een Bose-Einstein condensaat te maken. Vervolgens wordt overgegaan naar analyse van de resultaten. De tweetraps magneto-optische val voor strontium wordt beschreven, met het magneetreservoir en de repumping tussen de stappen. Daarnaast worden er eenvoudige simulaties van de dynamiek van verdampingskoeling getoond, met een omschrijving van de verdampingssequentie die tot een Bose-Einstein condensaat leidt. Uiteindelijk worden de BEC wolken geanalyseerd met het doel om de groei van de BEC fractie waar te nemen en om de inversie van de lengte-breedte verhouding te zien, wat één van de kenmerkende eigenschappen van een BEC is. Daarna worden metingen van de levensduur van het BEC in

de dipoolval getoond en metingen waarin het BEC wordt gebruikt als een nuttig middel om oscillatiefrequenties in de dipoolval te meten.

Hoofdstuk 7 is de eerste publicatie die volgt uit het nieuwe experiment: een nauwkeurige meting van de $^1S_0$ - $^3P_2$ overgangsfrequentie in ^{87}Sr. Deze specifieke overgang is interessant omdat hij ongeveer zo smal is als de $^1S_0$ - $^3P_0$ klokovergang in ^{87}Sr, maar hij is magnetisch. Dit feit maakt hem een slechte keuze voor een optische klok maar een goede keuze voor bijvoorbeeld het aanslaan van Raman-overgangen of voor positieafhankelijke detectietechnieken die gebaseerd kunnen zijn op het in of uit resonantie brengen van de overgang met behulp van een magneetveld. De absolute frequentie van de ^{87}Sr $^1S_0$ $(F = 9/2) - {}^3P_2$ $(F' = 7/2)$ overgang komt op $446\,648\,775(30)\,\mathrm{MHz}$, en is bepaald met $0.5\,\mathrm{MHz}$ onzekerheid ten opzichte van de overgangen $(J' - J'' = 32 - 33)(\nu' - \nu'' = 9 - 9)$ {a8, a9, a10, a11} in een heet gas van $^{127}\mathrm{I}_2$.

Het apparaat is nu in volledig werkende staat en klaar voor de volgende stappen, waaronder het maken van een rooster van optische pincetten en de bouw van een volledig werkende kwantumgas-microscoop voor de hand liggend lijken te zijn. Desalniettemin is de flexibiliteit van het apparaat duisdanig dat ook andere onderzoeksrichtingen ingeslagen kunnen worden, zonder al te grote of ingrijpende aanpassingen te hoeven maken.

Summary

This Thesis describes the design and construction of, and the first experiments on the new strontium quantum gas machine, built at the University of Amsterdam in the years 2014-2017. The result is a flexible apparatus that is suitable and convenient for a range of experiments including the ones beyond what was envisioned when it was planned.

The Introduction presents an overview of the useful features of strontium and the main ingredients of a quantum gas apparatus, with a particular example of the machine described in this Thesis. The main reason why strontium is attractive as an atomic species in this kind of experiments are its two electrons in the valence shell, which lead to different classes of optical transitions, namely broad dipole-allowed ones, narrow dipole-forbidden ones, and ultranarrow doubly-forbidden ones. This results in a convenient system for laser cooling, makes precision spectroscopy and atomic clock experiments possible, and also leads to the presence of metastable states, which can be useful in quantum gas microscopy or particular convenient schemes for two-photon Raman transitions, for example. In accordance with this, the machine is designed to be flexible for many applications, which is why there are three experimental chambers. The main chamber is the place where magneto-optical trapping and evaporative cooling to a quantum gas can be performed, and there are two side chambers, for the future quantum gas microscope and one is a glass cell for the experiments that are inconvenient or impossible in a steel chamber.

Chapter 1 presents the fundamental theory required to understand the different steps of laser cooling and to analyze quantum-degenerate samples. The governing equations are explained for optical molasses, the Zeeman slower, the magneto-optical trap, the ac Stark shifts in an optical dipole trap, and the evaporation process. Eventually, the basics of absorption imaging of ultracold clouds are explained. The Chapter ends with a derivation of the formulas that can be used for fitting cold thermal clouds, clouds around the Bose-Einstein condensation point, and almost pure Bose-Einstein condensates in absorption images. These fits allow one to extract quantities like the gas density, temperature, or Bose-Einstein condensate fraction, for example.

Chapter 2 describes the relevant theory and presents the calculations for single-atom-resolved and single-site-resolved imaging of strontium in a strongly-correlated optical lattice. This technique is called quantum gas microscopy. The conclusion is that fluorescence imaging on the broad $461\,\mathrm{nm}$ transition with simultaneous sideband cooling on the narrow $689\,\mathrm{nm}$ transition should surely result in enough photons being collected for high-fidelity imaging of the optical lattice site occupation. In particular, even though this requires a well-designed high-numerical-aperture objective, it is not necessary to put any optics inside vacuum, as long as the objective can be placed close enough to the viewport of the dedicated microscope chamber.

Chapter 3 explains two engineering topics that are important in constructing a quantum gas

apparatus, namely gas flow in an ultrahigh-vacuum environment, and electromagnet design. The first part presents the equations that can be used for calculating the expected background pressure in a vacuum system given certain pumps and residual leak rates from a dirtier chamber in the vacuum system, or from the outside, like the diffusion of helium through glass. The second part shows how rather high-field electromagnets can be made and efficiently water-cooled to be able to run a few hundred A of current through them. This leads to a high field and a low inductance, which is beneficial if fast switching is required.

Chapter 4 illustrated piece by piece the design and construction of the experimental apparatus. The chambers and important sections are presented in their dedicated sections, with the calculations relevant for our case, diagrams, photos, suppliers of the most parts, and the relevant notes and observations to keep in mind for almost any ultrahigh vacuum system for atomic physics.

Chapter 5 explains the laser systems used in our experiment. There are the three main ones: the $461\,\mathrm{nm}$ system for addressing the broad line, the $689\,\mathrm{nm}$ system for addressing the narrow line, and the $1064\,\mathrm{nm}$ system for optical dipole traps and the future optical lattice and optical transport between the chambers. The governing principles for the design of these laser systems are stated and the diagrams of their layout are presented. The main point is that for the visible systems we use the amplification of a locked master laser by injection-locking slave lasers to generate the required power, and the infrared system does not require absolute frequency locking, which makes it possible to use one of the widely-available high-power commercial systems.

Chapter 6 describes the experimental steps in the main chamber that are required to produce a Bose-Einstein condensate, and then goes on to present the analysis of the samples. It explains the two-stage magneto-optical trap for strontium, with the magnetic reservoir and repumping in between. There are also basic simulations of evaporative cooling dynamics, and then a presentation of the evaporation sequence which leads to a BEC. Finally, BEC samples are analyzed with the goal of observing the BEC fraction growth, the inversion of aspect ratio, which is the hallmark signature of a BEC, and then the BEC lifetime in the optical dipole trap is measured, and the BEC is used as a convenient tool for dipole trap frequency measurement.

Chapter 7 is the first publication from the new experiment, namely a precise measurement of the $^1S_0$ - $^3P_2$ transition frequency in ^{87}Sr. This particular line is interesting because it is approximately as narrow as the $^1S_0$ - $^3P_0$ clock line in ^{87}Sr, but it is magnetic; this makes it a bad choice for as a clock transition, but a very good candidate for driving Raman transitions or designing position-dependent detection schemes that can rely on tuning the atoms in and out of resonance with a magnetic field gradient, just to name two examples. The absolute frequency of the ^{87}Sr $^1S_0$ $(F = 9/2) - {}^3P_2$ $(F' = 7/2)$ is found to be $446\,648\,775(30)\,\mathrm{MHz}$, and it is determined with $0.5\,\mathrm{MHz}$ of uncertainly with respect to the secondary standard given by the transitions $(J' - J'' = 32 - 33)(\nu' - \nu'' = 9 - 9)$ {a8, a9, a10, a11} in $^{127}\mathrm{I}_2$ vapor.

The apparatus is now fully operational and ready for the next steps, among which the generation of optical tweezer arrays and the construction of the full quantum gas microscope

look like the clearest ones. However, the flexibility that it offers makes also other research direction possible, without extensive or too invasive modifications.

List of publications

Published article:

Oleksiy Onishchenko, Sergey Pyatchenkov, Alexander Urech, Chun-Chia Chen, Shayne Bennetts, Georgios A. Siviloglou, and Florian Schreck, *The frequency of the ultranarrow* $^1S_0$ - $^3P_2$ *transition in* ^{87}Sr, Phys. Rev. A 99, 052503 (2019).

Contributions: A lot of the work towards building the new quantum gas machine, refurbishing the iodine spectroscopy cell and setting up all the necessary optics for it, designing the scheme for lock-in detection of iodine signals, designing and setting up the spectroscopy lasers and the optical cavity lock (together with Alexander Urech), analyzing the data and writing the major portion of the paper.

Submitted for publication:

Ivo Knottnerus, Sergey Pyatchenkov, Oleksiy Onishchenko, Alexander Urech, Georgios A. Siviloglou, Florian Schreck, *Microscope objective for imaging atomic strontium with 0.63 micrometer resolution*, arXiv:1906.07167v2.

Contributions: supervising the first author of the paper in day-to-day work on this project, discussing and helping him with setting up and analyzing the measurements of the microscope objective resolution.

Acknowledgments

Het proefschrift is nu af, en het is een mooi moment voor een dankwoord aan alle mensen die op welke manier ook in deze tijd mij hebben geholpen, geleerd, of geïnspireerd. Ik ga dit dankwoord in het Engels schrijven zodat iedereen, die het leest, het goed kan begrijpen; velen van de hier genoemde mensen spreken geen Nederlands. Maar het is toch belangrijk voor mij om in het Nederlands te beginnen, niet alleen vanuit puur respect voor het feit dat dit onderzoek in Nederland heeft plaatsgevonden, maar ook omdat diep binnen mij weet ik dat het Nederlands wel mijn taal is, zoals geen andere taal. In Nederland voel ik me echt thuis; in geen ander land had ik dit specifiek gevoel.

It has been a wonderful, difficult, demanding, fruitful, inspiring almost five years. There has been hardship along the way, but what an intensive learning and formative experience for me it has been! And I mean that in every sense: learning to be a scientist, which includes both experiment and theory, and engineering as well; learning to be a mentor, with all the students whom it has been such a pleasure to supervise; actually learning to learn, to be efficient, to be fast; learning to stand up for myself, because, unfortunately, public and interpersonal relations do get into science, mostly in detrimental ways, and so I am doing my best to make Richard Feynman's quote at the beginning of this Thesis a reality; finally, learning so many other things outside the lab, like music, tango, languages, learning to be there for my love and for my friends, just learning to be a better person. It has been a real journey!

I would like to immediately express my gratitude to my supervisor Florian Schreck. He gave me the opportunity to embark on this journey, and it is in his lab that I went all the way from asking "How do you pump vacuum?" and "What does UHV mean?" to joining the rather small part of the Humanity that managed to make Bose-Einstein condensates. Under Florian's guidance I went from knowing next to nothing about experimental physics to being a researcher, to having the ability to build and operate a complex experiment, and to having the confidence to do so. After all, Florian trusted me and Georgios to build up a new experiment at the time when I personally was, in terms of my day-to-day experimental physics knowledge, very much like that optical table for the strontium quantum gas microscope: clear and empty. Florian, thanks for everything, thank you for your explanations, thank you for your help and trust, I appreciate it all! Thanks for letting me grow, together with the Sr QGM experiment. I wish you all the best with all your projects, and I wish success to the next generations of your students.

Furthermore, I am truly grateful to Georgios (Siviloglou). We designed the thing together, we built it together, we discussed and we made decisions, and in the meantime, you taught me so much! It has been a pleasure and a true honor to work with you, thank you for being my co-supervisor, and I really wish you all the best, and all the possible success in China. Enjoy it!

I would also like to thank Jook Walraven for being my independent advisor during the PhD time, for the many explanations, for the mini-course on atomic physics that he agreed to teach me and a couple of other young PhD students, for the insightful lecture notes. Jook, it was an honor being your teaching assistant for Atomic physics. You taught me a lot and you inspired me a lot.

Thanks to Robert Spreeuw, Klaasjan van Druten, Ben van Linden van den Heuvell, and René Gerritsma for the discussions that we had, for the insights, questions, and comments during the journal clubs, for organizing the journal clubs themselves. I wish you all lots of success. And I would like to express my gratitude to all the members of my Thesis Committee for accepting the invitation to join this Committee and to evaluate my Thesis.

I want to thank Sergey (Pyatchenkov), Alex (Urech), and Carla (Sanna). It has been a pleasure to work with you all, my colleagues, and also my friends. I enjoyed asking questions, I enjoyed explaining to you everything that I could explain. I enjoyed working as a team. Alex, you started as a Master student, and you decided to make a much larger commitment to the project; we can all thank you for that. I was technically supposed to be one of your supervisors, but I don't like that idea very much, we worked as colleagues; I find that to be a much better way, with you and with any other person joining the lab. Good luck now! And Carla, well, you joined us on the project, but we were already friends long before that, from the time that we shared the office, from the time I started learning Italian, and then never had time for it, and then went for Greek in the end :) I hope it didn't make you angry, and yes I will learn Italian, that's kind of obvious! Thank you, Carla! I always enjoy our conversations in and out of the lab, thank you for all your support and understanding, you are a wonderful friend.

I want to thank the members of the other teams in Florian's group, RbSr, and the Atom laser, for the discussions, help, and collaborations. In particular, I want to specifically thank Alessio (Ciamei): Alessio, you're a great scientist, and an excellent friend. Every discussion with you is enjoyable and intellectually stimulating, be it about physics, philosophy of science, art and Italian literature, the architecture of Rome, whatever. Thank you for sharing your knowledge and insights, you helped me analyze science deeper than I had thought before. It was an honor being your paranymph, and I am sure you will always keep doing great science. Alex (Bayerle), it was a pleasure meeting you and knowing you, with your friendly and always very supportive and informal chat. Thanks for the clock lasers and for your explanation of them. Lukas (Reichsöllner), thank you for your willingness to help, explain, and support, even after I left the lab. I really appreciate it, it's a pleasure being your colleague and friend. Chun-Chia (Chen), thanks for all the chats, all the jokes, all the help, all the insights, all the hints and techniques. And also, thank you for being a cool flatmate, already after I had left the lab, but it was a great time, I think the three of us in the house made a good company. And Denis (Kurlov), thank you for your theoretical insights and for the friendly coffee chats.

I am expressing my sincere gratitude also to all the Master and Bachelor students who worked with me during my PhD time, be it only for a two-week project, or for a full graduation Thesis. I enjoyed working with you all, I hope I taught you and inspired you, and you all for

sure taught me and inspired me as well. In particular, Ivo (Knottnerus), thank you for choosing our team, thank you for everything you did, thank you for making our group better, for your work and ideas, thank you for being a great person and an excellent scientist. I fondly remember us aligning the tweezer imaging system on the weekends and then going to Spar for pizza, for a truly scientific dinner :) And it's a pleasure to stay friends with you. Good luck with everything you do, and come back to the real physics :) Amy (van der Hel), thank you for working with us, thank you for strengthening our team, and I wish you all the success with your own PhD. Jan (Mathijssen), it was a pleasure working with you, thank you for all your contributions to the red laser system, and good luck at ARCNL now. You will do an excellent job. Thanks to all the members of the other atomic physics groups at UvA whom I got to know, with whom I got to talk, sometimes more, sometimes, less, sometimes become friends. Nataly (Cisternas), Julius (de Hond), Arthur (van Rooij), Henning (Fürst), Thomas (Feldker), Maarten (Soudijn), Jannis (Joger), Henrik (Hirzler), Norman (Ewald), thank you, and I wish you success with wherever your path takes you, be it physics or something outside of it.

I want to thank the engineers and the technicians from the mechanical and electronic workshops at UvA. It has been a pleasure, thank you for your help, teaching, and trust. Alix (Wattjes), thank you for organizing it all there on the mills, drills, and saws; you made the human-machine interfaces work smoothly. Tijs (van Roon), thank you not only for your direct help, which has been so valuable in our experiment, but also for taking your time to teach me, and to answer the "Why?", not only the "What?", I really appreciate it. Tjeerd (Weijers), Johan (Mozes), and Gerrit (Hardeman) thank you for your help. Hans (Ellermeijer), thank you for making all the effort with our electromagnets. It helped us enormously. Tristan (van Klingeren) and Sven (Koot), thank you for willing to help during that crazy MOT and dipole trap building stage when I was coming over multiple times per week saying "And can this optical post be cut at 45 degrees, preferably until tomorrow?"

I would also like to express my sincere gratitude to the staff of the Institute of Physics, to the secretaries, as well as to all the administration staff of the University of Amsterdam. Even though they are not involved in the details of day-to-day lab work, they set the stage for us to work efficiently, they take care of our larger work environment. In a broader context, I want to express my special gratitude and admiration to the beautiful City of Amsterdam, and to this wonderful Country, the Netherlands. This is that large stage where everyday life happens, and this stage is especially nurturing, inspiring, and supportive for a young and ambitious scientist, and, in my opinion, for any person in general, whatever her or his dreams are. It means a lot to me. On a very personal note, this became the first country and the society where I really find myself at home. I am happy to feel that.

I would like to thank the scholarship foundations that financed my studies and made it possible for me to get my Bachelor's and my Master's degrees. Those are the stepping stones towards my PhD and towards all of my future career, and, of course, crucial stages of my intellectual growth. At the Bachelor level, it was the Oechsle Scholarship at Lafayette College in Easton, PA, USA (2008-2012) and at the Master level it was the Justus & Louise van Effen

Excellence Scholarship at TU Delft in Delft, The Netherlands (2012-2014).

I am grateful to the late Wim Vassen, whose group I had the honor to join for my postdoc, and who gave me the opportunity to continue immediately in the field of atomic physics in Amsterdam, which I wanted to do. It is very sad and unfortunate that I didn't get much of a chance to work with Wim, apart from only a few meetings. Wim is not with us anymore, but his contributions to science live on, and our next achievements with metastable helium will of course be part of Wim's scientific heritage. I want to thank Kjeld Eikema and Wim Ubachs for inviting me to join Wim Vassen's project, and I would like to thank Kjeld and Rick Bethlem for taking the supervision of Wim's experiments and for their help during the group discussions and directly in the lab. I am grateful for that and I value it a lot. Ruud (van der Beek), it's a pleasure to be working with you now, it's been definitely a huge project to build up the whole machine on your own, great job, and we will do our best to also get new and cool results out of it. Also, thank you so much for taking the time to edit and improve the text of my summary in Dutch! Yuri (van der Werf) and Raphaël (Jannin), it's great working with you too, thank you for all the ideas, both the scientific ones and the one regarding having coffee and cookies in the afternoon. Well, that's fuel for the physicists :)

And now I want to express my gratitude to the people from outside the group and outside UvA, so to my personal circle. First of all, Vania (Gatsiou) and Georgios (Skantzaris), well, you know what your friendship means to me! We've known each other already for years, and all the conversations, both serious and funny, all the dinners that we cooked and had together, are such a wonderful part of life. I am glad and honored to be your friend, always! And of course thank you for all your help with Greek, you know that I love it. Now that this Thesis is done, I will get back to improving it. Caroline (Lubbers), I got to know you through Georgios, of course, and I am happy to know you and to be your friend. Thank you for welcoming me at your cozy home for those dinners with chocolate tastings, thank you for introducing me to the real Chocolate :) And get back to tango soon :) I would also like to take a moment here to express my warmest gratitude to Eleni Dimopoulou and Thanasis Skantzaris, my "Greek family". Eleni and Thanasis, you are really special, you welcome me in Athens in the best way that I could imagine; in addition, your family and your home became the start of a personal journey for me to the city and the culture that always influence who I am. And thank you for all the conversations and support, it all means so much to me! My warmest greetings also to the rest of your family, to Alexandra, Maria, and the two young children, I hope they grow up happy!

Nikoletta (Tsiarta), it is a real pleasure to be your friend. I enjoy our conversations, including those next to the coffee machine, with me pressing the button for the next cup, and then trying to convince you to try an espresso :) I wish you all the best in your next intellectual step and adventure in Girona, you will do great! And I know that our friendship will go on. Christian (Dickel), I am glad to have met you and gotten to know you while I was still in Delft. Thank you for all the chats, for all the invitations to those music nights, New Year's Eve parties, I felt welcome in your Delft home, and I felt your friendly support and understanding, us both being idealistic physicists, nerds, and musicians. All the best to you and Jasmin, and I truly

hope that our friendship will go on like it did here in the Netherlands, supported by science and music. Willemijn (Uilhoorn), I remember that you were the first person I got to know in the first physics lecture at TU Delft. Well, I can surely say that it was a fortunate meeting! Throughout these years, I am always honored to be your friend, and I know that our friendship will stay alive and strong no matter how hectic and busy our lives are. I am also grateful to you and your family for that warm invitation and welcome for the Sinterklaas arrival night in Naarden when I had just moved to Amsterdam. Hanna (Yendzhyievska), thanks for staying friends through all these years, for keeping up the connection. It's actually quite funny how our language of communication slowly drifted from being Ukrainian to being English in the course of time :) Isa (Mirallas), thank you for everything you taught me about music, thank you for your patience, your understanding, your support. I came to your classes with my singing skills being at absolute zero. Honestly, in the first month of those classes, I used a phone app with an audio spectrum analyzer to check if I was singing correct notes :) Well so it's been quite a learning path for me, thank you so much for guiding me.

And, of course, here is the moment to thank everyone who came into my life through tango, my other passion. My first tango teachers, Zaneta (Leonidi) and Take (Uto), I am grateful to you for introducing me to it all, when I had basically no idea what dance is. I just liked tango music, so I came to that dimly lit La Bodeguita room in the center of Den Haag to try it out, to see how I would like it. Well, I really liked it in the end, I guess much more than I had imagined when I decided to try it! In fact, I liked it so much, that a bit less than four years after those first classes in Den Haag, we were chatting in that dance hall at TangoLovers in the center of Athens, and then on top of that Zaneta and I didn't really need English already, we would switch to Greek; it was Athens, after all :) I wish you and your daughter all the best now in Kefallonia! I am grateful to all other teachers who I had the chance to learn from. Vanessa (Fatauros), and Damian (Rosenthal), your workshops and private classes helped me improve, discover new quality of movement, enjoy myself more, thank you so much! And I always cherish inside me a very special gratitude to the great Maestros Geraldin (Rojas) and Ezequiel (Paludi); your elegance as a couple in tango and in life transcends any borders. You not only teach, you inspire and you set an example. It's a true honor being your student and it's a true pleasure being your friend. I am fortunate to have met you. All the best wishes to Amapola too! Tamara (de Graaff) I am grateful to you for signing up for those lessons together with me, in the fall of 2014, when I had just moved to Amsterdam, and was not that good at tango, to say the least. Thank you for helping me learn! I really hope you enjoyed the path too, and you can be sure, I am glad and honored for every tanda we dance together. Becky (Brod), Hilde (Wassenaar), Jenny (Gaskins), Margot (Kraaikamp), Lena (Glücksmann Nilsson), thank you for joining the classes with me at different times. I really hope that you had a wonderful time, and I hope there are many more milongas for us to enjoy. I am grateful to all the other Ladies who I had the honor to share tango with, in milongas, festivals, practicas. Galja (Pletikapić), well you know how many bike rides and wines and chats deep in the night after the milonga we shared :) how many sincere laughs and jokes we shared and how honestly we support each other. It's been amazing, it's a pleasure,

I am glad to be your friend. Vanessa (Marangoni), well, that was an unexpected meeting :) And then you made it into a very elegant milonga clandestina in a hallway with wooden floor at Science Park. Thank you! Uta (Bussmeyer), thank you for being my friend, from the very first song we danced together. It's my honor and pleasure.

There are many other people who entered my life with joy, inspiration, help during these five years, and who I forgot to mention now. I am sorry about that. I am grateful to you, I hope you will not get angry, I appreciate you being in my life, and I hope to see you soon and talk to you again soon.

I would like to express my sincere gratitude to my parents, Larysa and Viktor. Thank you! Thanks for all the support, be it mental, physical (with me moving from place to place all over the world, across continents, across countries), or financial. It means a lot to me, and I appreciate it a lot! You know that I never take easy paths, and I myself tend to make those paths then even more complicated. Thank you for supporting me along those paths. And I would like to thank my grandma Nadiya for her sincere support, for coming over to visit me in Amsterdam, even at the age of almost 80. It was an honor for me.

Jacqui, my Angel, this Thesis started with a dedication to you, and this Thesis ends with my expression of complete love, admiration, respect, and support for you. I met you when I was already writing this Thesis, it all started with a simple conversation, actually about dance. Then it went on to philosophy, freedom, equality, science, then we started liking each other, well and then we realized that it was getting more beautiful every day. That trip in December of 2018 let us experience an absolutely unique story of love, I am totally grateful to you for deciding to take that trip with me! Jacqui, that special trip is going on, and I would like to thank you for being exactly who you are! You came into my life like a star, like an inspiration, you entered with true love, and it's my complete honor, pleasure, luck, blessing, and a dream that became reality. I am infinitely honored and happy to share my life with you and I am glad to dedicate this Thesis to you, wonderful, brilliant, awesome Jacqui!

Bibliography

[1] A. D. Ludlow *et al.*, *Optical atomic clocks*, Rev. Mod. Phys. **87**, 637 (2015).

[2] V. Andreev *et al.*, *Improved limit on the electric dipole moment of the electron*, Nature **562**, 355 (2018).

[3] M. H. Anderson *et al.*, *Observation of Bose-Einstein Condensation in a Dilute Atomic Vapor*, Science **269**, 198 (1995).

[4] R. H. Parker *et al.*, *Measurement of the fine-structure constant as a test of the Standard Model*, Science **360**, 191 (2018).

[5] A. D. Cronin, J. Schmiedmayer, and D. E. Pritchard, *Optics and interferometry with atoms and molecules*, Rev. Mod. Phys. **81**, 1051 (2009).

[6] I. Bloch, *Ultracold quantum gases in optical lattices*, Nat. Phys. **1**, 23 (2005).

[7] I. F. Silvera and J. T. M. Walraven, *Stabilization of Atomic Hydrogen at Low Temperature*, Phys. Rev. Lett. **44**, 164 (1980).

[8] K. B. Davis *et al.*, *Bose-Einstein Condensation in a Gas of Sodium Atoms*, Phys. Rev. Lett. **75**, 3969 (1995).

[9] C. C. Bradley, C. A. Sackett, and R. G. Hulet, *Bose-Einstein Condensation of Lithium: Observation of Limited Condensate Number*, Phys. Rev. Lett. **78**, 985 (1997).

[10] B. DeMarco and D. S. Jin, *Onset of Fermi Degeneracy in a Trapped Atomic Gas*, Science **285**, 1703 (1999).

[11] F. Dalfovo *et al.*, *Theory of Bose-Einstein condensation in trapped gases*, Rev. Mod. Phys. **71**, 463 (1999).

[12] S. Giorgini, L. P. Pitaevskii, and S. Stringari, *Theory of ultracold atomic Fermi gases*, Rev. Mod. Phys. **80**, 1215 (2008).

[13] W. Ketterle, D. S. Durfee, and D. M. Stamper-Kurn, *Making, probing and understanding Bose-Einstein condensates*, arXiv:cond-mat/9904034v2 (1999).

[14] W. Ketterle and M. W. Zwierlein, *Making, probing and understanding ultracold Fermi gases*, Nuovo Cimento Rivista Serie **31**, 247 (2008).

[15] J. Sakurai and J. J. Napolitano, *Modern Quantum Mechanics (2nd Edition)*, Pearson, 2010.

[16] C. J. Foot, *Atomic Physics*, Oxford University Press, 2005.

[17] G. Grynberg, A. Aspect, and C. Fabre, *Introduction to Quantum Optics: From the Semi-classical Approach to Quantized Light*, Cambridge University Press, 2010.

[18] S. G. Porsev and A. Derevianko, *Hyperfine quenching of the metastable $^3P_{0,2}$ states in divalent atoms*, Phys. Rev. A **69**, 042506 (2004).

[19] A. V. Taichenachev *et al.*, *Magnetic Field-Induced Spectroscopy of Forbidden Optical Transitions with Application to Lattice-Based Optical Atomic Clocks*, Phys. Rev. Lett. **96**, 083001 (2006).

[20] I. Courtillot *et al.*, *Efficient cooling and trapping of strontium atoms*, Opt. Lett. **28**, 468 (2003).

[21] X. Xu *et al.*, *Cooling and trapping of atomic strontium*, J. Opt. Soc. Am. B **20**, 968 (2003).

[22] H. Katori *et al.*, *Magneto-Optical Trapping and Cooling of Strontium Atoms down to the Photon Recoil Temperature*, Phys. Rev. Lett. **82**, 1116 (1999).

[23] S. Stellmer *et al.*, *Laser Cooling to Quantum Degeneracy*, Phys. Rev. Lett. **110**, 263003 (2013).

[24] S. Bennetts *et al.*, *Steady-State Magneto-Optical Trap with 100-Fold Improved Phase-Space Density*, Phys. Rev. Lett. **119**, 223202 (2017).

[25] S. Kraft *et al.*, *Bose-Einstein Condensation of Alkaline Earth Atoms:* ^{40}Ca, Phys. Rev. Lett. **103**, 130401 (2009).

[26] Y. Takasu *et al.*, *Spin-Singlet Bose-Einstein Condensation of Two-Electron Atoms*, Phys. Rev. Lett. **91**, 040404 (2003).

[27] H. J. Metcalf and P. van der Straten, *Laser Cooling and Trapping*, Springer, 1999.

[28] S. L. Campbell *et al.*, *A Fermi-degenerate three-dimensional optical lattice clock*, Science **358**, 90 (2017).

[29] J. Dalibard, *Introduction to the physics of artificial gauge fields*, arXiv:1504.05520 (2015).

[30] A. J. Daley *et al.*, *Quantum Computing with Alkaline-Earth-Metal Atoms*, Phys. Rev. Lett. **101**, 170504 (2008).

[31] M. Hermele, V. Gurarie, and A. M. Rey, *Mott Insulators of Ultracold Fermionic Alkaline Earth Atoms: Underconstrained Magnetism and Chiral Spin Liquid*, Phys. Rev. Lett. **103**, 135301 (2009).

[32] A. V. Gorshkov *et al.*, *Two-orbital SU(N) magnetism with ultracold alkaline-earth atoms*, Nat. Phys. **6**, 289 (2010).

[33] X. Zhang *et al.*, *Spectroscopic observation of SU(N)-symmetric interactions in Sr orbital magnetism*, Science **345**, 1467 (2014).

[34] O. Boada *et al.*, *Quantum Simulation of an Extra Dimension*, Phys. Rev. Lett. **108**, 133001 (2012).

[35] A. J. Daley, *Quantum computing and quantum simulation with group-II atoms*, Quantum Inf. Process. **10**, 865 (2011).

[36] C. Chin *et al.*, *Feshbach resonances in ultracold gases*, Rev. Mod. Phys. **82**, 1225 (2010).

[37] S. Stellmer, *Degenerate quantum gases of strontium*, PhD thesis, University of Innsbruck, 2013.

[38] S. Kato *et al.*, *Control of Resonant Interaction between Electronic Ground and Excited States*, Phys. Rev. Lett. **110**, 173201 (2013).

[39] K. M. R. van der Stam *et al.*, *Large atom number Bose-Einstein condensate of sodium*, Rev. Sci. Instrum. **78**, 013102 (2007).

[40] A. S. Flores *et al.*, *Simple method for producing Bose–Einstein condensates of metastable helium using a single-beam optical dipole trap*, Appl. Phys. B **121**, 391 (2015).

[41] C. Cohen-Tannoudji, B. Diu, and F. Laloë, *Quantum Mechanics*, 1st ed. Wiley-VCH, 1992.

[42] J. Dalibard, *Atomes ultra froids: notes de cours rédigées par Jean Dalibard*. URL: `http://www.phys.ens.fr/~dalibard/Notes_de_cours/DEA_atomes_froids_actuel.pdf` (visited on 06/19/2019).

[43] D. A. Steck, *Quantum and Atom Optics*. Available online at `http://atomoptics-nas.uoregon.edu/~dsteck/teaching/quantum-optics/`. (revision 0.12.2, 11 April 2018).

[44] C. E. Wieman and L. Hollberg, *Using diode lasers for atomic physics*, Rev. Sci. Instrum. **62**, 1 (1991).

[45] K. B. MacAdam, A. Steinbach, and C. Wieman, *A narrow-band tunable diode laser system with grating feedback, and a saturated absorption spectrometer for Cs and Rb*, Am. J. Phys. **60**, 1098 (1992).

[46] D. A. Steck, *Rubidium 87 D Line Data*. 2003. URL: `https://steck.us/alkalidata/rubidium87numbers.1.6.pdf` (visited on 11/27/2018).

[47] J. J. Sakurai and J. Napolitano, *Modern Quantum Mechanics*, 2nd ed. Addison-Wesley, 2011.

[48] M. M. Boyd *et al.*, *Nuclear spin effects in optical lattice clocks*, Phys. Rev. A **76**, 022510 (2007).

[49] P. J. Mohr, D. B. Newell, and B. N. Taylor, *CODATA recommended values of the fundamental physical constants: 2014*, Rev. Mod. Phys. **88**, 035009 (2016).

[50] *Inkscape: an open source vector graphics software.* Distributed under the General Public License. Available at `https://inkscape.org/`.

[51] W. D. Phillips and H. Metcalf, *Laser Deceleration of an Atomic Beam*, Phys. Rev. Lett. **48**, 596 (1982).

[52] E. Wille, *Preparation of an Optically Trapped Fermi-Fermi Mixture of* ^6Li *and* ^{40}K *Atoms and Characterization of the Interspecies Interactions by Feshbach Spectroscopy*, PhD thesis, University of Innsbruck, 2009.

[53] E. L. Raab *et al.*, *Trapping of Neutral Sodium Atoms with Radiation Pressure*, Phys. Rev. Lett. **59**, 2631 (1987).

[54] A. M. Steane, M. Chowdhury, and C. J. Foot, *Radiation force in the magneto-optical trap*, J. Opt. Soc. Am. B **9**, 2142 (1992).

[55] A. S. Arnold and P. J. Manson, *Atomic density and temperature distributions in magneto-optical traps*, J. Opt. Soc. Am. B **17**, 497 (2000).

[56] M. Gajda and J. Mostowski, *Three-dimensional theory of the magneto-optical trap: Doppler cooling in the low-intensity limit*, Phys. Rev. A **49**, 4864 (1994).

[57] S.-K. Choi *et al.*, *Three-dimensional analysis of the magneto-optical trap for (1+3)-level atoms*, Phys. Rev. A **77**, 015405 (2008).

[58] O. N. Prudnikov, A. V. Taichenachev, and V. I. Yudin, *Three-dimensional theory of the magneto-optical trap*, J. Exp. Theor. Phys. **120**, 587 (2015).

[59] J. Dalibard, *Des cages de lumière pour les atomes: la physique des pièges et des réseaux optiques*. URL: `http://www.phys.ens.fr/~dalibard/CdF/2013/Cours_2013.pdf` (visited on 10/22/2018).

[60] S. G. Porsev *et al.*, *Determination of Sr properties for a high-accuracy optical clock*, Phys. Rev. A **78**, 032508 (2008).

[61] R. Grimm, M. Weidemüller, and Y. B. Ovchinnikov, *Optical Dipole Traps for Neutral Atoms*, Adv. Atom. Mol. Opt. Phy **42**, 95 (2000).

[62] I. Bloch, *Quantum gases in optical lattices*, Physics World **17**, 25 (2004).

[63] C. Gross and I. Bloch, *Quantum simulations with ultracold atoms in optical lattices*, Science **357**, 995 (2017).

[64] A. Ashkin, *Optical trapping and manipulation of neutral particles using lasers*, Proc. Natl. Acad. Sci. U.S.A. **94**, 4853 (1997).

[65] N. Schlosser *et al.*, *Sub-poissonian loading of single atoms in a microscopic dipole trap*, Nature **411**, 1024 (2001).

[66] F. Le Kien, P. Schneeweiss, and A. Rauschenbeutel, *Dynamical polarizability of atoms in arbitrary light fields: general theory and application to cesium*, Eur. Phys. J. D **67**, 92 (2013).

[67] J Mitroy, M. S. Safronova, and C. W. Clark, *Theory and applications of atomic and ionic polarizabilities*, J. Phys. B **43**, 202001 (2010).

[68] W Yi *et al.*, *State-dependent, addressable subwavelength lattices with cold atoms*, New. J. Phys. **10**, 073015 (2008).

[69] M. S. Safronova *et al.*, *Development of a configuration-interaction plus all-order method for atomic calculations*, Phys. Rev. A **80**, 012516 (2009).

[70] M. Kozlov *et al.*, *CI-MBPT: A package of programs for relativistic atomic calculations based on a method combining configuration interaction and many-body perturbation theory*, Comput. Phys. Commun. **195**, 199 –213 (2015).

[71] C. Cohen-Tannoudji, J. Dupont-Roc, and G. Grynberg, *Photons and Atoms: Introduction to Quantum Electrodynamics*, Wiley, 1997.

[72] R. W. Schmieder, *Matrix Elements of the Quadratic Stark Effect on Atoms with Hyperfine Structure*, Am. J. Phys. **40**, 297 (1972).

[73] A. D. Ludlow, *The Strontium Optical Lattice Clock: Optical Spectroscopy with Sub-Hertz Accuracy*, PhD thesis, University of Colorado, 2008.

[74] M. Kozlov and S. Porsev, *Polarizabilities and hyperfine structure constants of the low-lying levels of barium*, Eur. Phys. J. D **5**, 59 (1999).

[75] M. S. Safronova, U. I. Safronova, and S. G. Porsev, *Polarizabilities, Stark shifts, and lifetimes of the In atom*, Phys. Rev. A **87**, 032513 (2013).

[76] M. S. Safronova, W. R. Johnson, and A. Derevianko, *Relativistic many-body calculations of energy levels, hyperfine constants, electric-dipole matrix elements, and static polarizabilities for alkali-metal atoms*, Phys. Rev. A **60**, 4476 (1999).

[77] M. S. Safronova *et al.*, *Blackbody-radiation shift in the Sr optical atomic clock*, Phys. Rev. A **87**, 012509 (2013).

[78] A. Kramida *et al.*, *NIST Atomic Spectra Database (version 5.6.1)*. URL: https://physics.nist.gov/asd (visited on 10/23/2018).

[79] G. Brooker, *Modern Classical Optics*, Oxford University Press, 2003.

[80] A. E. Siegman, *Lasers*, University Science Books, 1986.

[81] T. Oliphant, *Guide to NumPy*, 2nd ed. CreateSpace Independent Publishing Platform, 2015.

[82] E. Jones, T. Oliphant, P. Peterson, *et al.*, *SciPy: Open source scientific tools for Python*. Available at http://www.scipy.org/.

[83] J. D. Hunter, *Matplotlib: A 2D graphics environment*, Comput. Sci. Eng. **9**, 90 (2007).

[84] M. Newville, R. Otten, A. Nelson, *et al.*, *LMFIT: Non-Linear Least-Square Minimization and Curve-Fitting for Python*. Available at https://lmfit.github.io/lmfit-py/index.html.

[85] R. P. M. J. W. Notermans, *High-Precision Spectroscopy of Forbidden Transitions in Ultracold ^{4}He and ^{3}He*, PhD thesis, Vrije Universiteit Amsterdam, 2017.

[86] R. J. Rengelink, *A magic wavelength optical dipole trap for high-precision spectroscopy of ultracold metastable helium*, PhD thesis, Vrije Universiteit Amsterdam, 2018.

[87] B. E. A. Saleh and M. C. Teich, *Fundamentals of Photonics*, 2nd ed. Wiley, 2007.

[88] A. Banner, *The Calculus Lifesaver: All the Tools You Need to Excel at Calculus (Princeton Lifesaver Study Guides)*, 1st ed. Princeton University Press, 2007.

[89] O. J. Luiten, M. W. Reynolds, and J. T. M. Walraven, *Kinetic theory of the evaporative cooling of a trapped gas*, Phys. Rev. A **53**, 381 (1996).

[90] W. Ketterle and N. J. van Druten, *Evaporative Cooling of Trapped Atoms*, Adv. Atom. Mol. Opt. Phy **37**, 181 (1996).

[91] E. A. L. Henn *et al.*, *Evaporation in atomic traps: A simple approach*, Am. J. Phys. **75**, 907 (2007).

[92] J. Hu *et al.*, *Creation of a Bose-condensed gas of ^{87}Rb by laser cooling*, Science **358**, 1078 (2017).

[93] J. Dalibard, *Cohérence quantique et superfluidité dans les gaz atomiques*. URL: `https://www.college-de-france.fr/media/jean-dalibard/UPL378823497387772639_cours_2016.pdf` (visited on 02/21/2019).

[94] M. J. Holland, B. DeMarco, and D. S. Jin, *Evaporative cooling of a two-component degenerate Fermi gas*, Phys. Rev. A **61**, 053610 (2000).

[95] K. M. O'Hara *et al.*, *Scaling laws for evaporative cooling in time-dependent optical traps*, Phys. Rev. A **64**, 051403 (2001).

[96] M. D. Barrett, J. A. Sauer, and M. S. Chapman, *All-Optical Formation of an Atomic Bose-Einstein Condensate*, Phys. Rev. Lett. **87**, 010404 (2001).

[97] A. S. Tychkov *et al.*, *Metastable helium Bose-Einstein condensate with a large number of atoms*, Phys. Rev. A **73**, 031603 (2006).

[98] K. Hueck *et al.*, *Calibrating high intensity absorption imaging of ultracold atoms*, Opt. Express **25**, 8670 (2017).

[99] G. Reinaudi *et al.*, *Strong saturation absorption imaging of dense clouds of ultracold atoms*, Opt. Lett. **32**, 3143 (2007).

[100] J. F. Bertelsen, *Ultracold atomic gases: mixtures and molecules*, PhD thesis, University of Aarhus, 2007.

[101] I. S. Gradshteyn and I. M. Ryzhik, *Table of Integrals, Series, and Products*, 7th ed. Academic Press, 2007.

[102] Y. Castin and R. Dum, *Bose-Einstein Condensates in Time Dependent Traps*, Phys. Rev. Lett. **77**, 5315 (1996).

[103] H. K. Andersen, *Bose-Einstein condensates in optical lattices*, PhD thesis, University of Aarhus, 2008.

[104] I. H. A. Knottnerus, *Tweezer machine for Sr atoms using a homebuilt microscope objective from commercial lenses*, MSc Thesis. University of Amsterdam, Vrije Universiteit Amsterdam, 2018.

[105] N. Gemelke *et al.*, *In situ observation of incompressible Mott-insulating domains in ultracold atomic gases.* Nature **460**, 995 (2009).

[106] W. S. Bakr *et al.*, *A quantum gas microscope for detecting single atoms in a Hubbard-regime optical lattice*, Nature **462**, 74 (2009).

[107] J. F. Sherson *et al.*, *Single-atom-resolved fluorescence imaging of an atomic Mott insulator*, Nature **467**, 68 (2010).

[108] E. Haller *et al.*, *Single-atom imaging of fermions in a quantum-gas microscope*, Nat. Phys. **11**, 738 (2015).

[109] M. F. Parsons *et al.*, *Site-Resolved Imaging of Fermionic* ^6Li *in an Optical Lattice*, Phys. Rev. Lett. **114**, 213002 (2015).

[110] L. W. Cheuk *et al.*, *Quantum-Gas Microscope for Fermionic Atoms*, Phys. Rev. Lett. **114**, 193001 (2015).

[111] M. Miranda *et al.*, *Site-resolved imaging of ytterbium atoms in a two-dimensional optical lattice*, Phys. Rev. A **91**, 063414 (2015).

[112] R. Yamamoto *et al.*, *An ytterbium quantum gas microscope with narrow-line laser cooling*, New J. Phys. **18**, 023016 (2016).

[113] A. Cooper *et al.*, *Alkaline-Earth Atoms in Optical Tweezers*, Phys. Rev. X **8**, 041055 (2018).

[114] M. A. Norcia, A. W. Young, and A. M. Kaufman, *Microscopic Control and Detection of Ultracold Strontium in Optical-Tweezer Arrays*, Phys. Rev. X **8**, 041054 (2018).

[115] N. C. Jackson *et al.*, *Number-resolved imaging of* ^{88}Sr *atoms in a long working distance optical tweezer*, arXiv:1904.03233v2 (2019).

[116] C. Weitenberg *et al.*, *Single-spin addressing in an atomic Mott insulator*, Nature **471**, 319 (2011).

[117] D. Leibfried *et al.*, *Quantum dynamics of single trapped ions*, Rev. Mod. Phys. **75**, 281 (2003).

[118] S. Stenholm, *The semiclassical theory of laser cooling*, Rev. Mod. Phys. **58**, 699 (1986).

[119] Y. K. Kwok, *Applied Complex Variables for Scientists and Engineers*, 2nd ed. Cambridge University Press, 2010.

[120] M. N. Srnec, S. Upadhyay, and J. D. Madura, *A Python Program for Solving Schrödinger's Equation in Undergraduate Physical Chemistry*, J. Chem. Educ. **94**, 813 (2017).

[121] H. Häffner, C. Roos, and R. Blatt, *Quantum computing with trapped ions*, Phys. Rep. **469**, 155 (2008).

[122] A. M. Kaufman, B. J. Lester, and C. A. Regal, *Cooling a Single Atom in an Optical Tweezer to Its Quantum Ground State*, Phys. Rev. X **2**, 041014 (2012).

[123] M. M. Boyd, *High Precision Spectroscopy of Strontium in an Optical Lattice: Towards a New Standard for Frequency and Time*, PhD thesis, University of Colorado, 2007.

[124] *Super-resolution imaging*. Nat. Phot. Focus Issue **3**, 361 (2009).

[125] I. Knottnerus et al, *Microscope objective for imaging atomic strontium with 0.63 micrometer resolution*, arXiv:1906.07167v2 (2019).

[126] H. C. W. Beijerinck and N. F. Verster, *Velocity distribution and angular distribution of molecular beams from multichannel arrays*, J. Appl. Phys. **46**, 2083 (1975).

[127] B. Suurmeijer, T. Mulder, and J. Verhoeven, *Vacuum Science and Technology (original title: Basisboek Vacuümtechniek)*, The High Tech Institute and Settels Savenije van Amelsvoort, 2015.

[128] J. Simpson *et al.*, *Simple Analytic Expressions fro the Magnetic Field of a Circular Current Loop*. Tech. rep. NASA Technical Reports Server, 2001. Available at https://ntrs.nasa.gov/search.jsp?R=20010038494.

[129] Wolfram MathWorld, *Complete Elliptic Integral*. URL: http://mathworld.wolfram.com/CompleteEllipticIntegral.html (visited on 10/20/2018).

[130] O. Chubar, P. Elleaume, and J. Chavanne, *RADIA*. URL: http://www.esrf.eu/Accelerators/Groups/InsertionDevices/Software/Radia (visited on 06/19/2019).

[131] T. Meyrath, *Electromagnet Design Basics for Cold Atom Experiments*. 2004. URL: http://atomoptics-nas.uoregon.edu/~tbrown/files/relevant_papers/meyrath%20electromagnets.pdf (visited on 06/29/2019).

[132] G. Brown, *The Darcy-Weisbach Equation*. 2000. URL: https://bae.okstate.edu/faculty-sites/Darcy/DarcyWeisbach/Darcy-WeisbachEq.htm.

[133] J. M. McDonough, *Lectures in Elementary Fluid Dynamics: Physics, Mathematics, and Applications*. 2009. URL: http://web.engr.uky.edu/~acfd/me330-lctrs.pdf (visited on 11/06/2018).

[134] D. Apsley, *Topic T2: Flow in Pipes and Channels*. 2013. URL: https://personalpages.manchester.ac.uk/staff/david.d.apsley/lectures/hydraulics2/t2.pdf (visited on 11/06/2018).

[135] I. Nosske *et al.*, *Two-dimensional magneto-optical trap as a source for cold strontium atoms*, Phys. Rev. A **96**, 053415 (2017).

[136] J. R. De Laeter *et al.*, *Atomic weights of the elements. Review 2000 (IUPAC Technical Report)*, Pure Appl. Chem. **75**, 683 (2003).

[137] R. Senaratne *et al.*, *Effusive atomic oven nozzle design using an aligned microcapillary array*, Rev. Sci. Instrum. **86**, 023105 (2015).

[138] A. Boerboom, H. W. Reyn, and J. Kistemaker, *Heat of sublimation and vapour pressure of strontium*, Physica **30**, 254 (1964).

[139] H. J. Chizeck, E. Butterworth, and J. B. Bassingthwaighte, *Error Detection and Unit Conversion: Automated Unit Balancing in Modeling Interface Systems*, IEEE Eng. Med. Biol. Mag. **28**, 50 (2009).

[140] M. Schioppo *et al.*, *A compact and efficient strontium oven for laser-cooling experiments*, Rev. Sci. Instrum. **83**, 103101 (2012).

[141] D. J. Griffiths, *Introduction to Electrodynamics*, 3rd ed. Pearson Education, Inc, 1999.

[142] *Electrical symbols library for vector graphics.* Available at https://commons.wikimedia.org/wiki/File:Electrical_symbols_library.svg.

[143] C. Zosel, *A novel transport scheme for ultracold atoms*, MSc Thesis. Swiss Federal Institute of Technology Zurich, 2013.

[144] *Titanium Sublimation Pump & Controller Users Manual*. English. Version PN 900027, Rev E. Gamma Vacuum. 17 pp. Available at http://www.gammavacuum.com/downloads/manuals/900027_E.pdf.

[145] *Titanium Sublimation Pump & Controller Users Manual*. English. Version 3. Gamma Vacuum. 4 pp. Available at https://www.gammavacuum.com/files/9615/2448/9825/Gamma_TSP_v3.pdf.

[146] F. Schreck, *Mixtures of ultracold gases: Fermi sea and Bose-Einstein condensate of Lithium isotopes*, PhD thesis, Université Pierre et Marie Curie - Paris VI, 2002.

[147] *Hot vs. Cold Ionization Gauges*. Tech. rep. Stanford Research Systems. Available at https://www.thinksrs.com/downloads/pdfs/applicationnotes/IG1hotapp.pdf.

[148] P. A. Redhead, *Hydrogen in Vacuum Systems: An Overview*, AIP Conference Proceedings **671**, 243 (2003).

[149] C. D. Park *et al.*, *Reduction in hydrogen outgassing from stainless steels by a medium-temperature heat treatment*, J. Vac. Sci. Technol. A **26**, 1166 (2008).

[150] G. W. Kuhlman, *Forging of aluminum alloys*, In ASM Handbook: Volume 14A, p. 299, ASM International, Oxford, 2005.

[151] F. Schreck and T. Meyrath, *A Laboratory Control System for Cold Atom Experiments*. URL: http://www.strontiumbec.com/indexControl.html (visited on 11/24/2018).

[152] G. Hadley, *Injection locking of diode lasers*, IEEE J. Quantum Electron. **22**, 419 (1986).

[153] D. R. Leibrandt *et al.*, *Spherical reference cavities for frequency stabilization of lasers in non-laboratory environments*, Opt. Express **19**, 3471 (2011).

[154] B. Saxberg, B. Plotkin-Swing, and S. Gupta, *Active stabilization of a diode laser injection lock*, Rev. Sci. Instrum. **87**, 063109 (2016).

[155] S. Stellmer, R. Grimm, and F. Schreck, *Detection and manipulation of nuclear spin states in fermionic strontium*, Phys. Rev. A **84**, 043611 (2011).

[156] T. Zelevinsky *et al.*, *Narrow Line Photoassociation in an Optical Lattice*, Phys. Rev. Lett. **96**, 203201 (2006).

[157] B. Huang, *Linewidth Reduction of a Diode Laser by Optical Feedback for Strontium BEC Applications*, MSc Thesis. University of Innsbruck, 2009.

[158] E. D. Black, *An introduction to Pound–Drever–Hall laser frequency stabilization*, Am. J. Phys. **69**, 79 (2001).

[159] Franzen, A. *ComponentLibrary: a vector graphics library for illustrations of optics experiments.* Available at http://www.gwoptics.org/ComponentLibrary/.

[160] R. Paschotta, *Coherence Length*. 2018. URL: https://www.rp-photonics.com/coherence_length.html (visited on 10/18/2018).

[161] S. Stellmer, R. Grimm, and F. Schreck, *Production of quantum-degenerate strontium gases*, Phys. Rev. A **87**, 013611 (2013).

[162] A. Urech, *Work towards creating a quantum gas of strontium and the construction of* $^3P_0$*&*$^3P_2$ *ultranarrow-linewidth lasers*, MSc Thesis. University of Amsterdam, Vrije Universiteit Amsterdam, 2017.

[163] D. S. Barker *et al.*, *Enhanced magnetic trap loading for atomic strontium*, Phys. Rev. A **92**, 043418 (2015).

[164] L. R. Hunter, W. A. Walker, and D. S. Weiss, *Observation of an atomic Stark–electric-quadrupole interference*, Phys. Rev. Lett. **56**, 823 (1986).

[165] C. V. Sukumar and D. M. Brink, *Spin-flip transitions in a magnetic trap*, Phys. Rev. A **56**, 2451 (1997).

[166] J. Weiner *et al.*, *Experiments and theory in cold and ultracold collisions*, Rev. Mod. Phys. **71**, 1 (1999).

[167] S. Stellmer *et al.*, *Bose-Einstein Condensation of Strontium*, Phys. Rev. Lett. **103**, 200401 (2009).

[168] S. A. Tretter, *Communication System Design Using DSP Algorithms*, Springer Verlag US, 2008.

[169] E. Hecht, *Optics*, 4th ed. Addison Wesley, 2002.

[170] T. Mukaiyama *et al.*, *Recoil-Limited Laser Cooling of* ^{87}Sr *Atoms near the Fermi Temperature*, Phys. Rev. Lett. **90**, 113002 (2003).

[171] G. P. Greve, B Wu, and J. K. Thompson, *Laser cooling with adiabatic transfer on a Raman transition*, New J. Phys. **21**, 073045 (2019).

[172] S. J. M. Kuppens *et al.*, *Loading an optical dipole trap*, Phys. Rev. A **62**, 013406 (2000).

[173] A. Szczepkowicz *et al.*, *Optimal geometry for efficient loading of an optical dipole trap*, Phys. Rev. A **79**, 013408 (2009).

[174] Y. Huang, *A New Optical Trap System for Ultracold Strontium*, MSc Thesis. Rice University, 2013.

[175] C. J. Pethick and H. Smith, *Bose–Einstein Condensation in Dilute Gases*, 2nd ed. Cambridge University Press, 2008.

[176] S. Jochim, *Bose-Einstein Condensationof Molecules*, PhD thesis, University of Innsbruck, 2004.

[177] J. Szczepkowski *et al.*, *Analysis and calibration of absorptive images of Bose–Einstein condensate at nonzero temperatures*, Rev. Sci. Instrum. **80**, 053103 (2009).

[178] J. T. M. Walraven, *Quantum Gases lectures University of Amsterdam*. Available online at `https://staff.fnwi.uva.nl/j.t.m.walraven/walraven/Publications_files/2018-Quantum-Gases.pdf`. (version 7 April 2018).

[179] F. Gerbier *et al.*, *Experimental study of the thermodynamics of an interacting trapped Bose-Einstein condensed gas*, Phys. Rev. A **70**, 013607 (2004).

[180] G. K. Campbell, *^{87}Rubidium Bose-Einstein Condensates in Optical Lattices*, PhD thesis, Massachusetts Institute of Technology, 2006.

[181] C. C. Bradley, C. A. Sackett, and R. G. Hulet, *Analysis of in situ images of Bose-Einstein condensates of lithium*, Phys. Rev. A **55**, 3951 (1997).

[182] L. P. Pitaevskii and S. Stringari, *Bose-Einstein Condensation*, International Series of Monographs on Physics, Clarendon Press, 2003.

[183] D. S. Jin *et al.*, *Collective Excitations of a Bose-Einstein Condensate in a Dilute Gas*, Phys. Rev. Lett. **77**, 420 (1996).

[184] M.-O. Mewes *et al.*, *Collective Excitations of a Bose-Einstein Condensate in a Magnetic Trap*, Phys. Rev. Lett. **77**, 988 (1996).

[185] S. Stringari, *Collective Excitations of a Trapped Bose-Condensed Gas*, Phys. Rev. Lett. **77**, 2360 (1996).

[186] V. M. Pérez-García *et al.*, *Low Energy Excitations of a Bose-Einstein Condensate: A Time-Dependent Variational Analysis*, Phys. Rev. Lett. **77**, 5320 (1996).

[187] M. J. Martin *et al.*, *A Quantum Many-Body Spin System in an Optical Lattice Clock*, Science **341**, 632 (2013).

[188] L. F. Livi *et al.*, *Synthetic Dimensions and Spin-Orbit Coupling with an Optical Clock Transition*, Phys. Rev. Lett. **117**, 220401 (2016).

[189] S. L. Bromley *et al.*, *Dynamics of interacting fermions under spin-orbit coupling in an optical lattice clock*, Nat. Phys. **14**, 399 (2018).

[190] N. R. Cooper and A. M. Rey, *Adiabatic control of atomic dressed states for transport and sensing*, Phys. Rev. A **92**, 021401 (2015).

[191] J. P. Covey *et al.*, *2000-Times Repeated Imaging of Strontium Atoms in Clock-Magic Tweezer Arrays*, Phys. Rev. Lett. **122**, 173201 (2019).

[192] K. Shibata *et al.*, *A scalable quantum computer with ultranarrow optical transition of ultracold neutral atoms in an optical lattice*, Appl. Phys. B **97**, 753 (2009).

[193] A. V. Gorshkov *et al.*, *Alkaline-Earth-Metal Atoms as Few-Qubit Quantum Registers*, Phys. Rev. Lett. **102**, 110503 (2009).

[194] N. Yu and M. Tinto, *Gravitational wave detection with single-laser atom interferometers*, Gen. Relativ. Gravit. **43**, 1943–1952 (2011).

[195] P. W. Graham *et al.*, *New Method for Gravitational Wave Detection with Atomic Sensors*, Phys. Rev. Lett. **110**, 171102 (2013).

[196] S. Kolkowitz *et al.*, *Gravitational wave detection with optical lattice atomic clocks*, Phys. Rev. D **94**, 124043 (2016).

[197] S. Kato *et al.*, *Optical magnetic resonance imaging with an ultra-narrow optical transition*, Appl. Phys. B **108**, 31 (2012).

[198] K. Shibata *et al.*, *Optical spectral imaging of a single layer of a quantum gas with an ultranarrow optical transition*, Phys. Rev. A **89**, 031601 (2014).

[199] N. Goldman *et al.*, *Optical spectral imaging of a single layer of a quantum gas with an ultranarrow optical transition*, Rep. Prog. Phys. **77**, 126401 (2014).

[200] Y.-J. Lin *et al.*, *Bose-Einstein Condensate in a Uniform Light-Induced Vector Potential*, Phys. Rev. Lett. **102**, 130401 (2009).

[201] M. Mancini *et al.*, *Observation of chiral edge states with neutral fermions in synthetic Hall ribbons*, Science **349**, 1510 (2015).

[202] B. Song *et al.*, *Observation of symmetry-protected topological band with ultracold fermions*, Sci. Adv. **4**, (2018).

[203] F. Leroux *et al.*, *Non-Abelian adiabatic geometric transformations in a cold strontium gas*, Nat. Commun. **9**, 3580 (2018).

[204] F. Gerbier and J. Dalibard, *Gauge fields for ultracold atoms in optical superlattices*, New J. Phys. **12**, 033007 (2010).

[205] D. G. Green *et al.*, *Quantum chaos in ultracold collisions between Yb($^1S_0$) and Yb($^3P_2$)*, Phys. Rev. A **93**, 022703 (2016).

[206] S. Taie *et al.*, *Feshbach-Resonance-Enhanced Coherent Atom-Molecule Conversion with Ultranarrow Photoassociation Resonance*, Phys. Rev. Lett. **116**, 043202 (2016).

[207] Y. Takasu *et al.*, *Magnetoassociation of a Feshbach molecule and spin-orbit interaction between the ground and electronically excited states*, Phys. Rev. A **96**, 023602 (2017).

[208] A. Khramov *et al.*, *Ultracold Heteronuclear Mixture of Ground and Excited State Atoms*, Phys. Rev. Lett. **112**, 033201 (2014).

[209] H. Hara *et al.*, *A Three-Dimensional Optical Lattice of Ytterbium and Lithium Atomic Gas Mixture*, J. Phys. Soc. Jpn. **83**, 014003 (2014).

[210] W. Dowd *et al.*, *Magnetic field dependent interactions in an ultracold Li–Yb($^3P_2$) mixture*, New J. Phys. **17**, 055007 (2015).

[211] H. Konishi *et al.*, *Collisional stability of localized Yb($^3P_2$) atoms immersed in a Fermi sea of Li*, New J. Phys. **18**, 103009 (2016).

[212] M. L. González-Martínez and J. M. Hutson, *Magnetically tunable Feshbach resonances in Li + Yb(^3P_J)*, Phys. Rev. A **88**, 020701 (2013).

[213] A. Petrov, C. Makrides, and S. Kotochigova, *Magnetic control of ultracold ^{6}Li and ^{174}Yb($^3P_2$) atom mixtures with Feshbach resonances*, New J. Phys. **17**, 045010 (2015).

[214] T. Chen *et al.*, *Anisotropy induced Feshbach resonances in mixture of $^6Li(^2S) +^{171} Yb(^3P_2)$*, New J. Phys. **17**, 103036 (2015).

[215] A. Derevianko, *Feasibility of Cooling and Trapping Metastable Alkaline-Earth Atoms*, Phys. Rev. Lett. **87**, 023002 (2001).

[216] R. Santra, K. V. Christ, and C. H. Greene, *Properties of metastable alkaline-earth-metal atoms calculated using an accurate effective core potential*, Phys. Rev. A **69**, 042510 (2004).

[217] S. G. Bhongale *et al.*, *Quantum Phases of Quadrupolar Fermi Gases in Optical Lattices*, Phys. Rev. Lett. **110**, 155301 (2013).

[218] M. Lahrz *et al.*, *Detecting quadrupole interactions in ultracold Fermi gases*, Phys. Rev. A **89**, 043616 (2014).

[219] W.-M. Huang, M. Lahrz, and L. Mathey, *Quantum phases of quadrupolar Fermi gases in coupled one-dimensional systems*, Phys. Rev. A **89**, 013604 (2014).

[220] S. Taie *et al.*, *An SU(6) Mott insulator of an atomic Fermi gas realized by large-spin Pomeranchuk cooling*, Nat. Phys. **8**, 825 (2012).

[221] H. Ozawa *et al.*, *Antiferromagnetic Spin Correlation of SU(N) Fermi Gas in an Optical Superlattice*, Phys. Rev. Lett. **121**, (2018).

[222] H. Knöckel and E. Tiemann, *Program IODINESPEC5: Version for strontium quantum gas group, University of Amsterdam, Feb. 2017*, Institute of Quantum Optics, Leibniz University, Hannover, Germany.

[223] G. Ferrari *et al.*, *Precision Frequency Measurement of Visible Intercombination Lines of Strontium*, Phys. Rev. Lett. **91**, 243002 (2003).

[224] T. W. Hänsch, I. S. Shahin, and A. L. Schawlow, *High-Resolution Saturation Spectroscopy of the Sodium D Lines with a Pulsed Tunable Dye Laser*, Phys. Rev. Lett. **27**, 707 (1971).

[225] Y.-C. Huang *et al.*, *Precise frequency measurements of iodine hyperfine transitions at 671 nm*, Appl. Opt. **52**, 1448 (2013).

[226] D. J. McCarron, S. A. King, and S. L. Cornish, *Modulation transfer spectroscopy in atomic rubidium*, Meas. Sci. Technol. **19**, 105601 (2008).

[227] N. Poli *et al.*, *A simplified optical lattice clock*, Appl. Phys. B **97**, 27 (2009).

[228] A. Yamaguchi, *Metastable State of Ultracold and Quantum Degenerate Ytterbium Atoms: High-Resolution Spectroscopy and Cold Collisions*, PhD thesis, Kyoto University, 2008.

[229] J. E. Sansonetti and G. Nave, *Wavelengths, Transition Probabilities, and Energy Levels for the Spectrum of Neutral Strontium (SrI)*, J. Phys. Chem. Ref. Data **39**, 033103 (2010).

[230] S. M. Heider and G. O. Brink, *Hyperfine structure of* ^{87}Sr *in the* $^3P_2$ *metastable state*, Phys. Rev. A **16**, 1371 (1977).

[231] D. Bender, H. Brand, and V. Pfeufer, *Isotope shifts in transitions between low-lying levels of Sr I by laser-atomic-beam spectroscopy*, Z. Phys. A: Atoms and Nuclei **318**, 291 (1984).

[232] F. Buchinger *et al.*, *Influence of the N=50 shell closure on mean square charge radii of strontium*, Phys. Rev. C **32**, 2058 (1985).

[233] T. Takano, R. Mizushima, and H. Katori, *Precise determination of the isotope shift of* $^{88}Sr-^{87}Sr$ *optical lattice clock by sharing perturbations*, Appl. Phys. Express **10**, 072801 (2017).

[234] I. Courtillot *et al.*, *Accurate spectroscopy of Sr atoms*, Eur. Phys. J. D **33**, 161 (2005).

[235] A Yamaguchi *et al.*, *High-resolution laser spectroscopy of a Bose–Einstein condensate using the ultranarrow magnetic quadrupole transition*, New. J. Phys. **12**, 103001 (2010).

[236] S. Stellmer and F. Schreck, *Reservoir spectroscopy of* $5s5p\ ^3P_2$–$5snd\ ^3D_{1,2,3}$ *transitions in strontium*, Phys. Rev. A **90**, 022512 (2014).

[237] S. Uetake *et al.*, *Spin-dependent collision of ultracold metastable atoms*, Phys. Rev. A **86**, 032712 (2012).

[238] A. Dareau *et al.*, *Doppler spectroscopy of an ytterbium Bose-Einstein condensate on the clock transition*, Phys. Rev. A **91**, 023626 (2015).

[239] A. M. Kaufman, B. J. Lester, and C. A. Regal, *Cooling a Single Atom in an Optical Tweezer to Its Quantum Ground State*, Phys. Rev. X **2**, 041014 (2012).

[240] D. Barredo *et al.*, *Synthetic three-dimensional atomic structures assembled atom by atom*, Nature **561**, 79 (2018).

[241] L. R. Liu *et al.*, *Building one molecule from a reservoir of two atoms*, Science **360**, 900 (2018).

[242] S. Saskin *et al.*, *Narrow-Line Cooling and Imaging of Ytterbium Atoms in an Optical Tweezer Array*, Phys. Rev. Lett. **122**, 143002 (2019).

[243] G. Pagano, F. Scazza, and M. Foss-Feig, *Fast and Scalable Quantum Information Processing with Two-Electron Atoms in Optical Tweezer Arrays*, Adv. Quantum Technol. 1800067 (2019).